# Phaseless Electromagnetic Field Transformations for Magnitude-Only and Partially Coherent Field Data

Alexander Helmut Paulus

Vollständiger Abdruck der von der Fakultät für Elektrotechnik und Informationstechnik der Technischen Universität München zur Erlangung des akademischen Grades eines

*Doktors der Ingenieurwissenschaften*

genehmigten Dissertation.

# Zusammenfassung

Zukünftige Messverfahren zur elektromagnetischen Validierung und Verifikation von Antennen erfordern Nachbearbeitungsalgorithmen, die zuverlässig mit phasenlosen Daten arbeiten. Eine übliche Aufgabenstellung ist dabei die Bestimmung der Fernfeld (FF)-Strahlungseigenschaften einer unbekannten Antenne aus Nahfeld (NF)-Messungen, welche traditionell sowohl den Betrag als auch die Phase der mit einer Sondenantenne abgetasteten Felder voraussetzt. Während bei Vorhandensein der Phaseninformation lineare Gleichungssysteme gelöst werden müssen, führt das Fehlen der Phase auf das Problem der Phasenrekonstruktion. Die Rückgewinnung der Phase aus gemessenen Beträgen stellt ein seit Jahrzehnten aktives Forschungsgebiet dar und bleibt aufgrund der weitreichenden Anwendungsmöglichkeiten, allerdings auch aufgrund seiner Nichtlinearität, hochaktuell.

Diese Arbeit befasst sich mit der Phasenrückgewinnung im Rahmen von Antennenmessungen, wofür gängige Ansätze unzufriedenstellende Ergebnisse liefern. Zunächst werden die Theorie und grundlegende Routinen, die für elektromagnetische Feldtransformationen mit vollständiger Phaseninformation erforderlich sind, eingeführt und erläutert. Anschließend wird ein vielseitiges Rahmenwerk zur Behandlung von Optimierungsproblemen entworfen und eingesetzt, um bestehende konvexe und nichtkonvexe, sowie neu entwickelte Formulierungen für die Phasenrekonstruktion aus Betragsdaten zu untersuchen.

Dabei zeigt sich, dass sich die Qualität der gewonnenen Phase drastisch verschlechtert, wenn anstelle eines zufällig verteilten Datenmodells, welches in der Literatur weitverbreitet ist, das einer realistischen NF-Antennenmessung verwendet wird. Derselbe Trend zeichnet sich bei einer umfangreichen Untersuchung von Methoden zur Initialisierung der Phasenrekonstruktion mit Zufalls- und NF-Daten ab — zusätzlich ist der Unterschied stärker ausgeprägt, je größer die Dimensionen der Problemstellung werden. Variationen in der Leistungsfähigkeit diverser Lösungsansätze, z.B. im Vergleich von konvexen mit nichtkonvexen Algorithmen, sind angesichts dieser dominanten Abhängigkeit von der Qualität und Eignung der Messdaten nahezu vernachlässigbar. Diesbezüglich sind die Hauptunterschiede der Methoden in den benötigten Rechenzeiten und Speicherressourcen zu finden.

Ein wahrer Paradigmenwechsel wird mit der Einführung des Konzeptes von teilkohärenten Beobachtungen vollzogen. Die zumindest teilweise Kenntnis von Phasentermen erlaubt die Entwicklung und Anwendung von linearisierten, und damit zuverlässigen, Phasenrekonstruktionsalgorithmen, deren Anwendungsbereich keineswegs auf die Antennenmesstechnik beschränkt ist. Der Fall von teilkohärenten Messungen kann als eine Unterklasse des ursprünglichen Problems der Phasenrekonstruktion betrachtet werden: Hierbei wird vorausgesetzt, dass ein Teil der Einträge im Messvektor einen bekannten Phasenbezug aufweist. Effektiv reduziert sich dadurch die Anzahl der noch zu bestimmenden Phasenterme. Zwei praktisch relevante Möglichkeiten zur Aufzeichnung der nötigen Phasendifferenzen bei NF-Antennenmessungen werden in dieser Arbeit vorgestellt und besprochen: breitbandige NF-Messungen und Messungen mit Mehrkanalempfängern. In den Untersuchungen weisen die linearisierten Formulierungen für teilkohärente Daten große Ähnlichkeiten mit einer vollkohärenten Transformation auf. Insbesondere wird für Teilkohärenz ein deterministischer Schwellenwert für die zum Erfolg der Transformation benötigte Anzahl von Messungen hergeleitet. Dieser steht im starken Kontrast zu den lediglich probabilistischen Aussagen, welche für vollständig phasenlose Algorithmen existieren. Sobald dieser Schwellenwert überschritten wird, erhält man

ähnliche Ergebnisse wie bei einer Transformation mit vollständiger Phaseninformation, allerdings auf Kosten einer erhöhten Rauschempfindlichkeit.

Das Konzept der Phasenrekonstruktion wird anschließend für die Transformation von NF-Antennendaten unter dem Einfluss eines Störobjektes erweitert, wobei sowohl der Fall vollständiger als auch unvollständiger Phaseninformation betrachtet wird. Wie sich zeigt, sind die linearisierten Formulierungen mit teilkohärenten Daten, die über einen mehrkanaligen Empfänger gewonnen werden, in der Lage, den Einfluss eines Echoobjektes auf ein ähnliches Niveau zu reduzieren, wie es unter Nutzung vollständiger Phaseninformation möglich ist.

# Abstract

Future electromagnetic antenna validation and verification measurements require post-pro-cessing algorithms to reliably function with phaseless data. Typical tasks include the determination of far-field (FF) radiation properties of an unknown antenna under test (AUT) from near-field (NF) measurements, which have traditionally been carried out with knowledge of the magnitude and phase of the fields sampled with a probe antenna. While in this context processing of complex-valued data requires linear systems of equations to be solved, the lack of phase information leads to the so-called phase retrieval problem. Phase reconstruction has been an active field of research for decades and remains to be a hot topic, due to its widespread potential applications, however, also because of its nonlinearity.

This work tackles the task of phase retrieval in the context of antenna measurements, for which common approaches have been observed to perform poorly. The theory and basic, yet capable, routines for electromagnetic field transformations based on full phase information are introduced and explained first. Afterwards, a versatile optimization framework is set up and employed to compare existing convex and nonconvex, as well as newly designed formulations for the phase reconstruction from fully incoherent data. Drastic differences in phase retrieval performance are reported when comparing the results for a random data model, which is typically assumed in literature, with the results for realistic NF antenna data. A thorough investigation of phase retrieval initialization methods with random and NF data confirms the discrepancies, which are found to be more pronounced with increasing problem dimensions. Compared to the dominant data dependency, variations among solvers, e.g., convex compared to nonconvex algorithms, are observed to be of moderate degree. Notable differences are rather found in terms of the required computational complexity and resources.

A paradigm shift is achieved with the introduction of the concept of partially coherent observations, which allows for the design and application of linearized and reliable phase reconstruction algorithms — not limited to the application in antenna measurements. This sub-class of phase retrieval problems requires portions of phase differences to be available in the measurement vectors, which can for example be obtained by multi-frequency measurements or by measurements with multi-channel receivers (RXs). The behavior of the linearized formulations for partially coherent data is seen to be similar to that of fully coherent transformations. In particular, a deterministic threshold for the required number of measurements exists, which is in contrast to the probabilistic statements for completely phaseless algorithms. Once this threshold is exceeded, results similar to that of a coherent transformation are obtained — at the expense of an increased susceptibility to noise.

The same concepts can be extended to the task of echo object modeling in NF measurement scenarios with varying degrees of phase information. As seen in this work, the linearized formulations with partially coherent data obtained via multi-channel RXs are able to suppress echo contributions at a level similar to that possible with methods utilizing fully coherent data.

# Contents

*Contents*

# Acknowledgment

Munich, Germany

June, 2022

Alexander Paulus

# 1.  Introduction

This dissertation intends to provide essential knowledge and insights on the topic of phase retrieval in phaseless near-field (NF) far-field (FF) transformations (NFFFTs). Belonging to the fields of computational electromagnetics and antenna measurement techniques, field transformations represent a well established topic in high-frequency engineering. It is the existing solid theoretical background that allows to mainly focus on the *phaseless* aspects in this field, which are associated with the task of phase retrieval. As by-products of the investigations on phaseless NFFFTs, we will obtain tools allowing us to also tackle other nonlinear problems in electromagnetics and possibly beyond. Phase retrieval itself is not a problem that first occurred in high-frequency engineering, but stems from the field of optics [Fienup 1982; Gerchberg and Saxton 1972] and imaging [Fogel et al. 2016; Holloway et al. 2016; Tian and Waller 2015] with its many applications in X-ray crystallography [Harrison 1993; Miao et al. 2008, 2012; Pfeiffer et al. 2006], transmission (electron) microscopy [Coene et al. 1992; Faulkner and Rodenburg 2004; Kou et al. 2010], coherent diffraction imaging [Bacca et al. 2019; Guizar-Sicairos and Fienup 2008] and ptychography [Ramos et al. 2019].

Abstractly speaking, phase retrieval is the problem of recovering an unknown portion of a signal from its known parts. In case of complex numbers, magnitude and phase can be the known and unknown portions, respectively. While the task of phase retrieval arises naturally in the context of phaseless field transformations — where information about the phase of the measurement signal is not known — it may be difficult to quickly develop a feeling or intuition for the problem from its application in antenna measurements. Thus, it makes sense to start with another, maybe artificial, application of phase retrieval, which directly provides the motivated apprentice with imaginable quantities and, hopefully, a first insight of what is going on.

## 1.1  The Concept of Phase Retrieval

Geometric arrangements in two-dimensional space are often used to illustrate complicated problems in a simple but meaningful way. Luckily, we can construct a simple phase retrieval problem based on polygonal chains in two-dimensional space. Consider the point cloud in Fig. 1.1(a) which defines a low-polygonal representation of a dog from the side, also depicted in Fig. 1.1(b). Each vertex is defined by its $x$- and $y$-coordinate, which can be interpreted as the real and imaginary parts of complex numbers. The polygonal picture itself is generated by drawing the connection between specific vertices, shaping the contour of the dog. The image of the dog can thus uniquely be defined by stating the absolute coordinates of the vertices — a complex number for each vertex — or by defining the separation between each vertex to all other vertices in the cloud and to the origin of the coordinate system. In both ways, the picture is defined without any degrees of freedom (DoFs) left — the absolute locations of the vertices fixes the image in place. For the purpose of illustrating the task of phase retrieval, we will continue with the second way of defining the polygonal image, utilizing the separation vectors between the vertices. Since each vertex can be interpreted as a complex number, the difference between two vertices, i.e., the separation vector, is also a complex-valued scalar. Now, assume that we only have the magnitude information, i.e., we only know the distances between certain vertices, but not the orientation or absolute alignment of the vertices in the two-dimensional space. Again, knowing the complex separations between the vertices, i.e., length and orientation of the separation vectors, would allow us to immediately draw the original
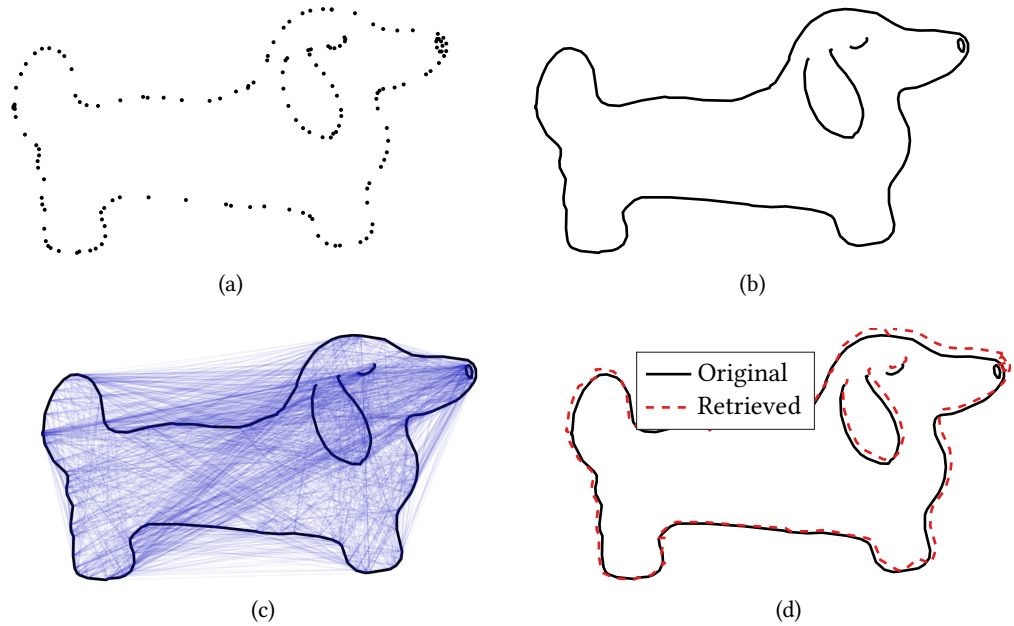
Fig. 1.1 Illustration of contour reconstruction as a phase retrieval problem. A two-dimensional point cloud in (a) defines the contour of a dog shown in (b). Knowing only the distances between pairs of points in the cloud, indicated by blue lines in (c), the task of reconstructing the locations of the points can be cast as a phase retrieval problem. Knowing the distances indicated in (c), the contour shown in (d) is retrieved.

image. In addition, knowing the complex separation of one vertex to the origin of the coordinate system would allow to place it at the very same location as the original arrangement. Dropping the phase information leaves us with our first phase retrieval problem, namely to reconstruct the image only knowing the relative distances between vertices to each other. It is also clear that for $n$ vertices there are in total $n(n-1)$ distances among the vertices as well as $n$ distances from the vertices to the origin of the coordinate system. Knowing all of these $n^2$ magnitudes guarantees that the image is uniquely defined. Finding the correct locations from these $n^2$ magnitudes yet remains a nontrivial task, as will be seen at a later point. Furthermore, one can see that knowing only the $n-1$ distances on the contour of the dog, even in addition to the distance of the first point to the origin — leading to a total of $n$ measurements —, can not guarantee a unique and correctly reconstructed contour in general. As there are $n$ unknown points, represented by $n$ complex numbers, there are in total $2n$ unknowns corresponding to the $x$- and $y$-coordinates or real and imaginary parts. So the number of measurements $m$, i.e., the number of distances between vertices, we have to consider, should be in the range $m \in \{2n, ..., n^2\}$ — hopefully at the lower end. Indeed, the number of measurements required by a phase retrieval algorithm in order to be successful is one of the core figures of merit used to compare phase retrieval methods and will be briefly discussed later.

In our particular example with the contour of the dog, knowing the $m = 15n$ distances indicated by thin blue lines in Fig. 1.1(c), the shape of the dog as depicted in Fig. 1.1(d) can be retrieved. Since the choice of algorithm is likely to have major impact on the results of phase retrieval, a manifold of approaches are investigated and discussed in this work.
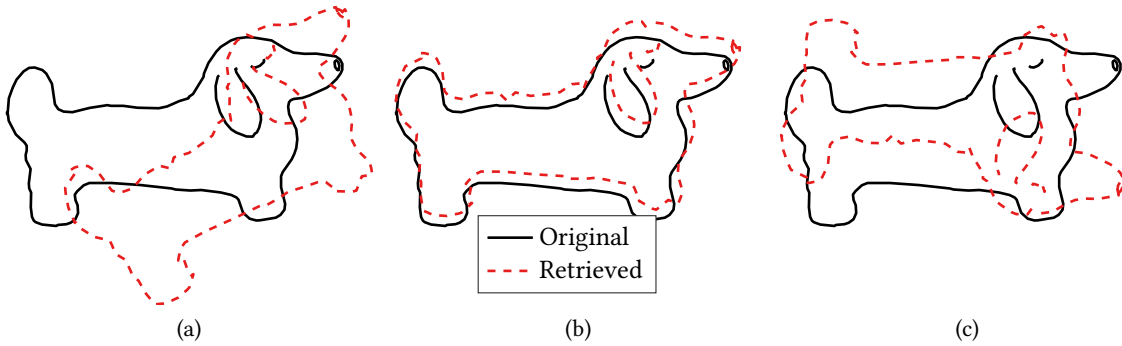
Fig. 1.2 Three exemplary trivial ambiguities that may occur in phase retrieval, illustrated for the problem in Fig. 1.1. The reconstruction in (a) exhibits an arbitrary rotation (global phase shift) that can not be resolved based on the magnitude information. In (b), the retrieved contour is translated in 2D space. Adding the absolute distance of one point to the origin of the coordinate system could fix this ambiguity. The complex conjugated solution in (c) exhibits the same distances between the points as the original contour. Here, complex conjugation leads to a mirrored image.

It should already be evident that a reconstruction based on magnitude information may at most agree with the ground truth up to an ambiguous global phase. In case of the contour reconstruction, the image can only be determined up to an arbitrary rotation around the origin of the coordinate system. In Fig. 1.1(d), this rotation has already been compensated for. Any solution multiplied with a scalar phase term exhibits the same magnitude information — this is commonly referred to as one trivial ambiguity of the phase retrieval problem. For the example of the dog, three possible trivial ambiguities are depicted in Fig. 1.2, including the already mentioned global phase shift. Dependent on the problem statement, some of them may be avoided, e.g., by arbitrarily fixing the phase of one entry in the measurement vector, the global phase is fixed. Since in Fig. 1.1(c) no distance between any point on the contour and the origin of the coordinate system has been considered, the contour of the dog can only be retrieved up to an arbitrary translation in $x$- and $y$-direction. As indicated in Fig. 1.2(c), phase retrieval algorithms may not be able to differentiate the solution from its complex conjugate, here leading to a mirrored dog shape.

So how can we make sure that there are no false solutions or other nontrivial ambiguities? This immediately leads to another essential question of phase retrieval: How can we ensure a unique solution? As this question is so fundamental, it may be especially unsatisfactory that there is no universal answer. The few existing statements in this direction are briefly discussed later in this thesis.

Let us leave aside the illustration of phase retrieval with two-dimensional point clouds and come back to the major focus of this thesis, namely the application of phase retrieval in the context of phaseless antenna field transformations. For the moment, it is sufficient to think of a phaseless field transformation as a two-fold post-processing technique for antenna measurement data. Dependent on the phaseless transformation approach, the two stages may not always be separable. Still, a two-part process could proceed as follows. Starting from magnitude-only data, a phase retrieval technique is applied to restore the corresponding phase, resulting in complex-valued

field information. The latter is then fed to an existing field transformation algorithm — a research topic of its own — in order to obtain the desired radiation characteristic of the AUT.

As a consequence, antenna field transformation algorithms assigned with the prefix "phaseless", "magnitude-only", "incoherent" or similar, commonly involve some form of phase retrieval. However, this seemingly simple separation of phase reconstruction and field transformation should not distract from a fundamental truth: Phase retrieval from phaseless antenna data is *different* than that from other magnitude data, e.g., taken from random distributions. While this statement may sound obvious and trivial, its consequences *are not*. In fact, the discrepancies in the data models employed with phase retrieval in various applications compared to that of NF antenna measurements are among the main reasons for the eligible existence of this dissertation. This claim will be seen to gain in sustainability when diving deeper into the thesis.

## 1.2 Outline

Two main ingredients are required for the treatment of phaseless antenna field transformations. First, electromagnetic field theory is necessary for the description and modeling of radiation phenomena, and second, a good knowledge of nonlinear optimization theory is required for the discussion of phase retrieval formulations. For the purpose of this thesis, time-harmonic electromagnetic fields are considered and described by equations in the frequency domain. Transient phenomena could be treated when working with a superposition of signals at multiple frequencies, which, for the sake of brevity, is not addressed in this work.

Starting with electromagnetics, Chapter 2 provides a selection of electromagnetic sources for the time-harmonic modeling of radiating objects as well as an excerpt of electromagnetic theorems. A particular focus is put on a parallelized implementation of the derived radiation operators for electric and magnetic current densities of infinitesimal extent. Afterwards, the core concepts of nonlinear nonconvex optimization in complex-valued variables are introduced in Chapter 3, at the end of which a versatile optimization framework is constructed. Electromagnetics and the optimization framework are then combined in Chapter 4, where the fundamentals of antenna field transformations with full phase information are presented. The results therein provide a clear picture of what is expected from the phaseless field transformations introduced in Chapter 5, which first details the task of phase retrieval and its initialization methods. Existing nonconvex techniques are recapitulated and put in perspective with proposed formulations implemented via the optimization framework. Furthermore, three existing convex retrieval algorithms are reviewed and applied to random as well as NF antenna data. The chapter ends with the presentation of an exact and direct phase retrieval algorithm for which a simplistic implementation is provided.

The rules truly change with the introduction of the concept of partially coherent measurements in Chapter 6. Partial coherence features a widespread field of applications while allowing to construct predictable and reliable algorithms. A thorough analysis of proposed linearized formulations for phase reconstruction with local phase information as well as spectral phase differences is provided, giving insights and further understanding of the phase retrieval problem. Showcasing further extensions of the concept of field transformations and phase retrieval, Chapter 7 deals with source-based obstacle modeling techniques with full and limited phase information, allowing to more realistically model NF antenna measurement setups. Finally, Chapter 8 summarizes and concludes this dissertation, not without providing recommendations for future research in this field.

At various points, the appendix can be consulted for supplementary information and detailed derivations. The aforementioned optimization framework has also been applied to other nonlinear field transformation tasks, e.g., showcasing the complementary problem of magnitude retrieval. For the sake of brevity and conciseness of this work, not all of these transformation concepts, e.g., where the probe and the AUT are unknown, are discussed. Furthermore, concluding remarks are scattered throughout this work, allowing to quickly grasp the core insights at the end of most larger sections. The rushed reader may find it helpful to skip lengthy parts and resort to these essential findings.

## 1.3 Notation

Throughout this thesis, vectors of arbitrary dimension, mainly used in numerical computations, will be denoted by bold, italic letters, e.g., $\boldsymbol{z}$, while matrices are represented by upper-case, bold, upright letters, e.g., $\mathbf{A}$. Vectors in three-dimensional space, for which the divergence and rotation are well defined, are written in bold, italic letters underlined by a bar, e.g., the electric field $\underline{\boldsymbol{E}}$. Dyads are written in bold, upright letters and are underlined, e.g., $\underline{\mathbf{I}}$. In general, anything in bold font represents a multidimensional quantity, while scalars are typeset in non-bold font. For vectors, $[\boldsymbol{b}]_i$ extracts the $i$th entry and for matrices $[\mathbf{A}]_{m,n}$ picks the entry in the $m$th row and $n$th column. The Euler number is written as e, and the imaginary unit as $\sqrt{-1} = \mathrm{j}$.

Particular nonlinear operators, mainly encountered in the context of optimization, are denoted by upper-case, calligraphic letters, e.g., $\mathcal{A}$. The real and imaginary parts of complex quantities can element-wise be obtained via the Re{.} and Im{.} operators. Complex conjugation is indicated by a horizontal line above the respective quantity, e.g., $\overline{z}$. The phase of a complex-valued quantity in radians is element-wise returned by the function $\angle\,(\boldsymbol{z})$. In all cases, the magnitude operator |.| applied to *any* quantity is evaluated *element-wise*. The same holds true when the exponential function is applied to vectors, i.e.,

$$\mathrm{e}^{\boldsymbol{z}} \equiv \mathrm{e}^{[\boldsymbol{z}]_i} \quad \forall i \in \{1, ..., n\}, \ \boldsymbol{z} \in \mathbb{C}^{n \times 1}. \tag{1.1}$$

An element-wise multiplication of vectors or matrices, i.e., the Hadamard product, is denoted by $\boldsymbol{a} \circ \boldsymbol{b}$.

The function diag (.), when applied to matrices, extracts the diagonal elements and forms a column vector, or, when applied to vectors, creates a diagonal matrix. The operation max (.) and min (.) return the maximum and minimum values from a vector. The functions $\lceil x \rceil$ and $\lfloor x \rfloor$ return the ceil and floor of real-valued scalars. Defined to operate on vectors, the function std(.) returns the standard deviation of a potentially complex-valued vector. The sign (.) function extracts the sign of scalar arguments, whereas the median of a vector quantity is returned by median (.). The trace and rank of a matrix $\mathbf{A}$ are denoted by $\mathrm{Tr}(\mathbf{A})$ and rank$(\mathbf{A})$. The inverse and — whenever the inverse does not exist — the Moore-Penrose pseudoinverse of a matrix $\mathbf{A}$ is denoted by $\mathbf{A}^{-1}$. The transpose and complex-conjugate transpose, i.e., Hermitian, of non-scalar quantities are denoted by $\boldsymbol{z}^{\mathrm{T}}$ and $\boldsymbol{z}^{\mathrm{H}}$, respectively.

# 2. Radiation of Electromagnetic Sources in Free Space

Phaseless antenna field transformations represent a challenging interdisciplinary task bringing together fundamental concepts from electromagnetics and procedures from optimization theory. We make a start by covering the essential equations governing electromagnetic radiation in isotropic, homogeneous, lossless media, e.g., free space. With the introduction of the uniqueness and equivalence theorem we are then able to treat problems in inhomogeneous space and, effectively, perform field transformations.

   We first discuss two ways of modeling sources of time-harmonic electromagnetic radiation, the spherical vector wave functions and the concept of current densities. More details will be provided on the topic of current densities with a focus on infinitesimally small electric and magnetic current densities, also referred to as Hertzian and Fitzgerald dipoles. For both models, a linear radiation operator, i.e., a matrix, relating radiated fields and source coefficients will be derived, where again more details are provided for the Hertzian and Fitzgerald dipoles. Afterwards, two crucial electromagnetic theorems — the uniqueness theorem and the equivalence theorem — are discussed, providing the theoretical reasoning for the principle of the field transformations of later chapters. Essentially, the theorems tell us how to apply the radiation operators in order to model and solve the field transformations discussed in the main part of this thesis.

## 2.1 Spherical Vector Wave Functions and Degrees of Freedom in Electromagnetic Radiation

This section closely follows the path of thought of [Hansen 2008] in order to determine a basis for the description of electromagnetic radiation in three-dimensional space. We solely concentrate on time-harmonic signals with a time dependency of $e^{+j\omega t}$. Transient effects could be modeled via a linear superposition of multiple frequencies, however, are not in the focus of this work.

   On a macroscopic level, all fields and waves within linear, isotropic and continuous media have experimentally been observed to follow the Maxwell equations [Jin 2015, p. 34]

$$\nabla \times \underline{H} = j\omega\varepsilon\underline{E} + \underline{J} \tag{2.1}$$

$$\nabla \times \underline{E} = -j\omega\mu\underline{H} - \underline{M} \tag{2.2}$$

$$\nabla \cdot \underline{D} = \rho_e \tag{2.3}$$

$$\nabla \cdot \underline{B} = \rho_m. \tag{2.4}$$

One of the many statements emerging from the Maxwell equations is that the electric field $\underline{E}$ and the magnetic field $\underline{H}$ at an angular frequency $\omega = 2\pi f$ are coupled and, at the same time, are generated by their respective sources, the electric and magnetic current densities $\underline{J}$ and $\underline{M}$. Whenever the frequency is nonzero, the electric field gives rise to a magnetic field and vice-versa via (2.1) and (2.2), allowing for a self-sustained, propagating electromagnetic field — the concept of *radiation*. The remaining two equations, (2.3) and (2.4), assign the electric and magnetic flux $\underline{D}$ and $\underline{B}$ to the charge densities $\rho_e$ and $\rho_m$. Due to the assumed linearity and isotropy, we may link fields and fluxes via

the material relations $\underline{D} = \varepsilon\underline{E}$ and $\underline{B} = \mu\underline{H}$, where the surrounding material is described by the scalar permittivity $\varepsilon$ and permeability $\mu$. Note that one commonly sets the right-hand side of (2.4) to zero, however, the discussion on the existence of magnetic monopoles is still ongoing [Ambrosio et al. 2002; Preskill 1984; Rajantie 2012].

Let us come back to our main task and derive a mathematical basis for the representation of electromagnetic fields. Starting from the Maxwell equations, one can show that in the source-free case, i.e., $\underline{J} = \underline{M} = \underline{0}$ and $\rho_e = \rho_m = 0$, the electric and magnetic fields fulfill the vector curl-curl equation

$$\nabla \times \left(\nabla \times \underline{C}\right) - k^2\underline{C} = \mathbf{0} \tag{2.5}$$

with the wavenumber $k = \omega\sqrt{\varepsilon\mu} = 2\pi/\lambda$. Skipping the details, one can then verify that the vector wave functions

$$\underline{f}_{1mn}(r, \vartheta, \varphi) = \frac{1}{\sqrt{2\pi}}\frac{1}{\sqrt{n(n+1)}}\left(-\text{sign}(m)\right)^m e^{-j\omega\varphi} z_n^{(4)}(kr)\left[j\,\text{sign}(m)\,T_1\underline{e}_\vartheta - T_2\underline{e}_\varphi\right] \tag{2.6}$$

$$\underline{f}_{2mn}(r, \vartheta, \varphi) = \frac{-1}{\sqrt{2\pi}}\frac{1}{\sqrt{n(n+1)}}\left(-\text{sign}(m)\right)^m e^{-j\omega\varphi}\frac{1}{2n+1}$$

$$\left[(n(n+1))\left(z_{n-1}^{(4)}(kr) + z_{n+1}^{(4)}(kr)\right)\overline{P}_n^{|m|}(\cos\vartheta)\,\underline{e}_r\right.$$

$$\left. - \left((n+1)z_{n-1}^{(4)}(kr) - nz_{n+1}^{(4)}(kr)\right)\left(T_2\underline{e}_\vartheta + j\,\text{sign}(m)\,T_1\underline{e}_\varphi\right)\right] \tag{2.7}$$

with

$$T_1 = \begin{cases} 0 & m = 0 \\ |m|\sin\vartheta\,\overline{P}_n^{|m|}(\cos\vartheta) \\ \quad +\frac{1}{2}\cos\vartheta\left[t_1\overline{P}_n^{|m|-1}(\cos\vartheta) + t_2\overline{P}_n^{|m|+1}(\cos\vartheta)\right] & |m| > 0 \end{cases} \tag{2.8}$$

$$T_2 = \begin{cases} t_2\overline{P}_n^1(\cos\vartheta) & m = 0 \\ \frac{1}{2}\left[t_2\overline{P}_n^{|m|+1}(\cos\vartheta) - t_1\overline{P}_n^{|m|-1}(\cos\vartheta)\right] & |m| > 0 \end{cases} \tag{2.9}$$

and

$$t_1 = \sqrt{(n-|m|+1)(n+|m|)} \tag{2.10}$$

$$t_2 = \sqrt{(n-|m|)(n+|m|+1)} \tag{2.11}$$

fulfill (2.5) in infinite homogeneous space for $n \in \{0, ..., \infty\}$ and $m \in \{-n, ..., n\}$ and represent a basis, also called *modes*, for electromagnetic field distributions in three-dimensional space [Hansen 2008; Klinkenbusch 2008]. The vectorial functions are evaluated at observation locations defined in terms of spherical coordinates $(r, \vartheta, \varphi)$, or in general, by a coordinate-independent vector $\underline{r}$. For observation locations at a fixed distance $r$, the basis functions are *orthogonal* to each other. The unit vectors in $r$-, $\vartheta$-, and $\varphi$-direction are denoted as $\underline{e}_r$, $\underline{e}_\vartheta$ and $\underline{e}_\varphi$. Here, $z_n^{(4)}$ is the spherical Hankel

function of the second kind, defined via

$$z_n^{(4)}(z) = j_n(z) - \mathrm{j}n_n(z) \tag{2.12}$$

with the spherical Bessel functions of the first and second kinds, $j_n(z)$ and $n_n(z)$, respectively. These particular wave functions correspond to a propagation direction away from the origin of the coordinate system, however, the direction can be reversed by flipping the sign of the imaginary part in (2.12). For the considerations in this work, only outward traveling waves in agreement with (2.12) are employed. The normalized associated Legendre functions are here defined as [Abramowitz and Stegun 2013]

$$\overline{P}_n^m(x) = (-1)^m \sqrt{\frac{(n+0.5)(n-m)!}{(n+m)!}} P_n^m(x) \tag{2.13}$$

with the unnormalized associated Legendre functions

$$P_n^m(x) = (-1)^m \left(1 - x^2\right)^{\frac{m}{2}} \frac{\mathrm{d}^m P_n(x)}{\mathrm{d}x^m}, \tag{2.14}$$

which are defined via the derivatives of the Legendre polynomials

$$P_n(x) = \frac{1}{2^n n!} \frac{\mathrm{d}^n}{\mathrm{d}x^n} \left(x^2 - 1\right)^n. \tag{2.15}$$

Any electric and magnetic field at a point $\underline{r}$ can then be written as a weighted sum of modes via

$$\underline{E}(\underline{r}) = k\sqrt{Z_{F0}} \sum_{s=1}^{2} \sum_{n=1}^{N \to \infty} \sum_{m=-n}^{n} Q_{smn} \underline{f}_{smn}(\underline{r}) \tag{2.16}$$

$$\underline{H}(\underline{r}) = \frac{\mathrm{j}k}{\sqrt{Z_{F0}}} \sum_{s=1}^{2} \sum_{n=1}^{N \to \infty} \sum_{m=-n}^{n} Q_{smn} \underline{f}_{(3-s)mn}(\underline{r}) \tag{2.17}$$

with the wave impedance of the surrounding material $Z_F = \sqrt{\frac{\mu}{\varepsilon}}$. The $Q_{smn} \in \mathbb{C}$ represent the coefficients of the spherical vector wave expansion. In practical applications, for example when modeling the fields emerging from a radiating object, the mode order $N$ is truncated according to

$$N_0 = \lceil kr_0 \rceil + n_1, \tag{2.18}$$

where $r_0$ is the radius of the minimum sphere enclosing the object. Since $r_0$ is measured with respect to the origin of the coordinate system employed with the vector wave functions, a lower order $N_0$ is required when aligning the radiating object with the center of the expansion. The scalar $n_1$ is often chosen as $n_1 = 10$ to ensure sufficient accuracy, however, especially for small sized objects, $n_1 = 3$ is experienced to be a more appropriate choice. Note that (2.18) becomes inaccurate as soon as "superdirectivity effects" occur, e.g., see [Hansen 1981; Hansen and Woodyard 1938; Oseen 1922], and more higher-order modes need to be considered. Furthermore, the spherical vector basis functions are singular at $r = 0$ with respect to the radial distance $r$ to the origin of the expansion. In fact, moving an observation location close to the equivalent radius $kr_0$ of the expansion may cause a strong increase of the *evanescent* fields, which correspond to highly reactive field components

associated with higher-order modes. The series in (2.16) and (2.17) still converge, though they may require large values of $N$, which can lead to numerical instabilities and limit the overall accuracy. Thus, the multipole representation of fields is commonly only referred to be accurate for observation points sufficiently far away from the corresponding spherical volume. Under this condition, the general validity of (2.18) implies that radiation represented in terms of a spherical multipole expansion of order $N_0$ can be considered to originate from within a spherical volume with radius $kr_0$. Sources of non-spherical shape, e.g., cylindrical structures in two dimensions [Zhang et al. 2007] or spheroidal structures [Li et al. 2004], can potentially be more efficiently represented by other types of expansions, i.e., requiring less basis functions.

It is common to reduce the triple sums above to a single summation, by introducing [Hansen 2008]

$$\sum_{s=1}^{2} \sum_{n=1}^{N} \sum_{m=-n}^{n} = \sum_{j=1}^{J} \tag{2.19}$$

with $J = 2N(N+2)$. For given $s$, $n$ and $m$, one can find $j = 2[n(n+1)+m-1]+s$. In reverse, one can determine $s$, $n$ and $m$ from $j$ by [Hansen 2008]

$$s = \begin{cases} 1 & j \text{ is odd} \\ 2 & j \text{ is even} \end{cases} \quad (2.20) \qquad n = \left\lfloor \sqrt{\frac{j-s}{2}} + 1 \right\rfloor \quad (2.21) \qquad m = \frac{j-s}{2} - n^2 - n + 1. \quad (2.22)$$

Since the fields in (2.16) and (2.17) depend linearly on the coefficients $Q_{smn}$, it is straightforward to derive a matrix-vector representation of the form

$$E = \left[ \underline{E}\left(\underline{r}_1\right)^{\mathrm{T}} \quad \cdots \quad \underline{E}\left(\underline{r}_m\right)^{\mathrm{T}} \right]^{\mathrm{T}} = A_{\text{SVW}}^{E} \left[ Q_1 \quad \cdots \quad Q_J \right]^{\mathrm{T}} = A_{\text{SVW}}^{E} z \tag{2.23}$$

$$H = A_{\text{SVW}}^{H} z \tag{2.24}$$

when stacking the fields at the $m$ locations $\underline{r}_1$ to $\underline{r}_m$ in the vectors $E$ and $H$. The involved linear operators, i.e., matrices, are commonly referred to as *forward operators* or *measurement matrices*. Due to the orthogonality of the spherical vector wave functions, the associated forward operators commonly exhibit a low condition number. Dependent on the problem at hand, the fields may be represented in terms of the appropriate components, e.g., by Cartesian $x$-, $y$- and $z$-components or by spherical $r$-, $\vartheta$- and $\varphi$-components. The matrix-vector form for describing the electromagnetic radiation of sources will be used throughout this thesis whenever the expansion coefficients are unknown. Note that the radiation operators still depend on other variables, such as the frequency or the locations of the observation points. As such they can be interpreted as linear and nonlinear operators, dependent on the parameter to consider. However, often the expansion coefficients are of main interest and all other parameters are assumed to be fixed, resulting in a comfortable linear dependency.

At this point, it is time to stress the meaning and the importance of (2.18). We have heard that, in line with (2.16) and (2.17), arbitrary electromagnetic field distributions in space can be represented with an infinite sum of spherical vector wave basis functions. According to (2.18), which assumes the source of radiation to be confined to a sphere of limited volume and not exceed a certain directivity, these infinite sums can be truncated and still resemble the original fields with good accuracy. Consequently, we know that fields caused by finite-sized radiators feature a limited

spatial variation that can be described by a bounded number of spherical vector wave functions. Again, this assumes that effects of superdirectivity are excluded. Due to the orthogonality of the vector wave functions for fixed radius $r$, this particular number of modes simultaneously equals the minimum number of unknowns required to completely describe the fields generated by any radiator fitting inside an imaginary spherical volume with the radius $r_0$[1]. Once the coefficients of these modes are fixed, the fields are fully constrained. This is why in general, the minimum number of basis functions required to accurately describe all possible fields emitted by a radiator of a certain geometry is referred to as the number of DoFs of this radiator (or its fields). Based on $N_0$ from (2.18), the number of relevant modes describing sources which *occupy a spherical volume* is given by [Hansen 2008]

$$J_{\text{DoF}} = 2N_0 \left( N_0 + 2 \right).\qquad(2.25)$$

Whenever an antenna does not fully occupy the spherical geometry associated with (2.25), its number of DoFs falls below that predicted (2.25). Its radiation can then be described more efficiently with a different basis. In particular, complex shaped antennas can be conveniently modeled with electric and magnetic current densities on a closely confined surface. While current densities generally represent a redundant basis and may lead to a larger number of coefficients than required for a modal expansion, they can impose strong limitations on the radiated fields and, consequently, on the associated DoFs. In particular, a basis that contains information about the geometric shape of the radiator can provide better phase retrieval results, e.g., faster convergence and higher accuracy, than less localized basis functions, regardless of the number of coefficients. As a downside, the redundancy may cause the corresponding radiation operator to become ill-conditioned, however, one can perform a rank-revealing singular value decomposition (SVD) to obtain a representation in terms of a basis of reduced size and improved condition number. In contrast, working with the minimum number of unknowns is often preferable, especially in the case of nonlinear and nonconvex optimization, in order to keep the computational effort and the number of local stationary points at a minimum.

In summary, the geometry of an electromagnetic source can more precisely be modeled via current-based representations, while modal expansions, e.g., spherical or cylindrical, tend to work with fewer coefficients and typically lead to better conditioned operators.

The process of modeling radiators by spherical vector wave functions or electric and magnetic current densities will become clearer once the essential electromagnetic theorems have been discussed.

**Concluding Remarks — Spherical Vector Wave Functions**  Spherical vector wave functions are a vectorial and potentially orthogonal basis, which fulfills Maxwell's equations. Any fields stemming from a finite spatial volume, see (2.18), can be expressed in terms of an appropriate and also finite spherical multipole expansion. Most importantly for us, there exists a linear relationship between the fields and the coefficients of the multipoles, which allows for the simple matrix-vector notation in (2.23) and (2.24).

---

[1]The uniqueness and equivalence principle clarify that the complete fields outside the source region are determined by the fields on a surface enclosing the radiating object. The orthogonality of the modes on a certain observation surface, i.e. a sphere, thus proves that the number of spherical vector wave functions is always the minimum required to describe the *complete* fields.

## 2.2 Radiation by Current Densities

Alternatively to a spherical multipole expansion, electromagnetic fields can be represented in terms of electric and magnetic current densities. As has been mentioned, a multipole expansion can efficiently represent radiation emerging from within a spherical volume. However, when a radiator does not fully consume the available spherical volume, e.g., in case of a wire dipole antenna, a more adequate representation may be achieved in terms of appropriately chosen current densities. The latter can easily be confined to arbitrary geometries, where the spatial distribution of the currents inherently imposes limitations on the fields.

In the following, the governing equations for evaluating the electric and magnetic field caused by electric and magnetic current densities are derived. Ideally, we aim at determining relations for the fields similar to (2.16) and (2.17) in case of the spherical vector wave functions, where, in the end, unknown coefficients are multiplied with known basis functions. In particular, the "basis functions" related to electric and magnetic line current densities of vanishing extent will be investigated. Due to their strong singularity, these point-like current densities are avoided in the computational treatment of electromagnetic scattering problems based on the method of moments (MoM), and are commonly replaced by low-order Rao-Wilton-Glisson (RWG) basis functions [Rao et al. 1982]. In NFFFTs, singularity treatments are most of the time not required as source and observation locations feature sufficient spatial separation, making infinitely small electric and magnetic current densities a simple and versatile approach.

### 2.2.1 Electric Field of Magnetic and Electric Current Densities

Equations for the electric field caused by electric and magnetic current densities at observation locations $\underline{r}$ can be found via the magnetic and electric vector potentials. Brief derivations are provided in Appendix A.1. The final relations of interest read as

$$\underline{E}_{\underline{J}}\left(\underline{r}\right) = -\frac{1}{4\pi}\sqrt{\frac{\mu}{\varepsilon}} \iiint \underline{J}\left(\underline{r}'\right) \cdot \left[\left(1 + \mathrm{j}kR + \frac{1}{\mathrm{j}kR}\right)\underline{\underline{I}} + \left(\frac{k}{\mathrm{j}R} - \frac{3}{R^2} - \frac{3}{\mathrm{j}kR^3}\right)\underline{R}\underline{R}\right]\frac{\mathrm{e}^{-\mathrm{j}kR}}{R^2}\mathrm{d}V' \quad (2.26)$$

$$\underline{E}_{\underline{M}}\left(\underline{r}\right) = -\frac{1}{4\pi} \iiint \underline{M}\left(\underline{r}'\right) \times \underline{R}\frac{\mathrm{e}^{-\mathrm{j}kR}}{R^3}\left(\mathrm{j}kR + 1\right)\,\mathrm{d}V', \quad (2.27)$$

where the source location of the current densities is denoted with $\underline{r}'$ and $R = \left\|\underline{R}\right\|_2$ is the relative distance defined via $\underline{R} = \underline{r} - \underline{r}'$.

With (2.26) and (2.27), general relations between electric and magnetic current densities and the thereof radiated electric fields are available. These relations are here written in a form such that the assumption of point-like current densities may easily be applied. More appropriate representations exist for other scenarios, for example when singularity treatments are required [Bao et al. 2020; Eibert and Hansen 1995; Järvenpää et al. 2003; Polimeridis and Mosig 2010; Rao et al. 1979; Rossi and Cullen 1999; Sievers et al. 2005; Taylor 2003; Tihon and Craeye 2018; Vipiana et al. 2013; Wilton et al. 1984], i.e., when source and observation regions are identical, overlapping or intersecting.

### 2.2.2 Electric Field of the Hertzian and Fitzgerald Dipole

Based on (2.26) and (2.27), one can now state equations for the cases of the Hertzian and the Fitzgerald dipole, which directly lead to discretized versions of the integral equations. While this is here done in the frequency domain, the concept of line current densities of vanishing extent can

also be applied in the time domain, leading to insightful equations [Zangwill 2013, pp. 727–728]. For both types of dipoles, the current densities are assumed to be of the form

$$\underline{J}\left(\underline{r}'\right) \propto I_{\text{src}}\,\underline{p}_{\text{src}}\,\delta_{\text{D}}\left(\underline{r}' - \underline{r}_{\text{src}}\right) \propto \underline{M}\left(\underline{r}'\right), \tag{2.28}$$

where the vector $\underline{r}_{\text{src}}$ is the location of the dipole, $\underline{p}_{\text{src}}$ is its real-valued orientation vector and the complex scalar $I_{\text{src}}$ represents its excitation coefficient. For the ease of use, we assume that the Dirac impulse $\delta_{\text{D}}(\underline{r}' - \underline{r}_{\text{src}})$ features the appropriate physical units. The index "$_{\text{src}}$" is used to mark quantities belonging to the *radiating sources*.

Inserting the infinitely small currents from (2.28) into (2.26) and (2.27), one obtains

$$\underline{E}_{\text{H}}\left(\underline{r}\right) = -\frac{1}{4\pi}\sqrt{\frac{\mu}{\varepsilon}}I_{\text{src}}\,\underline{p}_{\text{src}}\cdot\left[\left(1 + \mathrm{j}kR + \frac{1}{\mathrm{j}kR}\right)\underline{\underline{I}} + \left(\frac{k}{\mathrm{j}R} - \frac{3}{R^2} - \frac{3}{\mathrm{j}kR^3}\right)\underline{R}\underline{R}\right]\frac{\mathrm{e}^{-\mathrm{j}kR}}{R^2} \tag{2.29}$$

$$\underline{E}_{\text{F}}\left(\underline{r}\right) = -\frac{1}{4\pi}I_{\text{src}}\,\underline{p}_{\text{src}}\times\underline{R}\,\frac{\mathrm{e}^{-\mathrm{j}kR}}{R^3}\left(\mathrm{j}kR + 1\right), \tag{2.30}$$

where the filtering properties of the Dirac distribution has been employed to get rid of the integrals and the dependency on the source locations is hidden inside the relative difference $\underline{R} = \underline{r} - \underline{r}_{\text{src}}$.

Looking back at the representation of the electric field in terms of spherical vector wave functions in (2.16), a similar relation is available in terms of (2.29) and (2.30), however, only for a single Hertzian and Fitzgerald dipole. As part of the discussion on electromagnetic theorems later in this chapter, it will be shown how a finite sum of Hertzian and/or Fitzgerald dipoles can be employed to represent the fields stemming from a radiator of finite size, similar as it can be done with a spherical multipole expansion.

### 2.2.3 Dipole-Dipole Interactions of Hertzian and Fitzgerald Dipoles

So far, we have presented equations for the computation of the electric and magnetic field – physical quantities of vectorial nature – which could be measured if one was able to "receive with a Hertzian or Fitzgerald dipole", respectively. Only these infinitely small current densities are able to extract single field components at distinct points in space, something that can not be done with physically realizable antennas. However, as we will soon see, any receiver (RX) and radiator can be modeled by a finite number of Hertzian and/or Fitzgerald dipoles. As a direct consequence, one is required to compute the interaction between transmitting and receiving dipoles, where both sides may either be electric, magnetic or a combination of both.

The interaction between a transmitting Hertzian dipole and a receiving Hertzian dipole, as well as that between a transmitting Fitzgerald dipole and a receiving Hertzian dipole, can be determined by *testing* the fields with the respective dipoles. To be more precise, when testing an arbitrary field with a Hertzian dipole, the electric field component is projected onto the orientation of the testing Hertzian dipole. In contrast, when receiving with a Fitzgerald dipole, only the magnetic field component parallel to the observation dipole is extracted. The resulting equations obtainable

when testing the field radiated by a Hertzian or a Fitzgerald dipole with a Hertzian dipole read as

$$U_{\text{H}\to\text{H}}\left(\underline{r}\right) = -\frac{1}{4\pi}\sqrt{\frac{\mu}{\varepsilon}}I_{\text{obs}}\,I_{\text{src}}\,\underline{p}_{\text{obs}} \cdot \Big(\underline{p}_{\text{src}}$$

$$\cdot \left[\left(1 + \mathrm{j}kR + \frac{1}{\mathrm{j}kR}\right)\underline{\underline{I}} + \left(\frac{k}{\mathrm{j}R} - \frac{3}{R^2} - \frac{3}{\mathrm{j}kR^3}\right)\underline{\underline{RR}}\right]\frac{\mathrm{e}^{-\mathrm{j}kR}}{R^2}\Big) \qquad (2.31)$$

$$U_{\text{F}\to\text{H}}\left(\underline{r}\right) = -\frac{1}{4\pi}I_{\text{obs}}\,I_{\text{src}}\,\underline{p}_{\text{obs}} \cdot \left(\underline{p}_{\text{src}} \times \underline{R}\right)\frac{\mathrm{e}^{-\mathrm{j}kR}}{R^3}\left(\mathrm{j}kR + 1\right), \qquad (2.32)$$

where the subscript "$_{\text{obs}}$" is employed to mark quantities related to the observing dipole. The relative difference $\underline{R} = \underline{r}_{\text{obs}} - \underline{r}_{\text{src}}$ is defined accordingly in this context. Note that due to duality [Jin 2015], the magnetic field radiated by the Hertzian and the Fitzgerald dipoles can be found as $\underline{H}_{\text{H}} = -\underline{E}_{\text{F}}$ and $\underline{H}_{\text{F}} = \underline{E}_{\text{H}}$, respectively. As a direct consequence, testing with a Fitzgerald dipole can be represented via $U_{\text{H}\to\text{F}} = -U_{\text{F}\to\text{H}}$ and $U_{\text{F}\to\text{F}} = U_{\text{H}\to\text{H}}$.

**Concluding Remarks — Radiation by Current Densities**   There exists a linear relationship between the radiated fields and the underlying electric and magnetic current densities — just like it exists between fields and multipole coefficients in the case of spherical vector wave functions. Commonly, distributed volume or surface current densities are employed for the application in electromagnetic problems, where singularities in the integral equations need to be taken care of. These singularities are not relevant whenever source and observation locations are sufficiently separated in space, as it is the case in typical NFFFTs. Therefore, currents of vanishing extent may be employed, eliminating the need to evaluate the integrals and resulting in simplistic algebraic relations for the radiated fields.

### 2.2.4  Dipole-Dipole Forward and Adjoint Radiation Operators

The interaction between two spatially separated dipoles of infinitely small size can be generalized to an arbitrary number of transmitting and receiving dipoles. Assume that the excitation currents, locations and orientations of the radiating dipoles are collected in the quantities marked with a star as

$$\boldsymbol{I}^{\star} = \big[[I^{\star}]_1 \quad \cdots \quad [I^{\star}]_n\big]^{\mathrm{T}}, \qquad \boldsymbol{r}^{\star} = \big[\underline{r}_1^{\star\mathrm{T}} \quad \cdots \quad \underline{r}_n^{\star\mathrm{T}}\big]^{\mathrm{T}}, \qquad \boldsymbol{p}^{\star} = \Big[\underline{p}_1^{\star\mathrm{T}} \quad \cdots \quad \underline{p}_n^{\star\mathrm{T}}\Big]^{\mathrm{T}} \qquad (2.33)$$

whereas the currents, locations and orientations of the receiving dipoles are stacked in the primed variables

$$\boldsymbol{I}' = \big[[I']_1 \quad \cdots \quad [I']_m\big]^{\mathrm{T}}, \qquad \boldsymbol{r}' = \big[\underline{r}_1'^{\mathrm{T}} \quad \cdots \quad \underline{r}_m'^{\mathrm{T}}\big]^{\mathrm{T}}, \qquad \boldsymbol{p}' = \Big[\underline{p}_1'^{\mathrm{T}} \quad \cdots \quad \underline{p}_m'^{\mathrm{T}}\Big]^{\mathrm{T}}. \qquad (2.34)$$

The resulting stacked vectors are not limited to three dimensions. From here on, they are treated as quantities for numerical computations instead of physically meaningful vectors. Analogous to (2.31) and (2.32), we can write the received signals at the $o$th observing dipole caused by the $s$th

transmitting dipole as

$$
U_{\mathrm{H}\to\mathrm{H},o,s} = -\frac{1}{4\pi}\sqrt{\frac{\mu}{\varepsilon}}[I']_o\,[I^\star]_s\,\underline{p}'_o\cdot\Big(\underline{p}^\star_s
$$
$$
\cdot\left[\left(1+jkR_{o,s}+\frac{1}{jkR_{o,s}}\right)\mathbf{I}+\left(\frac{k}{jR_{o,s}}-\frac{3}{R_{o,s}^2}-\frac{3}{jkR_{o,s}^3}\right)\underline{R}_{o,s}\underline{R}_{o,s}\right]\frac{e^{-jkR_{o,s}}}{R_{o,s}^2}\Big) \tag{2.35}
$$

$$
U_{\mathrm{F}\to\mathrm{H},o,s} = -\frac{1}{4\pi}[I']_o\,[I^\star]_s\,\underline{p}'_o\cdot\Big(\underline{p}^\star_s\times\underline{R}_{o,s}\Big)\frac{e^{-jkR_{o,s}}}{R_{o,s}^3}\big(jkR_{o,s}+1\big), \tag{2.36}
$$

where

$$
\underline{R}_{o,s}=\underline{r}'_o-\underline{r}^\star_s,\quad\text{and}\quad R_{o,s}=\left\|\underline{R}_{o,s}\right\|_2. \tag{2.37}
$$

In a more compact matrix-vector notation, we can write

$$
\sum_{s=1}^{n}\left[U_{\mathrm{H}\to\mathrm{H},1,s}\quad\cdots\quad U_{\mathrm{H}\to\mathrm{H},m,s}\right]^{\mathrm{T}}=\boldsymbol{b}_{\mathrm{H}\to\mathrm{H}}=\mathbf{A}_{\mathrm{H}\to\mathrm{H}}\boldsymbol{I}^\star \tag{2.38}
$$

$$
\sum_{s=1}^{n}\left[U_{\mathrm{F}\to\mathrm{H},1,s}\quad\cdots\quad U_{\mathrm{F}\to\mathrm{H},m,s}\right]^{\mathrm{T}}=\boldsymbol{b}_{\mathrm{F}\to\mathrm{H}}=\mathbf{A}_{\mathrm{F}\to\mathrm{H}}\boldsymbol{I}^\star \tag{2.39}
$$

with the matrix entries in the $o$th row and $s$th column

$$
[\mathbf{A}_{\mathrm{H}\to\mathrm{H}}]_{o,s}=-\frac{1}{4\pi}\sqrt{\frac{\mu}{\varepsilon}}[I']_o\,\underline{p}'_o\cdot\Big(\underline{p}^\star_s
$$
$$
\cdot\left[\left(1+jkR_{o,s}+\frac{1}{jkR_{o,s}}\right)\mathbf{I}+\left(\frac{k}{jR_{o,s}}-\frac{3}{R_{o,s}^2}-\frac{3}{jkR_{o,s}^3}\right)\underline{R}_{o,s}\underline{R}_{o,s}\right]\frac{e^{-jkR_{o,s}}}{R_{o,s}^2}\Big) \tag{2.40}
$$

$$
[\mathbf{A}_{\mathrm{F}\to\mathrm{H}}]_{o,s}=-\frac{1}{4\pi}[I']_o\,\underline{p}'_o\cdot\Big(\underline{p}^\star_s\times\underline{R}_{o,s}\Big)\frac{e^{-jkR_{o,s}}}{R_{o,s}^3}\big(jkR_{o,s}+1\big). \tag{2.41}
$$

Again, due to duality, the operators in (2.40) and (2.41) allow for the computation of the remaining possible interactions in the form of

$$
\mathbf{A}_{\mathrm{H}\to\mathrm{F}}=-\mathbf{A}_{\mathrm{F}\to\mathrm{H}} \tag{2.42}
$$
$$
\mathbf{A}_{\mathrm{F}\to\mathrm{F}}=\mathbf{A}_{\mathrm{H}\to\mathrm{H}}. \tag{2.43}
$$

The evaluation of multiple electric, magnetic or mixed dipole-dipole interactions can thus be described by a simple matrix-vector product of the form

$$
\boldsymbol{b}=\mathbf{A}\boldsymbol{z}, \tag{2.44}
$$

where the operator $\mathbf{A}$ is again referred to as the *forward operator*.

Note that for modeling real-world problems, receiving fields via a single observation dipole alone is often not realistic. In most cases, the fields are sampled by a probe antenna which receives a signal proportional to a weighted sum of spatially distributed field values. The probe can be represented as consisting of multiple and appropriately weighted dipoles distributed in space. As

we will see soon, any electromagnetic radiator or sink can be represented in terms of suitably chosen *equivalent sources*. The presented dipole-dipole formalism is thus sufficient to treat arbitrary receiving or transmitting antennas.

Now that we have defined the forward operator $\mathbf{A}$, we can have a look at the adjoint operator $\mathbf{A}^{\mathrm{H}}$. Field transformation algorithms employing iterative solution strategies often make use of function calls to matrix-vector products with the forward operator, but also the adjoint operator $\mathbf{A}^{\mathrm{H}}$. This is of particular importance whenever the overall problem dimensions make the explicit storage of the forward operator unfeasible. The implementation of adjoint operators may lead to significant additional effort and, based on experience, is rather counter intuitive when sophisticated hierarchical techniques have been incorporated in the forward operator.

For the discussed dipole-dipole interactions, the entries of the adjoint operators are given as

$$[\mathbf{A}_{\mathrm{H}\to\mathrm{H}}]^{\mathrm{H}}_{o,s} = -\frac{1}{4\pi}\sqrt{\frac{\mu}{\varepsilon}}[\overline{I'}]_o\, \underline{p}'_o \cdot \left(\underline{p}^{\star}_s\right.$$

$$\left. \cdot \left[\left(1 - jkR_{o,s} - \frac{1}{jkR_{o,s}}\right)\underline{\mathbf{I}} - \left(\frac{k}{jR_{o,s}} + \frac{3}{R^2_{o,s}} - \frac{3}{jkR^3_{o,s}}\right)\underline{R}_{o,s}\underline{R}_{o,s}\right]\frac{e^{+jkR_{o,s}}}{R^2_{o,s}}\right) \quad (2.45)$$

$$[\mathbf{A}_{\mathrm{F}\to\mathrm{H}}]^{\mathrm{H}}_{o,s} = -\frac{1}{4\pi}[\overline{I'}]_o\, \underline{p}'_o \cdot \left(\underline{p}^{\star}_s \times \underline{R}_{o,s}\right)\frac{e^{+jkR_{o,s}}}{R^3_{o,s}}\left(-jkR_{o,s} + 1\right). \quad (2.46)$$

Due to the *symmetry* of the radiation operators with respect to the sources and observation dipoles, i.e., reciprocity, the adjoint operator for current densities can in practice be implemented via its forward operator. Simply call the forward operator with sources and observation dipoles swapped, while setting all coefficients of the sources (which are the new observers) to unity. At the same time, multiply the currents of the observation dipoles (which are the new sources) with the complex conjugate of the vector for which the matrix-vector product is to be evaluated. Employ this product as the excitation vector for the new sources. After calling the forward operator on this reciprocal problem, finally take the complex conjugate of the result. In this way, only one operator has to be implemented carefully and with high performance, while the adjoint can directly be computed with this procedure at negligible additional cost.

## 2.2.5 Parallelization of Dipole Radiation Operators

Now that we have discussed the necessary equations for basic operators describing electromagnetic radiation by dipoles of vanishing extent in free space, one can have a look at speeding up the computation process. This section bares strong similarities with the publications [Paulus and Eibert 2018a,b], which deal with high-performance implementations of the forward and adjoint radiation operators for Hertzian and Fitzgerald dipoles in free space.

The computation of a matrix-vector product is known to be an *embarrassingly parallel* problem, i.e., its computation can be performed by independent workers in parallel, without the need of significant communication or synchronization among the workers. Problems belonging to this class are known to be almost ideally parallelizable, with negligible overhead, leading to an almost linear performance improvement with increasing computational resources. With the end of Moore's law [Moore et al. 1975] for general purpose processors [Khan et al. 2018; Theis and Wong 2017; Williams 2017], hardware developers have been focusing on special-purpose hardware, e.g., graphics processing units (GPUs), for speeding up particular computation tasks, like machine learning [Steinkraus et al. 2005] or ray tracing [Gunther et al. 2007; Popov et al. 2007]. At first

glance this development may seem reactionary, especially considering the technological advances that humankind has made with general-purpose processors like central processing units (CPUs). However, special-purpose processors are currently seen as one way of artificially extending the validity of Moore's law — achieving more computation power — at the expense of the ease of programmability and applicability. Still, hardware developers have put effort in making their special-purpose hardware more accessible to general computation, and GPUs have found their way into scientific computing via frameworks like CUDA [Nvidia Corporation 2020a] or recent standards of OpenMP [OpenMP Architecture Review Board 2020]. Modern GPUs can perform an incredible amount of *simple* floating-point operations per second. Their performance does not stem from high clock rates, which has been the driving factor for improvements in the performance of CPUs for many years, instead, they rely on an extremely parallel hardware architecture. Essentially, GPUs have a large number of simple processing units, which resemble pruned processor cores in a multi-core CPU. Since the complexity of these units is kept at a minimum, the amount of units on a single GPU can be large. Consequently, GPUs are currently one of the fastest processing hardware when it comes to easily parallelizable tasks with simple computational routines requiring rather low precision, e.g., single- or half-precision arithmetics.

Looking back at the equations for the dipole radiation operators, one can see that the most complicated functions involved are sine, cosine, square-roots and divisions. Without sacrificing stability, all of these can be evaluated with reasonable precision, e.g., with 32-bit floating point arithmetics. In contrast, more care has to be taken when implementing the equations of the spherical vector wave functions. In total, the interactions between source dipoles and observation dipoles can be evaluated independently, due to the *embarrassingly parallel* attribute of the matrix-vector product and with rather low precision arithmetics — nearly ideal conditions for the parallelization on massively parallel hardware like GPUs.

Figure 2.1 shows computation times for the interactions from Fitzgerald to Hertzian dipoles versus the number of interactions. For these results, the number of source dipoles and observation dipoles was assumed to be equal, $n = m$. The computations were conducted on different hardware setups, ranging from a quad-core CPU, over virtual CPU clusters hosted in the Amazon Web Services (AWS) cloud, to eight high-end GPUs in a workstation. All computations were performed in single precision, with the fast-math option enabled and full optimization by the respective compiler. Experience has shown that single-precision computations with the fast-math option[2] provide four significant digits of accuracy with respect to double-precision computations. For practical applications, this is expected to be accurate enough. Whenever needed, double-precision computations can be performed on GPUs, however, at the expense of drastically increased computational effort — at least on consumer GPUs. For the CPU code, the Intel compiler 19.0 [Intel Corporation 2018] was used, while the GPU code was compiled with Nvidia CUDA 8.0 [Nvidia Corporation 2017]. The results for the DGX-1 [Nvidia Corporation 2016a] hardware were obtained on a Linux operating system, while the rest was run on Windows systems. The operator call is evaluated on-the-fly, meaning that the forward matrix is not constructed explicitly. Instead, only the geometry information belonging to the sources and the observers is stored, resulting in a linear memory complexity of $O(n)$. The computational complexity of the dipole-dipole evaluations remains to be $O(n^2)$.

First things to observe in Fig. 2.1 are the superior performance of the GPUs for larger numbers of interactions. At the same time, the communication overhead (memory transfers, etc.) increases

---

[2]The *fast-math* option attempts to make mathematical computations faster by allowing approximate operations and breaking strict IEEE compliance.
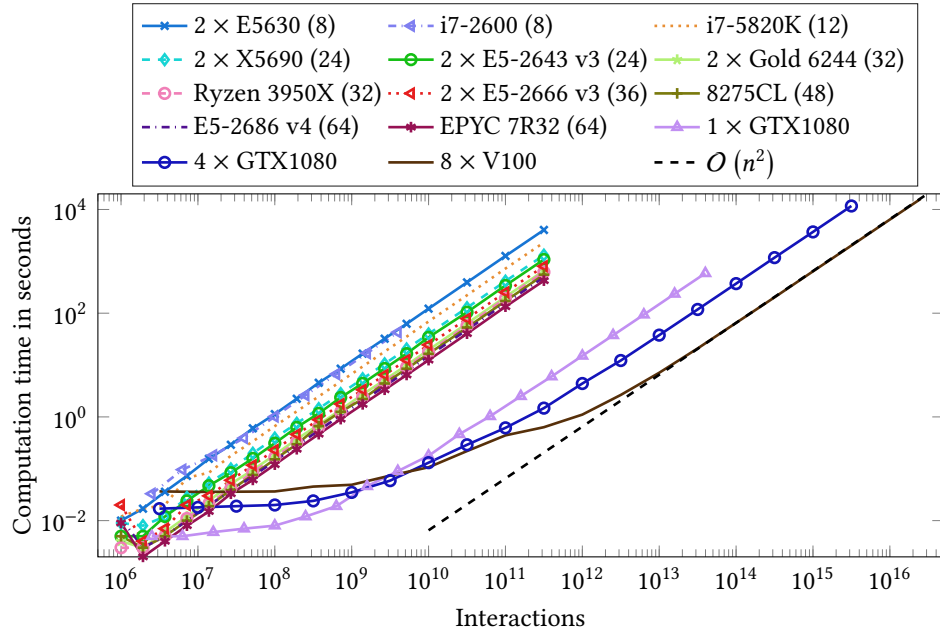
Fig. 2.1 Computation time of a single forward operator call versus the number of Fitzgerald to Hertzian dipole interactions with $n = m$. The black dashed line indicates the asymptotic behavior of a computational complexity of $O(n^2)$. Computations are run on various CPUs and GPUs. Setups performing the computations on the CPU have the number of threads mentioned within the brackets behind the labels. The setups with the Intel Xeon E5-2666, the Intel Xeon Platinum 8275CL, the Intel Xeon E5-2686 and the AMD EPYC 7R32 were utilized via the AWS cloud [Amazon Web Services Inc. n.d.]. The Nvidia GTX1080 GPUs [Nvidia Corporation 2016b] were connected to the mainboard via single PCIe 2.0 lanes. The Nvidia Tesla V100 SMX2 GPUs are part of a high-performance Nvidia DGX-1 workstation [Nvidia Corporation 2016a].

with the number of GPUs used, so that the full benefit of the GPUs only comes into play with more than $1 \times 10^{12}$ interactions, where four Nvidia GTX1080[3] [Nvidia Corporation 2016b] are around 3.976 times faster than a single GPU. When comparing sequential and parallel computations on the CPUs, similar and near-ideal speed increases were observed. At the time of writing, a quick test revealed that an Nvidia RTX3090[4] [Nvidia Corporation 2020b], with the same code re-compiled with CUDA 11.3 [Nvidia Corporation 2021] and exploiting the appropriate compute capabilities, is about four times as fast as a single GTX1080.

When comparing the hardware in terms of the number of dipole-dipole interactions that can be computed within 100 s, two Intel Xeon E5630 achieve $8.21 \times 10^9$, the Intel i7-2600 $9.27 \times 10^9$, the Intel i7-5820K $1.44 \times 10^{10}$, two Intel Xeon X5690 $2.49 \times 10^{10}$, two Intel Xeon E5-2643 v3 $3.02 \times 10^{10}$, an AMD Ryzen 9 3950X $5.31 \times 10^{10}$, a single Nvidia GTX1080 $6.73 \times 10^{12}$, four Nvidia GTX1080 around $2.78 \times 10^{13}$ and eight Nvidia Tesla V100 SMX2[5] roughly $1.55 \times 10^{14}$ interactions, respectively. On the AWS cloud, two Intel Xeon E5-2666 v3 can perform $4.00 \times 10^{10}$, the platform based on the

---

[3]Consumer GPU with 2560 CDUA cores at 1657 MHz [1797 MHz] [boost].

[4]Consumer GPU with 10 496 CDUA cores at 1395 MHz [1860 MHz] [boost].

[5]Professional GPU with 5120 CDUA cores at 1455 MHz [1530 MHz] [boost].

Intel Xeon Platinum 8275CL $5.87 \times 10^{10}$, the Intel Xeon E5-2686 v4 platform $6.49 \times 10^{10}$ and the AMD EPYC 7R32 setup $7.54 \times 10^{10}$ dipole-dipole interactions, respectively. This equals a maximum speedup of around 2057 comparing the fastest GPU and the fastest CPU setup. This comparison is not fair by any means, however, indicates that GPU systems may be faster compared to their common CPU counterparts by several orders of magnitude. Of course, the application must be well adapted to the GPU hardware architecture, which applies to the case of dipole-dipole interactions.

Lastly, it should be mentioned that also the numbers for a single GPU may be quite impressive. A single Nvidia GTX1080, which is a consumer graphics cards, is able to compute the interactions between more than $2 \times 10^6$ source dipoles to more than $2 \times 10^6$ observation dipoles within 100 s. Assuming that roughly $1 \times 10^2$ of those operator calls may be necessary in a field transformation, the computation time for problems with millions of unknowns is in the order of a few hours with a single consumer GPU. It is expected that most problems occurring in industrial applications can thus be handled within a reasonable time. Since the memory complexity is linear, larger problems may also be tackled with the same code. As reported in [Paulus and Eibert 2018b], the peak memory required for a field transformation with $n = 6\,471\,756$ and $m = 6\,487\,202$ on each GPU was around 464 MB. Thus, limited memory on GPUs is not expected to be a bottleneck. Still, when tackling problems with billions of unknowns, sophisticated techniques like the multi-level fast-multipole method (MLFMM) [Chew et al. 2001] may be required, featuring complexities in terms of memory and computation of $O\,(n \log n)$. In contrast to the direct evaluation of dipole-dipole interactions, parallelization of these complicated methods is not straightforward and is a topic of active research. A well known implementation of radiation operators of various equivalent sources based on the concept of the MLFMM is available in the framework of the fast irregular antenna field transformation algorithm (FIAFTA) [Eibert et al. 2010, 2015; Eibert and Schmidt 2009]. In this thesis, results of the FIAFTA are used as a reference for comparison with the results obtained with the dipole-radiation operators. Due to its favorable computational complexity, the operators of FIAFTA allow an elegant treatment of field transformation tasks with more than millions of unknowns.

**Concluding Remarks — Dipole-Dipole Interactions**   The computation of dipole-dipole interactions is a prime example of an $n$-body problem that is known to be embarrassingly parallel and therefore easy to parallelize. Additionally, the equations for radiation by dipole current densities of vanishing extent do not involve error-prone functions requiring high-precision arithmetic, as is the case for spherical vector wave functions. Exploiting the vast low-precision, i.e., single-precision, compute capabilities of modern GPUs makes the treatment of interactions between millions of dipoles feasible and competitive to fast implementations via hierarchical algorithms.

### 2.2.6 Spatial Derivative of Dipole-Dipole Interactions

In the course of this dissertation, the spatial derivative of the forward operator belonging to dipole-dipole interactions will be employed. Having full phase information available, this again leads to a linear operator in terms of the excitation coefficients of the source dipoles, while a nonlinear relationship will be obtained without any phase information. More details are provided in Section 5.4.5. Here, the derivative of dipole-dipole interactions with respect to the locations of the observation dipoles is determined. For convenience and simplicity of the equations, we limit our investigations to spatial derivatives in Cartesian coordinates.

We assume a representation of the $o$th observation and the $s$th source location as

$$\underline{r}'_o = \begin{bmatrix} [x']_o & [y']_o & [z']_o \end{bmatrix}^{\mathrm{T}}, \quad \underline{r}^{\star}_s = \begin{bmatrix} [x^{\star}]_s & [y^{\star}]_s & [z^{\star}]_s \end{bmatrix}^{\mathrm{T}} \tag{2.47}$$

and define the differentiated forward operators

$$\mathbf{A}^{r'} = \frac{\partial \mathbf{A}}{\partial r'} = \begin{bmatrix} \dfrac{\partial \mathbf{A}}{\partial \begin{bmatrix} [x']_1 & \ldots & [x']_m \end{bmatrix}^{\mathrm{T}}} \\[2ex] \dfrac{\partial \mathbf{A}}{\partial \begin{bmatrix} [y']_1 & \ldots & [y']_m \end{bmatrix}^{\mathrm{T}}} \\[2ex] \dfrac{\partial \mathbf{A}}{\partial \begin{bmatrix} [z']_1 & \ldots & [z']_m \end{bmatrix}^{\mathrm{T}}} \end{bmatrix} = \begin{bmatrix} \dfrac{\partial \mathbf{A}}{\partial x'} \\[1ex] \dfrac{\partial \mathbf{A}}{\partial y'} \\[1ex] \dfrac{\partial \mathbf{A}}{\partial z'} \end{bmatrix} \in \mathbb{C}^{3m \times n} = -\frac{\partial \mathbf{A}}{\partial r^{\star}} = -\mathbf{A}^{r^{\star}}. \tag{2.48}$$

Starting from (2.40), we find

$$\begin{aligned} \left[\mathbf{A}^{x'}_{\mathrm{H}\to\mathrm{H}}\right]_{o,s} &= \left[\frac{\partial \mathbf{A}_{\mathrm{H}\to\mathrm{H}}}{\partial [x']_o}\right]_{o,s} \\[2ex] &= -\frac{1}{4\pi}\sqrt{\frac{\mu}{\varepsilon}}[I']_o \underline{p}'_o \cdot \left(\underline{p}^{\star}_s \cdot \left[\left(\underline{\mathbf{I}}\left(jkR_{o,s} + 1 + \frac{1}{jkR_{o,s}}\right)\right.\right.\right. \\[2ex] &\quad \left. -\underline{R}_{o,s}\underline{R}_{o,s}\left(\frac{jk}{R_{o,s}} + \frac{3}{R^3_{o,s}} + \frac{3}{jkR^3_{o,s}}\right)\right)\left([x']_o - [x^{\star}]_s\right) \\[2ex] &\quad \cdot \frac{-\mathrm{e}^{-jkR_{o,s}}}{R^4_{o,s}}\left(jkR_{o,s} + 2\right) + \left(\underline{\mathbf{I}}\left(jk - \frac{1}{jkR^2_{o,s}}\right)\right)\frac{\left([x']_o - [x^{\star}]_s\right)}{R_{o,s}} \\[2ex] &\quad -\frac{\partial \underline{R}_{o,s}\underline{R}_{o,s}}{\partial [x']_o}\left(\frac{jk}{R_{o,s}} + \frac{3}{R^2_{o,s}} + \frac{3}{jkR^3_{o,s}}\right) \\[2ex] &\quad \left.\left.\left. +\underline{R}_{o,s}\underline{R}_{o,s}\left(\frac{jk}{R^2_{o,s}} + \frac{6}{R^3_{o,s}} + \frac{9}{jkR^4_{o,s}}\right)\frac{\left([x']_o - [x^{\star}]_s\right)}{R_{o,s}}\right)\frac{\mathrm{e}^{-jkR_{o,s}}}{R^2_{o,s}}\right]\right). \end{aligned} \tag{2.49}$$

Differentiation with respect to the $[y']_o$- or $[z']_o$-direction can be performed by replacing all occurrences of $[x']_o$ accordingly and by utilizing

$$\frac{\partial \underline{R}_{o,s}\underline{R}_{o,s}}{\partial [x']_o} = \begin{bmatrix} 2\left([x']_o - [x^{\star}]_s\right) & \left([y']_o - [y^{\star}]_s\right) & \left([z']_o - [z^{\star}]_s\right) \\ \left([y']_o - [y^{\star}]_s\right) & 0 & 0 \\ \left([z']_o - [z^{\star}]_s\right) & 0 & 0 \end{bmatrix} \tag{2.50}$$

$$\frac{\partial \underline{R}_{o,s}\underline{R}_{o,s}}{\partial [y']_o} = \begin{bmatrix} 0 & \left([x']_o - [x^{\star}]_s\right) & 0 \\ \left([x']_o - [x^{\star}]_s\right) & 2\left([y']_o - [y^{\star}]_s\right) & \left([z']_o - [z^{\star}]_s\right) \\ 0 & \left([z']_o - [z^{\star}]_s\right) & 0 \end{bmatrix} \tag{2.51}$$

$$\frac{\partial \underline{R}_{o,s}\underline{R}_{o,s}}{\partial [z']_o} = \begin{bmatrix} 0 & 0 & \left([x']_o - [x^{\star}]_s\right) \\ 0 & 0 & \left([y']_o - [y^{\star}]_s\right) \\ \left([x']_o - [x^{\star}]_s\right) & \left([y']_o - [y^{\star}]_s\right) & 2\left([z']_o - [z^{\star}]_s\right) \end{bmatrix}, \tag{2.52}$$

where the dyads are here represented in an abusive matrix notation. For clarification purposes, consider

$$
\begin{bmatrix} 2 & 0 & 3 \\ 1 & 0 & 4 \\ 5 & 0 & 0 \end{bmatrix} = 2\,\underline{e}_x\underline{e}_x + 3\,\underline{e}_x\underline{e}_z + \underline{e}_y\underline{e}_x + 4\,\underline{e}_y\underline{e}_z + 5\,\underline{e}_z\underline{e}_x \tag{2.53}
$$

with the unit vectors $\underline{e}_{x/y/z}$. Analogously, starting from (2.41), we can obtain

$$
\begin{aligned}
\left[\mathbf{A}_{\mathrm{F}\to\mathrm{H}}^{x'}\right]_{o,s} &= \left[\frac{\partial \mathbf{A}_{\mathrm{F}\to\mathrm{H}}}{\partial [x']_o}\right]_{o,s} \\
&= -\frac{1}{4\pi}[I']_o\,\underline{p}'_o \cdot \left(\underline{p}_s^{\star} \times \left[\underline{e}_x\left(\mathrm{j}kR_{o,s}+1\right)\right.\right.\\
&\quad \left.\left.-\underline{R}_{o,s}\left([x']_o - [x^{\star}]_s\right)\left(1 + \left(\mathrm{j}kR_{o,s}+2\right)\left(\mathrm{j}kR_{o,s}+1\right)\right)\right]\frac{\mathrm{e}^{-\mathrm{j}kR_{o,s}}}{R_{o,s}^5}\right).
\end{aligned} \tag{2.54}
$$

For the sake of brevity, the adjoint operators are not explicitly stated here.

## 2.3 Uniqueness Theorem and Equivalence Principle

Throughout this thesis, we consider electromagnetic field transformations as the main application for our phase retrieval algorithms. In order to motivate the validity and applicability of field transformations in the first place, we require at least a basic understanding of the underlying electromagnetic theorems. The intention of this section is not to replace the comprehensive range of profound books on this topic, but rather to give a brief summary of the essentials and to justify the formulations and procedures afterwards. For more details, the interested reader is referred to the excellent literature in this field, e.g., [Harrington 2001; Jin 2015].

We start by introducing the idea of the uniqueness theorem, which helps us to develop intuition for the equivalence principle. The latter will be the main motivation and justification for field transformation algorithms discussed in this thesis. Our line of thought is in close agreement with the procedure in [Jin 2015].

### 2.3.1 The Uniqueness Theorem

Are electromagnetic sources and fields *uniquely* related via Maxwell's equations? What do you need to know about the fields to determine the corresponding sources? The uniqueness theorem answers these questions and allows us to draw meaningful conclusions, yielding an intuitive explanation for the yet to follow equivalence principle.

Consider the general setup in Fig. 2.2. An arbitrarily shaped volume $V$ with material parameters $\varepsilon$, $\mu$ and the conductivity $\sigma$, its surface $\partial V$ and some interior volume current densities $\underline{J}_V$ and $\underline{M}_V$ is drawn. The unit-normal vector $\underline{n}$ is orthogonal on $\partial V$ and is pointing towards the exterior of $V$.
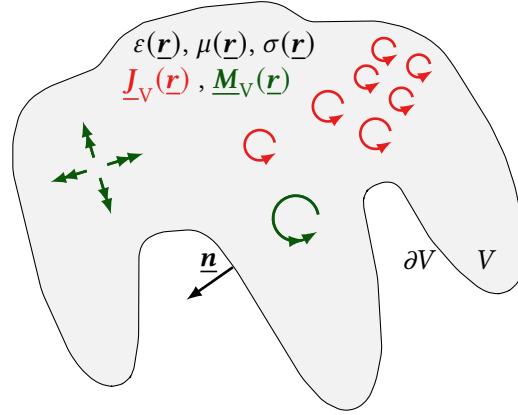
Fig. 2.2 Arbitrarily shaped volume $V$ with material properties, its surface $\partial V$ and interior electric and magnetic current densities $\underline{J}_V$ and $\underline{M}_V$. The unit-normal vector $\underline{n}$ points into the exterior, which may feature unspecified material properties.

For the sake of curiosity, we will now assume that the fields caused by the current densities are *not unique*, i.e., we assume that the sources generate two pairs of fields, namely

$$\nabla \times \underline{E}_1 = -j\omega\mu\underline{H}_1 - \underline{M}_V \tag{2.55}$$

$$\nabla \times \underline{H}_1 = j\omega\varepsilon\underline{E}_1 + \sigma\underline{E}_1 + \underline{J}_V \tag{2.56}$$

and

$$\nabla \times \underline{E}_2 = -j\omega\mu\underline{H}_2 - \underline{M}_V \tag{2.57}$$

$$\nabla \times \underline{H}_2 = j\omega\varepsilon\underline{E}_2 + \sigma\underline{E}_2 + \underline{J}_V. \tag{2.58}$$

Subtracting the second set of equations from the first one, the current densities cancel and we obtain

$$\nabla \times \underline{E}_\delta = -j\omega\mu\underline{H}_\delta \tag{2.59}$$

$$\nabla \times \underline{H}_\delta = j\omega\varepsilon\underline{E}_\delta + \sigma\underline{E}_\delta, \tag{2.60}$$

with $\underline{E}_\delta = \underline{E}_1 - \underline{E}_2$ and $\underline{H}_\delta = \underline{H}_1 - \underline{H}_2$. In case the field is unique, the difference between the fields has to vanish everywhere in space.

We continue to investigate the difference in the fields by exploiting that for vectors $\underline{a}$, $\underline{b}$ and $\underline{c}$, it holds that $\underline{a} \cdot (\underline{b} \times \underline{c}) = \underline{b} \cdot (\underline{c} \times \underline{a}) = \underline{c} \cdot (\underline{a} \times \underline{b})$. Applied to the problem at hand, this yields

$$\begin{aligned} 2\,\nabla \cdot \left(\underline{E}_\delta \times \overline{\underline{H}_\delta}\right) &= \overline{\underline{H}_\delta} \cdot \nabla \times \underline{E}_\delta - \underline{E}_\delta \cdot \nabla \times \overline{\underline{H}_\delta} \\ &= -j\omega\mu\overline{\underline{H}_\delta} \cdot \underline{H}_\delta - (\sigma - j\omega\bar{\varepsilon})\,\underline{E}_\delta \cdot \overline{\underline{E}_\delta} \\ &= -j\omega\mu \left|\underline{H}_\delta\right|^2 + (j\omega\bar{\varepsilon} - \sigma)\left|\underline{E}_\delta\right|^2. \end{aligned} \tag{2.61}$$

In order to evaluate the differences everywhere in space, we integrate over the complete volume and apply Gauss's theorem [Katz 1979; Zangwill 2013]

$$\iiint_V 2\,\nabla \cdot \left(\underline{E}_\delta \times \overline{\underline{H}_\delta}\right) \mathrm{d}V = \oiint_{\partial V} 2\left(\underline{E}_\delta \times \overline{\underline{H}_\delta}\right) \cdot \mathrm{d}\underline{\partial V} \tag{2.62}$$

$$= \iiint_V \left[-\mathrm{j}\omega\mu\left|\underline{H}_\delta\right|^2 + (\mathrm{j}\omega\overline{\varepsilon} - \sigma)\left|\underline{E}_\delta\right|^2\right]\mathrm{d}V. \tag{2.63}$$

Since $\underline{\mathrm{d}\partial V} = \underline{n}\mathrm{d}\partial V$, we conclude that the surface integral in (2.62) vanishes whenever either $\underline{n} \times \underline{E}_\delta = 0$ everywhere on $\partial V$, $\underline{n} \times \underline{H}_\delta = 0$ everywhere on $\partial V$ or both in connection, such that everywhere on $\partial V$ either of the two conditions is true.

As a first conclusion, we see that whenever two sets of sources contained in a volume $V$ exhibit the same tangential fields on the surface of the volume $\partial V$, their fields everywhere in the exterior space are identical. In reverse, whenever the tangential fields on a surface enclosing the source of the radiation are known, then the field everywhere in space is known. Especially the latter interpretation will become helpful when arriving at the equivalence principle. To be more precise, it is sufficient to either know the tangential electric *or* tangential magnetic field on the complete closed surface. Alternatively, a combination of both is possible, as long as tangential information on the complete surface is given. What remains to be shown is that indeed $\underline{E}_\delta$ and $\underline{H}_\delta$ are zero.

For example inserting that $\underline{n} \times \underline{E}_\delta = 0$ everywhere on $\partial V$, we arrive at

$$\iiint_V \left[-\mathrm{j}\omega\mu\left|\underline{H}_\delta\right|^2 + (\mathrm{j}\omega\overline{\varepsilon} - \sigma)\left|\underline{E}_\delta\right|^2\right]\mathrm{d}V = 0. \tag{2.64}$$

When assuming a complex-valued permittivity and permeability according to $\varepsilon = \varepsilon' - \mathrm{j}\varepsilon''$ and $\mu = \mu' - \mathrm{j}\mu''$ with $\varepsilon'', \mu'' \in \mathbb{R}_0^+$, we can split the integrand into its real and imaginary part [Jin 2015]

$$\iiint_V \left[\omega\mu''\left|\underline{H}_\delta\right|^2 + (\omega\varepsilon'' + \sigma)\left|\underline{E}_\delta\right|^2\right]\mathrm{d}V = 0 \tag{2.65}$$

$$\iiint_V \left[-\omega\mu'\left|\underline{H}_\delta\right|^2 + \omega\varepsilon'\left|\underline{E}_\delta\right|^2\right]\mathrm{d}V = 0. \tag{2.66}$$

From (2.65) we can immediately conclude that the fields are unique as long as $\omega \neq 0$ and there are losses ($\varepsilon'', \mu'' \neq 0$). According to [Jin 2015], the same conclusion holds true when both loss and frequency approach zero, leading to a lossless static case.

**Concluding Remarks — Uniqueness Theorem**    Whenever two sources enclosed in a volume $V$ generate the same tangential fields on the enclosing surface $\partial V$, their fields are identical everywhere outside of $V$. Either the tangential electric, the tangential magnetic or a combination of both fields needs to be identical on the whole closed surface for this to hold true. This is commonly referred to as the *uniqueness theorem*.

## 2.3.2 The Equivalence Theorem

As we have seen from the uniqueness theorem, the field distribution outside a source region is uniquely determined by the tangential field components on the surface of the source. Consequently, measuring the tangential fields of a radiating object on an enclosing surface yields information
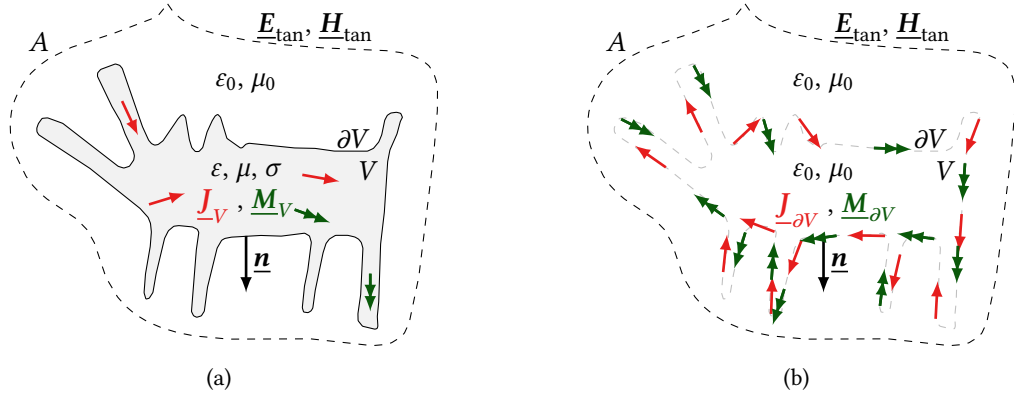
Fig. 2.3 Illustration of a common measurement principle of a radiating structure enclosed in the volume $V$ with surface $\partial V$, embedded in free space. The radiator may feature complicated material properties and exhibits volume current densities $\underline{J}_V(\underline{r})$ and $\underline{M}_V(\underline{r})$ causing the tangential fields $\underline{E}_{\text{tan}}$ and $\underline{H}_{\text{tan}}$ on the closed surface $A$. (a) The original problem with a possibly inhomogeneous material distribution and volumetric current densities. Utilizing the equivalence theorem, the problem can be recast as indicated in (b), only featuring equivalent surface current densities on $\partial V$ in homogeneous free space.

completely describing the field everywhere in the exterior, including the FF. The general idea of such a measurement is sketched in Fig. 2.3(a). The radiating structure may in general consist of complicated material distributions and feature volumetric current densities causing the radiation of electromagnetic fields. Based on the measured tangential fields, one would like to compute field values at arbitrary locations in space. However, tackling this problem in the form seen in Fig. 2.3(a) leads to a significant problem. Even if we already knew the volume current densities of the radiator, the calculation of the fields for potentially complex material distributions would require knowledge of the corresponding Green's function. On its own, this is a task of severe difficulty since analytic equations for the Green's function do only exist for certain canonical geometries and material distributions [Tai 1994]. Instead of directly working with Fig. 2.3(a), we would like to treat an *equivalent problem* of the form seen in Fig. 2.3(b). In particular, this equivalent problem does feature homogeneous material properties, i.e., vacuum, and the original volumetric current densities have been replaced by surface current densities on the boundary $\partial V$ of the source region. This would allow us to utilize the equations derived in Section 2.2 for the radiation in free space. As we will see in the following, the equivalence theorem enables us to represent the problem in Fig. 2.3(a) as the simpler problem in Fig. 2.3(b).

Note that there are at least two forms of the equivalence theorem often found in literature, the surface equivalence theorem and the volume equivalence theorem. All problems discussed in this thesis can be treated with the surface version of the equivalence theorem. Therefore, the volume equivalence is not treated further here.

We start by recalling the conditions for the electric and magnetic field at material inhomogeneities — exemplified in Fig. 2.4. The fields in the first and second medium are $\underline{E}_1$, $\underline{H}_1$ and $\underline{E}_2$, $\underline{H}_2$, respectively, and the unit-normal vector $\underline{n}$ is pointing into the second medium. Whenever the tangential components of the fields exhibit a jump at the boundary, i.e., whenever the tangential
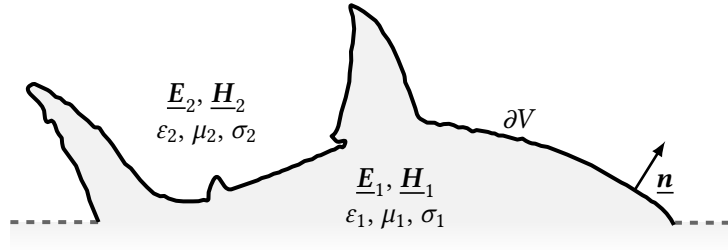
Fig. 2.4 Boundary $\partial V$ between two media. At the boundary, electric and magnetic surface current densities account for differences in the tangential components of the fields $\underline{E}_{1/2}$ and $\underline{H}_{1/2}$.

components of the fields at the boundary are not equal on both sides, surface current densities on the boundary according to [Jin 2015]

$$\underline{J}_{\partial V} = \underline{n} \times \left( \underline{H}_2 - \underline{H}_1 \right) \tag{2.67}$$

$$\underline{M}_{\partial V} = -\underline{n} \times \left( \underline{E}_2 - \underline{E}_1 \right) \tag{2.68}$$

are nonzero.

Now let us apply the boundary conditions to the problem in Fig. 2.5(a). Consider some radiating object with volume current densities $\underline{J}_1$ and $\underline{M}_1$ within its volume $V$ generating the fields $\underline{E}_1$ and $\underline{H}_1$ inside $V$ and in the exterior. As mentioned previously, the presence of material inhomogeneities does not allow for the direct utilization of the Green's function of free space. As indicated in Fig. 2.5(b), when replacing the original sources with the sources $\underline{J}_2$ and $\underline{M}_2$ while at the same time introducing the surface current densities

$$\underline{J}'_{\partial V} = \underline{n} \times \left( \underline{H}_1 - \underline{H}_2 \right) \tag{2.69}$$

$$\underline{M}'_{\partial V} = -\underline{n} \times \left( \underline{E}_1 - \underline{E}_2 \right), \tag{2.70}$$

we can conserve the fields in the exterior and replace the fields within $V$ by those generated by the new interior sources. Since we are not imposing any requirements on the new sources $\underline{J}_2, \underline{M}_2$ we can as well set them to zero and obtain the case depicted in Fig. 2.5(c). Knowing that interior fields are zero, we may arbitrarily modify the material inside of $V$, e.g., set it to the material of the exterior, here, vacuum. As a result, we obtain the model depicted in Fig. 2.5(d) where the complete space is homogeneous and the radiation outside of $V$ is modeled by the *equivalent surface current densities* $\underline{J}_{\partial V}$ and $\underline{M}_{\partial V}$, defined according to (2.69) and (2.70) with $\underline{E}_2 = \underline{H}_2 = \underline{0}$. The problem in Fig. 2.5(d) is effectively *equivalent* to the problem in Fig. 2.5(a), according to the *equivalence principle*. Throughout this thesis we also refer to this as the *Huygens' principle* or the *Huygens' equivalence principle*. As we have just observed, the (surface) equivalence principle allows us to describe the radiation outside the source region filled with arbitrary material by equivalent surface current densities placed on the surface of the source volume and radiating *in free space*. These equivalent surface current densities can then be replaced by another, suitable representation of the fields, e.g., by an expansion into spherical vector wave functions of adequate order. Consequently, problems of the form depicted in Fig. 2.5(a), where only the fields in the exterior of the source volume are of

interest, can be tackled with the radiation operators for sources in free space. The computational effort is drastically reduced — not only can we rely on simple surface current densities instead of volume current densities, but also we do not have to determine the specific Green's function for the problem at hand.

Looking back at the original problem of a common field transformation task depicted in Fig. 2.3(a), it is now clear that the (simpler) problem in Fig. 2.3(b) can be solved instead. The tangential fields, $\underline{E}_{\text{tan}}$ and $\underline{H}_{\text{tan}}$, are measured outside the original source region and the equivalence principle for the exterior can be applied, leading to the setup in Fig. 2.3(b). While the derivation of the equivalence required electric and magnetic surface current densities, in practice an arbitrary choice of currents, e.g., solely electric or magnetic, or a combination, may be employed as long as the DoFs of the tangential fields can be reproduced accurately. Dependent on the equivalent representation, the resulting forward operators will feature varying condition numbers and may or may not be well suited for a particular problem. See [Kornprobst et al. 2021a] for a detailed investigation on the choice and impact of equivalent sources on the performance of NFFFTs.

**Concluding Remarks — Surface Equivalence Theorem**   The radiation caused by sources within a certain volume $V$ — potentially featuring an inhomogeneous material distribution — can be reproduced by surface current densities located on the boundary $\delta V$ of this volume and radiating in homogeneous free space. In the exterior region, the fields of both sources are then identical. This equivalence is ensured by the *surface equivalence theorem*.
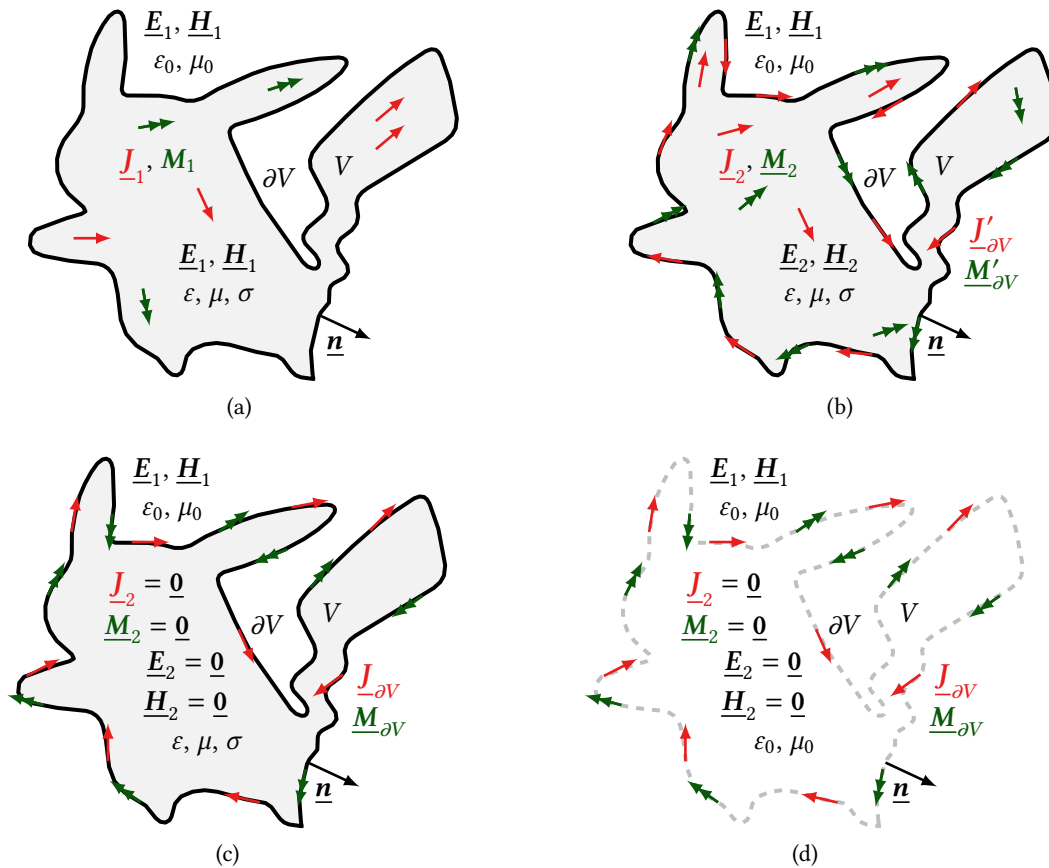
Fig. 2.5 Visualization of the surface equivalence theorem. The original problem in (a) with additional surface current densities and modified interior sources in (b). By setting the freely choosable interior sources to zero in (c), the interior becomes free of any fields and the material can be modified to equal the material of the exterior in (d). Thus (d) is equivalent to (a) with respect to the exterior fields, which are now generated by the equivalent surface current densities, $\underline{J}_{\partial V} = \underline{n} \times \underline{H}_1$ and $\underline{M}_{\partial V} = -\underline{n} \times \underline{E}_1$, evaluated on the boundary $\partial V$.

# 3. Optimization Theory, Wirtinger Calculus

The treatment of electromagnetic inverse problems involving nonlinearity, such as phase retrieval, is not possible without a decent knowledge of optimization theory. The reader is highly recommended to check the excellent and extensive literature in this field, e.g., [Boyd and Vandenberghe 2018; Nocedal and Wright 2006] for obtaining the basics of nonlinear and nonconvex optimization. Here, only the essential principles needed to understand the algorithms discussed later in this thesis are introduced in a condensed manner. This mainly involves the local minimization of nonlinear, nonconvex, real-valued functions and functionals of multivariate, complex-valued quantities. By splitting complex numbers into real and imaginary parts, the principles of real-valued optimization could be applied, however, due to its elegance and generality, the Wirtinger calculus [Brandwood 1983; Li and Adalı 2008; van den Bos 1994; Wirtinger 1927] is here employed to directly work with complex-valued quantities. If desired, the equations derived in terms of the Wirtinger calculus can, at any time, be transferred to the representation in terms of real and imaginary parts. Furthermore, it is assumed that the functions involved in the optimization task are sufficiently smooth, so that the machinery of smooth optimization and differentiation can be applied. However, exceptions such as the magnitude operation, which is nonsmooth at the origin, may be treated via the generalization to *weak derivatives* according to the Clarke subderivative [Borwein et al. 2006; Clarke 1989].

After laying a foundation with the basics of real-valued optimization in Section 3.1, the principle of Wirtinger derivatives and complex-valued optimization is introduced in Section 3.2. For reasons of simplicity and compactness, the univariate case is utilized in proofs and the results are afterwards extended to the multivariate case. With the mathematical tools in our hands, Section 3.3 elaborates on iterative, local, nonlinear, nonconvex optimization, where the concepts of the descent direction and step length are introduced. In particular, a variety of conjugate gradient methods as well as a memory-limited quasi-Newton method for computing the descent direction are discussed. Practical algorithms and rules for line search are recapitulated before a general optimization framework is proposed in Section 3.4. This framework supports the minimization and thus implementation of a manifold of field transformation algorithms which will be explored in the remainder of this dissertation.

## 3.1 Taylor's Theorem and Local Minimization for Real-Valued Variables

Let us start with the fact that a complex-valued function of real arguments, $t : \mathbb{R} \to \mathbb{C}$, is continuously real-differentiable in $\mathbb{R}$ if

$$t'(x) = \lim_{\delta \to 0} \frac{t(x+\delta) - t(x)}{\delta} \tag{3.1}$$

exists $\forall x$ with $\delta \in \mathbb{R}$ and is independent from the direction of $\delta$ approaching zero.

Now consider an at least twice continuously real-differentiable scalar function of real-valued arguments $g : \mathbb{R} \to \mathbb{R}$. According to Taylor's theorem [Nocedal and Wright 2006],

$$g(x+\delta) = g(x) + g'(x)\delta + \frac{1}{2}g''(x)\delta^2 + O(\delta^3) \tag{3.2}$$

provides an approximation of the function value at a location $(x + \delta) \in \mathbb{R}$ via first- and second-order derivatives at the location $x$, while higher-order terms in $O\left(\delta^3\right)$ are neglected. We call the representation in (3.2) the Taylor series of $g(x)$ at the point $(x + \delta)$.

Analogously, one can consider twice continuously real-differentiable scalar functions, $p : \mathbb{R}^{n \times 1} \rightarrow \mathbb{R}$, of multivariate real-valued arguments

$$x = \begin{bmatrix} [x]_1 & \cdots & [x]_n \end{bmatrix}^{\mathrm{T}} \in \mathbb{R}^{n \times 1}, \tag{3.3}$$

where the notation $\mathbb{R}^{n \times 1}$ indicates a column vector with $n$ rows. Instead of the scalar first- and second-order derivatives, we define their multivariate equivalent, the gradient and the Hessian operator [Nocedal and Wright 2006], as

$$\nabla_x = \frac{\partial}{\partial x} = \begin{bmatrix} \dfrac{\partial}{\partial [x]_1} \\ \vdots \\ \dfrac{\partial}{\partial [x]_n} \end{bmatrix}^{\mathrm{T}} \in \mathbb{R}^{1 \times n} \ \ \text{and} \ \ \nabla_x^2 = \frac{\partial}{\partial x}\left(\frac{\partial}{\partial x}\right)^{\mathrm{T}} = \begin{bmatrix} \dfrac{\partial^2}{\partial [x]_1^2} & \cdots & \dfrac{\partial^2}{\partial [x]_1 [x]_n} \\ \vdots & \ddots & \vdots \\ \dfrac{\partial^2}{\partial [x]_n [x]_1} & \cdots & \dfrac{\partial^2}{\partial [x]_n^2} \end{bmatrix} \in \mathbb{R}^{n \times n}. \tag{3.4}$$

Whenever the variable of differentiation is evident from the context, the respective subscript of the gradient and Hessian operator is suppressed for brevity. The multivariate equivalent to (3.2) thus reads as

$$p(x + \delta) = p(x) + \nabla p(x)\,\delta + \frac{1}{2}\delta^{\mathrm{T}}\nabla^2 p(x)\,\delta + O\left(\delta^3\right). \tag{3.5}$$

The notation $O\left(\delta^3\right)$ includes terms which scale with third or higher order when $\delta$ is modified.

A widespread task is to determine a (local) minimum of a specific cost function. Given the above multivariate formulation with the cost function $p$, we can show that any local minimizer $x^\star$ requires that

$$\nabla p\left(x^\star\right) = 0. \tag{3.6}$$

(*first-order necessary optimality condition*)

Similar to the idea in [Nocedal and Wright 2006], this can be shown by contradiction, when assuming $\nabla p(x^\star) \neq 0$. Then we can arbitrarily pick $\delta = -\nabla p(x^\star)^{\mathrm{T}}$ and find

$$\nabla p\left(x^\star\right)\delta = -\nabla p\left(x^\star\right)\left(\nabla p\left(x^\star\right)^{\mathrm{T}}\right) = -\left\|\nabla p\left(x^\star\right)\right\|_2^2 < 0. \tag{3.7}$$

Inserting (3.7) in (3.5) and neglecting second- and higher-order terms, we find

$$p\left(x^\star - \nabla p\left(x^\star\right)^{\mathrm{T}}\right) = p\left(x^\star\right) - \left\|\nabla p\left(x^\star\right)\right\|_2^2 \ \Rightarrow p\left(x^\star - \nabla p\left(x^\star\right)^{\mathrm{T}}\right) < p\left(x^\star\right), \tag{3.8}$$

which contradicts the assumption that $x^\star$ is a local minimizer. By similar considerations, one can show that the Hessian matrix is positive semidefinite at any local minimizer $x^\star$ of the cost function

$p$, i.e.,

$$\nabla^2 p\left(x^\star\right) \geq 0. \tag{3.9}$$
(*second-order necessary optimality condition*)

If more precisely, the Hessian is positive definite, i.e.,

$$\nabla^2 p\left(x^\star\right) > 0, \tag{3.10}$$
(*second-order sufficient optimality condition*)

then $x^\star$ is guaranteed to be a local minimizer [Nocedal and Wright 2006].

While local minimizers automatically correspond to globally optimal points in the case of convex cost functions, they can correspond to highly inaccurate solutions for nonconvex optimization tasks. However, the problem of determining the globally optimal solution of a nonconvex cost function belongs to the class of non-deterministic polynomial-time hard (NP-hard) problems [Bovet and Crescenzi 1993]. Thus, it can be assumed that no algorithm exists which can find the globally optimal solution of a nonconvex optimization problem in the multivariate case of $n$ variables within "polynomial time". In other words, when increasing the number of unknowns $n$, the relation between $n$ and the required computation time can not be expressed in terms of a polynomial of arbitrary order in $n$. Global optimization techniques including genetic algorithms [Davis 1990], particle swarm optimization [Clerc 2006; Kennedy and Eberhart 1995; Poli et al. 2007] or simulated annealing [Davis 1990; Hwang 1988] applied to nonconvex cost functions can only achieve a globally optimal solution within reasonable time for small problems. Difficulties are also caused by the so-called *curse of dimensionality*, which states that the number of local stationary points, i.e., points where first-order derivatives are zero, increases *exponentially* with the problem dimensions. In practice, a local optimizer applied to a nonconvex problem may thus not only get stuck in local minima, but may also experience slow convergence in the proximity of any stationary point, e.g., a saddle point. From a numerical point of view, the convergence rate can drop so drastically that a saddle point can not be distinguished from a local minimum with finite precision arithmetic. In order to escape from certain local stationary points, techniques like numerical continuation [Fadili et al. 2004; Mobahi and Fisher III 2015; Trzasko and Manduca 2009; Xiao and Zhang 2012], also referred to as majorization-minimization [Qiu et al. 2016; Qiu and Palomar 2017; Sun et al. 2016], have been developed.

When encountering high-dimensional nonconvex problems, e.g., phase retrieval, a first and straightforward way is to apply local optimization techniques. Although they can not be guaranteed to lead to the globally optimal solution, in practice they often provide adequate results at, compared to an alternative global search, negligible computational costs.

## 3.2 Wirtinger Derivatives and Complex-Valued Optimization

In the course of optimization problems defined in this work, the concept of multivariate derivatives with respect to complex-valued variables, e.g., in the form of a properly defined gradient, is required. Therefore, building on the results obtained for smooth functions of real-valued arguments, the basics for complex differentiation are introduced — again starting with the univariate case and then generalizing to multivariate definitions.

Consider a scalar complex number $z = (x + jy) \in \mathbb{C}$ with the real-valued scalars $x, y \in \mathbb{R}$. We define a complex-valued function of complex arguments, $g : \mathbb{C} \to \mathbb{C}$, in terms of its real and imaginary parts $u(x, y,)$ and $v(x, y)$, respectively, as $g(z) = u(x, y) + jv(x, y)$. For the complex derivative

$$g'(z) = \lim_{\Delta z \to 0} \frac{g(z + \Delta z) - g(z)}{\Delta z} \tag{3.11}$$

to be well-defined, it has to be independent of the direction of $\Delta z$ approaching zero. This is the case whenever the Cauchy-Riemann conditions

$$\frac{\partial u}{\partial x} = \frac{\partial v}{\partial y} \quad \text{and} \quad \frac{\partial v}{\partial x} = -\frac{\partial u}{\partial y} \tag{3.12}$$

are fulfilled. Equivalently, both functions $u(x, y)$ and $v(x, y)$ have to satisfy the Laplace equation, i.e.,

$$\Delta u = \frac{\partial^2 u}{\partial x^2} + \frac{\partial^2 u}{\partial y^2} = 0 \quad \text{and} \quad \Delta v = \frac{\partial^2 v}{\partial x^2} + \frac{\partial^2 v}{\partial y^2} = 0. \tag{3.13}$$

The function $g(z)$ is then said to be *holomorphic* or *complex-analytic* and $u$ and $v$ are called *harmonic*.

As a direct consequence, a real-valued function of complex-valued arguments, $f : \mathbb{C} \to \mathbb{R}$, can only be harmonic in case it is constant, since

$$f(z) = u(x, y) \quad \to \quad \frac{\partial u}{\partial x} \overset{!}{=} \frac{\partial v}{\partial y} = 0 \quad \Rightarrow \quad \frac{\partial u}{\partial x} \overset{!}{=} 0. \tag{3.14}$$

Thus, $f(z) = |z| = \sqrt{x^2 + y^2}$ or $f(z) = |z|^2 = x^2 + y^2$ are not complex-differentiable in the classical sense, so that a gradient can not be defined accordingly, which is, however, necessary to optimize $f$ with respect to $z$.

An extension to the above theory, allowing to define a gradient for non-holomorphic functions, was first silently employed by Poincare [Poincaré 1899] and investigated in detail by Wirtinger [Wirtinger 1927], after whom the *Wirtinger calculus* was named. The same principles are known under the term of $\mathbb{CR}$-calculus in English literature [Brandwood 1983; Li and Adalı 2008; van den Bos 1994]. We start by observing the simple relationships

$$\begin{bmatrix} z \\ \bar{z} \end{bmatrix} = \underbrace{\begin{bmatrix} 1 & j \\ 1 & -j \end{bmatrix}}_{\mathbf{J}} \begin{bmatrix} x \\ y \end{bmatrix} \quad \text{and} \quad \begin{bmatrix} x \\ y \end{bmatrix} = \underbrace{\frac{1}{2} \begin{bmatrix} 1 & 1 \\ -j & j \end{bmatrix}}_{\mathbf{J}^{-1} = \frac{1}{2}\mathbf{J}^{\mathrm{H}}} \begin{bmatrix} z \\ \bar{z} \end{bmatrix} \tag{3.15}$$

connecting the complex scalar $z$ and its complex conjugate $\bar{z}$ to their real and imaginary parts $x$ and $y$ via the matrix $\mathbf{J}$. It is noteworthy that one can write $g(z) = \hat{g}(x, y) = \tilde{g}(z, \bar{z})$, i.e., $g$ can be interpreted as a function of the two *independent* variables $x$ and $y$ or $z$ and $\bar{z}$, respectively. For the sake of brevity, we here do not explicitly distinguish between $g$, $\hat{g}$ and $\tilde{g}$, instead, silently accept that $g$ may depend on $z$, $x$ and $y$, and $z$ and $\bar{z}$. Next one can determine [Remmert 1991, p. 65]

$$\frac{\partial x(z, \bar{z})}{\partial z} = \frac{\partial x(z, \bar{z})}{\partial \bar{z}} = \frac{1}{2} \quad \text{and} \quad \frac{\partial y(z, \bar{z})}{\partial z} = \frac{-j}{2}, \quad \frac{\partial y(z, \bar{z})}{\partial \bar{z}} = \frac{j}{2}, \tag{3.16}$$

where again $z$ and $\overline{z}$ were considered as *independent* variables. Assuming that $f$ is real-differentiable with respect to $x, y, z$ and $\overline{z}$ when treating these quantities as real-valued scalars, we can find

$$\frac{\partial g\left(x\left(z,\overline{z}\right), y\left(z,\overline{z}\right)\right)}{\partial z} = \frac{\partial g}{\partial x}\frac{\partial x}{\partial z} + \frac{\partial g}{\partial y}\frac{\partial y}{\partial z} = \frac{1}{2}\left(\frac{\partial g}{\partial x} - \mathrm{j}\frac{\partial g}{\partial y}\right) \tag{3.17}$$

$$\frac{\partial g\left(x\left(z,\overline{z}\right), y\left(z,\overline{z}\right)\right)}{\partial \overline{z}} = \frac{\partial g}{\partial x}\frac{\partial x}{\partial \overline{z}} + \frac{\partial g}{\partial y}\frac{\partial y}{\partial \overline{z}} = \frac{1}{2}\left(\frac{\partial g}{\partial x} + \mathrm{j}\frac{\partial g}{\partial y}\right), \tag{3.18}$$

or equivalently

$$\mathbb{C}^{1\times 2} \ni \begin{bmatrix} \frac{\partial}{\partial z} \\ \frac{\partial}{\partial \overline{z}} \end{bmatrix}^{\mathrm{T}} = \begin{bmatrix} \frac{\partial}{\partial x} \\ \frac{\partial}{\partial y} \end{bmatrix}^{\mathrm{T}} \frac{1}{2}\mathbf{J}^{-1} \quad \text{and} \quad \begin{bmatrix} \frac{\partial}{\partial x} \\ \frac{\partial}{\partial y} \end{bmatrix}^{\mathrm{T}} = \begin{bmatrix} \frac{\partial}{\partial z} \\ \frac{\partial}{\partial \overline{z}} \end{bmatrix}^{\mathrm{T}} \mathbf{J}. \tag{3.19}$$

Compliance with the Cauchy-Riemann equations can now be written in terms of the newly introduced derivatives, namely in the form of $\frac{\partial g}{\partial \overline{z}} = 0$.

Let us return to our main point of interest, namely to determine a Taylor series representation for functions of complex-valued variables with appropriately defined gradient and Hessian operators. Therefore, consider an univariate, complex-valued and at least twice continuously real-differentiable function $f^{\star} : \mathbb{C} \to \mathbb{R}$. Interpreting the scalar complex argument $z = x + \mathrm{j}y$ as a two-dimensional real-valued vector, one can write $f^{\star}$ as a multivariate function $f : \mathbb{R}^{2\times 1} \to \mathbb{C}$ of two real-valued arguments and determine its Taylor series analogous to (3.5) in the form of

$$f\left(\mathbf{r} + \Delta\mathbf{r}\right) = f\left(\mathbf{r}\right) + \nabla f\left(\mathbf{r}\right)\Delta\mathbf{r} + \frac{1}{2}\Delta\mathbf{r}^{\mathrm{T}}\nabla^2 f\left(\mathbf{r}\right)\Delta\mathbf{r} + O\left(\Delta\mathbf{r}^3\right) \tag{3.20}$$

with

$$\mathbf{r} = \begin{bmatrix} x & y \end{bmatrix}^{\mathrm{T}}, \quad \Delta\mathbf{r} = \begin{bmatrix} \Delta x & \Delta y \end{bmatrix}^{\mathrm{T}}, \quad \frac{\partial}{\partial \mathbf{r}} = \begin{bmatrix} \frac{\partial}{\partial x} & \frac{\partial}{\partial y} \end{bmatrix}. \tag{3.21}$$

In passing, we observe that the first-order necessary optimality condition at a local stationary point $\mathbf{r}^{\star}$ requires [Brandwood 1983]

$$\nabla f\left(\mathbf{r}^{\star}\right) \overset{!}{=} \mathbf{0}^{\mathrm{T}} \quad \Rightarrow \quad \begin{bmatrix} \frac{\partial f\left(\mathbf{r}^{\star}\right)}{\partial x} & \frac{\partial f\left(\mathbf{r}^{\star}\right)}{\partial y} \end{bmatrix} \overset{!}{=} \begin{bmatrix} 0 & 0 \end{bmatrix} = \begin{bmatrix} \frac{\partial f\left(\mathbf{r}^{\star}\right)}{\partial z} & \frac{\partial f\left(\mathbf{r}^{\star}\right)}{\partial \overline{z}} \end{bmatrix}\begin{bmatrix} 1 & \mathrm{j} \\ 1 & -\mathrm{j} \end{bmatrix} \tag{3.22}$$

$$\Rightarrow \quad \begin{bmatrix} \frac{\partial f\left(\mathbf{r}^{\star}\right)}{\partial z} & \frac{\partial f\left(\mathbf{r}^{\star}\right)}{\partial \overline{z}} \end{bmatrix} \overset{!}{=} \begin{bmatrix} 0 & 0 \end{bmatrix}. \tag{3.23}$$

Note that this slightly abusive notation implies that $f$ can again be interpreted as function of $z$ and $\overline{z}$ via (3.15), just like $f^{\star}$. This is exactly the core idea behind the Wirtinger calculus: Instead of working with real and imaginary parts, the complex-valued numbers and their complex conjugate are considered independent quantities. As will be seen in a moment, this alternative dependency is especially beneficial when working with real-valued cost functions. What remains to be done now is to rewrite (3.20) in terms of $z$ and $\overline{z}$ instead of $x$ and $y$.

With the introduction of the *conjugate coordinates* $c$ with

$$c = \begin{bmatrix} z & \bar{z} \end{bmatrix}^{\mathrm{T}}, \quad \Delta c = \begin{bmatrix} \Delta z & \overline{\Delta z} \end{bmatrix}^{\mathrm{T}}, \quad \frac{\partial}{\partial c} = \begin{bmatrix} \frac{\partial}{\partial z} & \frac{\partial}{\partial \bar{z}} \end{bmatrix} \tag{3.24}$$

and utilizing (3.15) and (3.19), we can find

$$\frac{\partial}{\partial r} \Delta r = \frac{\partial}{\partial c} \mathbf{J} \mathbf{J}^{-1} \Delta c = \frac{\partial}{\partial c} \Delta c \tag{3.25}$$

and

$$\begin{aligned}
\frac{1}{2} \Delta r^{\mathrm{T}} \frac{\partial}{\partial r} \left( \frac{\partial}{\partial r} \right)^{\mathrm{T}} \Delta r &= \frac{1}{2} \Delta r^{\mathrm{H}} \frac{\partial}{\partial r} \left( \frac{\partial}{\partial r} \right)^{\mathrm{H}} \Delta r = \frac{1}{2} \left( \mathbf{J}^{-1} \Delta c \right)^{\mathrm{H}} \frac{\partial}{\partial r} \left( \mathbf{J}^{\mathrm{H}} \left( \frac{\partial}{\partial c} \right)^{\mathrm{H}} \right) \mathbf{J}^{-1} \Delta c \\
&= \frac{1}{2} \Delta c^{\mathrm{H}} \mathbf{J}^{-1,\mathrm{H}} \frac{\partial}{\partial c} \left( \mathbf{J}^{\mathrm{H}} \left( \frac{\partial}{\partial c} \right)^{\mathrm{H}} \right) \mathbf{J} \mathbf{J}^{-1} \Delta c \\
&= \frac{1}{2} \Delta c^{\mathrm{H}} \frac{\partial}{\partial c} \left( \frac{\partial}{\partial c} \right)^{\mathrm{H}} \Delta c. \tag{3.26}
\end{aligned}$$

In agreement with [Kreutz-Delgado 2009], one can define the corresponding (multivariate) gradient and Hessian operators as

$$\boldsymbol{\nabla}_c = \begin{bmatrix} \frac{\partial}{\partial z} & \frac{\partial}{\partial \bar{z}} \end{bmatrix} = \begin{bmatrix} \frac{\partial}{\partial [z]_1} & \cdots & \frac{\partial}{\partial [z]_n} & \frac{\partial}{\partial \overline{[z]_1}} & \cdots & \frac{\partial}{\partial \overline{[z]_n}} \end{bmatrix} \in \mathbb{C}^{1 \times 2n} \tag{3.27}$$

$$\nabla_c^2 = \frac{\partial}{\partial c} \left( \frac{\partial}{\partial c} \right)^{\mathrm{H}} = \begin{bmatrix} \boldsymbol{\nabla}_{zz}^2 & \boldsymbol{\nabla}_{\bar{z}z}^2 \\ \boldsymbol{\nabla}_{z\bar{z}}^2 & \boldsymbol{\nabla}_{\bar{z}\bar{z}}^2 \end{bmatrix} \in \mathbb{C}^{2n \times 2n} \tag{3.28}$$

$$= \begin{bmatrix}
\frac{\partial}{\partial [z]_1} \left( \frac{\partial}{\partial [z]_1} \right)^{\mathrm{H}} & \cdots & \frac{\partial}{\partial [z]_n} \left( \frac{\partial}{\partial [z]_1} \right)^{\mathrm{H}} & \frac{\partial}{\partial \overline{[z]_1}} \left( \frac{\partial}{\partial [z]_1} \right)^{\mathrm{H}} & \cdots & \frac{\partial}{\partial \overline{[z]_n}} \left( \frac{\partial}{\partial [z]_1} \right)^{\mathrm{H}} \\
\vdots & \ddots & \vdots & \vdots & \ddots & \vdots \\
\frac{\partial}{\partial [z]_1} \left( \frac{\partial}{\partial [z]_n} \right)^{\mathrm{H}} & \cdots & \frac{\partial}{\partial [z]_n} \left( \frac{\partial}{\partial [z]_n} \right)^{\mathrm{H}} & \frac{\partial}{\partial \overline{[z]_1}} \left( \frac{\partial}{\partial [z]_n} \right)^{\mathrm{H}} & \cdots & \frac{\partial}{\partial \overline{[z]_n}} \left( \frac{\partial}{\partial [z]_n} \right)^{\mathrm{H}} \\
\frac{\partial}{\partial [z]_1} \left( \frac{\partial}{\partial \overline{[z]_1}} \right)^{\mathrm{H}} & \cdots & \frac{\partial}{\partial [z]_n} \left( \frac{\partial}{\partial \overline{[z]_1}} \right)^{\mathrm{H}} & \frac{\partial}{\partial \overline{[z]_1}} \left( \frac{\partial}{\partial \overline{[z]_1}} \right)^{\mathrm{H}} & \cdots & \frac{\partial}{\partial \overline{[z]_n}} \left( \frac{\partial}{\partial \overline{[z]_1}} \right)^{\mathrm{H}} \\
\vdots & \ddots & \vdots & \vdots & \ddots & \vdots \\
\frac{\partial}{\partial [z]_1} \left( \frac{\partial}{\partial \overline{[z]_n}} \right)^{\mathrm{H}} & \cdots & \frac{\partial}{\partial [z]_n} \left( \frac{\partial}{\partial \overline{[z]_n}} \right)^{\mathrm{H}} & \frac{\partial}{\partial \overline{[z]_1}} \left( \frac{\partial}{\partial \overline{[z]_n}} \right)^{\mathrm{H}} & \cdots & \frac{\partial}{\partial \overline{[z]_n}} \left( \frac{\partial}{\partial \overline{[z]_n}} \right)^{\mathrm{H}}
\end{bmatrix}. \tag{3.29}$$

The second-order expansion of a complex-valued function can now be written as

$$f(c + \Delta c) = f(c) + \boldsymbol{\nabla}_c f(c) \, \Delta c + \frac{1}{2} \Delta c^{\mathrm{H}} \boldsymbol{\nabla}_c^2 f(c) \, \Delta c + O\left( \Delta c^3 \right), \tag{3.30}$$

which is nothing more than an alternative representation of (3.20). From the previous investigations, it should be believable that (3.30) is valid for multivariate considerations, i.e., when $f^\star(z) : \mathbb{C}^{n \times 1} \to \mathbb{C}$. In the following, we will thus consider the multivariate case. The curios reader may wonder

about the benefits of (3.30) compared to the representation with purely real variables in (3.20). In fact, the representation based on the conjugate coordinates requires $2n$ complex-valued quantities in the gradient, while the formulation based on real and imaginary parts only contains $2n$ real-valued variables for the first-order derivative. However, in a moment it will be shown that for real-valued cost functions only $n$ complex-valued terms belonging to either $z$ or $\bar{z}$ are necessary. Splitting of variables and derivatives into two portions is then no longer required, making the Wirtinger formulation more elegant and compact compared to (3.20) when working with first-order methods.

At this point it makes sense to state rules for the Wirtinger derivatives for the composition $f(h(z))$ of two functions, where $z \in \Omega_z$ may be complex- or real-valued vectors and the range of $h$ and $f$ is denoted by $\Omega_h$ and $\Omega_f$. The most general case relevant here is encountered when $\Omega_z = \mathbb{C}^{n \times 1}$, $\Omega_h = \mathbb{C} = \Omega_f$, for which one can find

$$\frac{\partial \bar{f}}{\partial \bar{z}} = \overline{\left( \frac{\partial f}{\partial z} \right)} \quad (3.31) \qquad \frac{\partial \bar{f}}{\partial z} = \overline{\left( \frac{\partial f}{\partial \bar{z}} \right)} \quad (3.32) \qquad \frac{\partial f(h(z))}{\partial z} = \frac{\partial f}{\partial h} \frac{\partial h}{\partial z} + \frac{\partial f}{\partial \bar{h}} \frac{\partial \bar{h}}{\partial z}. \quad (3.33)$$

Whenever the outermost function returns real-valued scalars, i.e., $\Omega_z = \mathbb{C}^{n \times 1}$, $\Omega_h = \mathbb{C}$ and $\Omega_f = \mathbb{R}$, further simplifications can be observed with

$$\overline{\left( \frac{\partial f}{\partial z} \right)} = \frac{\partial f}{\partial \bar{z}} \quad (3.34) \qquad \frac{\partial f(h(z))}{\partial z} = \frac{\partial f}{\partial h} \frac{\partial h}{\partial z} + \overline{\left( \frac{\partial f}{\partial h} \right)} \frac{\partial \bar{h}}{\partial z}. \quad (3.35)$$

For $h$ and $f$ returning real values, i.e., $\Omega_z = \mathbb{C}^{n \times 1}$, $\Omega_h = \mathbb{R} = \Omega_f$, the derivative

$$\frac{\partial f(h(z))}{\partial z} = \frac{\partial f}{\partial h} \frac{\partial h}{\partial z} \quad (3.36)$$

holds true[1]. Lastly, consider the special case when real-valued input vectors are assumed and $h$ returns complex-valued scalars, i.e., $\Omega_z = \mathbb{R}^{n \times 1}$, $\Omega_h = \mathbb{C}$ and $\Omega_f = \mathbb{R}$, leading to[2]

$$\frac{\partial f(h(z))}{\partial z} = 2 \operatorname{Re} \left\{ \frac{\partial f}{\partial h} \frac{\partial h}{\partial z} \right\}, \quad (3.38)$$

which will become important at a later point. Table 3.1 summarizes the Wirtinger derivatives for the considered cases of two composite functions.

---

[1]The rule in (3.36) can be shown and illustrated with an example: $f(h(z)) = 3(\bar{z}z)$. Employing (3.19), we expect $\frac{\partial f}{\partial z} = 3\bar{z}$. With the chain rule (3.33), we find $\frac{\partial f}{\partial h} \frac{\partial h}{\partial z} + \frac{\partial f}{\partial \bar{h}} \frac{\partial \bar{h}}{\partial z} = 3\bar{z} + \frac{\partial f}{\partial \bar{h}} \frac{\partial \bar{h}}{\partial z}$, which tells us that $\frac{\partial f}{\partial \bar{h}}$ has to be zero. Intuitively, this also makes sense, since consequently the chain rule for the Wirtinger derivatives only has to be applied whenever the parent function is complex-valued. For example consider $f(h_1(h_2(z)))$, with $f : \mathbb{R} \to \mathbb{R}$, $h_1 : \mathbb{C} \to \mathbb{R}$, $h_2 : \mathbb{C} \to \mathbb{C}$ and $z \in \mathbb{C}$. The chain rule then equals

$$\frac{\partial f(h_1(h_2(z)))}{\partial z} = \frac{\partial f}{\partial h_1} \left( \frac{\partial h_1}{\partial h_2} \frac{\partial h_2}{\partial z} + \frac{\partial h_1}{\partial \bar{h_2}} \frac{\partial \bar{h_2}}{\partial z} \right). \quad (3.37)$$

[2]The rule in (3.38) can be shown by combining (3.35) with (3.32).

Tab. 3.1 Wirtinger derivatives for $f\left(h\left(z\right)\right)\,:\,\Omega_z \to \Omega_h \to \Omega_f$.

| $\Omega_z$ | $\Omega_h$ | $\Omega_f$ | $\frac{\partial \overline{f}}{\partial \overline{z}}$ | $\frac{\partial \overline{f}}{\partial z}$ | $\frac{\partial f}{\partial z}$ |
|---|---|---|---|---|---|
| $\mathbb{C}^{n \times 1}$ | $\mathbb{C}$ | $\mathbb{C}$ | $\overline{\left(\frac{\partial f}{\partial z}\right)}$ | $\overline{\left(\frac{\partial f}{\partial \overline{z}}\right)}$ | $\frac{\partial f}{\partial h}\frac{\partial h}{\partial z} + \frac{\partial f}{\partial \overline{h}}\frac{\partial \overline{h}}{\partial z}$ |
| $\mathbb{C}^{n \times 1}$ | $\mathbb{C}$ | $\mathbb{R}$ | $\frac{\partial f}{\partial \overline{z}}$ | $\frac{\partial f}{\partial z}$ | $\frac{\partial f}{\partial h}\frac{\partial h}{\partial z} + \overline{\left(\frac{\partial f}{\partial h}\right)}\frac{\partial \overline{h}}{\partial z}$ |
| $\mathbb{C}^{n \times 1}$ | $\mathbb{R}$ | $\mathbb{R}$ | $\frac{\partial f}{\partial \overline{z}}$ | $\frac{\partial f}{\partial z}$ | $\frac{\partial f}{\partial h}\frac{\partial h}{\partial z}$ |
| $\mathbb{R}^{n \times 1}$ | $\mathbb{R}$ | $\mathbb{C}$ | $\overline{\left(\frac{\partial f}{\partial z}\right)}$ | $\overline{\left(\frac{\partial f}{\partial \overline{z}}\right)}$ | $2\,\mathrm{Re}\left\{\frac{\partial f}{\partial h}\frac{\partial h}{\partial z}\right\}$ |

Regarding the Hessian matrix, we can identify some simplifications. When $f : \mathbb{C}^{n \times 1} \to \mathbb{C}$, one finds

$$\boldsymbol{\nabla}^2_{zz}f = \frac{\partial}{\partial z}\left(\frac{\partial f}{\partial z}\right)^H = \left(\boldsymbol{\nabla}^2_{zz}f\right)^H \tag{3.39}$$

$$\boldsymbol{\nabla}^2_{\overline{z}z}f = \frac{\partial}{\partial \overline{z}}\left(\frac{\partial f}{\partial z}\right)^H = \left(\frac{\partial}{\partial z}\left(\frac{\partial f}{\partial \overline{z}}\right)^H\right)^H = \left(\boldsymbol{\nabla}^2_{z\overline{z}}f\right)^H \tag{3.40}$$

and in case $f : \mathbb{C}^{n \times 1} \to \mathbb{R}$, we obtain

$$\overline{\boldsymbol{\nabla}^2_{zz}f} = \overline{\frac{\partial}{\partial z}\left(\frac{\partial f}{\partial z}\right)^H} \stackrel{(3.31)}{=} \frac{\partial}{\partial \overline{z}}\left(\frac{\partial f}{\partial z}\right)^T \stackrel{(3.34)}{=} \frac{\partial}{\partial \overline{z}}\left(\frac{\partial f}{\partial \overline{z}}\right)^H = \boldsymbol{\nabla}^2_{\overline{z}\overline{z}}f \tag{3.41}$$

$$\boldsymbol{\nabla}^2_{\overline{z}z}f = \frac{\partial}{\partial \overline{z}}\left(\frac{\partial f}{\partial z}\right)^H \stackrel{(3.34)}{=} \frac{\partial}{\partial z}\overline{\left(\frac{\partial f}{\partial z}\right)}^H \stackrel{(3.34)}{=} \frac{\partial}{\partial z}\left(\frac{\partial f}{\partial \overline{z}}\right)^H = \overline{\boldsymbol{\nabla}^2_{z\overline{z}}f}. \tag{3.42}$$

Utilizing the rules of the Wirtinger calculus for real-valued functions, we can see

$$\frac{\partial f\left(c\right)}{\partial c}\Delta c = \frac{\partial f}{\partial z}\Delta z + \frac{\partial f}{\partial \overline{z}}\overline{\Delta z} \stackrel{(3.34)}{=} \frac{\partial f}{\partial z}\Delta z + \overline{\frac{\partial f}{\partial z}}\overline{\Delta z} = 2\,\mathrm{Re}\left\{\frac{\partial f}{\partial z}\Delta z\right\} \tag{3.43}$$

and

$$\begin{aligned}
\frac{1}{2}\Delta c^H \boldsymbol{\nabla}^2_c f\left(c\right)\Delta c &= \frac{1}{2}\begin{bmatrix}\Delta z \\ \Delta \overline{z}\end{bmatrix}^H \begin{bmatrix}\boldsymbol{\nabla}^2_{zz}f\left(c\right) & \boldsymbol{\nabla}^2_{\overline{z}z}f\left(c\right) \\ \boldsymbol{\nabla}^2_{z\overline{z}}f\left(c\right) & \boldsymbol{\nabla}^2_{\overline{z}\overline{z}}f\left(c\right)\end{bmatrix}\begin{bmatrix}\Delta z \\ \Delta \overline{z}\end{bmatrix} \\
&= \frac{1}{2}\left[\Delta z^H \boldsymbol{\nabla}^2_{zz}f\left(c\right)\Delta z + \overline{\Delta z}^H \boldsymbol{\nabla}^2_{\overline{z}\overline{z}}f\left(c\right)\overline{\Delta z}\right] \\
&\quad + \frac{1}{2}\left[\Delta z^H \boldsymbol{\nabla}^2_{\overline{z}z}f\left(c\right)\overline{\Delta z} + \overline{\Delta z}^H \boldsymbol{\nabla}^2_{z\overline{z}}f\left(c\right)\Delta z\right] \\
&\stackrel{(3.41),(3.42)}{=} \mathrm{Re}\left\{\Delta z^H \boldsymbol{\nabla}^2_{zz}f\left(c\right)\Delta z + \Delta z^H \boldsymbol{\nabla}^2_{\overline{z}z}f\left(c\right)\overline{\Delta z}\right\},
\end{aligned} \tag{3.44}$$

such that one can write

$$f(z + \Delta z) = f(z) + 2\operatorname{Re}\left\{\frac{\partial f}{\partial z}\Delta z\right\} + \operatorname{Re}\left\{\Delta z^{\mathrm{H}}\boldsymbol{\nabla}_{zz}^2 f(c)\,\Delta z + \Delta z^{\mathrm{H}}\boldsymbol{\nabla}_{\bar{z}z}^2 f(c)\,\overline{\Delta z}\right\} + O\left(\Delta z^3\right). \qquad (3.45)$$

Consequently, only $z$ or $\bar{z}$ is required for first-order methods, making (3.45) similar to (3.20) in terms of computational effort and memory requirements. When determining analytic derivatives, only a differentiation with respect to $z$ is required to determine the gradient, whereas derivatives with respect to the real and imaginary parts are needed in (3.20).

Analogous to the real-valued case and as indicated in (3.23), one can show the *first-order necessary optimality condition* at a first-order optimal stationary point $z^\star$ to be

$$\left(\frac{\partial f(z^\star)}{\partial z}\right)^{\mathrm{H}} = \boldsymbol{0}. \qquad (3.46)$$

This is again seen by contradiction, via

$$\Delta z = -\left(\frac{\partial f(z^\star)}{\partial z}\right)^{\mathrm{H}} \qquad (3.47)$$

$$\rightarrow f(z^\star + \Delta z) = f(z^\star) - 2\left\|\frac{\partial f(z^\star)}{\partial z}\right\|_2^2 + O\left(\Delta z^2\right) \qquad (3.48)$$

$$\Rightarrow f(z^\star + \Delta z) < f(z^\star) \quad \text{if} \quad \left\|\frac{\partial f(z^\star)}{\partial z}\right\|_2^2 \neq 0. \qquad (3.49)$$

In other words, a lower cost function value can be achieved in the direction $-\left(\frac{\partial f(z^\star)}{\partial z}\right)^{\mathrm{H}}$ as long as a nonzero partial derivative in (3.46) exists.

Consequently, the complex gradient is defined as

$$\boldsymbol{\nabla}_z = \left(\frac{\partial}{\partial z}\right)^{\mathrm{H}} = \left[\frac{\partial}{\partial[z]_1} \quad \cdots \quad \frac{\partial}{\partial[z]_n}\right]^{\mathrm{H}} \in \mathbb{C}^{n \times 1}. \qquad (3.50)$$

**Concluding Remarks — Wirtinger Derivatives**   The Wirtinger calculus represents one of two ways to approach optimization theory in complex-valued variables. Instead of splitting complex quantities into their real and imaginary parts and treating these as new variables, the Wirtinger formalism allows to directly work with complex and complex conjugate terms and, thus, provides a consistent mathematical extension to real-valued differentiation. In particular, real-valued cost functions are seen to be elegantly treatable allowing for a potentially more compact representation and easier implementation than when working with separate real and imaginary quantities.

## 3.3  Nonlinear and Nonconvex Optimization

In the previous section, we have derived the necessary equations to pursue optimization of smooth, non-convex, nonlinear and multivariate cost functions and functionals with respect to complex-

valued variables. In general, we consider minimization tasks of the form

$$\min_{z \in \mathbb{C}^{n \times 1}} f(z), \tag{3.51}$$

where a cost function $f : \mathbb{C}^{n \times 1} \to \mathbb{R}$ is minimized with respect to complex-valued variables $z \in \mathbb{C}^{n \times 1}$. In certain cases, a minimization with respect to real-valued unknowns is considered, for which the required equations have already been discussed.

Minimization of cost functions will be performed based on first-order derivative information, i.e., the gradient, while second- and higher-order derivatives, which are for example required by the Newton method, are not explicitly considered here. There are three main reasons for this restrictive approach. First, the effort to determine analytic formulas increases drastically with the order of differentiation. Second, higher-order derivatives mainly affect the speed of convergence, however, rarely make up for success or failure of a formulation. Third, for an efficient implementation of higher-order derivatives, either the computational effort and/or the memory requirements increase considerably. The presented formulations and framework are supposed to scale well and be suitable for large problems with millions of unknowns and entries in the measurement vector. As will be seen later, there exist techniques which at least approximate information about the second-order derivative based on the gradient of the cost function and, thus, achieve a faster convergence.

Here, we will focus on general first-order minimization techniques that iteratively determine the solution

$$z_{k+1} = z_k + \alpha_k p_k \tag{3.52}$$

after $k$ iterations as a sum of the solution at the previous iteration and a *descent direction* $p_k \in \mathbb{C}^{n \times 1}$ weighted with the *step length* $\alpha_k$. Commonly, one restricts the step length to not change the phase of the descent direction, i.e., $\alpha_k \in \mathbb{R}^+$.

### 3.3.1 Descent Direction

The descent direction at the $k$th iteration in (3.52) is required to compute the new solution vector $z_{k+1}$ at the $(k+1)$th iteration. In general, $p_k$ can be chosen arbitrarily as long as the value of the underlying cost function can be reduced in the direction of $p_k$, i.e.,

$$\exists \alpha_k \ \text{ s.t. } \ f(z_k + \alpha_k p_k) < f(z_k). \tag{3.53}$$

As shown in Section 3.2, this is, up to first-order, ensured whenever

$$\text{Re}\left\{\boldsymbol{\nabla} f(z_k)^{\text{H}} p_k\right\} < 0, \tag{3.54}$$

or when choosing

$$p_k^{\text{GD}} = -\boldsymbol{\nabla} f(z_k), \tag{3.55}$$

which is commonly known as the *steepest descent* or *gradient descent* direction [Cauchy 1847]. Solvers featuring the gradient descent direction are known to suffer from low convergence speeds and therefore require a larger number of iterations until convergence [Asmundis et al. 2013]. Despite

Tab. 3.2 Excerpt of conjugate gradient methods and their associated weighting $\beta_k$ in (3.56).

| Reference | Weighting $\beta_k$ |
|---|---|
| Fletcher-Reeves [Fletcher and Reeves 1964] | $\beta_k^{\mathrm{FR}} = \dfrac{g_k^{\mathrm{H}} g_k}{g_{k-1}^{\mathrm{H}} g_{k-1}}$ |
| Polak-Ribière/Polyak [Polak and Ribiere 1969; Polyak 1969] | $\beta_k^{\mathrm{PR}} = \dfrac{\mathrm{Re}\{g_k^{\mathrm{H}} \gamma_k\}}{g_{k-1}^{\mathrm{H}} g_{k-1}}$ |
| Modified Polak-Ribière [Gilbert and Nocedal 1992] | $\beta_k^{\mathrm{PR+}} = \max\left\{\beta_k^{\mathrm{PR}}, 0\right\}$ |
| Hestenes-Stiefel [Hestenes and Stiefel 1952] | $\beta_k^{\mathrm{HS}} = \dfrac{\mathrm{Re}\{g_k^{\mathrm{H}} \gamma_k\}}{\mathrm{Re}\{\gamma_k^{\mathrm{H}} p_{k-1}\}}$ |
| Liu and Storey [Liu and Storey 1991] | $\beta_k^{\mathrm{LS}} = \dfrac{\mathrm{Re}\{g_k^{\mathrm{H}} \gamma_k\}}{\mathrm{Re}\{p_{k-1}^{\mathrm{H}} g_{k-1}\}}$ |
| Based on Dai and Yuan [Dai and Yuan 1999] | $\beta_k^{\mathrm{DY}} = \dfrac{\|g_k\|_2^2}{2\,\mathrm{Re}\{p_{k-1}^{\mathrm{H}} \gamma_k\}}$ |
| Based on Hager and Zhang [Hager and Zhang 2005] | $\beta_k^{\mathrm{HZ}} = \dfrac{\mathrm{Re}\left\{\left(\gamma_k - 2p_{k-1}\dfrac{\|\gamma_k\|_2^2}{\mathrm{Re}\{p_{k-1}^{\mathrm{H}}\gamma_k\}}\right)^{\mathrm{H}} g_k\right\}}{\mathrm{Re}\{p_{k-1}^{\mathrm{H}} \gamma_k\}}$ |

being slow, the steepest descent method is known to feature a stable convergence behavior [Nagy and Palmer 2003].

Throughout this thesis, we assume that $p_k$ truly is a descent direction, i.e., (3.54) is fulfilled.

**Nonlinear Conjugate Gradient Method**

Improved convergence speed with respect to the steepest descent approach is usually observed with *conjugate gradient* methods, which determine the descent direction according to

$$p_k^{\mathrm{CG}} = \begin{cases} -\nabla f(z_k), & \text{if } k = 0 \\ -\nabla f(z_k) + \beta_k p_{k-1}, & \text{if } k \geq 1 \end{cases}. \tag{3.56}$$

At the first iteration, all conjugate gradient methods utilize the steepest descent direction, while later iterations employ a weighted sum of the gradient at the current iteration and the descent direction of the previous iteration. The weighting factor $\beta_k$ can be computed in various ways, all of which lead to different versions of the conjugate gradient method. An overview of nonlinear conjugate gradient versions and relatively recent developments is available in [Hager and Zhang 2006]. Note that most of the approaches have been developed for real-valued optimization and need to be adapted to the complex case — for some variants this is shown in [Sorber et al. 2012]. A brief collection of conjugate gradient formulations is given in Tab. 3.2, which utilizes the definitions of $g_k = \nabla f(z_k)$ and $\gamma_k = \nabla f(z_k) - \nabla f(z_{k-1})$. The variety of modified nonlinear conjugate gradient methods seems to be endless, and further alternatives requiring tunable parameters are available [Sun and Liu 2015].

While all versions share the same maximum linear convergence rate, their actual performance for a particular minimization problem varies. A comparison of these variants of the nonlinear conjugate gradient method for the application of phase retrieval is given in Fig. 3.1. The details of the phase retrieval approach are not of interest here, however, it can be observed that certain
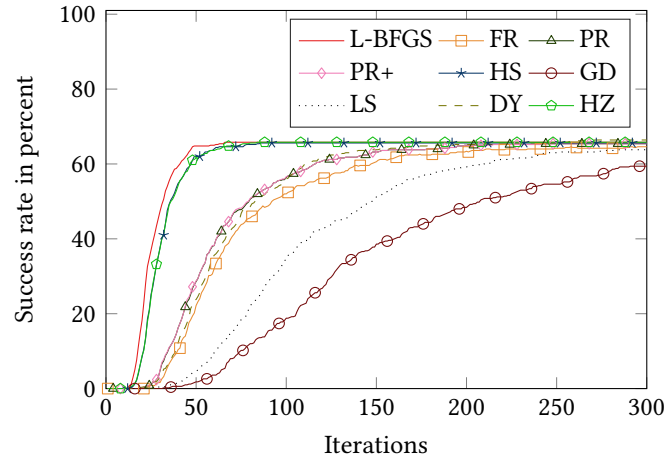
Fig. 3.1 Performance of nonlinear conjugate gradient methods applied to the task of phase retrieval. Details of the retrieval algorithm are not relevant — only an impression of the differences in performance shall be gained. Depicted is the chance of having converged to an accurate solution within a certain number of iterations. As references, the results for the L-BFGS method with $L = 1 \times 10^2$ and the gradient descent method (here GD) are added. All solvers utilize the same line search algorithm. See Tab. 3.2 for a list of abbreviations used.

versions of the nonlinear conjugate gradient method require less iterations than others. As a point of interest, the result for the memory-limited Broyden-Fletcher-Goldfarb-Shanno (L-BFGS) method for $L_{\text{mem}} = 1 \times 10^2$ is added. Due to the nonconvexity of the problem at hand, non of the methods compared in Fig. 3.1 achieves a success rate of 100%. Most importantly, all methods achieve a similar success rate when being allowed to perform a sufficient number of iterations. In terms of convergence rate, one could conclude that the conjugate gradient versions by Hestenes and Fletcher [Hestenes and Stiefel 1952], Hager and Zhang [Hager and Zhang 2005], as well as the L-BFGS method [Andrei 2010; Liu and Nocedal 1989; Nocedal and Wright 2006] are preferable. However, this limited investigation is not sufficient to draw conclusions of general validity. Besides, certain conjugate gradient variants have been reported to perform inferior in other applications, e.g., Fletcher and Reeves [Powell 1976]. More details on the silently added L-BFGS method are provided in the following.

**Memory-Limited Quasi-Newton Method**

The convergence rate of local optimization algorithms is fundamentally limited by the order of the Taylor series, e.g., see (3.30), employed for the computation of the descent direction. While conjugate gradient formulations rely only on information about the gradient and achieve linear rates of convergence, Newton's method [Nocedal and Wright 2006] incorporates the Hessian matrix and thus can yield quadratic convergence locally. Since the full evaluation of the Hessian can be computationally expensive, quasi-Newton methods have emerged that operate with efficient approximations of the second-order derivative information, i.e., the Hessian matrix. In this context, the L-BFGS method accelerates the convergence speed by utilizing a memory-limited version of the Hessian matrix for the computation of the descent direction. The Hessian matrix is approximated via the gradient information of the last $L_{\text{mem}}$ iterations. According to the available memory, larger

---

**Algorithm 1** Computation of the L-BFGS descent direction $\boldsymbol{p}_k$ at current iteration $k$
$[\boldsymbol{p}_k]$ = L-BFGS $(\boldsymbol{\nabla} f(\boldsymbol{z}_k), L_{\text{mem}}, \text{stored } \boldsymbol{s}_i \text{ and } \boldsymbol{y}_i)$

---

**Input:** gradient at current iteration $\boldsymbol{\nabla} f(\boldsymbol{z}_k)$ and stored vectors $\boldsymbol{s}_i$ and $\boldsymbol{y}_i$ of at most $L_{\text{mem}}$ previous iterations

**Output:** L-BFGS descent direction $\boldsymbol{p}_k$

*Abbreviations:*

$\boldsymbol{s}_i = \boldsymbol{z}_{i+1} - \boldsymbol{z}_i$

$\boldsymbol{y}_i = \boldsymbol{\nabla} f(\boldsymbol{z}_{i+1}) - \boldsymbol{\nabla} f(\boldsymbol{z}_i)$

$\rho_i = \frac{1}{\text{Re}\{\boldsymbol{y}_i^{\text{H}} \boldsymbol{s}_i\}}$

1: $\boldsymbol{q} = \boldsymbol{\nabla} f(\boldsymbol{z}_k)$

2: **for** $i = k - 1$ **to** $k - L_{\text{mem}}$ **do**

3: $\quad \alpha_i = \rho_i \text{Re}\{\boldsymbol{s}_i^{\text{H}} \boldsymbol{q}\}$

4: $\quad \boldsymbol{q} = \boldsymbol{q} - \alpha_i \boldsymbol{y}_i$

5: **end for**

6: $\boldsymbol{p}_k = \frac{\text{Re}\{\boldsymbol{s}_{k-1}^{\text{H}} \boldsymbol{y}_{k-1}\}}{\|\boldsymbol{y}_{k-1}\|_2^2} \boldsymbol{q}$

7: **for** $i = k - L_{\text{mem}}$ **to** $k - 1$ **do**

8: $\quad \beta = \rho_i \text{Re}\{\boldsymbol{y}_i^{\text{H}} \boldsymbol{p}_k\}$

9: $\quad \boldsymbol{p}_k = \boldsymbol{p}_k + \boldsymbol{s}_i(\alpha_i - \beta)$

10: **end for**

11: $\boldsymbol{p}_k = -\boldsymbol{p}_k$

12: **return** $\boldsymbol{p}_k$

---

values for $L_{\text{mem}}$ can be chosen to improve the convergence and reduce the overall computation time. For large problems and restricted memory resources, smaller values can be used, eventually reducing the overall performance to that of the nonlinear conjugate gradient methods, which only utilize quantities from one previous iteration. A possible implementation of the L-BFGS method and more theoretical details are described in [Nocedal and Wright 2006] and are repeated in Alg. 1. Care has to be taken to correctly manage the stored quantities $\boldsymbol{s}_i$ and $\boldsymbol{y}_i$ and avoid redundant computations when implementing Alg. 1. As seen in Fig. 3.1 and also reported in [Ji and Tie 2016], the L-BFGS method performs favorably well for the task of phase retrieval and usually outperforms conjugate gradient solvers. Its adjustable memory footprint makes it a perfect candidate for the framework of this thesis, as it flexibly allows to treat large problems while trading as much of the available memory resources as possible for reduced computation times.

**Concluding Remarks — Computation of the Descent Direction** The two principal components necessary for the iterative solution of optimization problems, as indicated in (3.52), are a step length and a descent direction. The choice of the optimization method, e.g., conjugate gradient or a Newton method, determines the computation of the descent direction. Among the investigated first-order methods, moderate performance differences have been observed for the application in phase retrieval, where the L-BFGS method mostly stands out because of its flexibility in terms of memory requirements. Additionally, it employs the first-order derivatives in order to generate an estimate of second-order information, effectively improving the convergence rate. For the purpose of the optimization tasks in this work, low-memory footprint, first-order algorithms are considered as the workhorse for the yet-to-be-defined nonlinear optimization tasks for large problems. Second-order methods, e.g., Newton methods, may be expected to exhibit a faster convergence rate, however, at the downside of consuming more memory and/or computation time.

### 3.3.2 Line Search

Aside the descent direction, (3.52) requires the *step length* $\alpha_k$ for the computation of the solution at the next iteration. As such, $\alpha_k$ is determined as part of a *line search*, which itself is a one dimensional

minimization task of the form

$$\min_{\alpha_k \in \mathbf{R}^+} \Phi\left(\alpha_k\right) \quad \text{with} \quad \Phi\left(\alpha_k\right) = f\left(z_k + \alpha_k p_k\right). \tag{3.57}$$

Note that we have assumed $p_k$ to truly be a descent direction, i.e., to fulfill (3.54). Dependent on the cost function $f(z)$, there may or may not exist an analytic solution to (3.57). Furthermore, the line search optimization itself may be nonlinear and nonconvex, making it unfeasible to exactly determine the optimal value. Thus, one often wants to find a sufficiently good approximate solution to (3.57) at the expense of reasonable computational cost.

The quality and performance of a line search strongly impacts the overall behavior of the underlying iterative algorithm. While a small step length ensures convergence to a local stationary point, the convergence speed may quickly drop and lead to a large number of iterations. Too large step sizes sometimes lead to an increase in the cost function value and can cause the iterative method to become unstable and diverge.

A simple yet inefficient method to ensure convergence at an acceptable rate is called *backtracking*. The backtracking approach starts at a predefined maximum step length $\alpha_m$ at which the cost function is evaluated. In case of a *sufficient* decrease, which will be defined later, of the function value is observed, the method terminates. Otherwise, the current step length is reduced and the cost function is evaluated again. The procedure is repeated until a sufficient decrease has been achieved or the step size has reached a lower bound. In this way, theoretically the solution to (3.57) is found, allowing for the largest decrease in the cost function in the given direct $p_k$. However, the procedure may require an unfeasible number of cost function evaluations to terminate.

There are several criteria widely used in the literature to describe conditions that must be satisfied by the step length to lead to global convergence of iterative solvers for nonlinear and nonconvex optimization problems. The probably most commonly applied requirements are the so-called *Wolfe* or *strong Wolfe conditions*. Alternatively, one can use the *Goldstein conditions* [Nocedal and Wright 2006], which are not explicitly discussed here for brevity.

**Strong Wolfe Conditions**

In case of real-valued variables $z_k$, $p_k \in \mathbf{R}^{n \times 1}$, the Wolfe conditions can be expressed as [Nocedal and Wright 2006]

$$f\left(z_k + \alpha_k p_k\right) \leq f\left(z_k\right) + c_1 \alpha_k \nabla f_k^{\mathrm{T}} p_k \tag{3.58}$$

$$\nabla f\left(z_k + \alpha_k p_k\right)^T p_k \geq c_2 \nabla f_k^{\mathrm{T}} p_k \tag{3.59}$$

with $c_{1/2} \in \mathbf{R}^+$, $0 < c_1 < c_2 < 1$. As the condition in (3.59) may be fulfilled by step lengths not close to a minimizer of $\Phi(\alpha_k)$, one often considers the *strong* Wolfe conditions, which, in the case of complex-valued vectors $z_k$, $p_k \in \mathbf{C}^{n \times 1}$, read as

$$f\left(z_k + \alpha_k p_k\right) \leq f\left(z_k\right) + c_1 \alpha_k 2 \operatorname{Re}\left\{\nabla f_k^{\mathrm{H}} p_k\right\} \tag{3.60}$$

$$\left|2 \operatorname{Re}\left\{\nabla f\left(z_k + \alpha_k p_k\right)^{\mathrm{H}} p_k\right\}\right| \leq c_2 \left|2 \operatorname{Re}\left\{\nabla f_k^{\mathrm{H}} p_k\right\}\right|. \tag{3.61}$$

Since (3.60) imposes a requirement on the reduction of the cost functional with respect to the step length, it is referred to as the *sufficient decrease condition* and sometimes also called *Armijo*
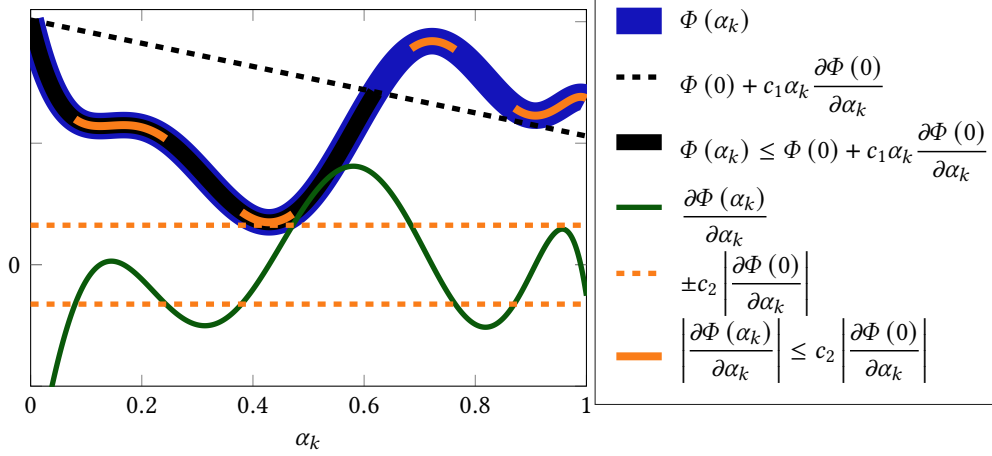
Fig. 3.2 Visualization of the strong Wolfe conditions for a polynomial cost function. The dashed lines indicate the strong Wolfe conditions for a particular choice of $c_1$ and $c_2$.

*condition*. Analogously, (3.61) limits the value of the derivative for a permissible step length and is appropriately called the *curvature condition*.

In accordance with (3.38), we notice that

$$\frac{\partial \Phi (\alpha_k)}{\partial \alpha_k} = \frac{\partial f (z_k + \alpha_k \boldsymbol{p}_k)}{\partial \alpha_k} = \frac{\partial f (z)}{\partial z} \frac{\partial z}{\partial \alpha_k} + \frac{\partial f (z)}{\partial \overline{z}} \frac{\partial \overline{z}}{\partial \alpha_k} = \frac{\partial f (z)}{\partial z} \frac{\partial z}{\partial \alpha_k} + \frac{\overline{\partial f (z)}}{\partial z} \frac{\partial \overline{z}}{\partial \alpha_k}$$

$$= 2 \operatorname{Re} \left\{ \frac{\partial f (z)}{\partial z} \frac{\partial z}{\partial \alpha_k} \right\} = 2 \operatorname{Re} \left\{ \nabla f_k^{\mathrm{H}} \boldsymbol{p}_k \right\}, \tag{3.62}$$

which allows to rewrite the strong Wolfe conditions as

$$\Phi (\alpha_k) \leq \Phi (0) + c_1 \alpha_k \frac{\partial \Phi (0)}{\partial \alpha_k} \tag{3.63}$$

$$\left| \frac{\partial \Phi (\alpha_k)}{\partial \alpha_k} \right| \leq c_2 \left| \frac{\partial \Phi (0)}{\partial \alpha_k} \right|. \tag{3.64}$$

Note that the derivative-vector product $(\frac{\partial f(z)}{\partial z})\boldsymbol{x}$ for the evaluation of (3.62) is required. Along with the gradient-vector product $(\frac{\partial f(z)}{\partial z})^{\mathrm{H}}\boldsymbol{y}$, this is the second fundamental derivative that will be needed when tackling general cost functions and functionals. Figure 3.2 illustrates the strong Wolfe conditions for an exemplary cost function. The *sufficient decrease condition* is indicated by the dashed black line and regions of $\Phi(\alpha_k)$ fulfilling this condition are marked with a solid black line. Similarly, the *curvature condition* imposes restrictions (dashed orange lines) on the magnitude of the slope of the cost function, displayed by the solid green line. Regions of the cost function fulfilling the curvature condition are marked in orange. A line search based on the strong Wolfe conditions is terminated as soon as an $\alpha_k$ is found within an area marked simultaneously in black and orange.

**Line Search Based on the Strong Wolfe Conditions**

An iterative line search procedure determining an $\alpha_k$ satisfying (3.63) and (3.64) is described in [Nocedal and Wright 2006]. For convenience we recapitulate the approach and explain the procedure in detail.

This particular line search relies on three procedures, the most central of which is given in Alg. 2. Two subroutines, the "zoom"-function and an interpolation method, here a quadratic interpolation, are shown in Alg. 3 and Alg. 4. The quadratic interpolation requires the computation of three quantities, $\Phi(\alpha_1)$, $\Phi(\alpha_1)$ and the derivative $\Phi'(\alpha_1)$ in order to obtain the minimum of a quadratic approximation of the cost function within the interval $[\alpha_1, \alpha_2]$. While interpolations of higher order may yield more accurate surrogates of the true cost function and thus allow for a termination of the line search procedure within less iterations, the evaluation of the cost function and its derivative at more sample points is required. For the presented line search algorithm, the quadratic interpolation in Alg. 4 has been observed to yield accurate results while most of its required quantities have already been computed as part of Algs. 2 and 3.

The line search procedure in Alg. 2 requires an initial guess $\alpha_i$, a fixed maximum step length $\alpha_m$ and the two parameters $c_1$ and $c_2$ as part of the strong Wolfe conditions. The procedure tests the current choice for the step length $\alpha_i$ in terms of the strong Wolfe conditions and calls the "zoom"-function once an interval $[\alpha_{LO}, \alpha_{HI}]$ containing a compliant step length is found. In case no such interval is identified within the first iteration, a new trial point for $\alpha_k$ is determined based on the quadratic interpolation in the interval $[\alpha_i, \alpha_m]$ via Alg. 4 and the next iteration is started. Assuming that there exists a solution to the strong Wolfe conditions within the maximum step length of $\alpha_m$, the procedure will eventually call the "zoom"-function. Inside this function, the two bounds $\alpha_{LO}$ and $\alpha_{HI}$ are repeatedly refined via the quadratic interpolation until a promising step length is found. An example of the line search procedure for the exemplary cost function of Fig. 3.2 is depicted in Fig. 3.3 and described in the caption thereof.

**Initial Guess for the Line Search**

In order to speed up any practical line search algorithm, a proper initial guess $\alpha_i$ for the step length at the current iteration $k$ is required. Such an initial guess for the computation of $\alpha_k$ for $k > 1$ can for example be made via

$$\alpha_i = \lambda_i \alpha_{k-1} \frac{\|\boldsymbol{p}_{k-1}\|_2}{\|\boldsymbol{p}_k\|_2} \quad \text{with} \quad \lambda_i \in [0, 1], \tag{3.65}$$

where [Birgin 2001] has considered the case $\lambda_i = 1$, however, [Babaie-Kafaki et al. 2010] reports to have observed better empirical performance for $\lambda_i = 0.75$. Alternatively, one can use [Nocedal and Wright 2006]

$$\alpha_i = \alpha_{k-1} \frac{\left\| \mathrm{Re} \left\{ \boldsymbol{\nabla} f (\boldsymbol{x}_{k-1})^{\mathrm{H}} \boldsymbol{p}_{k-1} \right\} \right\|_2}{\left\| \mathrm{Re} \left\{ \boldsymbol{\nabla} f (\boldsymbol{x}_k)^{\mathrm{H}} \boldsymbol{p}_k \right\} \right\|_2}, \tag{3.66}$$

which is based on the assumption that the first-order change of the cost function at the new iteration will be the same as that of the last iteration.

For $k = 0$, meaning the first call to the line search procedure, the above equations can not be used as no information about previous iterations is available. Thus, either second-order derivative

---

**Algorithm 2** Line search fulfilling the strong Wolfe conditions, after [Nocedal and Wright 2006]
$\alpha_k = \text{LS\_Strong\_Wolfe}\,(\alpha_i, \alpha_m, c_1, c_2, )$

---

**Input:** initial guess $\alpha_i$, maximum step length $\alpha_m > 0$ and parameters $c_1, c_2$

**Output:** step length $\alpha_k$ fulfilling the strong Wolfe conditions
*Abbreviation:*
$\Phi'(\alpha) = \frac{\partial \Phi(\alpha)}{\partial \alpha}$

1: $\alpha_0 = 0$
2: $\alpha_1 = \alpha_i$
3: $i = 1$
4: **while** 1 **do**
5:     compute $\Phi(\alpha_i)$
    *Insufficient decrease? $\Rightarrow$ acceptable point must be between $\alpha_{i-1}$ and $\alpha_i$*
6:     **if** $\Phi(\alpha_i) > \Phi(0) + c_1 \alpha_i \Phi'(0)$ **then**
7:       $\alpha_k = \text{zoom}\,(\alpha_{i-1}, \alpha_i)$ and **break**
8:     **end if**
    *Function increased? $\Rightarrow$ local minimum must be between $\alpha_{i-1}$ and $\alpha_i$*
9:     **if** $\Phi(\alpha_i) \geq \Phi(\alpha_{i-1})$ **then**
10:      $\alpha_k = \text{zoom}\,(\alpha_{i-1}, \alpha_i)$ and **break**

11:     **end if**
12:     compute $\Phi'(\alpha_i)$
    *Sufficiently low curvature? (sufficient decrease already fulfilled) $\Rightarrow \alpha_i$ is an acceptable point*
13:     **if** $|\Phi'(\alpha_i)| \leq c_2 \,|\Phi'(0)|$ **then**
14:      $\alpha_k = \alpha_i$ and **break**
15:     **end if**
    *Positive curvature? $\Rightarrow$ local minimum must be between $\alpha_{i-1}$ and $\alpha_i$*
16:     **if** $\Phi'(\alpha_i) \geq 0$ **then**
17:      $\alpha_k = \text{zoom}\,(\alpha_{i-1}, \alpha_i)$ and **break**
18:     **end if**
    *Pick larger $\alpha_i$, e.g., via quadratic or cubic interpolation*
19:     $\alpha_{i+1} = \text{quadinterp}\,(\alpha_i, \alpha_m)$
20:     $i = i + 1$
21: **end while**
22: **return** $\alpha_k$

---

information is utilized to compute an initial guess as part of the Newton-Raphson method [Nocedal and Wright 2006], or $\alpha_i = 1$ is used, which is seen to eventually work for Newton-type solvers. As a bad initial guess for the first step length should be compensated for by the line search at the expense of additional computation time, the overall effect on the convergence of the optimization algorithm is expected to be rather negligible.

**Concluding Remarks — Line Search**    Iterative optimization techniques, e.g., the nonlinear conjugate gradient method, require a step length computation, i.e., a line search, in order to guarantee convergence. Various approaches exist for finding a more or less optimal step length for a given descent direction. There always is a trade-off between computational effort within the line search and the quality of the determined step length. In this work, the line search presented in [Nocedal and Wright 2006] is employed, featuring a quadratic interpolation routine. Being based on the strong Wolfe conditions, this search algorithm is experienced to determine rather high-quality step lengths compared to simpler techniques like backtracking.

---

**Algorithm 3** "zoom"-function, after [Nocedal and Wright 2006]

$\alpha_k = \text{zoom}\left(\alpha_{\text{LO}}, \alpha_{\text{HI}}\right)$

---

**Input:** $\alpha_{\text{LO}}$ and $\alpha_{\text{HI}}$, bounding an interval which contains

an $\alpha_k$ that fulfills the strong Wolfe conditions

**Output:** step length $\alpha_k$ fulfilling the strong Wolfe conditions

*Abbreviation:*

$\Phi'\left(\alpha\right) = \frac{\partial \Phi(\alpha)}{\partial \alpha}$

1: **while** 1 **do**

2:    $\alpha_i = \text{quadinterp}\left(\alpha_{\text{LO}}, \alpha_{\text{HI}}\right)$

3:    compute $\Phi\left(\alpha_i\right)$

    *Insufficient decrease? $\Rightarrow$ acceptable point must be between $\alpha_{LO}$ and $\alpha_i$*

4:    **if** $\Phi\left(\alpha_i\right) > \Phi\left(0\right) + c_1 \alpha_i \Phi'\left(0\right)$ **then**

5:        $\alpha_{\text{HI}} = \alpha_i$

    *Function increased? $\Rightarrow$ local minimum must be between $\alpha_{LO}$ and $\alpha_i$*

6:    **else if** $\Phi\left(\alpha_i\right) \geq \Phi\left(\alpha_{\text{LO}}\right)$ **then**

7:        $\alpha_{\text{HI}} = \alpha_i$

8:    **else**

9:        compute $\Phi'\left(\alpha_i\right)$

        *Solution found?*

10:       **if** $\left|\Phi'\left(\alpha_i\right)\right| \leq c_2 \left|\Phi'\left(0\right)\right|$ **then**

11:         $\alpha_k = \alpha_i$ and **break**

12:       **end if**

       *"Ascending" slope found (from $\alpha_{LO}$ to $\alpha_{HI}$)? $\Rightarrow$ swap $\alpha_{LO}$ and $\alpha_{HI}$*

13:       **if** $\Phi'\left(\alpha_i\right)\left(\alpha_{\text{HI}} - \alpha_{\text{LO}}\right) \geq 0$ **then**

14:        $\alpha_{\text{HI}} = \alpha_{\text{LO}}$

15:       **end if**

16:       $\alpha_{\text{LO}} = \alpha_i$

17:    **end if**

18: **end while**

19: **return** $\alpha_k$

---

**Algorithm 4** Quadratic interpolation function

$\alpha = \text{quadinterp}\left(\alpha_1, \alpha_2\right)$

---

**Input:** $\alpha_1$ and $\alpha_2$

**Output:** $\alpha = \min\limits_{\alpha \in [\alpha_1, \alpha_2]} \Phi_{\text{q}}\left(\alpha\right) \approx a\alpha^2 + b\alpha + c$

*Abbreviation:*

$\Phi'\left(\alpha\right) = \frac{\partial \Phi(\alpha)}{\partial \alpha}$

1:  $a = \frac{\Phi(\alpha_2) - \Phi(\alpha_1) + \Phi'(\alpha_1)(\alpha_1 - \alpha_2)}{(\alpha_1 - \alpha_2)^2}$

2:  $b = \Phi'\left(\alpha_1\right) - 2\alpha_1 a$

3:  $\alpha = -\frac{b}{2a}$

  *Optional:*

4:  $\left(c = \Phi\left(\alpha_2\right) - \alpha_2 b - \alpha_2^2 a\right)$

5:  **return** $\alpha$

---
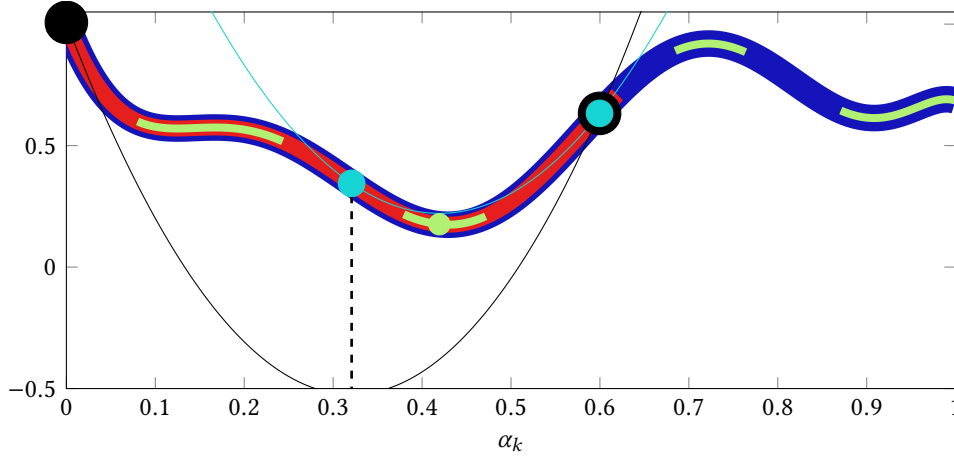
Fig. 3.3 Visualization of the line search procedure fulfilling the strong Wolfe conditions. The cost function is drawn in blue, the region fulfilling the sufficient decrease condition is marked with red and parts of low curvature are indicated by green lines. We pick $\alpha_i = 0.6$ and start in Alg. 2. The initial guess (right black dot) does not fulfill the "if"-statements in lines 6, 9 and 13. However, the curvature $\Phi'(\alpha_i)$ is positive, and in line 17 the "zoom"-function, Alg. 3, is entered. Within "zoom", a quadratic interpolation, Alg. 4, between $\alpha_{LO} = 0$ (left black dot) and $\alpha_{HI} = \alpha_i$ (right black dot) is computed (black solid line). From that, $\alpha_i \approx 0.32$ is set to be at the minimum of the quadratic approximation of the cost function (left cyan dot). All further "if"-statements within this iteration of the "zoom"-function are not fulfilled, such that only line 13 is considered and the new $\alpha_{LO} = \alpha_i$ is assigned. The next iteration again starts with a quadratic approximation (cyan solid line) leading to the new $\alpha_i \approx 0.42$ at its minimum (green dot). Again the conditions in lines 4 and 6 are not fulfilled, however, the current iterate ensures the *curvature condition* (indicated by the green curve) and the algorithm terminates in line 11, returning $\alpha_k = \alpha_i \approx 0.42$. The sufficient decrease condition was met from the beginning.

## 3.4 A General Nonlinear Optimization Framework

With all the tools discussed in the previous sections, a general minimization framework for smooth and differentiable cost functions and functionals of complex- and real-valued variables can be constructed. The main purpose is to handle unconstrained minimization of the form

$$\min_{z \in \mathbb{R}^{n \times 1}/\mathbb{C}^{n \times 1}} f(z) \quad \text{with} \quad f(z) = \alpha_{OF} \|\mathcal{A}(z) - d\|_2^{2p_{OF}}. \tag{3.67}$$

Denoting $c_{OF} = \alpha_{OF} p_{OF} \|\mathcal{A}(z) - d\|^{2p_{OF}-2}$, the required derivatives for $z \in \mathbb{C}^{n \times 1}$ can be written as

$$\frac{\partial f(z)}{\partial z} = c_{OF} \left[ (\mathcal{A}(z) - d)^{H} \frac{\partial \mathcal{A}(z)}{\partial z} + (\mathcal{A}(z) - d)^{T} \frac{\overline{\partial \mathcal{A}(z)}}{\partial z} \right] \tag{3.68}$$

and

$$\left(\frac{\partial f\left(z\right)}{\partial z}\right)^{\mathrm{H}} = c_{\mathrm{OF}}\left[\left(\frac{\partial \mathcal{A}\left(z\right)}{\partial z}\right)^{\mathrm{H}}\left(\mathcal{A}\left(z\right) - d\right) + \left(\frac{\partial \overline{\mathcal{A}\left(z\right)}}{\partial z}\right)^{\mathrm{H}}\overline{\left(\mathcal{A}\left(z\right) - d\right)}\right]. \tag{3.69}$$

In accordance with (3.38), real-valued unknowns $z \in \mathbf{R}^{n \times 1}$ result in

$$\frac{\partial f\left(z\right)}{\partial z} = 2\,c_{\mathrm{OF}}\mathrm{Re}\left\{\left(\mathcal{A}\left(z\right) - d\right)^{\mathrm{H}}\frac{\partial \mathcal{A}\left(z\right)}{\partial z}\right\} \tag{3.70}$$

and

$$\left(\frac{\partial f\left(z\right)}{\partial z}\right)^{\mathrm{H}} = 2\,c_{\mathrm{OF}}\mathrm{Re}\left\{\left(\frac{\partial \mathcal{A}\left(z\right)}{\partial z}\right)^{\mathrm{H}}\left(\mathcal{A}\left(z\right) - d\right)\right\}. \tag{3.71}$$

In either case, the derivatives strongly depend on the particular choice for the involved nonlinear operator $\mathcal{A}$. The vector $d$ represents the *measured information*, which may be available in various ways and formats.

Though (3.67) resembles an unconstrained optimization problem, side constraints or further cost functions can be added to $f\left(z\right)$ with an appropriate weighting $\alpha_{\mathrm{OF}}$ in the form of *soft constraints*. For example, a formulation promoting sparsity in the solution vector can be achieved by adding an $\ell_1$-norm term of the solution vector [Jin and Maass 2012; Lee et al. 2007; Park and Hastie 2007; Schmidt et al. 2007]. The main challenge then remains to identify an appropriate scaling $\alpha_{\mathrm{OF}}$ in order to obtain adequate results for a wide class of problems.

The equations derived above for the gradient and the Hermitian of the derivative of the cost function can now be combined with a first-order technique, such as a nonlinear conjugate gradient or L-BFGS method, along with a line search based on the strong Wolfe conditions. As long as the user provides the quantities

$$\mathcal{A}\left(z\right),\;\; d,\;\; \frac{\partial \mathcal{A}\left(z\right)}{\partial z},\;\; \frac{\partial \overline{\mathcal{A}\left(z\right)}}{\partial z},\;\; \left(\frac{\partial \mathcal{A}\left(z\right)}{\partial z}\right)^{\mathrm{H}}\;\; \text{and}\;\; \left(\frac{\partial \overline{\mathcal{A}\left(z\right)}}{\partial z}\right)^{\mathrm{H}}, \tag{3.72}$$

the framework can be employed to minimize almost arbitrary cost functions. Throughout this thesis, a variety of nonlinear operators $\mathcal{A}$ with their corresponding measurements $d$ will be considered for the implementation of electromagnetic field transformations. Pseudo-code for the optimization framework referring to all necessary equations and algorithms is given in Alg. 5.

When investigating a new formulation, one commonly needs to verify the obtained equations for the above derivatives. For the line search, we can see from (3.62) that checking the derivatives contained in (3.68) or (3.70) can directly be done via finite differences, e.g.,

$$\frac{\partial \Phi\left(\alpha\right)}{\partial \alpha} = \frac{\partial f\left(z + \alpha p\right)}{\partial \alpha} = 2\,\mathrm{Re}\left\{\frac{\partial f\left(z\right)}{\partial z}p\right\} \approx \frac{\Phi\left(\alpha + \delta\right) - \Phi\left(\alpha\right)}{\delta} \tag{3.73}$$

with an appropriately chosen $\delta \in \mathbb{R}^{+}$. Thus, from (3.73) we can verify the correctness of analytic derivatives of cost functions in a (possibly complex-valued) direction $p$ via finite differences. Note that for a satisfactory check, we would need to evaluate this equation for a sufficient number of

---

**Algorithm 5** Optimization framework based on the L-BFGS solver and a line search fulfilling the strong Wolfe conditions
$z$ = FRAMEWORK ($z_i$, parameters)

---

**Input:** initial guess $z_i$ and the parameters

- defining the optimization problem in (3.72),
- $L_{mem}$ used in the L-BFGS solver in Alg. 1,
- $c_1$ and $c_2$ for the line search with strong Wolfe conditions in Alg. 2
- and $\alpha_{OF}$ and $p_{OF}$ in (3.67)

**Output:** local stationary point $z$ of (3.67)

1: $k = 1$
2: $z_k = z_i$
3: $\boldsymbol{\nabla} f(z_k) \leftarrow$ (3.69) or (3.71)
4: **while** not converged or below iteration limit **do**
5:     **if** $k > 1$ **then**
6:        $\boldsymbol{p}_k \leftarrow$ from Alg. 1
7:        $\alpha_i \leftarrow$ (3.65) or (3.66)
8:     **else**
9:        $\boldsymbol{p}_k = -\boldsymbol{\nabla} f(z_k)$
10:        $\alpha_i = 1$
11:     **end if**
    *Based on experience:*
12:     $\alpha_m = 3\max([\alpha_1, ..., \alpha_k])$
13:     $\alpha_k \leftarrow$ from Algs. 2, 3 and 4, requiring (3.68) or (3.70)
14:     $z_{k+1} = z_k + \alpha_k \boldsymbol{p}_k$
15:     $\boldsymbol{\nabla} f(z_{k+1}) \leftarrow$ (3.69) or (3.71)
    *Compute and manage storage of:*
16:     $\boldsymbol{s}_k = \alpha_k \boldsymbol{p}_k, \boldsymbol{y}_k = \boldsymbol{\nabla} f(z_{k+1}) - \boldsymbol{\nabla} f(z_k)$
17:     $k = k + 1$
18: **end while**
19: **return** $z = z_k$

---

directions. The same holds true when validating the gradient, where a similar procedure can be applied to

$$2\,\mathrm{Re}\left\{ \boldsymbol{p}^H \left( \frac{\partial f(z)}{\partial z} \right)^H \right\} \approx \left( \frac{f(z + \delta \boldsymbol{p}) - f(z)}{\delta} \right)^H \tag{3.74}$$

for various $\boldsymbol{p}$. There are other methods for checking the gradient, however, the above simplistic checks have proven to be flexible to utilize and sufficiently accurate in the development of the methods in this work. The author highly recommends using (3.73) and (3.74) to anyone interested in implementing their own cost function.

**Concluding Remarks — Nonlinear Optimization Framework** In a condensed manner, Alg. 5 puts the optimization theory discussed within Chapter 3 and specific implementations of subroutines into practice. At its core, smooth, nonlinear cost functions of multivariate quantities are minimized via the L-BFGS method utilizing a line search procedure based on the strong Wolfe conditions. The unknowns may be complex- or real-valued and the user has to provide equations for the involved operator as well as the corresponding derivatives. In the following, the framework will be applied to a variety of cost functions in the context of phase retrieval.

# 4. Near-Field Far-Field Transformation with Phase Information

The electromagnetic radiation operators and theorems are now combined with optimization theory concepts to perform a first test with NFFFTs operating on fully coherent data [Bucci et al. 1991; Eibert et al. 2010, 2015; Eibert and Schmidt 2009; Petre and Sarkar 1992; Schmidt et al. 2008]. The working principle of NFFFTs with phase information is introduced in Section 4.1 and employs the electromagnetic theorems and radiation operators discussed in Chapter 2 — the same theory as well as operators remain applicable for other field transformations, including those without any or with incomplete phase information. The corresponding problem statement, i.e., a linear system of equations, is solved in Section 4.2, where a simplistic implementation of an NFFFT with phase information based on the introduced optimization framework is provided. A brief comparison with other iterative solvers for linear systems of equations is given in Section 4.3 with synthetic and real-world NF antenna data.

## 4.1 Near-Field Far-Field Transformation Principle

Over the last decades, antenna measurements in the NF region of an AUT have become a popular alternative to their FF and compact range counterparts [Capoglu et al. 2012; Osipov et al. 2013; Qureshi et al. 2013]. This trend has strongly been driven by the comparably low costs for NF measurements that can be performed in smaller and thus cheaper anechoic chambers. The reduction in space requirements comes with the downside of a mathematical transformation that has to be performed, often numerically, in order to obtain the FF characteristic of the AUT from the measured NF samples. A general setup of an NFFFT is depicted in Fig. 4.1(a). The arrangement is in close agreement with that depicted in Fig. 2.5(d), which was found via the equivalence principle applied to Fig. 2.5(a). As part of this equivalent problem, the AUT is represented in terms of *equivalent sources*, e.g., discretized surface current densities or spherical vector wave functions radiating in free space. The complete problem domain is filled with a homogeneous material, e.g., in most of the cases free space, allowing to utilize the known Green's function of free space and, ultimately, the corresponding radiation operators. From the uniqueness theorem we know that a radiator is completely described by the tangential components of its fields evaluated on a closed surface surrounding the radiator. Indicated in Fig. 4.1(a), these tangential fields are sampled by probe antennas yielding not single field components, but in general a spatially weighted version of those fields[1]. As indicated in the figure, we allow the probe antennas to sample the fields in an arbitrary, irregular manner, not restricted to regular sampling schemes on canonical surfaces. Thus, the main task illustrated in Fig. 4.1(a) is to determine the equivalent AUT representation from the measured

---

[1]The fact that real-world probe antennas are not able to directly extract specific field components at discrete points in space — as is theoretically possible via Hertzian and Fitzgerald dipoles — motivates the need of *probe correction* techniques [Cornelius and Heberling 2017; Laitinen et al. 2005; Leibfritz and Landstorfer 2006; Paris et al. 1978; Schmidt et al. 2008; Yaghjian 1986]. Based on the (surface) equivalence principle, the known probe antenna can be modeled in terms of a surface current density, e.g., multiple Hertzian dipoles, in order to account for the radiation or reception characteristic of the probe. As such, an accurate probe correction can be implemented on basis of the dipole-dipole interactions of Chapter 2 at the cost of an increased computational burden. However, more advanced and potentially efficient probe correction techniques are out of the scope of this work.
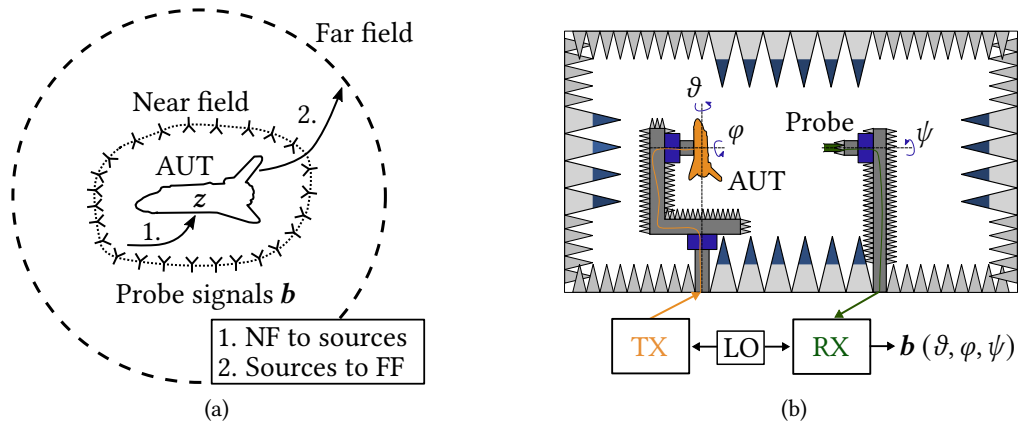
Fig. 4.1 (a) Illustration of the NFFFT principle. Based on NF measurements $b$ on arbitrary and irregular surfaces, an AUT representation $z$ is determined by solving an inverse problem. The FF of the AUT can then be computed from the resulting solution. (b) A simplified illustration of a classical spherical NF measurement setup with a shared LO between the TX and the RX, resulting in measured probe signals with full phase information.

probe signals, which are assumed to be acquired in the radiating NF of the AUT. Once the source coefficients are known, the fields everywhere in space can be evaluated, including the FF.

Now that we have seen the general principle of NF antenna measurements and transformations in Fig. 4.1(a), let us have a look at practical realizations of such measurements. Figure 4.1(b) illustrates a classical spherical measurement setup with the core components of practical relevance, including the transmitter (TX) and RX hardware, as well as a shared local oscillator (LO) providing a stable phase reference to both of them. Commonly, NF antenna measurements are performed in the controlled environment of an anechoic chamber. Such chambers are rooms enclosed by a metallic shield, the inner walls of which are equipped with electromagnetic absorbers. The enclosing made of highly conductive material prohibits disturbances from outside of the chamber to affect the fields in the interior and vice-versa. The absorbers inside the chamber are placed on objects which could potentially cause reflections and scattering disturbances during the measurement. This typically includes the conducting walls, the floor and the ceiling, metal parts for mounting the AUT and the probe, as well as other highly conductive objects belonging to the positioning systems. In this way, radiators placed inside the chamber effectively experience a free-space environment, while external disturbances are reduced to a minimum.

Other components indicated in Fig. 4.1(b) are mechanical parts for rotation of either the mounting structures for the probe antenna or the AUT. Dependent on the desired measurement type, the tangential fields of the AUT are acquired by the probe on a closed surface around the AUT. By rotating the AUT around two axes, the probe can effectively be moved around and relative to the AUT on a spherical surface. By rotating the probe around the $\psi$-axis, a second polarization can be acquired with the same probe antenna. Aside these spherical measurements, other canonical surfaces are commonly employed, like truncated planes or the lateral surface of cylinders. Measurements at a single frequency are conducted by using a continuous wave signal at the TX feeding the AUT. At any relative probe position, a vectorial RX acquires a complex-valued probe signal. Information on the radiation behavior of the AUT within a broad range of frequencies is usually obtained

by changing the frequency of the continuous wave signal and repeating the measurement. At the lower end of the operational frequency range, the performance of the chamber is dominated by the size of the absorbers, with larger absorbers allowing lower frequencies to be measured accurately. As indicated in Fig. 4.1(b), the transmitting and the receiving hardware commonly share an LO for the generation of their internal clocks. In this way, there is a stable phase relation between the transmitted and the received signals. Practical measurement setups may vary in the way how TX and RX clocks are linked, but the principle remains the same so that TX and RX are synchronized with each other. Breaking this synchronization results in loss of phase information, yielding a phaseless NF measurement. Because of the necessity of a synchronization, the electronic measurement devices, cables and mechanical components limit the highest usable frequency in an anechoic chamber. As phase stability of cables, measurement devices and mechanical joints are not relevant for the magnitude of the probe signal, phaseless measurements are often expected to increase the usable frequency range of measurement setups. Note that all these components may also suffer from magnitude instabilities which are, however, commonly assumed to have a minor contribution to the overall error budged of the measurement setup. More information on the error analysis of antenna NF measurement setups is for example provided in [Newell 1988; Pelland et al. 2013].

## 4.2 Optimization Based Transformation with Full Phase Information

Let us leave the real-world measurement setup and come to the task of field transformation. As we have seen in Chapter 2, the interactions between some radiating sources, e.g., the equivalent sources of the AUT, and observers, e.g., equivalent sources of the probe antennas, can be described by linear radiation operators. Thus, the problem of an NFFFT can be written in form of the linear system of equations

$$\mathbf{A}z = b \tag{4.1}$$

where the matrix $\mathbf{A} \in \mathbb{C}^{m \times n}$ describes the relation between unknown coefficients of the AUT field representation $z \in \mathbb{C}^{n \times 1}$ and the measurement vector $b \in \mathbb{C}^{m \times 1}$. The latter is obtained by one or more probes during $m$ acquisitions in the NF of the AUT. The AUT FF can then directly be computed as the FF of a solution to (4.1). However, a solution to (4.1) does only provide a correct AUT representation once a sufficient number of measurements has been acquired. In this context, this does not necessarily require $n \leq m$ and in fact $n > m$ is often encountered in current based representations of the AUT. Still, the number of measurements has to be larger or equal to the DoFs of the AUT. In practice, a trade-off between the overall measurement time — and thus cost — and the number of acquisition points is made. In order to speed up the measurement process by reducing the number of measurements, approaches based on the principles of compressed sensing [Donoho 2006; Foucart and Rauhut 2013] have been investigated for NF antenna measurements in recent years [Cornelius et al. 2016; Larsson 2016].

While state of the art NFFFT algorithms utilizing fast implementations of the forward operator $\mathbf{A}$ can efficiently solve (4.1) for large problems, e.g., see Section 2.2.5, the requirement of accurately knowing the phase of the measured probe signal imposes a major challenge in NF antenna measurements. Methods solely operating on the magnitude of the probe signal would allow the

usage of cheaper phaseless measurement equipment and open up the field for NF measurements in frequency regions where stable phase acquisition is not possible.

The purpose of this section is to illustrate the solution of field transformations with full phase information before, in later chapters, incoherent measurement data is tackled.

A solution to (4.1) is commonly computed by applying any solver of quadratic linear systems of equations to the normal equation

$$\mathbf{A}^{\mathrm{H}}\mathbf{A}z = \mathbf{A}^{\mathrm{H}}\boldsymbol{b}. \tag{4.2}$$

Alternatively, one sometimes applies the normal equation of the form

$$\mathbf{A}\mathbf{A}^{\mathrm{H}}z = \boldsymbol{b}. \tag{4.3}$$

The normal equations suffer from the squared condition number of the matrix $\mathbf{A}$. However, solvers like the generalized minimal residual (GMRES) [Saad and Schultz 1986] solver perform very well even for ill-conditioned linear systems. A detailed discussion on which normal equation to choose for the application in field transformation algorithms is available in [Kornprobst et al. 2021a].

An alternative to solving the normal equations (4.2) or (4.3), is to reformulate (4.1) as an optimization problem. In accordance with the optimization framework of this thesis, we can try to solve (3.67) with

$$\mathscr{A}_0\left(z\right) = \mathbf{A}z \quad \text{and} \quad \boldsymbol{d}_0 = \boldsymbol{b}, \tag{4.4}$$

resulting in

$$\frac{\partial \mathscr{A}_0\left(z\right)}{\partial z} = \mathbf{A} \tag{4.5}$$

$$\frac{\partial \overline{\mathscr{A}_0\left(z\right)}}{\partial z} = \mathbf{0} \tag{4.6}$$

$$\left(\frac{\partial \mathscr{A}_0\left(z\right)}{\partial z}\right)^{\mathrm{H}} = \mathbf{A}^{\mathrm{H}} \tag{4.7}$$

$$\left(\frac{\partial \overline{\mathscr{A}_0\left(z\right)}}{\partial z}\right)^{\mathrm{H}} = \mathbf{0}. \tag{4.8}$$

For reasons of simplicity, we may choose $p_{\mathrm{OF},0} = 1$ and $\alpha_{\mathrm{OF},0} = 1$. Due to the convenient resulting structure of the problem, an exact line search can be performed and the derivative in (3.68) is not required. The optimal step length can be found by searching for $\alpha_{\mathrm{opt}}$, for which

$$\frac{\partial f_0\left(\boldsymbol{x} + \alpha_{\mathrm{opt}}\boldsymbol{p}\right)}{\partial \alpha} = 0. \tag{4.9}$$

We write

$$\begin{aligned}
f_0\left(z' = z + \alpha\boldsymbol{p}\right) &= \|\mathbf{A}z' - \boldsymbol{b}\|^2 = \left(\mathbf{A}z' - b\right)^{\mathrm{H}}\left(\mathbf{A}z' - b\right) \\
&= \left(\mathbf{A}z + \alpha\mathbf{A}\boldsymbol{p}\right)^{\mathrm{H}}\left(\mathbf{A}z + \alpha\mathbf{A}\boldsymbol{p}\right) - \left(\mathbf{A}z + \alpha\mathbf{A}\boldsymbol{p}\right)^{\mathrm{H}}\boldsymbol{b} - \boldsymbol{b}^{\mathrm{H}}\left(\mathbf{A}z + \alpha\mathbf{A}\boldsymbol{p}\right) + \boldsymbol{b}^{\mathrm{H}}\boldsymbol{b} \\
&= \alpha^2 \underbrace{\left[\left(\mathbf{A}\boldsymbol{p}\right)^{\mathrm{H}}\left(\mathbf{A}\boldsymbol{p}\right)\right]}_{a} \\
&\quad + \alpha \underbrace{\left[2\mathrm{Re}\left\{\left(\mathbf{A}z\right)^{\mathrm{H}}\mathbf{A}\boldsymbol{p} - \boldsymbol{b}^{\mathrm{H}}\mathbf{A}\boldsymbol{p}\right\}\right]}_{b} \\
&\quad + \left[-2\mathrm{Re}\left\{\left(\mathbf{A}z\right)^{\mathrm{H}}\boldsymbol{b}\right\}\left(\mathbf{A}z\right)^{\mathrm{H}}\left(\mathbf{A}z\right) + \boldsymbol{b}^{\mathrm{H}}\boldsymbol{b}\right]
\end{aligned} \tag{4.10}$$

which leads to

$$\frac{\partial f_0 \left( z + \alpha p \right)}{\partial \alpha} = 2a\alpha + b \overset{!}{=} 0 \tag{4.11}$$

$$\Rightarrow \alpha_{\text{opt}} = -\frac{b}{2a}, \tag{4.12}$$

which always corresponds to a local minimum since

$$\frac{\partial^2 f_0 \left( z + \alpha_{\text{opt}} p \right)}{\partial \alpha^2} = 2a > 0 \quad \text{when} \quad \mathbf{A} p \neq \mathbf{0}. \tag{4.13}$$

Now the optimization framework in Alg. 5 can be called with the quantities stated in (4.4) and in (4.5) to (4.8). Instead of the iterative line search, the optimal step length in (4.12) can be utilized.

In order to evaluate the performance of field transformation algorithms in general, a few quantities of interest have to be defined. Here, we will often consider the scale-invariant, complex NF deviation

$$\epsilon_c \left( \mathbf{A} z, b \right) = \min_{c \in \mathbb{C}} \frac{\| c\mathbf{A}z - b \|_2}{\| b \|_2} \quad \text{and} \quad \epsilon_{c,\text{dB}} \left( \mathbf{A} z, b \right) = 20 \log_{10} \left( \epsilon_c \left( \mathbf{A} z, b \right) \right). \tag{4.14}$$

In most cases, only the pattern of $\mathbf{A}z$ is of importance and not its absolute scale. Therefore, we allow the solution to exhibit an arbitrary complex scaling, which is compensated in (4.14) by the factor $c$. Especially in the case of phaseless transformations, the solution exhibits an arbitrary global phase shift, which is also taken care of by the scaling $c$. The optimal factor $c$, for which the minimum is attained in (4.14), is derived in Appendix A.2.

Aside the directly available NF deviation, we are interested in the resulting FF deviations at various observation angles. Again, we are not interested in the absolute scaling or the absolute phase of the fields, instead, only in the field distribution. Thus, we consider the vector-valued, scale-invariant, complex relative field deviation

$$\epsilon_c \left( E_1, E_0 \right) = \frac{| cE_1 - E_0 |}{\max \left( | E_0 | \right)}, \quad \text{with} \quad c = \min_{c \in \mathbb{C}} \frac{\| cE_1 - E_0 \|_2}{\| E_0 \|_2}$$
$$\text{and} \quad \epsilon_{c,\text{dB}} \left( E_1, E_0 \right) = 20 \log_{10} \left( \epsilon_c \left( E_1, E_0 \right) \right) \tag{4.15}$$

defined between two vectors of field data, $E_1$ and $E_0$. The magnitude operators as well as the divisions are performed element-wise. Unless explicitly mentioned differently, this relative error is used in all plots of FFs whenever a "deviation" or "error" is mentioned.

## 4.3  Numerical Comparison of Iterative Solvers

A brief comparison of the formulation (4.4) utilizing the optimization framework and common solvers for linear systems of equations accessible in Matlab [Matlab 2021] is depicted in Fig. 4.2. The complex NF deviation $\epsilon_c$ is readily available during the solution process inside the framework and the relative residual of GMRES [Saad and Schultz 1986], the least squares (LSQR) [Paige and Saunders 1982] algorithm and the quasi-minimal residual (QMR) [Freund and Nachtigal 1991] method applied to the normal system of equations in (4.3) is identical to $\epsilon_c$. As a result, the performance of all solvers can directly be compared in terms of the relative NF deviation. In Fig. 4.2(a), the convergence behavior of the solvers is illustrated. The underlying transformation problem is that of a spherical

Fig. 4.2 Comparison of formulation (4.4) to standard solvers in Matlab [Matlab 2021]. The linear system corresponds to an NFFFT of a HF907 horn antenna at 18 GHz, with $n = 2 \times 10^4$ unknowns and $m = 90\,300$ measurements. The computation was performed in single precision on GPUs. All solvers start from a zero initial guess. GMRES and QMR were applied to the normal system of equations in (4.3). (a) Convergence behavior of the solvers. (b) FF of the HF907, transformed with the FIAFTA utilizing a form of GMRES and with the dipole code using formulation (4.4).

NF measurement of an HF907 horn antenna [Rohde & Schwarz GmbH & Co. KG n.d.] at 18 GHz. At this frequency, the minimum sphere of the antenna roughly has a diameter of $18\lambda$. No probe correction was applied and the antenna was represented by Hertzian and Fitzgerald dipoles on a spherical surface. For reasons of better conditioning, the fields radiated by the Fitzgerald dipoles are weighted with the free-space wave impedance. The details of the NF measurement setup are not of interest here, as all solvers have to work with the same linear forward operator. In total, $n = 2 \times 10^4$ unknowns and $m = 90\,300$ measurement samples were utilized. The forward operator was evaluated on four Nvidia GTX 1080 GPUs [Nvidia Corporation 2016b] in single precision. For the developed solver based on the L-BFGS method, the number of stored vectors for approximating second-order derivative information was set to $L_{\mathrm{mem}} = 1 \times 10^2$. The solver based on $\mathcal{A}_0$ does not converge as quickly as GMRES, however, can compete with the low-memory solvers LSQR and QMR. As one can easily modify the solver to incorporate further regularization, e.g., sparsity via $\ell_1$-regularization, the performance is rated as highly satisfactory.

Looking at the obtained FF, Fig. 4.2(b) depicts the dominant co-polar field component in the plane with $\varphi = 0°$. As a reference, the transformation result with the FIAFTA utilizing a GMRES solver is added. The relative difference between the FFs is seen to be below $-47\,\mathrm{dB}$ — which is also true for the complete, three-dimensional radiation characteristic. Given the fact that these are transformations of noisy real-world measurements, the agreement is felt to be satisfactory.

The convergence behavior and the obtained FF for another example with $n = 6\,471\,756$ and $m = 6\,487\,202$ is depicted in Fig. 4.3. Electric and magnetic dipoles on an equilateral triangular surface with an edge length of $554\lambda$ are used to model a triple-reflector in a planar NF measurement setup at 64 GHz. The field samples were acquired at regularly distributed points on a measurement plane in front of the reflector. The FF obtainable via the NFFFT has a limited valid region of roughly $\pm 60°$ away from the main beam of the reflector. Again, the fields radiated by the Fitzgerald dipoles
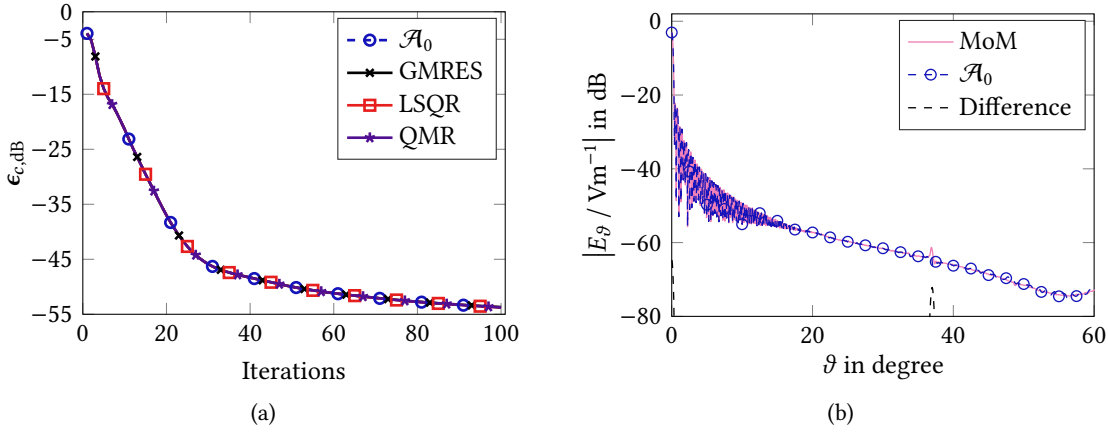
Fig. 4.3 Comparison of formulation (4.4) to standard solvers in Matlab [Matlab 2021]. The linear system corresponds to an NFFFT of a triple reflector at 64 GHz, with $n = 6\,471\,756$ unknowns. The $m = 6\,487\,202$ measurements were acquired on a *regularly sampled* plane in front of the reflector. The computation was performed in single precision on GPUs. All solvers start from a zero initial guess. GMRES and QMR were applied to the normal system of equations in (4.3). (a) Convergence behavior of the solvers. (b) FF of the reflector, obtained with a MoM solver [Eibert 2007] and with the dipole code for NF data using formulation (4.4).

were scaled by the free-space wave impedance. As a reference, the FF directly computed via a MoM solution [Eibert 2007] was used. The forward operators were evaluated in single precision on four Nvidia GTX 1080 and the solver settings were identical to these in the previous example with the HF907 antenna.

From the convergence curves in Fig. 4.3(a), we see a surprisingly similar behavior of all solvers, potentially indicating a well conditioned forward operator.

In Fig. 4.3(b), the dominant field component in the plane with $\varphi = 90°$ is depicted. Despite the single-precision computations, the agreement with the MoM reference within the valid region is fully satisfactory and the maximum relative error in this plane remains below $-64\,\mathrm{dB}$.

The transformation of the triple-reflector was repeated with measurements irregularly distributed on a plane in front of the reflector, where random variations of at most $1/\sqrt{2}\,\lambda$ of the measurement locations in normal direction of the plane occurred. The results are depicted in Fig. 4.4. Experience shows that the irregular distribution of measurement points can worsen the performance of fast hierarchical algorithms, e.g., with an MLFMM, for the evaluation of the radiation operators. For the transformation based on dipoles, a similar performance is observed as in the regular case, with comparable errors in the FF depicted in Fig. 4.4(b). All algorithms except GMRES exhibit an almost identical behavior, where GMRES returns a negligibly worse result. In total, computation times for formulation (4.4), GMRES, LSQR and QMR were 41 813 s, 41 997 s, 41 392 s and 82 827 s, respectively. QMR seems to have performed twice the number of matrix-vector products, since it assumes a rectangular but not Hermitian matrix, and thus did not take advantage of the fact that the given normal matrix is Hermitian. In terms of memory consumption, formulation (4.4), GMRES, LSQR and QMR required roughly 26.3 GB, 20.5 GB, 3.6 GB and 4.5 GB, respectively. The memory consumption was logged via "logman.exe" under Windows 7 [Microsoft Corporation 2021], where the "private bytes" of all Matlab processes were counted. The memory consumption was computed
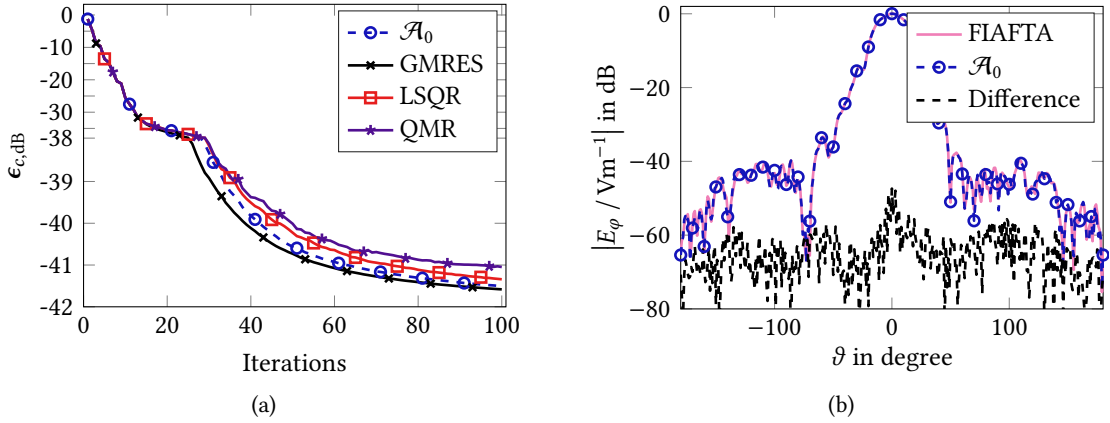
(a)  (b)
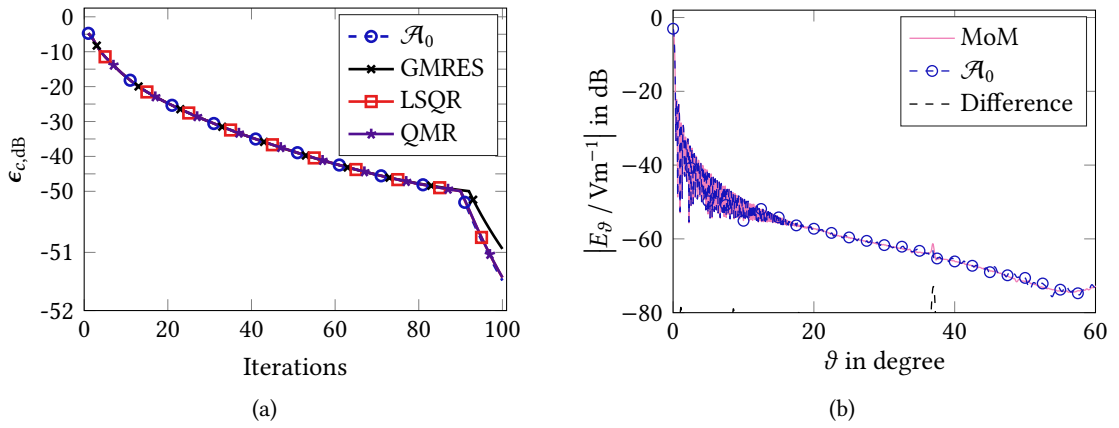
Fig. 4.4 Comparison of formulation (4.4) to standard solvers in Matlab [Matlab 2021]. The linear system corresponds to an NFFFT of a triple reflector at 64 GHz, with $n = 6\,471\,756$ unknowns. The $m = 6\,487\,202$ measurements were acquired on an *irregularly sampled* plane ($1/\sqrt{2}\,\lambda$ random distortions normal to the plane) in front of the reflector. The computation was performed in single precision on GPUs. All solvers start from a zero initial guess. GMRES and QMR were applied to the normal system of equations in (4.3). (a) Convergence behavior of the solvers. (b) FF of the reflector, obtained with a MoM solver [Eibert 2007] and with the dipole code for NF data using formulation (4.4).

as the maximum amount of private bytes occupied during the solution process minus the baseline of memory consumption prior to each solver call. Note that the memory requirement of the L-BFGS solver of the optimization framework used for formulation (4.4) can basically be adjusted and no optimization of the framework in terms of memory has been performed. Since $L_{\text{mem}} = 1 \times 10^2$, the L-BFGS solver has reached its maximum memory consumption at the 100th iteration, while GMRES would continuously require more memory with further iterations — until restarted. In addition, the framework is fully implemented in Matlab, while GMRES, LSQR and QMR are called as C-functions from Matlab.

**Concluding Remarks — Field Transformation with Phase** NFFFTs with full phase information have evolved to useful and well established tools for antenna engineers. Full probe correction and arbitrary measurement locations on irregular sampling grids are supported by various transformation algorithms. Since the problem formulation is linear, efficient methods for the solution of linear systems are directly applicable and can handle the possible ill-conditioning of the forward operators. Recently, considerable effort is put into the fast and flexible evaluation of the forward operator, allowing to solve problems with billions of unknowns. In this respect, it is felt that the topic of NFFFTs with full phase information has matured to a degree that the problem of a transformation can generally be said to be *solved*, while fine details may be further improved on.

# 5. Phaseless Near-Field Far-Field Transformation

Things get more interesting when the synchronization between TX and RX in Fig. 4.1(b) is removed. As a consequence, the phase information in the measurement vector becomes unreliable and the transformation from Chapter 4 can not be applied. There is a large manifold of applications in which a synchronization is no longer possible or feasible. Reasons include that the AUT is some kind of *active* antenna, where the TX hardware is integrated into the antenna geometry and does not feature an additional interface for a reference signal. Typical examples of this case are measurements of radiating systems as a whole, e.g., smartphones to which no external device can be connected. Furthermore, synchronization of TX and RX becomes increasingly difficult at higher frequencies and is a topic of active research at optical frequencies [Kudielka and Klaus 1999; Sunada et al. 2014; Weiner et al. 2017; Ye et al. 2003]. Regardless of frequency, scalar measurement equipment, which provides only power or magnitude information and no phase information, is generally far less expensive than vectorial devices, which can capture phase and magnitude.

Mathematically, a phaseless NFFFT needs to find the solution to the inverse problem

$$|\mathbf{A}x| = |b|, \tag{5.1}$$

where $|.|$ is taken element-wise. Equation (5.1) is known as the *phase retrieval* problem, which has already received a lot of attention over the last decades, e.g., [Bauschke et al. 2002; Elser 2003; Fienup 1982; Sun et al. 2018]. The antenna community has not been inactive and plenty of effort was spent on investigations on phaseless NFFFTs in general, e.g., [Álvarez-Narciandi et al. 2021; Bangun et al. 2019a,b; Breinbjerg and Alvarez 2019; Bucci et al. 1999; Isernia et al. 1996a; Pierri et al. 1999; Pierri and Moretta 2020; Schnattinger et al. 2014; Soldovieri et al. 2005; Wang et al. 2020b]. In particular, phaseless NFFFTs with reference antennas [Berlt et al. 2020; Castaldi and Pinto 2000; Laviada and Las-Heras 2013; Laviada Martinez et al. 2014; Sánchez and Castañer 2018; Sánchez et al. 2020a,b], transformations exploiting multi-frequency data [Knapp et al. 2021; Paulus et al. 2020] or spatial derivatives [Paulus and Eibert 2020] have been performed. Sometimes specialized probe antennas are employed [Costanzo et al. 2001, 2005; Costanzo and Di Massa 2001, 2008; Paulus et al. 2017a,c; Sánchez et al. 2020a] or multiple measurement surfaces [Fuchs et al. 2020; Isernia et al. 1996a; Las-Heras et al. 2020; Moretta and Pierri 2019; Razavi and Rahmat-Samii 2010; Schmidt and Rahmat-Samii 2009; Varela et al. 2021, 2019; Yaccarino and Rahmat-Samii 1995, 1997, 1999], which have, however, been reported to be less effective than particular probe antennas [Knapp et al. 2019a,b]. While most approaches rely on nonconvex retrieval algorithms, their convex alternatives have also been employed for field transformations [Moretta and Pierri 2019; Paulus et al. 2017c].

Other than that, investigations in phaseless scattering [Costanzo and Lopez 2020; Estatico et al. 2020] and diagnostics of printed circuit boards [Wang et al. 2020a] have been conducted.

Before we dive deeper into the task of phase retrieval, let us become aware of the following line of thought. Because of the more uniform and smaller spatial variations in the magnitude of radiated fields compared to the distribution of the phase, it is often assumed that phaseless field transformations are less sensitive to measurement inaccuracies due to the omission of phase information. In reality, however, the opposite seems more reasonable. The sharp and rapid changes in the phase of the field impose strong restrictions and imply a large information content. In various

investigations it has been observed that probe antennas with rapidly varying radiation patterns are particularly suited for phaseless measurements, see for example the treatment of special probe antennas in later sections of this work. One possible explanation could be that highly sensitive probe antennas allow mapping of the non-measurable phase to strongly varying magnitude signals, again providing large information content. However, to obtain reliable data with such probes, their position and radiation characteristic must be precisely known. Essentially, one should keep in mind that disregarding phase information does not allow for free lunch [Macready and Wolpert 1996; Wolpert and Macready 1997].

The content of this chapter is organized as follows. First, the topics of uniqueness and sampling complexity in the scope of phase retrieval are briefly introduced in Sections 5.1 and 5.2, providing a rudimentary overview of relevant literature and existing approaches. Things get practical in Section 5.3, where methods for the estimation of an initial guess for phase retrieval are reviewed and tested. Proper starting points are essential for nonconvex phase retrieval methods and are often assumed for convergence proofs and guarantees of sampling complexities of reconstruction algorithms. With decent initialization techniques in our toolbox, Section 5.4 provides a comprehensive collection of nonconvex phase retrieval algorithms, all of which can be easily implemented via the earlier described optimization framework or in even simpler form. In Section 5.5, existing convex phase retrieval methods, which are less prone to inaccurate initial guesses, are discussed and utilized. At their core, most of the convex techniques rely on semidefinite relaxations applied to formulations derived via bilinear forms. As shown in Section 5.6, an exact and linear representation of the phase retrieval problems is possible employing these bilinear forms, however, leading to the worst possible sampling complexity of any phase retrieval algorithm. Nevertheless, a simplistic implementation of this direct and exact phase retrieval algorithm closes the chapter.

**Motivating Remarks — Phase Retrieval for Antenna Field Transformations**   With plenty of research activity focused on the simple-looking nonlinear system of equations in (5.1) for more than four decades, one might expect that the problem has already been solved. Surprisingly, this is not the case in the field of computational electromagnetics, although there are certain applications for which satisfactory solutions exist. One important point to mention is that the difficulty of phase retrieval depends primarily on the measurement matrix $\mathbf{A}$, which itself commonly models an underlying physical process. This data dependency will become more clear in the following chapters and sections.

## 5.1  Uniqueness of Phase Retrieval

The question of *uniqueness* regarding the phase retrieval problem is a research topic of its own, e.g., see [Bendory et al. 2017; Devaney and Chidlaw 1978; Ji et al. 2019; Seldin and Fienup 1990]. Essentially, the task is to determine the smallest number of measurements — assuming a certain measurement type — for which there exists an injective mapping between the measurement magnitudes and the phases to be reconstructed. Be aware that for certain measurement models no uniqueness proof exists at all — independent from the number of measurements — and that trivial ambiguities may persist. Lending to the historical roots of the phase retrieval problem, uniqueness was first considered in the field of optics, where the forward operator most often consists of a Fourier transformation [Lane et al. 1987]. Thus, there are plenty of results for the case of Fourier measurements showing that one-dimensional phase retrieval of these measurements suffers from

ambiguities that can be resolved only if at least one dimension is added [Bates 1982], e.g., for phase retrieval of two-dimensional signals such as images, uniqueness can be achieved. More recently, it has been shown that slight modifications of the one-dimensional Fourier phase retrieval problem also ensure uniqueness [Huang et al. 2016]. Since the question of uniqueness at its core depends on the particular forward operator, there are very few statements on when the problem is uniquely posed in the field of antenna measurements. In [Razavi and Rahmat-Samii 2008] it is claimed that planar NF measurements on a single plane are *likely* to result in a unique solution, while measurements on two-planes are *extremely likely* to result in a unique solution. Regarding FF measurements, [Inan and Diaz 2011] shows that uniqueness can be achieved by performing at least two sets of measurements differing by a quadratic phase function. For data consisting of generic frames, the information theoretic limit of measurements required for uniqueness is given by $m \geq 4n - 4$ and $m \geq 2n - 1$ in the complex and real case, respectively [Balan et al. 2006; Bandeira et al. 2013; Bodmann and Hammen 2015; Conca et al. 2015]. Note that in [Balan et al. 2006] $m \geq 4n - 2$ is claimed to be a sufficient bound for the complex-valued case. Generic frames simply represent a redundant system of vectors in a Hilbert space. In practical applications, these lower bounds are rarely reached, nonetheless they are often used as a rule of thumb for the required number of measurements. Thus, it is expected that for the real-valued case, $m/n \geq 2$ yields a "high" chance of success for certain algorithms, while $m/n \geq 4$ is frequently regarded to be suitable for the complex-valued case. Again, these rules of thumb can fail if the measurement data is strongly different from that of a random process, e.g., if the data exhibits structure, as it is the case with NF antenna measurements. Uniqueness can also be investigated by looking at the occurrence of stationary points in nonconvex phase retrieval formulations — once only a single minimum remains, the problem has become convex and potentially unique. The existence of stationary points has been investigated thoroughly, e.g., see [Isernia et al. 1996b; Pierri and Moretta 2020; Soldovieri et al. 2005; Sun et al. 2018], and will briefly be touched upon later.

**Concluding Remarks — Unique Phase Retrieval**   Uniqueness proofs for phase retrieval only exist for a few data models, where for complex-valued generic frames $m \geq 4n - 4$ was shown to ensure a unique solution. This threshold may be taken as a rule of thumb, however, in practice, more measurements are recommended when working with NF antenna data. Limited by a finite measurement accuracy, the main task in many real-world applications remains to be the determination of a *sufficiently accurate* solution, something that is, to a certain degree, possible even in the presence of ambiguous solutions.

## 5.2 Sampling Complexity

The term *sampling complexity* refers to a commonly used metric for comparing phase retrieval algorithms. Recent publications on the topic of phase retrieval often state proofs for the correct convergence of their algorithms. However, in order to prove convergence, mathematicians have mainly relied on simple data models, for example that of normally distributed forward matrices. Based on this data model, a condition can be imposed on the ratio of the number of measurements to unknowns, $m/n$, so that the algorithms are able to find the correct solution. In this context, the sampling complexity describes the required number of measurements in a Bachmann-Landau notation. Since $O(n)$ measurements (rows) are required for the solution of a linear system of equations (with full phase), this *linear sampling complexity* is the ideal lower information theoretic

limit of all phase retrieval algorithms. This bound is said to be achieved by some existing convex and nonconvex algorithms. Still, it should be noted that even if an algorithm is claimed to feature a linear sampling complexity, this behavior may not be observed for data with different structure, i.e., if the forward operator is not normally distributed. Also, often an appropriate initialization technique is assumed, which itself may only be proven to work well with Gaussian data. These are the main reasons why claims of superior sampling complexities should be taken with a pinch of salt, and why considerable effort is being spent on trying to generalize the statements valid for Gaussian data to that of different structures [Gross et al. 2015]. On the other side, and as will be shown in Section 5.6, a complexity of $O(n^2)$ is the worst possible case. All information about the problem is available within $O(n^2)$ measurements. Any algorithm featuring a higher sampling complexity is guaranteed to be doing something wrong. Furthermore, investigations on the geometric structure of the phase retrieval problem have revealed that in the case of Gaussian data and for $m \geq O(n \log^3 n)$, phase retrieval itself behaves with high probability like a convex problem [Sun et al. 2018]. At the risk of pointing out the obvious, the reader is reminded that any superlinear sampling complexity will sooner or later lead to excessive measurement effort when tackling problems of increasing size.

When exploiting prior knowledge on the phase retrieval problem at hand, e.g., sparsity on the solution vector, even lower sampling complexities can be achieved, for example see [Netrapalli et al. 2015]. Here, we do not further investigate sparsity promoting methods [Baechler et al. 2019; Jaganathan et al. 2013; Pauwels et al. 2018; Qiu and Palomar 2017; Shechtman et al. 2014; Wang et al. 2018c] since they can only be applied to phaseless NFFFTs in rare cases.

A summary of the sampling complexities of common phase retrieval algorithms is given in Tab. 5.1. The list is far from complete and shall only give a brief impression of the proven, or sometimes claimed, sampling complexities. Keep in mind that the complexities stated here are all based on normally distributed data. Algorithms with the same sampling complexities in Tab. 5.1 may exhibit a different behavior for real-world data.

**Concluding Remarks — Sampling Complexity**    The sampling complexity is a widely used metric for comparing phase retrieval algorithms. Utilizing the Bachmann-Landau notation, the sampling complexity states how many measurement samples, dependent on the number of unknowns, are required for a specific algorithm to provably converge to the correct solution. Similar to the discussion on the uniqueness of phase retrieval, particular data models — often normally distributed data — are assumed in most proofs, which drastically reduces the significance of claimed complexities when encountering different kinds of data. In particular, the practitioner may remain skeptical about the reliability of these statements when working with phaseless NFFFTs and is well advised to acquire more measurement samples than predicted by complexity considerations.

## 5.3 Spectral Initializers for Phase Retrieval

Nonconvex optimization methods heavily rely on a proper starting point. The *closer* this initial guess $z_i$ is to the true solution $z_t$ — ideally within its basin of attraction —, the fewer iterations are required until convergence and the lower the chance of getting trapped in a local stationary point during the optimization process. Thus, most publications which present new nonconvex phase retrieval algorithms require the starting point to be in the proximity of the true solution in order

Tab. 5.1 Phase retrieval algorithms and claimed sampling complexities — for complex-valued normally distributed data.

| Algorithm | Sampling complexity | Behavior |
|---|---|---|
| PhaseLift [Candès et al. 2013] | $O(n \log n) \,/\, O(n)$ [Candès and Li 2014; Candès et al. 2013] | convex |
| PhaseCut [Waldspurger et al. 2015] | $O(n)^1$ [Mroueh and Rosasco 2014] | convex |
| PhaseMax [Goldstein and Studer 2018] | $O(n)^2$ [Goldstein and Studer 2018] | convex |
| AltMinPhase [Netrapalli et al. 2015] | $O(n \log^3 n)$ [Netrapalli et al. 2015] | nonconvex |
| Wirtinger flow [Candès et al. 2015b] | $O(n \log n)$ [Candès et al. 2015b] | nonconvex |
| Truncated Wirt. flow[3] [Chen and Candès 2017] | $O(n)$ [Chen and Candès 2017] | nonconvex |

[1] Claimed — proof is not found in [Mroueh and Rosasco 2014] and [Waldspurger et al. 2015].

[2] Assuming a constant angle between the anchor vector and the true solution.

[3] Same holds for variants [Luo et al. 2020; Pinilla et al. 2018; Wang et al. 2017, 2018a; Yuan and Wang 2017; Zhang and Liang 2016; Zhang et al. 2017].

to prove convergence properties of their algorithms. In this context, the closeness between two solution vectors is commonly described in terms of the *cosine similarity*, which is briefly introduced.

This section starts by recapitulating the concept of *spectral initializers*, a popular class of algorithms for the generation of initial guesses for phase retrieval. Due to the large supply of existing spectral methods, which often feature minor deviations among each other, only the equations for and discussion of a potentially small selection of techniques is provided here. Most effort is spent on empirical performance analyses of the methods for random normally distributed data and NF antenna data. Since phase retrieval is known to perform better for randomly distributed data than for more realistic data models, similar behavior is expected for initialization techniques. In fact, the discrepancies in real-world performance have already led to first theoretical analyses of partial orthogonal matrices — in contrast to random normally distributed matrices — in the context of phaseless initialization methods [Dudeja et al. 2020].

Spectral initialization methods all share a common concept. The initial guess is given by the eigenvector corresponding to the largest eigenvalue of a particular matrix. Variation among the techniques is mainly limited to the form of the relevant matrix, of which the basic structure is given by

$$\mathbf{Y}(t) = \tfrac{1}{m}\mathbf{A}^{\mathrm{H}}\mathrm{diag}(t)\,\mathbf{A}, \qquad \mathbf{Y} \in \mathbb{C}^{n \times n} \tag{5.2}$$

and which depends on the vector $t \in \mathbb{R}^{m \times 1}$.

The most prominent method, called the *spectral initialization*, was introduced in [Candès et al. 2015b] and is based on

$$t_{\mathrm{spec}} = |\boldsymbol{b}|^2 .$$

(5.3)

Soon, various alternatives of this spectral method were proposed, e.g., the *optimal spectral initialization* [Luo et al. 2019; Mondelli and Montanari 2019] with

$$t_{\mathrm{opt}} = \frac{|\boldsymbol{b}|^2 - 1}{|\boldsymbol{b}|^2 - 1 + \sqrt{\frac{m}{n}}}.$$

(5.4)

The division in (5.4) is performed element-wise for every entry of the squared-magnitude vector $|\boldsymbol{b}|^2$. Note that there is one particular condition for (5.4) to be working as intended by its creators, namely that $\mathrm{mean}(|\boldsymbol{b}|^2) = 1$. By scaling the measurement vector before applying the initialization method, this condition can always be fulfilled.

Initially designed for *isometric* matrices, the *null initialization* [Chen et al. 2018; Liu et al. 2018] requires computation of the eigenvector corresponding to the *smallest* eigenvalue of (5.2), with

$$[t_{\mathrm{nu}}]_i = \begin{cases} 0 & |[\boldsymbol{b}]_i| \geq b_{\mathrm{nu}} \\ 1 & \text{else} \end{cases},$$

(5.5)

which removes the influence of all measurements with magnitudes above a certain threshold. According to [Chen et al. 2018], this is equivalent to finding the eigenvector to the largest eigenvalue for the complementary set, i.e., of the set where all $|[\boldsymbol{b}]_i| < b_{\mathrm{nu}}$ are set to zero. Furthermore, the method can be applied to non-isometric matrices by performing the **QR**-decomposition of **A** and applying the null initialization on **Q**, yielding $z'_{\mathrm{nu}}$ and obtaining the initial guess by $z_{\mathrm{nu}} = \mathbf{R}^{-1} z'_{\mathrm{nu}}$. In this thesis, the null initialization is realized by determining the eigenvector corresponding to the largest eigenvalue of (5.2) with the complementary definition to (5.5). As matrices being nonisometric by nature are investigated, the **QR**-decomposition is applied. As done in the original paper, the threshold $b_{\mathrm{nu}} = \mathrm{median}\,(|\boldsymbol{b}|)$ is chosen such that half of the measurements are filtered out. Algorithm 6 illustrates the procedure based on an implementation via power iterations [Leon 2015; Mises and Pollaczek-Geiringer 1929]. For reasons of reduced computational effort and complexity, results without the **QR**-decomposition will partially be reported, as well as results obtained via the implementation taken from [Chandra et al. 2019, 2017]. In any case, the particular implementation at hand will be explicitly mentioned.

A *truncated* initializer was proposed in [Wang et al. 2018a] via

$$[t_{\mathrm{tr}}]_i = \begin{cases} 1 & |[\boldsymbol{b}]_i| \geq b_{\mathrm{tr}} \\ 0 & \text{else} \end{cases},$$

(5.6)

where we here choose $b_{\mathrm{tr}}$ such that $1/6$ of all available measurements are considered and the rest is dropped. It can be seen that this formulation corresponds to the claimed dual of (5.5), except that no isometric matrix is required. Accordingly, one can expect the null initialization, to a certain degree, to also work with nonisometric matrices and without applying the **QR**-decomposition.

---

**Algorithm 6** Null initialization with QR-decomposition
$z_i = \mathrm{NULL}\,(A, |b|, b_{\mathrm{nu}}, k_{\mathrm{it}})$

---

**Input:** forward operator $A$, measurements $|b|$, threshold $b_{\mathrm{nu}}$, iterations $k_{\mathrm{it}}$

**Output:** $z_i$, with $|Az_i| \overset{!}{\approx} |b|$

1: $\forall i \in \{1, ..., m\},\ [t]_i = \begin{cases} 1 & |[b]_i| \geq b_{\mathrm{nu}} \\ 0 & \text{else} \end{cases}$

2: $QR = A$
3: $V = Q^H \mathrm{diag}\,(t)\,Q$
4: $P_R = RR^{-1}$

5: $z_i \sim \mathcal{CN}\,(0, 1)$
6: $z_i = Rz_i$
7: **while** $k \leq k_{\mathrm{it}}$ **do**
8: $\quad z_i = Vz_i$
9: $\quad z_i = P_R z_i$
10: $\quad z_i = z_i / \|z_i\|$
11: **end while**
12: $z_i = Q^H \mathrm{diag}\,(|b|)\,e^{j\angle(Qz_i)}$
13: **return** $z_i = R^{-1} z_i$

---

Lastly, we consider the *weighted* initialization [Wang et al. 2018b] with

$$[t_{\mathrm{w}}]_i = \begin{cases} |[b]_i|^{\gamma_{\mathrm{w}}} & |[b]_i| \geq b_{\mathrm{w}} \\ 0 & \text{else} \end{cases}, \tag{5.7}$$

which only considers a subset of the measurements with the largest magnitude and weights them with the exponent $\gamma_{\mathrm{w}}$, which we here set, in agreement with the original publication, as $\gamma_{\mathrm{w}} = 0.5$. Furthermore, the following results are based on picking only the largest 23% of the measurements.

### Numerical Analysis of Spectral Methods

Figure 5.1(a) illustrates the importance of a proper initialization when performing phase retrieval via a nonconvex algorithm. For a fixed oversampling ratio of $m/n = 4$, the number of unknowns $n$ was swept and the chance of a successful phase reconstruction was computed. The forward operator and the solution vector were randomly picked from a complex-valued normal distribution. In the range of $n \in \{2, ..., 1 \times 10^3\}$ and $n \in \{1001, ..., 1 \times 10^4\}$, the reconstruction was performed $5 \times 10^3$ and $5 \times 10^2$ times, respectively. The number of trials for larger $n$ was reduced in order to keep the overall computation time reasonable. Success was declared once an error in (4.14) of below $-45\,\mathrm{dB}$ was achieved. At most $5 \times 10^3$ iterations of a nonconvex solver (see formulation (5.16) in the next section) were performed. The curves depicted show the chance of a successful reconstruction when starting from a randomly drawn initial guess and one based on (5.3). For a fixed sampling ratio, the spectral method ensures a decent initial guess up to a larger problem dimension than is the case for a random starting point. Nevertheless, the improvement does not completely remove the dependency on the problem dimension, so that the success rate drops for $n$ close to $1 \times 10^4$.

The results in Fig. 5.1(a) can be explained by looking at the quality of the initial guesses. One indicator for this is the scale-invariant, complex NF deviation associated with the initial guess $\epsilon_c\,(Az_i, b)$ as given in (4.14). Alternatively, the *cosine similarity*

$$\chi\,(x, y) = \frac{\mathrm{Re}\,\{x^H y\}}{\|x\|\,\|y\|}, \tag{5.8}$$

(a)

(b)
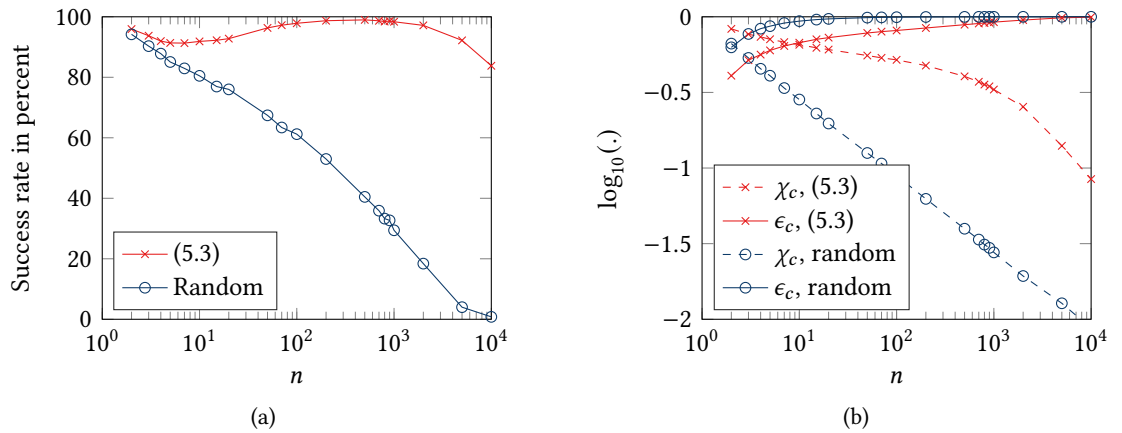
Fig. 5.1 The effect of the initial guess on the task of phase retrieval for a nonconvex algorithm and a fixed $m/n = 4$, for complex-valued normally distributed measurement matrices and solution vectors. In both plots, $5 \times 10^3$ runs were performed up to $n = 1 \times 10^3$ and $5 \times 10^2$ repetitions have been performed for $n > 1 \times 10^3$. (a) Success rate when starting from a random initial guess and one generated via the spectral method in (5.3). Success was declared once $\epsilon_{c,\mathrm{dB}} \leq -45\,\mathrm{dB}$. (b) Mean values (before the logarithm is applied) of the cosine similarity and the complex NF deviation. The cosine similarity and the complex NF deviation are computed for the initial guess as $\chi_c(z_\mathrm{i}, z_\mathrm{t})$ and $\epsilon_c(\mathbf{A}z_\mathrm{i}, \boldsymbol{b})$.

defined for two complex-valued vectors $\boldsymbol{x}$ and $\boldsymbol{y}$, can be considered. Arbitrary global phase shifts are accounted for when considering

$$\chi_c(\boldsymbol{x}, \boldsymbol{y}) = \max_{c \in \mathbb{C}} |\chi(c\boldsymbol{x}, \boldsymbol{y})| = \frac{|\boldsymbol{x}^\mathrm{H}\boldsymbol{y}|}{\|\boldsymbol{x}\|\,\|\boldsymbol{y}\|}. \tag{5.9}$$

The cosine similarity represents the angle spanned by two vectors in the form of $\angle(\boldsymbol{x}, \boldsymbol{y}) = \mathrm{acos}(\chi(\boldsymbol{x}, \boldsymbol{y}))$. Commonly, we assume that the ideal initial guess is collinear to the true solution, yielding $\chi = 1$. In our application, $\chi_c$ is expected to represent the more honest and easy-to-use metric and will mainly be applied throughout this work.

Figure 5.1(b) depicts the quality of the initial guess, drawn randomly and generated via (5.3). In the range of $n \in \{2, ..., 1 \times 10^3\}$ and $n \in \{1001, ..., 1 \times 10^4\}$, initial guesses in $5 \times 10^3$ and $5 \times 10^2$ cases were investigated, respectively. The curves depict the average values of the respective figures of merit. It is clear that the larger the problem dimension, the less likely do two random vectors point into a similar direction. Thus, deciding for a random initial guess results in a larger distance to the correct solution, eventually leading to a worse performance for nonconvex phase retrieval algorithms. The spectral method in (5.3) achieves a less steep decrease of the cosine similarity as well as a slower increase of the NF deviation for larger problem sizes.

As will be evident from further investigations, the assumption of randomly distributed measurement matrices often leads to phase retrieval problems that are easier to solve than those encountered with real-world NF antenna data. It can not be stressed sufficiently that forward operators belonging to field transformations are unlikely to exhibit the random structure of Gaussian measurement matrices. While the results in Fig. 5.1 are based on random data, Fig. 5.2(b) depicts the performance

of initialization methods for data stemming from a synthetic NF measurement setup. The implementation of the methods was taken from the PhasePack library [Chandra et al. 2019, 2017]. Three implementation variants were investigated for the null initialization. One is based on the computation of the smallest eigenvalue without any **QR**-decomposition, was taken directly from [Chandra et al. 2019, 2017] and is drawn with a dotted line in the figures. An alternative implementation is based on Alg. 6 with $k_{it} = 1 \times 10^2$ iterations, which computes the largest eigenvalue via power iterations and employs the **QR**-decomposition (solid line). Results for the latter implementation without the **QR**-decomposition have been added and are drawn with dashed lines. In this setup, the AUT is represented by a spherical vector wave expansion with $N_0 = 15$, leading to $n = J = 510$ coefficients. For each ratio of $m/n$, $1 \times 10^3$ repetitions with randomly drawn $z_t$ have been conducted. The measurement vectors consist of the magnitude of the tangential field components of the electric field acquired on a spherical surface with radius $2\lambda$. The sampling locations of the electric field are almost uniformly distributed on the sphere via a Fibonacci mapping [Keinert et al. 2015]. Comparing results for this rather realistic setup with those obtained for random measurement matrices in Fig. 5.2(a), notable differences can be observed. While all methods are able to obtain a better initial guess when adding more random measurements in Fig. 5.2(a), the improvement in Fig. 5.2(b) is less pronounced and the overall achievable cosine similarity is lower. Leaving aside the various implementations of the null initialization, one can see that in the case of NF data the variations among the initializers are less pronounced than in the case of random data. For both data structures, the optimal spectral method can be said to perform best. Among the null initialization methods, the one employing the **QR**-decomposition and computing the largest eigenvalue is the best for random data, while dropping the decomposition seems to be favorable in case of NF data[1]. It should be kept in mind that the results in Fig. 5.2 are merely a snapshot for a single fixed problem dimension of $n = 510$.

How do these methods behave for NF data when the number of unknowns increases? Figure 5.3(b) gives an impression of what to expect. Spherical vector wave functions were used to generate NF data on a spherical surface, now with a rather large radius of $14\lambda$ to ensure measurements of the radiating and not of the reactive NF. Again, an almost uniform sampling via a Fibonacci mapping [Keinert et al. 2015] was utilized to distribute the locations where the tangential electric field was acquired. For all values of $n$, $1 \times 10^2$ repetitions for randomly drawn $z_t$ have been performed and the average of the cosine similarity $\chi_c(z_i, z_t)$ was evaluated. The oversampling ratio was fixed at $m/n = 4$. As previously, the implementation of the methods was taken from the PhasePack library [Chandra et al. 2019, 2017], and the implementations of the null initialization based on Alg. 6 were added. Comparing the resulting curves with those obtained with the spectral method in (5.3) for random data in Fig. 5.1(b) and in Fig. 5.3(a), a drastically worse performance is observed. While in Figs. 5.1(b) and 5.3(a) the spectral method achieves a less steep slope up to $n \approx 1 \times 10^3$, the initialization methods applied to NF data exhibit the same downward trend as a random initial guess in Fig. 5.3(b). Also, there seems to be no clear winner among the initializers for NF data, as

---

[1]The results obtained via the implementation from PhasePack (dotted lines), based on computing the smallest eigenvalue and not applying the **QR**-decomposition, are not identical to that of the complementary approach (dashed lines). Based on the theory of the null initialization, the latter two formulations should yield identical results, at least for isometric matrices. Since both approaches do not employ the **QR**-decomposition and are based on different algorithms for the computation of the largest and smallest eigenvalues, identical results are not to be expected in this context. However, based on extensive empirical studies, the author was not able to reproduce the claimed correspondence between the smallest eigenvector and the largest eigenvector for the complementary condition in (5.5), even for isometric matrices and employing identical methods for the computation of the eigenvectors. The author recommends to utilize one of the other spectral methods in practice.
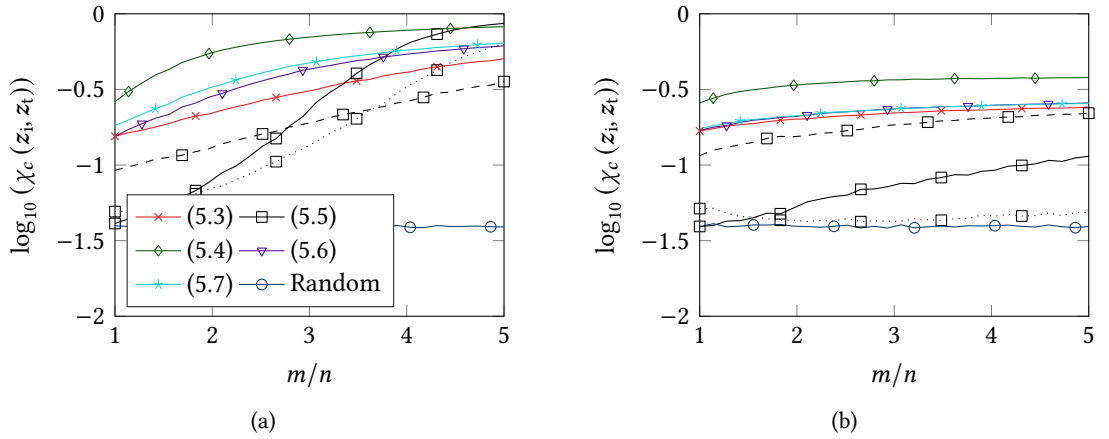
Fig. 5.2 Average cosine similarity achieved with various initialization methods [Chandra et al. 2019, 2017]. For the null initialization, the implementation from [Chandra et al. 2019, 2017] via the smallest eigenvalue (without **QR**) (dotted) and the implementation based on the largest eigenvalue according to Alg. 6, with (solid) and without (dashed) **QR**-decomposition, have been employed. With $n = 510$, each ratio of $m/n$ was simulated $1 \times 10^3$ times with randomly drawn $z_t$. (a) Complex-valued normally distributed data. (b) For data from a synthetic spherical NF measurement setup with a vector spherical wave expansion with $N_0 = 15$, resulting in $J = 510 = n$. The tangential electric field is sampled on a spherical surface with radius $2\lambda$ at locations computed via a Fibonacci mapping [Keinert et al. 2015].

one method superior at fewer unknowns may be outperformed by another approach for larger $n$. Only the null initializer taken from PhasePack seems to be rather inappropriate for NF data in general and should be avoided. For random data, the optimal spectral method is observed to be the best choice, as seen in Fig. 5.3(a). Note that the null initialization employing the **QR**-decomposition was only applied up to $n = 1 \times 10^3$ as the computational burden was too large to compute results for more unknowns within a feasible amount of time.

As a final test, the initialization methods were applied to NF data of AUTs of medium and large electrical size. The results are summarized in Tab. 5.2. Besides the spectral methods discussed, initial guesses were computed by solving the linear system of equations assuming a zero phase of the measurement vector and the resulting cosine similarity is reported in the last column of the table. For all datasets, the solution of an NFFFT with full phase information was considered as the true solution vector $z_t$. Note that dependent on the equivalent source representation, the solution vector may not be unique. Thus, the cosine similarity of the radiated fields — not of the solution vectors themselves — is used as a figure of merit. Unless otherwise mentioned, the null initialization has been applied via Alg. 6 with $k_{it} = 1 \times 10^2$ power iterations and $b_{nu} = \text{median}(|b|)$. In most of the cases, the spectral methods are observed to perform similar, however, the original method in (5.3) is seen to exhibit the most consistent performance. At the expense of a larger computational effort, solving the linear system with a zero phase guess outperforms the spectral methods in all except one of the considered scenarios.

Tab. 5.2 Cosine similarity $\log_{10}\chi_c\,(\mathbf{A}z_\mathrm{i}, \mathbf{A}z_\mathrm{t})$ obtained with initializers applied to NF data.

| Dataset | (5.3) | (5.4) | (5.5) | (5.6) | (5.7) | Random | $\mathbf{A}^{-1}\,\lvert\boldsymbol{b}\rvert$ |
|---|---|---|---|---|---|---|---|
| HF907[1] | $-0.59$ | $-0.59$ | $-0.79$[4] | $-0.59$ | $-0.59$ | $-2.40$ | $-0.80$ |
| QYAGI1[2] | $-0.25$ | $-0.23$ | $-0.72$ | $-0.43$ | $-0.27$ | $-1.29$ | $-0.08$ |
| HORNAR[3] | $-1.70$ | $-1.55$ | $-1.58$ | $-1.86$ | $-1.73$ | $-2.07$ | $-0.12$ |
| LOGPER[5] | $-1.03$ | $-1.62$ | $-0.98$ | $-0.80$ | $-1.46$ | $-1.63$ | $-0.58$ |
| LOGPERLCs[5] | $-0.89$ | $-1.27$ | $-0.98$ | $-1.32$ | $-1.20$ | $-1.45$ | $-0.49$ |
| REFL[6] | $-0.52$ | $-5.20$ | $-0.74$ | $-5.41$ | $-6.34$ | $-0.70$ | $-0.47$ |
| REFLLCs[6] | $-6.6 \times 10^{-3}$ | $-6.5 \times 10^{-3}$ | $-1.7 \times 10^{-2}$ | $-6.3 \times 10^{-3}$ | $-6.3 \times 10^{-3}$ | $-5.1 \times 10^{-2}$ | $-2.7 \times 10^{-3}$ |

[1] Spherical NF measurement setup, $n = 20 \times 10^3$, $m = 90.3 \times 10^3$, also see description of Fig. 4.2.

[2] Synthetic NF data from a CST simulation [3DS Simulia 2019] of a planar quasi-Yagi antenna [Kaneda et al. 2002; Qian et al. 1999]. NF samples on sphere of radius $2\lambda$ at 10 GHz, according to a Fibonacci mapping. Minimum sphere radius of the AUT $\approx 0.83\lambda$. Equivalent sources: Hertzian and Fitzgerald dipoles, $n = 2 \times 10^3$. Measurements: $m = 1 \times 10^4$. For more information, see Fig. 5.15 and the related discussion.

[3] Planar synthetic NF data from a Feko simulation [Altair Engineering Inc. 2018] of a 2D horn-antenna array ($4 \times 4$). NF data on two planes was acquired. Equivalent sources: Hertzian dipoles, $n = 795$. Measurements: $m = 3 \times 10^4$. For more details, see Fig. 5.16 and the description thereof.

[4] Determined the largest eigenvector (via the power method) without applying the **QR**-decomposition.

[5] Simulated NF data of a logarithmic-periodic dipole antenna at 60 MHz, with $m = 2790$ magnitudes and $n = 646$ spherical vector wave functions. More details can be found in Fig. 6.6 and the description thereof. For the "LCs"-case, available knowledge of partial coherence is added in the form of LCs, resulting in $m = 6510$.

[6] Simulated planar NF data of a reflector antenna fed by a Hertzian dipole at 500 MHz, with $m = 5004$ magnitudes and $n = 1000$ unknown Hertzian dipoles. More details can be found in the caption and the discussion of Fig. 6.5. The phase differences among sub-sets of the measurements are incorporated for the "LCs"-case via additional rows in the forward operator, resulting in $m = 15\,004$.
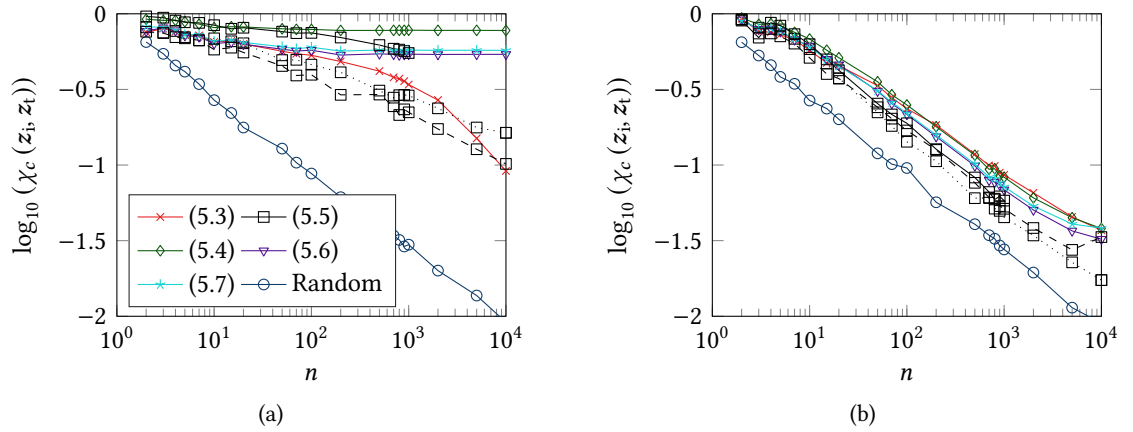
Fig. 5.3 Average of the cosine similarity $\chi_c(z_i, z_t)$ for $m/n = 4$. For each number of unknowns $n \in \{2, ..., 1 \times 10^4\}$, $1 \times 10^2$ runs with randomly drawn $z_t$ were performed. (a) Based on complex-valued normally distributed data. (b) For NF data similar to that used in Fig. 5.2b, with a measurement radius of $14\lambda$. Implementations of the methods are taken from [Chandra et al. 2019, 2017]. For the null initialization, the implementation from [Chandra et al. 2019, 2017] via the smallest eigenvalue (without **QR**) (dotted) and the implementation based on the largest eigenvalue according to Alg. 6, with (solid) and without (dashed) **QR**-decomposition, have been employed.

**Concluding Remarks — Initialization Methods**   In parallel to the development of the vast amount of existing nonconvex phase retrieval algorithms, a manifold of methods for the generation of a proper starting solution has been proposed. Often, the convergence guarantees for new retrieval algorithms are linked to the availability of an initial guess in the *proximity* of the true solution, e.g., within its convergence basin. In line with the derivation of conditions for *uniqueness* and *sampling complexity*, the quality of initializers is mainly ensured for random normally distributed data. Since typical NF antenna data does not fit to the assumption of randomly distributed data, drastic discrepancies in the performance of the considered *spectral initializations* has been observed. For random data, the investigated algorithms are able to provide starting solutions that are in the proximity of the true solution, almost independent from the problem dimensions. Changing the data model to that of NF antenna measurements, the same methods return initial guesses that are only slightly better than starting from random solutions. With increasing problem dimensions, the quality of the starting solution further deteriorates, rendering the approaches almost useless. Based on these first impressions, the task of phase retrieval for the application in phaseless field transformation algorithms is expected to remain a challenging task.

## 5.4  Nonconvex Phaseless Solvers

The phase retrieval problem in (5.1) can be tackled in various ways and the approaches are commonly differentiated in terms of convex and nonconvex algorithms. For the latter class in particular, a variety of formulations exists, e.g., [Cai et al. 2019; Candès et al. 2015b; Chen et al. 2018; Fienup

1982; Gerchberg and Saxton 1972; Netrapalli et al. 2015; Pinilla et al. 2018; Wang et al. 2017, 2018b; Zhang and Liang 2016].

For reasons of completeness and due to its remarkable simplicity and widespread use, the algorithm by Gerchberg and Saxton [Gerchberg and Saxton 1972], which was later generalized by Fienup [Fienup 1982], is reviewed in the following. Their work can be seen as one of the earliest methods to reconstruct phase distributions iteratively and which is applicable to phase reconstruction with arbitrary forward operators $\mathbf{A}$. Afterwards, the optimization framework of Section 3.4 is employed to derive a manifold of potential phase retrieval algorithms. The methods are compared for random normally distributed and synthetic NF data and, where applicable, the influence of parameter values is investigated. It should be mentioned that some of the discussed algorithms bear similarities with the Wirtinger Flow algorithm [Candès et al. 2015b], which, although not being the first of its kind, e.g., see [Schnattinger et al. 2014], is one of the most prominent representatives of nonconvex phase retrieval algorithms based on the Wirtinger calculus and employing a gradient descent optimization.

### 5.4.1 The Gerchberg-Saxton Algorithm

In their original paper [Gerchberg and Saxton 1972], Gerchberg and Saxton describe an iterative, projection-based phase retrieval procedure for the determination of phase distributions from image and diffraction plane pictures. This problem is highly related to the general problem of phase retrieval in (5.1), however, features a small difference, namely that not only information about the magnitudes in the measurement domain, i.e., $|\mathbf{b}|$, but also about the coefficients $|\mathbf{z}|$ in the source domain is available. The method can easily be modified to exclude knowledge of $|\mathbf{z}|$, as shown in the following. Also caused by the nature of their application, the relevant forward operator in the original publication was taken to be a Fourier transform. Here, we consider a more general form with arbitrary matrices.

The Gerchberg-Saxton algorithm is based on repeatedly projecting a phase distribution, either in the source or the observation domain, to the respective other domain, enforcing the knowledge of the magnitudes, back-projecting to the original domain and again enforcing the knowledge of magnitudes in that domain. The unknowns in this process can either be defined in the source or in the observation domain. In either case, the complementary quantities can be computed at most at the expense of solving a linear system of equations. For example assuming the phase distribution of the sources as unknowns, they are first projected to the observation domain. In the observation domain, the knowledge of the observation magnitudes is enforced and the resulting quantity is projected back to the source domain where the source magnitudes are enforced. Within the class of nonconvex phase retrieval algorithms, these projection-based methods represent a solid and popular choice with a variety of applications [Chen et al. 2018; Elser 2003; Yaccarino and Rahmat-Samii 1997].

Assuming knowledge of $|\mathbf{z}|$ and $|\mathbf{b}|$, this process can, at the $k$th iteration and dependent on the choice of unknowns, be written as

$$\text{observation domain: } \mathbb{R}^m \ni \boldsymbol{\varphi}_{b,k+1} = \angle\left(\mathbf{A}\operatorname{diag}\left(|\mathbf{z}|\right)\mathrm{e}^{\mathrm{j}\angle\left(\mathbf{A}^{-1}\operatorname{diag}(|\mathbf{b}|)\mathrm{e}^{\mathrm{j}\boldsymbol{\varphi}_{b,k}}\right)}\right) \tag{5.10}$$

$$\text{source domain: } \mathbb{R}^n \ni \boldsymbol{\varphi}_{z,k+1} = \angle\left(\mathbf{A}^{-1}\operatorname{diag}\left(|\mathbf{b}|\right)\mathrm{e}^{\mathrm{j}\angle\left(\mathbf{A}\operatorname{diag}(|\mathbf{z}|)\mathrm{e}^{\mathrm{j}\boldsymbol{\varphi}_{z,k}}\right)}\right) \tag{5.11}$$

where the connection between the phase distributions in the respective domains is given by

$$\boldsymbol{\varphi}_z = \angle\left(\mathbf{A}^{-1}\mathrm{diag}\left(|\boldsymbol{b}|\right)\mathrm{e}^{\mathrm{j}\boldsymbol{\varphi}_b}\right) \quad \Leftrightarrow \quad \boldsymbol{\varphi}_b = \angle\left(\mathbf{A}\,\mathrm{diag}\left(|\boldsymbol{z}|\right)\mathrm{e}^{\boldsymbol{\varphi}_z}\right). \tag{5.12}$$

Be reminded that the exponential function $\mathrm{e}^z$ is evaluated element-wise for each entry in a vector $z$. For ease of understanding, it is recommended to read (5.10) and (5.11) from the innermost bracket in the exponent on the right towards the equality sign. The unknowns are first multiplied to the known magnitudes and afterwards projected to the opposing domain. The phase is extracted and again multiplied to the known magnitudes in that domain. Last, the quantities are projected back to the original domain and the phase is extracted, which can then be inserted in the next iteration.

Applying the same ideas to the case where no knowledge about the magnitudes in the source domain is given, we find

$$\text{observation domain: } \mathbb{R}^m \ni \boldsymbol{\varphi}_{b,k+1} = \angle\left(\mathbf{A}\mathbf{A}^{-1}\mathrm{diag}\left(|\boldsymbol{b}|\right)\mathrm{e}^{\mathrm{j}\boldsymbol{\varphi}_{b,k}}\right) \tag{5.13}$$

$$\text{source domain: } \mathbb{C}^n \ni \boldsymbol{z}_{k+1} = \mathbf{A}^{-1}\mathrm{diag}\left(|\boldsymbol{b}|\right)\mathrm{e}^{\mathrm{j}\angle(\mathbf{A}\boldsymbol{z}_k)} \tag{5.14}$$

and the unknowns are related to each other via

$$\boldsymbol{z} = \mathbf{A}^{-1}\mathrm{diag}\left(|\boldsymbol{b}|\right)\mathrm{e}^{\mathrm{j}\boldsymbol{\varphi}_b} \quad \Leftrightarrow \quad \boldsymbol{\varphi}_b = \angle\left(\mathbf{A}\boldsymbol{z}\right). \tag{5.15}$$

Comparing (5.14) with (5.11), we see that the number of unknowns has practically doubled, as now there are $n$ complex-valued instead of real-valued unknowns. For a typical phase retrieval task, we can assume that $m > 2n$ such that (5.14) features less unknowns than (5.13). For completeness, possible implementations of (5.10), (5.11), (5.13) and (5.14) are given in Algs. 7, 8, 9 and 10, respectively.

In Fig. 5.4, the performance of the four variants of the Gerchberg-Saxton algorithm for complex-valued normally distributed data and for NF data of spherical vector wave functions is depicted. The number of unknowns was set to $n = 10$ and for each value of $m/n$, $5 \times 10^4$ transformations where conducted. Success was declared once an NF deviation of $\epsilon_{c,\mathrm{dB}} \leq -45\,\mathrm{dB}$ was obtained for $k_{\max} = 5 \times 10^2$. For the NF data, the tangential electric field was sampled on a spherical surface with a radius of $\lambda$. The sample locations were almost uniformly distributed on the measurement sphere according to a Fibonacci mapping [Keinert et al. 2015]. As can be seen for both types of data, the formulations provided with the additional knowledge of $|\boldsymbol{z}|$ in the source domain require less information about the magnitudes in the observation domain to achieve the same success rate as their counterparts without source-domain knowledge. In total, the pairs of variants are seen to perform almost identically. More importantly, there is a decisive difference between the success rate for random data and for the considered NF data. With the latter, more measurement samples are required to allow the phase retrieval algorithms to provide an accurate solution. This quality discrepancy between Gaussian data and NF data widens further with increasing problem dimension, which is not explicitly shown here. In other words, for larger and more relevant problem dimensions, phase retrieval algorithms may perform well with random Gaussian data while exhibiting a vanishing success rate for realistic NF data.

**Concluding Remarks — Gerchberg-Saxton Algorithm(s)**   With their pioneer work, Gerchberg and Saxton [Gerchberg and Saxton 1972] laid the foundation for the class of iterative, *projection-based* phase retrieval algorithms. Due to its general applicability and simplicity, their algorithm has

---

**Algorithm 7** Gerchberg-Saxton in observation domain with source restrictions

$z = \mathrm{GS}_4\left(z_0, |z|, |b|, \mathbf{A}, k_{\max}\right)$

---

**Input:** initial guess $z_0$, iterations $k_{\max}$,
  measurements $|b|$,
  source magnitudes $|z|$
  and operator $\mathbf{A}$

**Output:** $z$, where $|\mathbf{A}z| = |b|$

 1: $k = 1$
 2: $\varphi_{b,k} = \angle\left(\mathbf{A}\,\mathrm{diag}\left(|z|\right) e^{j\angle(z_0)}\right)$
 3: **while** $k \le k_{\max}$ **do**
 4:   $z' = \mathbf{A}^{-1}\mathrm{diag}\left(|b|\right) e^{j\varphi_{b,k}}$
 5:   $\varphi_{b,k+1} = \angle\left(\mathbf{A}\,\mathrm{diag}\left(|z|\right) e^{j\angle(z')}\right)$
 6: **end while**
 7: **return** $z = \mathbf{A}^{-1}\mathrm{diag}\left(|b|\right) e^{j\varphi_{b,k+1}}$

---

**Algorithm 8** Gerchberg-Saxton in source domain with source restrictions

$z = \mathrm{GS}_3\left(z_0, |z|, |b|, \mathbf{A}, k_{\max}\right)$

---

**Input:** initial guess $z_0$, iterations $k_{\max}$,
  measurements $|b|$,
  source magnitudes $|z|$
  and operator $\mathbf{A}$

**Output:** $z$, where $|\mathbf{A}z| = |b|$

 1: $k = 1$
 2: $\varphi_{z,k} = \angle\left(\mathbf{A}^{-1}\mathrm{diag}\left(|b|\right) e^{j\angle(\mathbf{A}z_0)}\right)$
 3: **while** $k \le k_{\max}$ **do**
 4:   $b' = \mathbf{A}\,\mathrm{diag}\left(|z|\right) e^{j\varphi_{z,k}}$
 5:   $\varphi_{z,k+1} = \angle\left(\mathbf{A}^{-1}\mathrm{diag}\left(|b|\right) e^{j\angle(b')}\right)$
 6: **end while**
 7: **return** $z = \mathrm{diag}\left(|z|\right)\varphi_{z,k+1}$

---

**Algorithm 9** Gerchberg-Saxton in observation domain

$z = \mathrm{GS}_2\left(z_0, |b|, \mathbf{A}, k_{\max}\right)$

---

**Input:** initial guess $z_0$, iterations $k_{\max}$,
  measurements $|b|$ and operator $\mathbf{A}$

**Output:** $z$, where $\left|\mathbf{A}\mathbf{A}^{-1}b\right| = |b|$

 1: $k = 1$
 2: $\varphi_{b,k} = \angle\left(\mathbf{A}z_0\right)$
 3: **while** $k \le k_{\max}$ **do**
 4:   $\varphi_{b,k+1} = \angle\left(\mathbf{A}\mathbf{A}^{-1}\mathrm{diag}\left(|b|\right) e^{j\varphi_{b,k}}\right)$
 5: **end while**
 6: **return** $z = \mathbf{A}^{-1}\mathrm{diag}\left(|b|\right) e^{j\varphi_{b,k+1}}$

---

**Algorithm 10** Gerchberg-Saxton in source domain

$z = \mathrm{GS}_1\left(z_0, |b|, \mathbf{A}, k_{\max}\right)$

---

**Input:** initial guess $z_0$, iterations $k_{\max}$,
  measurements $|b|$ and operator $\mathbf{A}$

**Output:** $z$, where $|\mathbf{A}z| = |b|$

 1: $k = 1$
 2: $z_k = z_0$
 3: **while** $k \le k_{\max}$ **do**
 4:   $z_{k+1} = \mathbf{A}^{-1}\mathrm{diag}\left(|b|\right) e^{j\angle(\mathbf{A}z_k)}$
 5: **end while**
 6: **return** $z = z_{k+1}$

---

been employed as the de facto reference for newly developed phase reconstruction algorithms ever since. Leaving aside its relatively large computational burden, it still performs rather favorably when compared with modern reconstruction approaches in terms of the achievable success rate.

### 5.4.2 Standard Nonconvex Formulation

We now rewrite the phase retrieval problem in a form that can be treated with the optimization framework in Alg. 5. One can find a solution to (5.1) by determining a minimum to the cost function in (3.67) with a nonlinear operator according to

$$\mathcal{A}_1 = \left[(\mathbf{A}z) \circ \left(\overline{\mathbf{A}z}\right)\right]^{p_1} = |\mathbf{A}z|^{2p_1} \quad \text{and} \quad d_1 = |b|^{2p_1}. \tag{5.16}$$

Note that the utilization of normal equations known from the solution of linear systems may partially be transferred to the phaseless case as well. A corresponding modification of (5.16) is discussed in the Appendix A.4. Furthermore, (5.16) does not represent the only way of determining
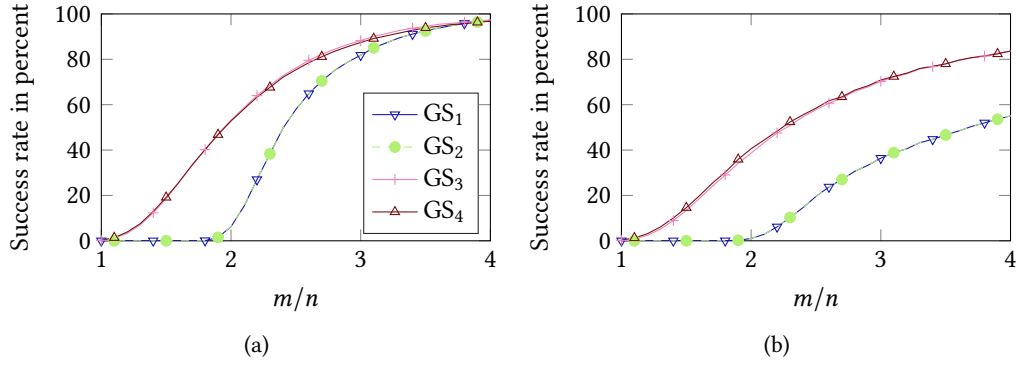
Fig. 5.4 Success rate of the four variants of the Gerchberg-Saxton method in Algs. 10 to 7 with $n = 10$ unknowns for complex-valued normally distributed data in (a) and NF data from spherical vector wave functions in (b). For each ratio of $m/n$, $5 \times 10^4$ repetitions were run. A transformation was counted as successful, if $\epsilon_{c,\mathrm{dB}} \leq -45\,\mathrm{dB}$ was achieved. The number of iterations $k_{\max}$ was set to $5 \times 10^2$.

the unknown source coefficients independent from the phase information. In Appendix A.5, a phase-invariant optimization approach is presented, which yields similar results as (5.16).

The derivatives required for minimizing the corresponding cost function in the optimization framework can be written as

$$\frac{\partial \mathcal{A}_1\,(z)}{\partial z} = p_1 \mathrm{diag}\left(|\mathbf{A}z|^{2p_1-2} \circ \overline{\mathbf{A}z}\right)\mathbf{A} \tag{5.17}$$

$$\left(\frac{\partial \mathcal{A}_1\,(z)}{\partial z}\right)^{\mathrm{H}} = p_1 \mathbf{A}^{\mathrm{H}}\mathrm{diag}\left(|\mathbf{A}z|^{2p_1-2} \circ \mathbf{A}z\right) \tag{5.18}$$

$$\frac{\partial \overline{\mathcal{A}_1\,(z)}}{\partial z} = \overline{\frac{\partial \mathcal{A}_1\,(z)}{\partial z}} \tag{5.19}$$

$$\left(\frac{\partial \overline{\mathcal{A}_1\,(z)}}{\partial z}\right)^{\mathrm{H}} = \overline{\left(\frac{\partial \mathcal{A}_1\,(z)}{\partial z}\right)^{\mathrm{H}}}. \tag{5.20}$$

While the optimization framework comprises a reliable line search algorithm, an analytical equation for the optimal step length can be favorable in terms of computation time and convergence rate. When setting $p_{\mathrm{OF},1} = \alpha_{\mathrm{OF},1} = p_1 = 1$, it is possible to derive the optimal step length for $\mathcal{A}_1$ analytically. One can state

$$f_1\,(z' = z + \alpha p) = \left\||\mathbf{A}z'|^2 - |b|^2\right\|_2^2 = |\mathbf{A}z'|^{2,\mathrm{H}}\,|\mathbf{A}z'|^2 - 2\,|\mathbf{A}z'|^{2,\mathrm{H}}\,|b|^2 + |b|^{2,\mathrm{H}}\,|b|^2 \tag{5.21}$$

leading to

$$f_1\,(z') = \alpha^4 \underbrace{\left[\left\||\mathbf{A}p|^2\right\|_2^2\right]}_{a_1} + \alpha^3 \underbrace{\left[4\,\mathrm{Re}\left\{\overline{\mathbf{A}z} \circ \mathbf{A}p\right\}^{\mathrm{H}}|\mathbf{A}p|^2\right]}_{b_1}$$

$$+ \alpha^2 \underbrace{\left[ 4 \left\| \mathrm{Re} \left\{ \overline{\mathbf{A}z} \circ \mathbf{A}p \right\} \right\|_2^2 + 2 \left| \mathbf{A}p \right|^{2,\mathrm{H}} \left( \left| \mathbf{A}z \right|^2 - \left| b \right|^2 \right) \right]}_{c_1}$$

$$+ \alpha \underbrace{\left[ 4 \, \mathrm{Re} \left\{ \overline{\mathbf{A}z} \circ \mathbf{A}p \right\}^{\mathrm{H}} \left( \left| \mathbf{A}z \right|^2 - \left| b \right|^2 \right) \right]}_{d_1} + \underbrace{\left[ \left\| \left| \mathbf{A}z \right|^2 - \left| b \right|^2 \right\|_2^2 \right]}_{e_1}. \tag{5.22}$$

Since (5.22) is a polynomial of forth order, the cost function based on $\mathcal{A}_1$ is in general nonconvex. In order to determine the optimal $\alpha$, one needs to find all minima of this quartic polynomial with real-valued coefficients. This can be done by searching for zeros of the cubic polynomial

$$\frac{\partial f_1 \left( z + \alpha p \right)}{\partial \alpha} = 4a_1 \, \alpha^3 + 3b_1 \, \alpha^2 + 2c_1 \, \alpha + d_1 \stackrel{!}{=} 0. \tag{5.23}$$

The zeros of cubic polynomials can be found analytically, e.g., see [Press 2003, pp. 179–180], which is, for real-valued coefficients, reviewed in Alg. 11. Since we assume that $p$ is a true descent direction, there must be a solution to (5.23) for $\alpha \geq 0$. However, there may be up to three real-valued zeros, so that we need to make sure to pick the one belonging to a true local minimum. The latter is ensured whenever one chooses a positive real-valued zero at which the cost function exhibits a positive second-order derivative. Assuming that one has found the optimal step length from Alg. 11, this value can partially be used for $p_1 \neq 1$, e.g., as an initial guess $\alpha_\mathrm{i}$ of an iterative line search.

As derived in [Isernia et al. 1996b], (5.22) can be simplified under the assumption that $|\mathbf{A}z| = |b|$, i.e., that one starts the line search at the optimum. In this particular case, (5.22) reduces to

$$f_1 \left( z' \right) \stackrel{|\mathbf{A}z|=|b|}{=} \alpha^4 \underbrace{\left[ \left\| \left| \mathbf{A}p \right|^2 \right\|_2^2 \right]}_{a_1} + \alpha^3 \underbrace{\left[ 4 \, \mathrm{Re} \left\{ \overline{\mathbf{A}z} \circ \mathbf{A}p \right\}^{\mathrm{H}} \left| \mathbf{A}p \right|^2 \right]}_{b_1} + \alpha^2 \underbrace{\left[ 4 \left\| \mathrm{Re} \left\{ \overline{\mathbf{A}z} \circ \mathbf{A}p \right\} \right\|_2^2 \right]}_{c_1'} \tag{5.24}$$

$$= \alpha^2 \left( \alpha^2 a_1 + \alpha b_1 + c_1' \right). \tag{5.25}$$

The first order derivative with respect to the step length then equals

$$\frac{\partial f_1 \left( z' = z + \alpha p \right)}{\partial \alpha} \stackrel{|\mathbf{A}z|=|b|}{=} \alpha \left( 4\alpha^2 a_1 + 3\alpha b_1 + 2c_1' \right). \tag{5.26}$$

Ideally, (5.26) should exhibit a single zero at $\alpha = 0$, so that only the zeros of the second-order polynomial inside the parentheses need to be considered, for which one obtains

$$\alpha_{1/2} = \frac{-3b_1 \pm \sqrt{9b_1^2 - 32a_1 c_1'}}{8a_1}. \tag{5.27}$$

It has to be kept in mind that it is sufficient to find a condition that ensures no further real-valued zeros for $\alpha$ (except at $\alpha = 0$) exist. This strong limitation comes from the fact that $\alpha \in \mathbb{R}$ was assumed in the derivation of (5.27). Thus, from (5.27) and as claimed in [Isernia et al. 1996b; Moretta

and Pierri 2019; Soldovieri et al. 2005], as soon as

$$\frac{b_1^2}{a_1 c_1'} < \frac{32}{9} \tag{5.28}$$

is fulfilled, no other local stationary points should be encountered and the problem becomes convex. More insight may be provided by writing (5.28) in the form of a squared cosine similarity as

$$\chi_c^2 \left( \mathrm{Re} \left\{ \overline{\mathbf{A}\mathbf{z}} \circ \mathbf{A}\mathbf{p} \right\}, |\mathbf{A}\mathbf{p}|^2 \right) < \frac{8}{9}, \tag{5.29}$$

for which usually the following observation is made [Isernia et al. 1996b]. Increasing the number of measurements can only increase the values of $a_1$ and $c_1'$, as both are made up of positive contributions only, while the positive and negative terms in $b_1$ may eventually cancel and lead to a smaller ratio in (5.29). Though this statement is true in general, it provides very little practical help on how to construct measurement setups which automatically fulfill (5.29) and thus lead to a convex optimization problem.

As a point of interest, researchers have compared nonconvex phase retrieval formulations similar to that in (5.16) for two values of $p_1 \in \{0.5, 1\}$, corresponding to an optimization with respect to $|\mathbf{b}|$ or $|\mathbf{b}|^2$. While there have been well-argued claims that from a theoretical point of view $p_1 = 1$ should be superior [Leone 1997], also due to its bandlimitedness [Yaccarino and Rahmat-Samii 1995], practical evidence and other publications [Wang et al. 2017, 2018a,c; Zhang and Liang 2016] claim that $p_1 = 0.5$ features a superior convergence behavior and has thus been often favored. A brief comparison between both values can be drawn from the results shown in Fig. 5.5. For a tiny problem with $n = 10$ unknowns and forward matrices as well as solution vectors drawn from a complex-valued normal distribution, phase retrieval was performed via the formulation in (5.16) with $p_1 = 1$ and $p_1 = 0.5$. At most $5 \times 10^3$ iterations were allowed and the initial guess was computed via the spectral method via 40 power iterations. A transformation was called successful in case a complex deviation according to (4.14) below $-45$ dB was achieved. For every ratio of $m/n$, $5 \times 10^3$ problems have been solved. Figure 5.5(a) shows the success rate of the transformation for two cases, one for a complex-valued random normally distributed forward operator and one exhibiting a random operator with additional structure. In the second case, a scaled identity matrix with $n$ rows and $n$ columns was added to the upper part of the originally random operator, causing the first $n$ rows to be diagonally dominant. While the formulation with $p_1 = 1$ achieves a larger success rate than $p_1 = 0.5$ for both types of matrices, the average number of iterations $k_{\mathrm{it,av}}$ required for convergence is also larger, as can be seen in Fig. 5.5(b). Especially, the case of the structured matrix requires the formulation with $p_1 = 1$ to perform drastically more iterations than with $p_1 = 0.5$. In summary, we see that indeed $p_1 = 1$ may increase our chance of finding the correct solution to the phase retrieval problem, however, possibly requiring significantly more iterations for convergence. Especially for real-world forward operators exhibiting structure due to the underlying physical and nonrandom process, the formulation $p_1 = 0.5$ may yield better results within considerably less time. Still, it seems reasonable to refine a solution obtained with $p_1 = 0.5$ via a few iterations with $p_1 = 1$ and possibly obtain a better result.

A more comprehensive impression on the effect of $p_1$ in (5.16) on the phase retrieval performance can be obtained from Fig. 5.6. Complex-valued normally distributed data on one side, NF data from

---

[2]In Matlab [Matlab 2021], the operators are constructed via A = randn(m,n)+1i*randn(m,n); and
  A = randn(m,n)+1i*randn(m,n)+100*rand(1,1)*[eye(n);zeros(m-n,n)];

---

**Algorithm 11** Determine roots of a cubic polynomial $x^3 + ax^2 + bx + c$ after [Press 2003], $\quad a, b, c \in \mathbb{R}$, $[x_1, x_2, x_3] = \text{cubic\_roots}\,(a, b, c)$

---

**Input:** $a, b, c$

**Output:** roots $x_1, x_2, x_3$

1: $Q = \frac{a^2 - 3b}{9}$ and $R = \frac{2a^3 - 9ab + 27c}{54}$

2: **if** $R^2 < Q^3$ **then**

3: $\quad \vartheta = \arccos\left(\frac{R}{\sqrt{Q^3}}\right)$

4: $\quad x_1 = -2\sqrt{Q}\cos\left(\frac{\vartheta}{3}\right) - \frac{a}{3}$

5: $\quad x_2 = -2\sqrt{Q}\cos\left(\frac{\vartheta + 2\pi}{3}\right) - \frac{a}{3}$

6: $\quad x_3 = -2\sqrt{Q}\cos\left(\frac{\vartheta - 2\pi}{3}\right) - \frac{a}{3}$

7: **else**

8: $\quad A = -\text{sgn}\,(R)\left[|R| + \sqrt{R^2 - Q^3}\right]^{1/3}$

9: $\quad B = \begin{cases} Q/A, & A \neq 0 \\ 0, & A = 0 \end{cases}$

10: $\quad x_1 = (A + B) - \frac{a}{3}$

11: $\quad x_2 = -\frac{1}{2}(A + B) - \frac{a}{3} + \text{j}\frac{\sqrt{3}}{2}(A - B)$

12: $\quad x_3 = -\frac{1}{2}(A + B) - \frac{a}{3} - \text{j}\frac{\sqrt{3}}{2}(A - B)$

13: **end if**

14: **return** $x_1, x_2, x_3$

---

a spherical vector wave distribution on the other side, was used to run the approach in (5.16) for $1 \times 10^3$ times for each pair of number of unknowns $n$ and parameter value $p_1$. In case of the NF data, the tangential electric field was acquired on three spherical surfaces of radii $5\lambda$, $10\lambda$ and $15\lambda$, such that in total an oversampling ratio of $m/n = 8$ was obtained. The sample locations where almost uniformly distributed according to a Fibonacci mapping [Keinert et al. 2015]. For the random data, $m/n = 4$ was utilized. The initial guess was computed via the optimal spectral method in (5.4) taken from the PhasePack [Chandra et al. 2019, 2017] library. The required number of iterations $k_{\text{it}}$ for achieving a success rate greater or equal to 90% for the random data and (only) 10% in case of the NF data is depicted in Figs. 5.6(a) and 5.6(c), respectively. A reconstruction was assumed to be successful once $\epsilon_{c,\text{dB}} \leq -45$ dB was achieved. It can be observed that $p_1 = 1$, i.e., a minimization in the squared magnitude, does not correspond to the most efficient parameter value in terms of the number of iterations, neither for complex-valued random data, nor for synthetic NF data. However, for the latter a value of $p_1 = 1$ seems to maximize the success rate in most cases. For both types of data, a steady increase in the required number of iterations with increasing problem dimension can be observed, though, this effect is by far more pronounced with NF data. While for Gaussian data a value of $p_1 \approx 0.7$ seems to be a suitable choice, smaller values of $p_1$ seem to be better for NF data with very few unknowns. Interestingly, both figures feature a region around $p_1 \approx 1.4$, where the transformation performance is very sensitive to the value of $p_1$. This range of the parameter $p_1$ should be avoided, as the phase retrieval formulation requires a much larger number of iterations for convergence. In Figs. 5.6(b) and 5.6(d), the overall achievable success rate for a maximum number of iterations of $\log_{10}(k_{\text{it}}) = \log_{10}(5 \times 10^3) \approx 3.7$ is depicted. Again the unstable region around $p_1 \approx 1.4$ is visible.

**Concluding Remarks — Standard Nonconvex Formulation**   A variety of existing phase retrieval formulations is based on the minimization of nonconvex cost functions, e.g., featuring an operator like $\mathcal{A}_1$. Despite the occurrence of local stationary points, nonconvex optimization-based methods often perform favorable in real-world applications — once provided with a proper initial guess and suitable measurement data. In particular the formulation with $\mathcal{A}_1$ features relatively low computation cost per iteration and, backed with the L-BFGS method and a solid line search, converges faster than for example a gradient descent approach with fixed step length. Empirical
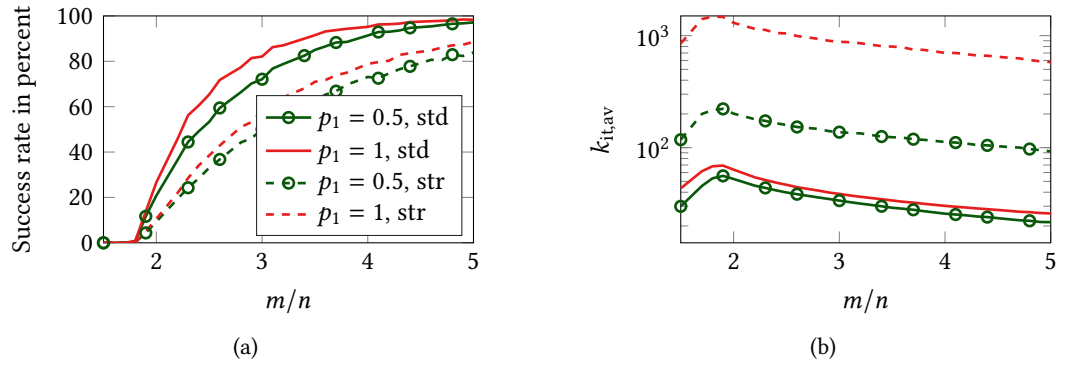
Fig. 5.5 Comparison of cost functions. Either minimizing $|\mathbf{A}z| - |\boldsymbol{b}|$ ($p_1 = 0.5$) or $|\mathbf{A}z|^2 - |\boldsymbol{b}|^2$ ($p_1 = 1$). Here, $n = 10$ and the considered forward matrices are either taken from a complex-valued normal distribution ("std") or feature some structure ("str")[2]. The initial guess is always computed via 40 power iterations of the spectral method. (a) The success rate. (b) The average number of iterations performed $k_{\text{it,av}}$.

results show that a minimization with respect to the squared magnitudes yields a larger success rate than compared to an optimization of the magnitudes, however, at the expense of a slower convergence rate. The core issue of this approach — and actually of all existing phase retrieval methods — is the strong performance variation dependent on the type of magnitude data. Realistic NF antenna data is observed to be far inferior to random normally distributed data, resulting in lower reconstruction quality with similar amounts of measurements. This issue further worsens when going to problems of larger size.

### 5.4.3 Scale-Invariant Formulation

The core idea of the following formulation has already been introduced and applied in [Paulus et al. 2018a; Paulus et al. 2017a]. Here, the approach is presented as part of the optimization framework and more information about the underlying principle is provided. In particular, a performance comparison to the standard approach is conducted and results for synthetic spherical NF antenna measurements are discussed.

**Formulation and Derivatives**

A modified formulation of (5.16) can be found in the form of

$$\mathcal{A}_2 = \left[ \mathbf{A}z \circ \overline{\mathbf{A}z} \right]^{p_2} c_{\text{si}}(z) = |\mathbf{A}z|^{2p_2} c_{\text{si}}(z) \quad \text{with} \quad \boldsymbol{d}_2 = |\boldsymbol{b}|^{2p_2}, \tag{5.30}$$

with the solution dependent scaling

$$c_{\text{si}}(z) = \frac{\boldsymbol{d}_2^{\mathrm{T}} |\mathbf{A}z|^{2p_2}}{\left\| |\mathbf{A}z|^{2p_2} \right\|_2^2} \in \mathbb{R}. \tag{5.31}$$
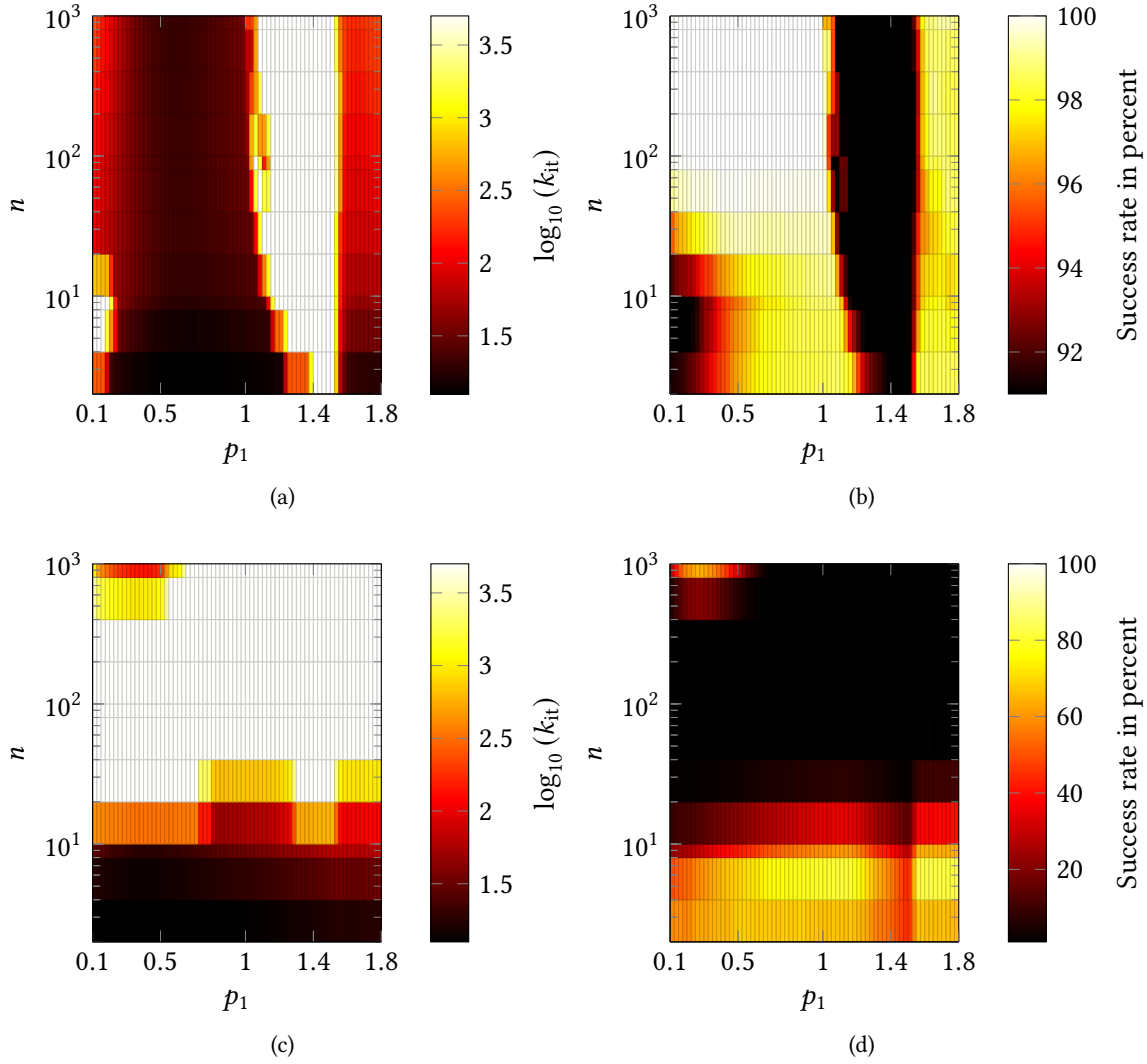
Fig. 5.6 Phase retrieval performance of formulation (5.16). In (a) and (b), for complex-valued normally distributed operators and data with $m/n = 4$. For (c) and (d), realistic NF data from a spherical wave expansion and $m/n = 8$ was utilized. The initial guess is generated via the optimal spectral method defined by (5.4). In (a) and (c), the number of iterations $k_{it}$ required to achieve a success rate of greater or equal to 90% and 10%, respectively, dependent on the number of unknowns $n$ and the parameter $p_1$ in (5.16) is depicted. Success is declared, once $\epsilon_{c,dB} \leq -45$ dB is achieved. In (b) and (d), the overall success rate obtained with a maximum number of iterations of $k_{it} = 5 \times 10^3$ is drawn.

The factor $c_{\mathrm{si}}$ ensures that the difference between $\mathcal{A}_2$ and $\boldsymbol{d}_2$ has zero mean regardless of the absolute scaling of the solution or measurement vector. In contrast to this, the gradient (see (3.71)) of the standard formulation can easily get dominated by improper scaling of the current solution, which can slow down the convergence rate. For example, consider a solution that has the correct magnitude distribution but is too large by a factor of 10, i.e., $|\mathbf{A}z|^2 = 10\,|\boldsymbol{b}|^2$. For $p_1 = 1$, the gradient of the standard formulation then involves the nonzero term $\mathcal{A}_1 - \boldsymbol{d}_1 = 10\,|\boldsymbol{b}|^2$. Since $c_{\mathrm{si}}\,(z) = 1/10$ in this case ($p_2 = 1$), the gradient for the scale-invariant formulation will contain $\mathcal{A}_2 - \boldsymbol{d}_2 = 0$ and, thus, be zero. Since $c_{\mathrm{si}}$ reduces the impact of scaling and biases, the corresponding cost functional is more sensitive to the meaningful differences in terms of the distributions of $\mathbf{A}z$ and $\boldsymbol{b}$. At the same time, the formulation fosters larger step lengths that would otherwise, e.g., in the standard formulation, lead to an improper absolute scaling of the solution vector.

The required derivatives applied to vectors $\boldsymbol{y}$ of appropriate size can be found as

$$
\frac{\partial \mathcal{A}_2\,(z)}{\partial z}\boldsymbol{y} = c_{\mathrm{si}}\,(z)\,p_2 \mathrm{diag}\left(|\mathbf{A}z|^{2p_2-2}\circ\overline{\mathbf{A}z}\right)\mathbf{A}\boldsymbol{y}
$$
$$
+ \frac{p_2\,|\mathbf{A}z|^{2p_2}}{\left\||\mathbf{A}z|^{2p_2}\right\|_2^2}\underbrace{\left(\boldsymbol{d}_2^{\mathrm{T}} - 2c_{\mathrm{si}}\,(z)\,|\mathbf{A}z|^{2p_2,\,\mathrm{T}}\right)\mathrm{diag}\left(|\mathbf{A}z|^{2p_2-2}\circ\overline{\mathbf{A}z}\right)\mathbf{A}\boldsymbol{y}}_{\in\mathbb{C}^{1\times1}} \tag{5.32}
$$

$$
\frac{\partial \overline{\mathcal{A}_2\,(z)}}{\partial z}\boldsymbol{y} = \overline{\frac{\partial \mathcal{A}_2\,(z)}{\partial z}\boldsymbol{y}} \tag{5.33}
$$

$$
\left(\frac{\partial \mathcal{A}_2\,(z)}{\partial z}\right)^{\mathrm{H}}\boldsymbol{y} = p_2\mathbf{A}^{\mathrm{H}}\mathrm{diag}\left(|\mathbf{A}z|^{2p_2-2}\circ\mathbf{A}z\right)\left(c_{\mathrm{si}}\,(z)\,\boldsymbol{y} + \frac{\left(\boldsymbol{d}_2 - 2c_{\mathrm{si}}\,(z)\,|\mathbf{A}z|^{2p_2}\right)}{\left\||\mathbf{A}z|^{2p_2}\right\|_2^2}\underbrace{|\mathbf{A}z|^{2p_2,\,\mathrm{T}}\,\boldsymbol{y}}_{\in\mathbb{C}^{1\times1}}\right) \tag{5.34}
$$

$$
\left(\frac{\partial \overline{\mathcal{A}_2\,(z)}}{\partial z}\right)^{\mathrm{H}}\boldsymbol{y} = \overline{\left(\frac{\partial \mathcal{A}_2\,(z)}{\partial z}\right)^{\mathrm{H}}\boldsymbol{y}}. \tag{5.35}
$$

This time due to the complexity of the equations, an analytic derivation of the optimal step length seems unfeasible and one is well advised to rely on the iterative line search procedure of the optimization framework. However, due to the similarity of $\mathcal{A}_2$ and $\mathcal{A}_1$, it is easily seen that again the resulting cost function is nonconvex.

**Scale-Invariance Principle**

The motivation for using (5.30) instead of (5.16) can be obtained from Fig. 5.7(a), which shows a comparison of the line search process of both methods for $p_1 = p_2 = 0.5$. For this example, the forward operator $\mathbf{A}$ and the solution vector $z$ were randomly chosen from a complex Gaussian distribution. The measurement vector was set according to $\boldsymbol{b} = \mathbf{A}z$, i.e., free of noise. The value of the cost functions $f_1$ and $f_2$ in the direction of the gradients $\boldsymbol{\nabla} f_1(z_0)$ and $\boldsymbol{\nabla} f_1(z_0)$ at a point $z_0 = (\mathbf{A}^{\mathrm{H}}\boldsymbol{b})\,/\,\left\|\mathbf{A}^{\mathrm{H}}\boldsymbol{b}\right\|_2$ is depicted. There are several things to notice. First, the formulation with (5.30) can achieve a lower cost function value within this particular search direction — and thus more progress with this iteration — when compared to (5.16). Second, there seems to be a non-negligible difference between the gradients, since both curves with markers exhibit a considerably different minimum cost function value. Third and most interestingly, one can observe the dashed line to almost exhibit a zero slope in the region $\alpha \geq 0$, including $\alpha = 0$. In the direction of $\boldsymbol{\nabla} f_1(z_0)$, the

Tab. 5.3 Cosine similarities of gradients of $f_{1/2}$ with and without inherent scaling.

| | $z_0$ with $\|z_0\|_2 = 1$ | |
|---|---|---|
| | $\mathbf{A}^{\mathrm{H}}\boldsymbol{b}$ | random |
| $\chi_c\left(z_0, \boldsymbol{\nabla} f_1(z_0)\right)$ | 0.71 | 0.38 |
| $\chi_c\left(z_0, \boldsymbol{\nabla} f_2(z_0)\right)$ | 0.33 | 0.45 |
| $\chi_c\left(\mathbf{A}z_0, \mathbf{A}\boldsymbol{\nabla} f_1(z_0)\right)$ | 0.87 | 0.47 |
| $\chi_c\left(\mathbf{A}z_0, \mathbf{A}\boldsymbol{\nabla} f_2(z_0)\right)$ | $\approx 0$ | 0.57 |

cost function $f_2$ can almost not be minimized further, however, cost function $f_1$ can be improved in this direction and there is a drastic difference between $f_1(z_0)$ and $f_2(z_0)$. This indicates that the similarity between $\boldsymbol{\nabla} f_1(z_0)$ and $z_0$ should be large and that $z_0 - \alpha \boldsymbol{\nabla} f_1(z_0) \approx \alpha' z_0$ approximately holds true, allowing no further improvement when $\alpha'$ is already chosen in an optimal manner, which is automatically done by formulation (5.30). This conjecture seems to be correct when looking at the optimally-scaled cosine similarity defined in (5.9), and stated in Tab. 5.3 for the quantities of interest here. When $z_0 = (\mathbf{A}^{\mathrm{H}}\boldsymbol{b}) / \left\|\mathbf{A}^{\mathrm{H}}\boldsymbol{b}\right\|_2$, the gradient of $f_2$ yields a direction which is less collinear to the starting point than the gradient of $f_1$. Applying the forward operator, the difference is even more severe, where the gradient of $f_2$ provides a direction which is almost orthogonal to $z_0$ in terms of the radiated fields.

For the same example, quite different observations are made when picking a randomly distributed $z_0$. The result can be seen in Fig. 5.7(b). Again, formulation (5.30) allows for a larger decrease in the cost function than (5.16). However, this time the gradients seem to be rather similar, both allowing for a decrease of the opposing cost function. This is also visible from the cosine similarities, expressing a rather similar, if not opposing trend, in Tab. 5.3.

Illustrated from another point of view, a line search for formulation (5.16) is similar to

$$\min_{\alpha} \ \left\| \left|\mathbf{A}\left(z + \alpha \boldsymbol{p}\right)\right| - |\boldsymbol{b}| \right\|_2, \tag{5.36}$$

which is a one-dimensional optimization problem. In contrast, formulation (5.30) corresponds to the two-dimensional optimization

$$\min_{\alpha_1, \alpha_2} \ \left\| \alpha_1 \left|\mathbf{A}\left(z + \alpha_2 \boldsymbol{p}\right)\right| - |\boldsymbol{b}| \right\|_2. \tag{5.37}$$

Note that the optimization of (5.37) in $\alpha_1$ is automatically performed as all occurring derivatives already depend on the scaling factor $c_{\mathrm{si}}(z)$ in (5.31). Eventually, this leads to an increased convergence rate of the minimization process.

**Empirical Comparison with the Standard Formulation**

Further similarities and differences between the scale-invariant formulation and the standard approach are now investigated for phaseless randomly distributed and NF antenna data.

**Success Rate and Iteration Count**  A brief comparison of the formulations (5.16) and (5.30) has been performed for complex-valued normally distributed data, as well as for NF data of spherical vector wave functions evaluated on a measurement sphere with a radius of $\lambda$. The chance of a
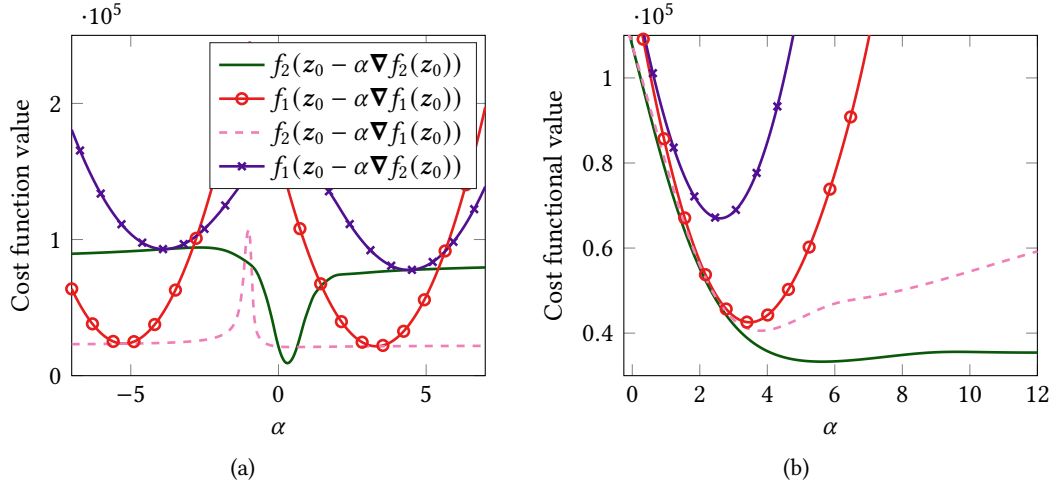
Fig. 5.7 Comparison of the formulations in (5.16) and (5.30). Depicted are the values of the cost functions $f_1$ and $f_2$ in the direction of the gradients $\boldsymbol{\nabla} f_1$ and $\boldsymbol{\nabla} f_2$ for varying step lengths $\alpha$. The example was computed for a complex random Gaussian distributed forward operator $\mathbf{A} \in \mathbb{C}^{50 \times 22}$. The gradients were normalized, $\|\boldsymbol{\nabla} f\|_2 = 1$, for ease of plotting. (a) $\boldsymbol{z}_0 = (\mathbf{A}^{\mathrm{H}}\boldsymbol{b}) / \|\mathbf{A}^{\mathrm{H}}\boldsymbol{b}\|_2$. (b) For a randomly chosen point $\boldsymbol{z}_0$.

successful transformation, equivalent to a resulting NF deviation $\epsilon_{c,\mathrm{dB}}(\mathbf{A}\boldsymbol{z}, \boldsymbol{b}) \leq -45\,\mathrm{dB}$, for varying oversampling ratios $m/n$ is depicted in Figs. 5.8(a) and 5.8(b). The respective required average number of iterations $k_{\mathrm{it,av}}$ is provided in Figs. 5.8(c) and 5.8(d). All solvers at most performed $5 \times 10^3$ iterations. However, termination also occurred once a magnitude NF deviation of $\epsilon_{c,\mathrm{dB}}(|\mathbf{A}\boldsymbol{z}|, |\boldsymbol{b}|) \leq -100\,\mathrm{dB}$ was reached, or the relative change in the NF deviation over multiple iterations falls below a threshold, i.e., stagnation is observed. For both types of data and parameter values of $p_{1/2}$, the number of iterations performed on average with (5.30) is lower than with (5.16). This trend is more clearly pronounced when $p_{1/2} = 1$, i.e., when the optimization is performed in terms of the squared magnitudes. While (5.30) does lead to a slightly larger success rate for normally distributed data, no clear winner emerges for the considered NF data.

**Synthetic Antenna Data**    The performance of $\mathcal{A}_1$ and $\mathcal{A}_2$ with $p_{1/2} \in \{0.5, 1\}$ is now compared for synthetic NF data of a Vivaldi antenna acquired on two spherical surfaces. The simulation setup is illustrated in Fig. 5.9(a), where the original AUT is located within the red box and, for the purpose of an NFFFT, is model by $n = 4 \times 10^3$ equivalent Hertzian dipoles placed on an enclosing sphere (blue circle). The measurement spheres feature radii of $50\lambda$ and $90\lambda$ and are approximately centered around the AUT. With a minimum sphere diameter of $\approx 10\lambda$, the FF distance of this AUT is roughly $180\lambda$ such that one could expect sufficient field variations among the two measurement spheres and, thus, a decent phase reconstruction. Distribution of the equivalent sources as well as the sample locations on the spheres was done according to a Fibonacci mapping [Keinert et al. 2015], yielding almost uniformly placed quantities. In total $m = 32 \times 10^3$ measurements of the tangential electric field were provided to the transformation algorithms, where half of them were acquired on each measurement sphere.
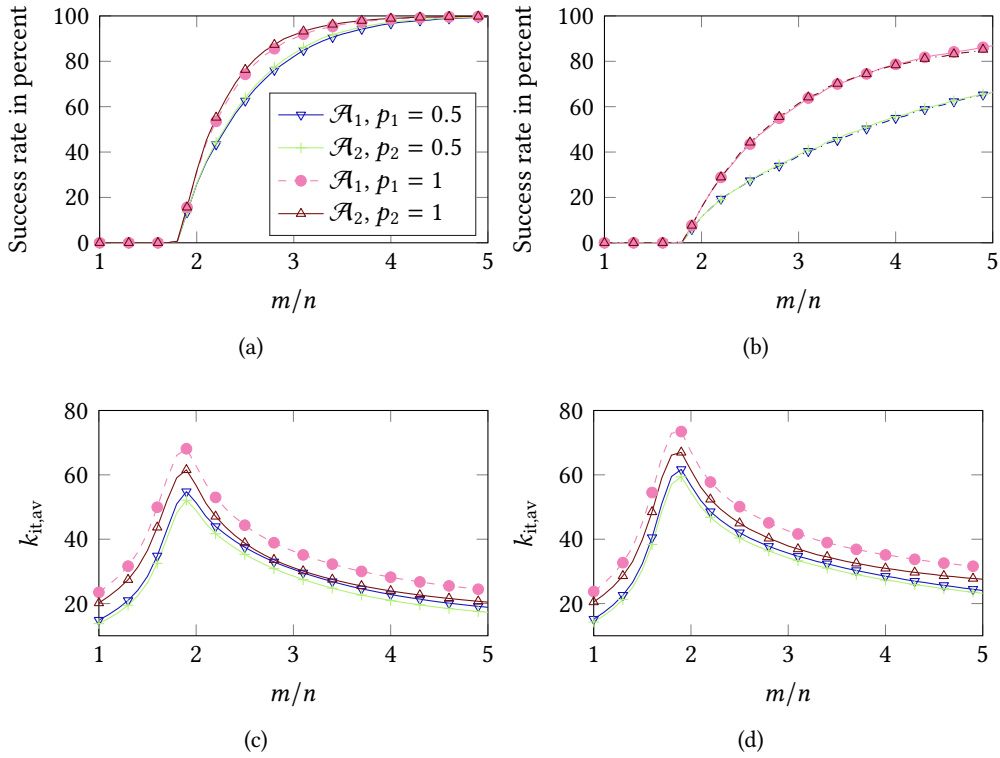
Fig. 5.8 Comparison of phase retrieval formulations based on $\mathcal{A}_1$ and $\mathcal{A}_2$ in (5.16) and (5.30), respectively. In (a) and (b), the achievable success rate for $n = 10$ is depicted for complex-valued normally distributed data and NF data stemming from a spherical multipole expansion, respectively. For each value of $m/n$, $5 \times 10^4$ repetitions were run and the algorithms were started from an initial guess computed via the optimal spectral method. Success is declared, once $\epsilon_{c,\mathrm{dB}}(\mathbf{A}z, \boldsymbol{b}) \leq -45$ dB is achieved. In (c) and (d), the corresponding average number of iterations until solver termination, denoted by $k_{\mathrm{it,av}}$, is given. Solver termination either occurred after the maximum number of $5 \times 10^3$ iterations had been reached, or, an NF deviation of $\epsilon_{c,\mathrm{dB}}(|\mathbf{A}z|, |\boldsymbol{b}|) \leq -100$ dB was observed.

Figure 5.9(b) gives an impression of the convergence behavior of the phaseless solvers, as well as that of the fully coherent transformation. The coherent approach is able to determine a solution with an NF deviation in terms of the probe magnitudes of below $-66$ dB after $2 \times 10^2$ iterations — a solution with a complex NF deviation of $-63$ dB. The lowest magnitude NF deviations of the phaseless solvers are around $-23$ dB and $-34$ dB for the variants with $p_{1/2} = 0.5$ and $p_{1/2} = 1$, respectively. However, despite the relatively good agreement of the probe signals in terms of their magnitude and squared magnitude, the corresponding complex NF deviations are still as high as $-0.05$ dB, $-3.3$ dB and $-2.6$ dB for $\mathcal{A}_{1/2}^{0.5}$, $\mathcal{A}_1^1$ and $\mathcal{A}_2^1$, respectively. Here, the superscript indicates the value of $p_{1/2}$. Interestingly, while the choice of $p_{1/2} = 0.5$ leads to a faster initial convergence rate, $p_{1/2} = 1$ leads to lower NF deviations at the point of termination due to stagnation. Furthermore, the scale-invariant version improves the convergence rate in the beginning, while only leading to a lower magnitude NF deviation for $p_2 = 1$ compared to the standard formulation. Overall, the impression is gained that it can be difficult to judge a phaseless transformation result solely based

on the achieved magnitude NF deviation $\epsilon_{c,\mathrm{dB}}(|\mathbf{A}\mathbf{z}|, |\mathbf{b}|)$, however, its complex counterpart is not available in practice.

For reasons of completeness, Figs. 5.9(c) to 5.9(f) depict the FF radiation characteristic computed from the determined source coefficients. The magnitude of the dominant electric field component in the $\vartheta = 90°$ plane containing the main beam of the AUT is drawn. The complex field deviations are computed after normalization of the curves to their values at the location of the maximum of the reference. Interestingly, the determined magnitude of the FF seems to agree quite well with the reference, however, the reconstructed phase distribution seems to be false, resulting in large complex deviations. As expected from the better agreement of the magnitude and phase in the NF, the results obtained with $p_{1/2} = 1$ exhibit lower total FF deviations, especially visible in the main-beam region.

**Concluding Remarks — Scale-Invariant Formulation**   The main idea of the scale-invariant formulation is to achieve faster convergence by inherently compensating for improper scaling of the solution vector at all times — allowing for longer step lengths within the line search. In practice, a slightly reduced number of iterations and an overall performance close to that of the standard formulation is observed.
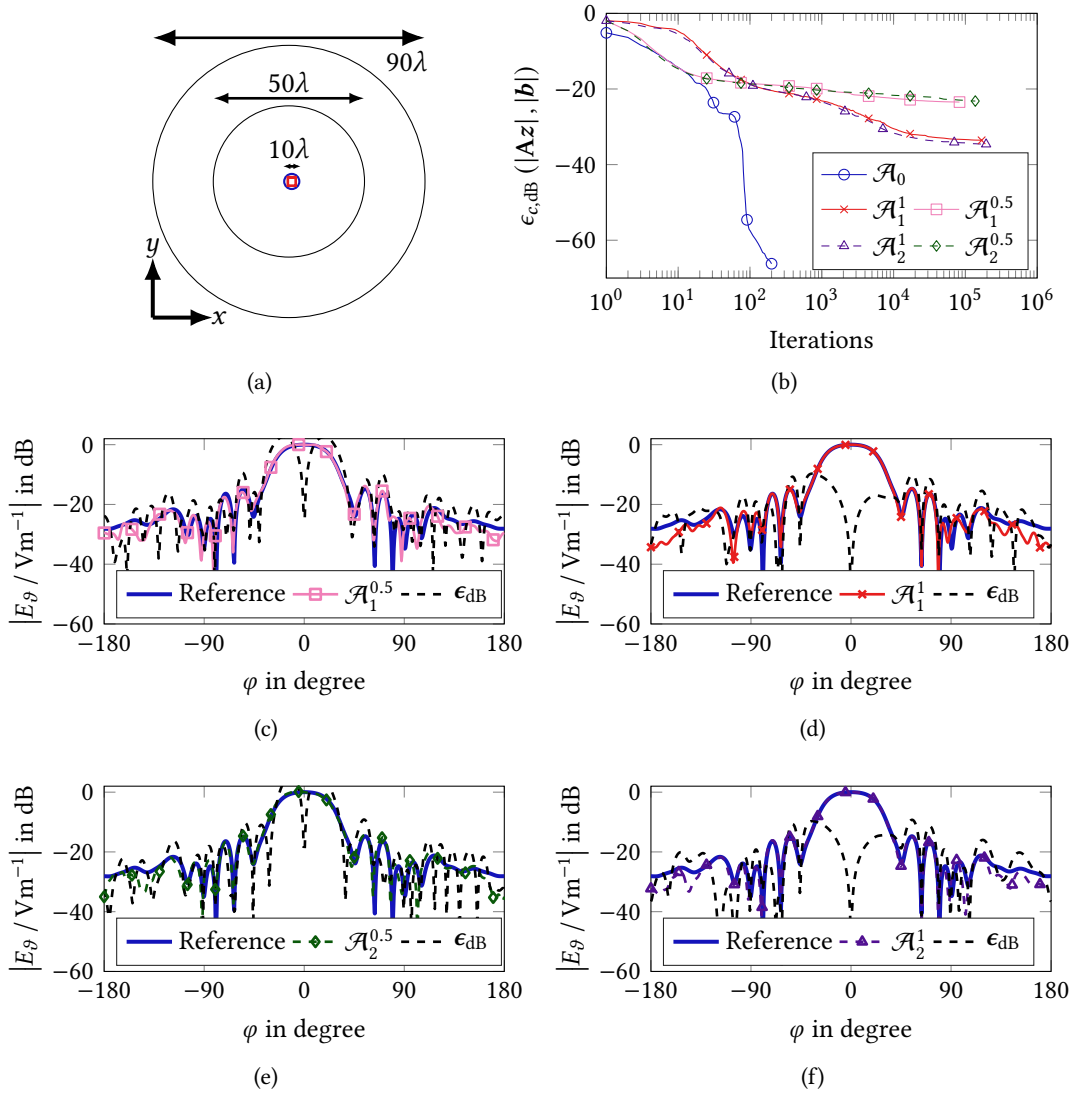
Fig. 5.9 Simulation setup and transformation results for synthetic NF data of a Vivaldi antenna. (a) NF data on two spherical surfaces is acquired, yielding $m = 32 \times 10^3$, half on each sphere and distributed according to a Fibonacci mapping [Keinert et al. 2015]. The original AUT is located within the red box, while $n = 4 \times 10^3$ equivalent Hertzian dipoles placed on an enclosing sphere (blue circle) are employed in the transformation. The FF distance for an AUT of this size is $\approx 180\lambda$. (b) Convergence of the two phaseless solvers $\mathcal{A}_{1/2}^{0.5/1}$ with $p_{1/2} = 0.5$ or $p_{1/2} = 1$, indicated by the superscript, in comparison to a fully coherent transformation with $\mathcal{A}_0$. (c) to (f) The resulting FF radiation characteristic in the $\vartheta = 90°$ plane, where only the dominant field component is depicted. The complex deviation computed after normalizing each curve to its respective value at the maximum of the reference is rather large, even though the pattern magnitudes agree pretty well.

### 5.4.4 Projector-Based Formulations

So far, the considered phase retrieval formulations are either based on the minimization of nonlinear cost functions dependent on source domain quantities, or utilize alternating projections between observation and source domain, like the Gerchberg-Saxton variants discussed in Section 5.4.1. This observation immediately raises the question: Can we combine both approaches? The answer is yes, and the following two formulations showcase how this can be achieved.

**Projector Approach — Real-Valued Phases**

Consider the nonlinear operator

$$\mathcal{A}_5 = \left(\mathbf{A}\mathbf{A}^{-1} - \mathbf{I}\right) \operatorname{diag}\left(|\boldsymbol{b}|\right) \mathrm{e}^{\mathrm{j}\boldsymbol{z}} = \mathbf{B}_5 \mathrm{e}^{\mathrm{j}\mathbf{F}\boldsymbol{z}} \quad \text{with} \ \ \boldsymbol{d}_5 = \mathbf{0}, \quad \boldsymbol{z} \in \mathbb{R}^{m \times 1} \tag{5.38}$$

containing the projector $\left(\mathbf{A}\mathbf{A}^{-1} - \mathbf{I}\right)$. The formulation in (5.38) searches for real-valued phase terms in $\boldsymbol{z}$, such that the combination of magnitude and phase $|\boldsymbol{b}| \circ \mathrm{e}^{\mathrm{j}\boldsymbol{z}}$ corresponds to an electromagnetic field that is physically realizable with the given equivalent sources. By searching for a real-valued term in the exponent, the problem becomes nonlinear, however, automatically enforces that the resulting phase terms feature a magnitude of one. The fundamental difference between this formulation and that of previous sections lies in the utilization of the projector matrix $\left(\mathbf{A}\mathbf{A}^{-1} - \mathbf{I}\right)$. This projector ensures that all determined phase terms, paired with the measurement magnitudes in the diagonal matrix $\operatorname{diag}\left(|\boldsymbol{b}|\right)$, are in the feasible range of the measurement matrix $\mathbf{A}$. As such, the formulation in (5.38) potentially enforces more restrictions on the reconstructed phases than inherently done in the methods of the sections above. This additional filtering property comes at the downside of the increased computational effort associated with the pseudoinverse $\mathbf{A}^{-1}$.

Here, we state the derivatives for the rather general form of $\mathcal{A}_5 = \mathbf{B}_5 \mathrm{e}^{\mathrm{j}\mathbf{F}\boldsymbol{z}}$ with possibly complex-valued matrices $\mathbf{B}_5$ and $\mathbf{F}$. Note that since we are optimizing for real-valued quantities, the equations of (3.70) and (3.71) should be used. Still, for the general case of $\boldsymbol{z} \in \mathbb{C}^{m \times 1}$, the derivatives read as

$$\frac{\partial \mathcal{A}_5}{\partial \boldsymbol{z}} = \mathrm{j}\mathbf{B}_5 \operatorname{diag}\left(\mathrm{e}^{\mathrm{j}\mathbf{F}\boldsymbol{z}}\right) \mathbf{F} \tag{5.39}$$

$$\left(\frac{\partial \mathcal{A}_5}{\partial \boldsymbol{z}}\right)^{\mathrm{H}} = -\mathrm{j}\mathbf{F}^{\mathrm{H}} \operatorname{diag}\left(\mathrm{e}^{-\mathrm{j}\mathbf{F}\boldsymbol{z}}\right) \mathbf{B}_5^{\mathrm{H}} \tag{5.41}$$

$$\frac{\partial \overline{\mathcal{A}}_5}{\partial \boldsymbol{z}} = -\mathrm{j}\overline{\mathbf{B}_5} \operatorname{diag}\left(\mathrm{e}^{-\mathrm{j}\mathbf{F}\boldsymbol{z}}\right) \mathbf{F} \tag{5.40}$$

$$\left(\frac{\partial \overline{\mathcal{A}}_5}{\partial \boldsymbol{z}}\right)^{\mathrm{H}} = \mathrm{j}\mathbf{F}^{\mathrm{H}} \operatorname{diag}\left(\mathrm{e}^{\mathrm{j}\mathbf{F}\boldsymbol{z}}\right) \mathbf{B}_5^{\mathrm{T}}. \tag{5.42}$$

**Projector Approach — Source Coefficients**

Consider the formulation

$$\mathcal{A}_6 = \left(\mathbf{A}\mathbf{A}^{-1} - \mathbf{I}\right) \operatorname{diag}\left(|\boldsymbol{b}|\right) \mathrm{e}^{\mathrm{j}\angle(\mathbf{A}\boldsymbol{z})} = \mathbf{B}_6 \frac{\mathbf{A}\boldsymbol{z}}{|\mathbf{A}\boldsymbol{z}|} \quad \text{with} \ \ \boldsymbol{d}_6 = \mathbf{0}, \quad \boldsymbol{z} \in \mathbb{C}^{n \times 1}, \tag{5.43}$$

which searches for complex source coefficients, such that the resulting phase distribution physically correctly matches the measured magnitudes. The formulation is similar to that in (5.38), with the difference that one does not directly determine phase values but, instead, coefficients for the equivalent sources. With growing oversampling ratios, the number of unknowns is expected to be smaller than the number of phase terms. This may be an advantage for electrically larger problems requiring millions of unknowns and measurement entries.
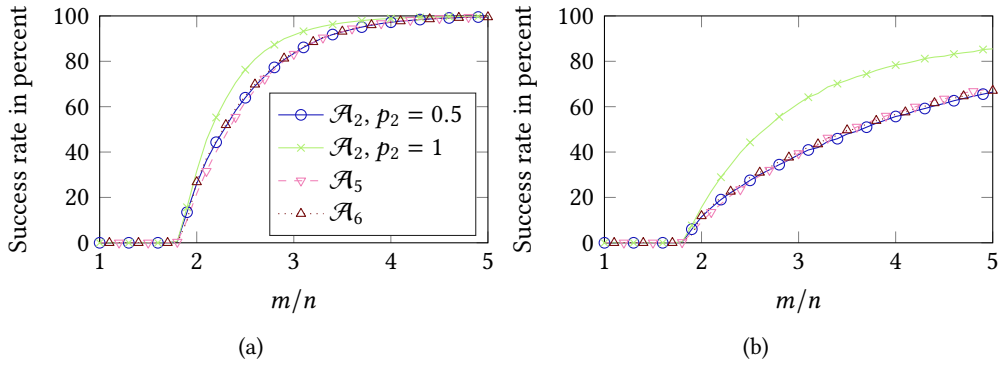
Fig. 5.10 Comparison of phase retrieval formulations based on $\mathcal{A}_5$ and $\mathcal{A}_6$ with that of $\mathcal{A}_2$. In (a) and (b), the achievable success rate for $n = 10$ with complex-valued normally distributed data and NF data stemming from a spherical multipole expansion, respectively, is depicted. Starting from an initial guess computed via the optimal spectral method, $5 \times 10^4$ repetitions are run for each value of $m/n$. Success is declared, once $\epsilon_{c,\mathrm{dB}}(\mathbf{Az}, \mathbf{b}) \leq -45$ dB is achieved.

The required derivatives equal

$$\frac{\partial \mathcal{A}_6}{\partial z} = \tfrac{1}{2} \mathbf{B}_6 \operatorname{diag}\left(\frac{1}{|\mathbf{Az}|}\right) \mathbf{A} \qquad (5.44)$$

$$\left(\frac{\partial \mathcal{A}_6}{\partial z}\right)^{\mathrm{H}} = \tfrac{1}{2} \mathbf{A}^{\mathrm{H}} \operatorname{diag}\left(\frac{1}{|\mathbf{Az}|}\right) \mathbf{B}_6^{\mathrm{H}} \qquad (5.46)$$

$$\frac{\partial \overline{\mathcal{A}_6}}{\partial z} = -\tfrac{1}{2} \overline{\mathbf{B}_6} \operatorname{diag}\left(\frac{\overline{\mathbf{Az}} \circ \overline{\mathbf{Az}}}{|\mathbf{Az}|^3}\right) \mathbf{A} \qquad (5.45)$$

$$\left(\frac{\partial \overline{\mathcal{A}_6}}{\partial z}\right)^{\mathrm{H}} = -\tfrac{1}{2} \mathbf{A}^{\mathrm{H}} \operatorname{diag}\left(\frac{\mathbf{Az} \circ \mathbf{Az}}{|\mathbf{Az}|^3}\right) \mathbf{B}_6^{\mathrm{T}}. \qquad (5.47)$$

**Numerical Results**

A brief comparison of the two projection-based formulations with the scale-invariant approach from (5.30) has been performed for complex-valued normally distributed and NF data stemming from a spherical multipole expansions. For the latter, the tangential electric field was evaluated on a measurement sphere with a radius of $\lambda$, where the sample locations were almost uniformly distributed according to a Fibonacci mapping [Keinert et al. 2015]. The obtainable success rates for $n = 10$ and when starting from an initial guess computed via the optimal spectral method are drawn in Fig. 5.10. All solvers at most performed $k_{\max} = 5 \times 10^3$ iterations and success was declared once $\epsilon_{c,\mathrm{dB}}(\mathbf{Az}, \mathbf{b}) \leq -45$ dB was achieved.

For both data types, the projection-based approaches fall behind the performance of the scale-invariant formulation operating on the squared magnitudes. While in the case of random data, their success rate is similar to that of $\mathcal{A}_2$ for $p_2 = 0.5$, they exhibit a slight advantage for the considered NF data. With the need for the evaluation of the computationally expensive pseudoinverse, this raised chance of success is paid for with drastically increased runtimes. When comparing $\mathcal{A}_5$ and $\mathcal{A}_6$, a rather controversial trend is observed. While $\mathcal{A}_6$ is slightly superior for random data, it falls behind $\mathcal{A}_5$ for the particular example of NF data. While the differences are minor for the small number of unknowns, more decisive differences could be encountered for electrically larger examples.

**Concluding Remarks — Projector Approaches**    Two projector-based and optimization-driven phase retrieval formulations were presented. The latter can be considered hybrids of alternating-projection based methods, e.g., Gerchberg-Saxton, and classical nonconvex-minimization based approaches, e.g., the standard formulation with $\mathcal{A}_1$. Here, they were seen to feature a similar performance than other solvers, however, requiring considerably more computational resources. Still for the considered NF data, slight improvements over the scale-invariant solver operating on the magnitudes were observed.

### 5.4.5  Exploiting Spatial Derivative Information

The following section is partially in line with the ideas presented in [Paulus and Eibert 2020]. All aforementioned formulations have used the identical type of phaseless information, in the form of magnitudes of signals acquired with single, or possibly multiple, probe antennas at varying points in space. Assuming that one can sample the three-dimensional field distribution with the probe antenna on a sufficiently fine grid, it seems reasonable that one can make approximate statements on the *spatial derivative* of this probe antenna signal, e.g., utilizing finite differences. Since one has no phase information, this knowledge is limited to the spatial derivative of the magnitude of the probe signal. Taking a look back at Section 2.2.6, we see that we have already determined the spatial derivative of the forward operator for the case of dipole-dipole interactions. What remains to be found is the spatial derivative of the magnitude of the dipole-dipole interactions.

One can write this operator as

$$\mathcal{A}^{r'}(z) = \frac{\partial |\mathbf{A}z|}{\partial r'} = \mathrm{Re}\left\{\left(\frac{\partial \mathbf{A}}{\partial r'}z\right) \circ e^{-j\boldsymbol{\varphi}^{r'}}\right\} = \mathrm{Re}\left\{\left(\mathbf{A}^{r'}z\right) \circ e^{-j\boldsymbol{\varphi}^{r'}}\right\} \tag{5.48}$$

where

$$\boldsymbol{\varphi}^{r'} = \left[\angle\left(\mathbf{A}z\right)^{\mathrm{T}} \quad \angle\left(\mathbf{A}z\right)^{\mathrm{T}} \quad \angle\left(\mathbf{A}z\right)^{\mathrm{T}}\right]^{\mathrm{T}} \in \mathbb{R}^{3m \times 1}. \tag{5.49}$$

A short derivation of (5.48) is given in Appendix A.3, while $\mathbf{A}^{r'}$ is derived in Section 2.2.6.

Even though assumed not to be measurable, one can find the derivative of the phase of the received signal with respect to the observation location as

$$\frac{\partial \operatorname{atan2}\left(\mathrm{Im}\left\{\mathbf{A}z\right\}, \mathrm{Re}\left\{\mathbf{A}z\right\}\right)}{\partial r'} = \frac{\partial \angle\left(\mathbf{A}z\right)}{\partial r'} = \boldsymbol{M} \circ \mathrm{Im}\left\{\left(\mathbf{A}^{r'}z\right) \circ e^{-j\boldsymbol{\varphi}^{r'}}\right\}, \tag{5.50}$$

where atan2 returns the two-argument arcus tangent, and with

$$\boldsymbol{M} = \left[\frac{1}{|\mathbf{A}z|}^{\mathrm{T}} \quad \frac{1}{|\mathbf{A}z|}^{\mathrm{T}} \quad \frac{1}{|\mathbf{A}z|}^{\mathrm{T}}\right]^{\mathrm{T}} \in \mathbb{R}^{3m \times 1}. \tag{5.51}$$

Equation (5.50) shows that the phase of the electromagnetic fields can rapidly vary at locations with vanishing fields. A detailed derivation of (5.50) is also given in Appendix A.3. For completeness, one can find

$$\frac{\partial \mathbf{A}z}{\partial r'} = \left(\frac{\partial |\mathbf{A}z|}{\partial r'} + j\,|\mathbf{A}z|\,\frac{\partial \angle(\mathbf{A}z)}{\partial r'}\right) \circ e^{j\angle(\mathbf{A}z)} \tag{5.52}$$

relating the derivative of the complex probe signals with the derivative of the magnitude and the phase.

There are interesting observations to be made. For example, looking at (5.48) one finds that whenever

$$\frac{\partial |\mathbf{A}z|}{\partial r'} = \mathbf{0} \neq |\mathbf{A}z| \quad \text{and} \quad \left| \mathbf{A}^{r'}z \right| \neq \mathbf{0},$$

$$\Rightarrow \quad \angle \left( \mathbf{A}'z \circ \overline{\mathbf{A}z} \right) = \pm \frac{\pi}{2}, \tag{5.53}$$

i.e., there is an ambiguous but fixed phase relation between the phase of the spatial derivative of the complex-valued fields and the original fields at the same location. However, the variable sign of $\pm \pi/2$ and the fact that we can not estimate when $|\mathbf{A}^{r'}z| \neq \mathbf{0}$ makes this knowledge rather impractical. Still, a possible formulation for enforcing the phase differences between two quantities with linear dependency on the unknowns while not knowing both magnitudes is derived in Appendix A.6.

Here, the focus is put on how to exploit the spatial derivative information in (5.48) via

$$\mathscr{A}_7 = \mathscr{A}^{r'}(z) = \frac{\partial |\mathbf{A}z|}{\partial r'} \quad \text{with} \quad d_7 = \frac{\partial |b|}{\partial r'}. \tag{5.54}$$

The required derivatives then read as

$$\frac{\partial \mathscr{A}_7}{\partial z} = \frac{1}{2}\text{diag}\left( e^{-j\varphi^{r'}} \right) \mathbf{A}^{r'} + \tfrac{1}{4}\text{diag}\left( M \circ \left( \overline{\mathbf{A}^{r'}z} - \left( \mathbf{A}^{r'}z \right) \circ e^{-2j\varphi^{r'}} \right) \right) \mathbf{A} \tag{5.55}$$

$$\left( \frac{\partial \mathscr{A}_7}{\partial z} \right)^{\text{H}} = \frac{1}{2}\left( \mathbf{A}^{r'} \right)^{\text{H}} \text{diag}\left( e^{j\varphi} \right) + \tfrac{1}{4}\mathbf{A}^{\text{H}}\text{diag}\left( M \circ \left( \mathbf{A}^{r'}z - \left( \overline{\mathbf{A}^{r'}z} \right) \circ e^{2j\varphi^{r'}} \right) \right) \tag{5.56}$$

$$\frac{\partial \overline{\mathscr{A}}_7}{\partial z} = \frac{\partial \mathscr{A}_7(z)}{\partial z} \tag{5.57} \qquad\qquad \left( \frac{\partial \overline{\mathscr{A}}_7}{\partial z} \right)^{\text{H}} = \left( \frac{\partial \mathscr{A}_7(z)}{\partial z} \right)^{\text{H}}. \tag{5.58}$$

There are several things to notice. First, dependent on the number of spatial directions in which the derivative is computed, the number of "measurements available to the algorithm" will be one, two or three times the number of measurements of the previous formulations. Second, (5.54) is the first phase retrieval problem where the phases are to be reconstructed based on *nonlinear measurements* of the source quantity $z$. As such, (5.54) belongs to a more general — and potentially more difficult — class of phase retrieval problems as required in the case of the linear measurement operator encountered with common magnitude-only NF measurements. Still any additional information, even if this requires nonlinear measurements, may be beneficial for the original problem of phaseless NFFFTs.

**Synthetic NF Data for Random Dipoles**  The following results have also been presented in [Paulus and Eibert 2020]. Exemplary field data radiated by randomly excited distributions of 30 Hertzian dipoles placed tangentially on a spherical surface with a diameter of $0.7\lambda$ was generated. The frequency was set to 3 GHz. Two orthogonal polarizations, the $\vartheta$- and the $\varphi$-component, of the NF were sampled by eight two-element antenna arrays, each featuring single Hertzian dipoles as elements, on a sphere with a diameter of $\lambda$. In order to achieve an almost uniform sample distribution, a Fibonacci mapping was employed [Keinert et al. 2015]. The synthetic measurement setup is depicted in Fig. 5.11(a), where the original Hertzian dipoles are represented by green

arrows and the $n = 100$ equivalent Hertzian dipoles used as sources in the transformations are indicated by dark red arrows. The eight probe arrays, four per polarization, are placed at all sample locations, illustrated by blue circles. As an example, one of the probe arrays is depicted in Fig. 5.11(a), symbolized by the two red arrows connected via a red line — representing the two Hertzian dipole elements. All eight probe arrays exhibit the same horizontal separation of $2\lambda$ between the two elements. In theory, the four probe arrays per polarization allow for an analytical computation of the phase difference between the elements via an interferometric relation [Costanzo et al. 2005; Costanzo and Di Massa 2008; Knapp et al. 2019b; Paulus et al. 2017a,c]. More details about this concept of local phase information will be provided in Section 5.6 and in Chapter 6. Here, it is sufficient to imagine these particular probe arrays to provide more restrictions and knowledge about the field radiated by the AUT.

In Fig. 5.11(b), the success rate of the phase retrieval formulation exploiting the spatial derivative of the probe signals and that of the scale-invariant phase retrieval via the operator $\mathcal{A}_2$ is drawn. Results for various choices of the oversampling ratio $m/n$ are depicted. For each value of $m/n$, $5\times10^2$ random AUT excitations have been treated and a transformation is called successful once a complex NF deviation according to (4.14) below $-40\,\mathrm{dB}$ is achieved. This value is close to the reference NF deviation of $-48\,\mathrm{dB}$, which can be achieved with this kind of equivalent AUT representation and exploiting full phase information. All solvers were started from the same initial guess generated via 40 power iterations of the spectral method. Afterwards at most $4 \times 10^2$ solver iterations were performed. At first glance, the new formulation is seen to obtain a drastically larger success rate for lower values of the sampling ratio. However it should be kept in mind that since all three spatial derivatives have been considered inside the operator $\mathcal{A}_7$, the actual available number of measurements is threefold of that given to $\mathcal{A}_2$. So the observable advantage should largely be caused by the additional measurements. On the other side, only utilizing the spatial derivative information does yield high success rates in the regime of large oversampling values. While the best choice for phase retrieval, either $\mathcal{A}_2$ or $\mathcal{A}_7$, for the particular example at hand may depend on $m/n$, combinations of the formulations can also be considered. The solid blue line in Fig. 5.11(b) refers to first optimizing $\mathcal{A}_2$ and using the solution thereof as a starting point for $\mathcal{A}_7$. By reversing this order, the performance depicted by the solid green line can be achieved. In fact, the latter does only feature a slight disadvantage over solely using $\mathcal{A}_7$ for small values of $m/n$ while performing well for larger $m/n$, where it is superior to all other formulations and combinations thereof.

Admittedly, the presented phase retrieval formulation exploiting the spatial derivative of the magnitudes of probe signals has its flaws. In the presented form, there are severe doubts about its applicability for real-world NF antenna measurements, where noise contributions will additionally make it harder to construct the necessary spatial derivatives with adequate accuracy. The magnetic field, which inherently contains information about combinations of spatial derivatives of the electric field, is easier to measure. However, it remains to be verified to what extent this mixture of spatial derivatives provides a similar information gain as single derivatives. Despite this significant downside, the approach and the results above showcase important aspects of phaseless NFFFTs. First, phase reconstruction based on nonlinear measurements may seem like an unnecessary complication, however, may be a key to tailoring optimized approaches explicitly working with phaseless NF antenna data. Every piece of information, including restrictions caused by the underlying Maxwell equations, has to be exploited in order to obtain best results. This directly leads to the second conclusion or guideline to be drawn from the results: Despite the extra nonlinearity or costs, keep in mind to always employ all potentially available information.
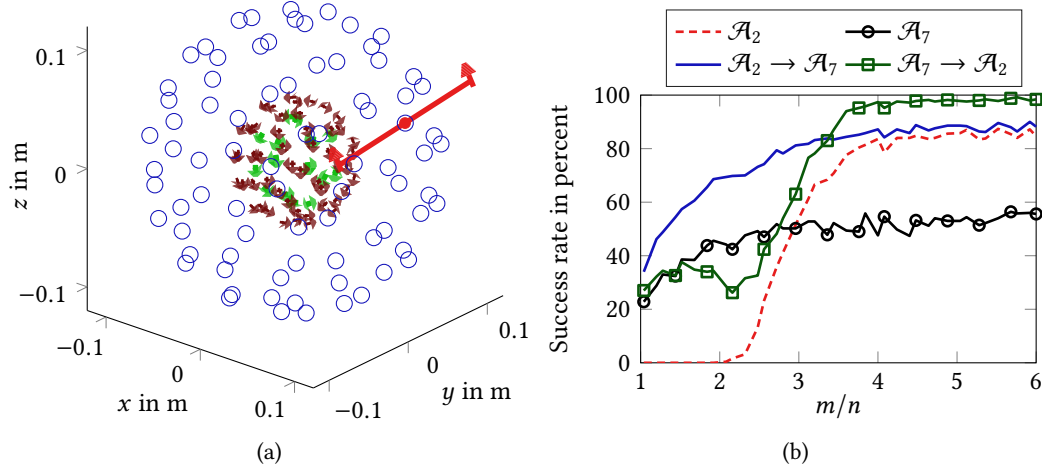
Fig. 5.11 (a) Synthetic NF generation setup at a frequency of 3 GHz. The green arrows indicate the randomly excited AUT dipoles while dark red arrows refer to the equivalent source dipoles. The blue circles represent the almost uniformly distributed sampling locations. The light red arrows illustrate two dipoles of a special probe, centered at an exemplary sample location (red filled circle). (b) Success rates for phaseless NFFFTs based on the operator $\mathcal{A}_2$ and the proposed operator $\mathcal{A}_7$. Note that due to the three spatial derivatives, $\mathcal{A}_7$ effectively utilizes the ratio of $3m/n$. Best results can be obtained when combining both approaches, e.g., starting $\mathcal{A}_2$ from the solution of $\mathcal{A}_7$ or the other way round. © IEEE 2020.

**Concluding Remarks — Spatial Derivative Information**   While all discussed phase retrieval formulations represent "genneral purpose" solvers, the utilization of spatial derivative information is so far limited to the case of NF antenna data. By imposing restrictions on the spatial derivative of the magnitude of the probe signals, additional nonlinear measurements of the source coefficients are made available. The resulting reconstruction problem features a more severe degree of nonlinearity and, on its own, does not allow for a more accurate phase retrieval. However, it can directly be combined with general purpose phase retrieval solvers to utilize all available data, effectively yielding increased success rates. While of arguable practical relevance, the formulation proves a major point. Always try to exploit as much information available as possible — even if this requires the treatment of highly nonlinear aspects.

### 5.4.6 Linearized Phase Retrieval

Another approach to tackle the phase retrieval problem can be found when having a closer look at the magnitude of the forward operator applied to a solution vector modified by a small perturbation $\Delta z$. One can find

$$
\begin{aligned}
|\mathbf{A}\,(z + \Delta z)|^2 = {} & |\mathbf{A}z|^2 + |\mathbf{A}\Delta z|^2 \\
& + 2 \underbrace{\left[ \operatorname{Re}\left\{ \operatorname{diag}\left(\mathbf{A}z\right) \overline{\mathbf{A}} \right\} \quad \operatorname{Im}\left\{ \operatorname{diag}\left(\mathbf{A}z\right) \overline{\mathbf{A}} \right\} \right]}_{\mathbf{C}_8 \in \mathbb{R}^{m \times 2n}} \underbrace{\begin{bmatrix} \operatorname{Re}\left\{ \Delta z \right\} \\ \operatorname{Im}\left\{ \Delta z \right\} \end{bmatrix}}_{\Delta z' \in \mathbb{R}^{2n \times 1}}.
\end{aligned}
\tag{5.59}
$$

Thus, one can write

$$
|\mathbf{A}\,(z + \Delta z)|^2 = |\mathbf{A}z|^2 + |\mathbf{A}\Delta z|^2 + \mathbf{C}_8 \Delta z' \stackrel{!}{=} |b|^2
\tag{5.60}
$$

$$
\Rightarrow |\mathbf{A}z|^2 + \mathbf{C}_8 \Delta z' \stackrel{!}{\approx} |b|^2,
\tag{5.61}
$$

from which, neglecting the $O\left(\Delta z^2\right)$ term, we may state a linear update rule for the real and the imaginary part of $\Delta z$ as

$$
\Delta z' \approx \mathbf{C}_8^{-1}\left(|b|^2 - |\mathbf{A}z|^2\right).
\tag{5.62}
$$

Equation (5.62) does not necessarily yield an appropriately scaled solution that ensures higher-order terms $O\left(\Delta z^2\right)$ are truly negligible. However, one can combine the descent direction in (5.62) with the exact line search result in (5.23) belonging to the standard nonconvex formulation with $p_1 = 1$. Note that the computational effort of solving (5.62) is relatively large, since a linear system of equations has to be solved in every iteration. Still, this linearized phase retrieval formulation is very appealing, since it can easily be implemented without requiring any derivatives or the minimization framework, which is otherwise required for most approaches throughout this thesis. Employing the analytic line search based on a cubic polynomial, the algorithm can indeed be compared to the popular Gerchberg-Saxton algorithm, which features a similar computational effort. A minimalistic implementation is provided in Alg. 12.

A brief comparison with the scale-invariant phase retrieval formulation based on $\mathcal{A}_2$ and the Gerchberg-Saxton algorithm in the form of Alg. 10 has been performed. Complex-valued randomly distributed data and synthetic field data generated from spherical vector wave functions evaluated on the surface of a sphere with radius $\lambda$ was considered. For the NF data, the sampling is done

---

**Algorithm 12** Linearized phase retrieval
$z = \text{LPR}_8\left(z_0, |b|, \text{A}, k_{\max}\right)$

---

**Input:** initial guess $z_0$, iterations $k_{\max}$,
        measurements $|b|$ and operator $\text{A}$
**Output:** $z$, where $|\text{A}z| = |b|$

1: $k = 1$

2: $z_k = z_0$

3: **while** $k \leq k_{\max}$ **do**

4:     $\text{C}_8 = 2\left[\text{Re}\left\{\text{diag}\left(\text{A}z_k\right)\overline{\text{A}}\right\}\right.$
             $\left.\text{Im}\left\{\text{diag}\left(\text{A}z_k\right)\overline{\text{A}}\right\}\right]$

     *Descent direction $p_k$:*

5:     $\left[\text{Re}\left\{p_k\right\}^{\text{T}} \quad \text{Im}\left\{p_k\right\}^{\text{T}}\right]^{\text{T}} = \Delta z_k'$
            $= \text{C}_8^{-1}\left(|b|^2 - |\text{A}z_k|^2\right)$

     *Step length $\alpha$ via (5.22), (5.23) and Alg. 11:*

6:     $a_1 = \left\|\,|\text{A}p_k|^2\right\|_2^2$

7:     $b_1 = 4\text{Re}\left\{\overline{\text{A}z_k} \circ \text{A}p_k\right\}^{\text{H}} |\text{A}p_k|^2$

8:     $c_1 = 4\left\|\text{Re}\left\{\overline{\text{A}z_k} \circ \text{A}p_k\right\}\right\|_2^2$
            $+2\,|\text{A}p_k|^{2,\text{H}}\left(|\text{A}z_k|^2 - |b|^2\right)$

9:     $d_1 = 4\text{Re}\left\{\overline{\text{A}z_k} \circ \text{A}p_k\right\}^{\text{H}}\left(|\text{A}z_k|^2 - |b|^2\right)$

10:    $[\alpha_1, \alpha_2, \alpha_3] = \text{cubic\_roots}\left(\frac{3b_1}{4a_1}, \frac{c_1}{2a_1}, \frac{d}{4a_1}\right)$
      *Pick real-valued $\alpha$:*

11:    $\mathbb{R} \ni \alpha \in \{\alpha_1, \alpha_2, \alpha_3\}$

12:    $z_{k+1} = z_k + \alpha p_k$

13: **end while**

14: **return** $z = z_{k+1}$

---

according to a Fibonacci mapping [Keinert et al. 2015], resulting in an almost uniform spatial distribution of the acquisition points. The obtained success rates are drawn in Fig. 5.12 and indicate that the performance of Alg. 12 is between that of $\mathscr{A}_2$ with $p_2 = 1$ and that of the Gerchberg-Saxton variant. Especially for the considered NF data, the linearized formulation outperforms the Gerchberg-Saxton method, while featuring a similar computational effort as well as programming complexity.

**Concluding Remarks — Linearized Phase Retrieval**    The combination of the iterative update rule in (5.62) with the analytic step length computation of (5.23) represents a simple to implement, yet rather well performing retrieval algorithm. Computational complexity and implementation effort are similar to that of the Gerchberg-Saxton algorithms, while the observed success rates seem to be superior.

### 5.4.7 Cosine-Similarity Maximization

Consider the cost function defined via the nonlinear operator in (5.16). While an analytical equation for the optimal step length for this approach has been derived in (5.22), one can exploit the same approach to determine the optimal step length and descent direction when starting from $z = 0$. Inserting $z = 0$ in (5.22) yields

$$f_1\left(z' = \alpha p\right) = \alpha^4 \left\|\,|\text{A}p|^2\right\|_2^2 - 2\alpha^2 |\text{A}p|^{2,\text{H}} |b|^2 + \left\|\,|b|^2\right\|_2^2. \tag{5.63}$$

A first-order optimality condition for (5.63) in terms of the step length corresponds to

$$\frac{\partial f_1\left(\alpha p\right)}{\partial \alpha} = 4\alpha^3 \left\|\,|\text{A}p|^2\right\|_2^2 - 4\alpha^2 |\text{A}p|^{2,\text{H}} |b|^2 \overset{!}{=} 0. \tag{5.64}$$
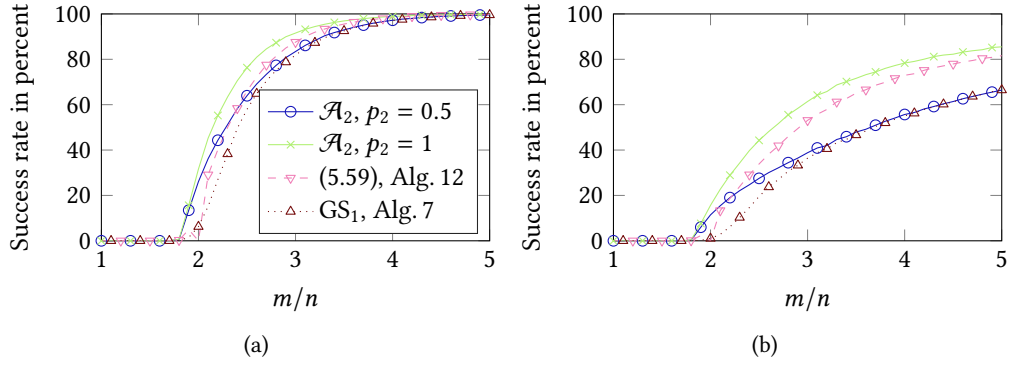
Fig. 5.12 Comparison of the linearized phase retrieval formulation based on (5.59), implemented via Alg. 12, with that of $\mathcal{A}_2$ and the Gerchberg-Saxton variant in Alg. 10. In (a) and (b), the achievable success rate for $n = 10$ with complex-valued normally distributed data and NF data stemming from a spherical multipole expansion, respectively, is depicted. For each value of $m/n$, $5 \times 10^4$ repetitions have been run, where the algorithms have been started from an initial guess computed via the optimal spectral method. Success is declared, once $\epsilon_{c,\text{dB}}(\mathbf{A}z, b) \leq -45\,\text{dB}$ is achieved.

The solution to this equation is

$$\alpha^2 \overset{!}{=} \frac{|\mathbf{A}p|^{2,\text{H}}\,|b|^2}{\left\||\mathbf{A}p|^2\right\|_2^2} \tag{5.65}$$

and can be interpreted as *the first-order optimal step length when starting from a zero initial guess into the descent direction* $p$. The optimal step length of (5.65) can now be inserted into (5.63) in order to determine the optimal descent direction. Knowing that the minimum value of (5.63) is zero, one can write

$$1 - \left(\frac{|\mathbf{A}p|^{2,\text{H}}\,|b|^2}{\left\||\mathbf{A}p|^2\right\|_2^2 \left\||b|^2\right\|_2^2}\right) \overset{!}{=} 0, \tag{5.66}$$

which is a nonlinear equation in $p$, defining the *ideal search direction when starting from a zero initial guess and employing the first-order optimal step length*. Interestingly, (5.66) contains the cosine similarity between the generated magnitudes $|\mathbf{A}p|$ and the measured magnitudes $|b|$. It is not surprising that maximizing the similarity between these quantities leads to a potential solution of the phase retrieval problem.

Employing the notation of the the provided optimization framework, the minimization problem in (5.66) can be rewritten as

$$\mathcal{A}_9 = -\left[\frac{|\mathbf{A}z|^{p_{91},\text{T}}\,|b|^{p_{91}}}{\left\||\mathbf{A}z|^{p_{91}}\right\|_2 \left\||b|^{p_{91}}\right\|_2}\right]^{p_{92}} = -\left[\chi\left(|\mathbf{A}z|^{p_{91}}, |b|^{p_{91}}\right)\right]^{p_{92}}, \quad z \in \mathbb{C}^{n \times 1} \quad \text{with } d_9 = -1. \tag{5.67}$$

The required derivatives can be found as

$$\frac{\partial \mathcal{A}_9\left(z\right)}{\partial z} = -\frac{p_{91}p_{92}}{2}\left[\chi\left(|\mathbf{A}z|^{p_{91}}, |b|^{p_{91}}\right)\right]^{p_{92}-1}$$
$$\mathrm{diag}\left(\frac{|b|^{p_{91},\mathrm{T}}}{\left\||\mathbf{A}z|^{p_{91}}\right\|_2\left\||b|^{p_{91}}\right\|_2} - \frac{|\mathbf{A}z|^{p_{91},\mathrm{T}}\,|b|^{p_{91}}\,|\mathbf{A}z|^{p_{91},\mathrm{T}}}{\left\||\mathbf{A}z|^{p_{91}}\right\|_2^2\left\||b|^{p_{91}}\right\|_2}\right)$$
$$\mathrm{diag}\left(|\mathbf{A}z|^{p_{91}-2}\circ\overline{\mathbf{A}z}\right)\mathbf{A} \tag{5.68}$$

$$\left(\frac{\partial \mathcal{A}_9\left(z\right)}{\partial z}\right)^{\mathrm{H}} = -\frac{p_{91}p_{92}}{2}\left[\chi\left(|\mathbf{A}z|^{p_{91}}, |b|^{p_{91}}\right)\right]^{p_{92}-1}$$
$$\mathbf{A}^{\mathrm{H}}\mathrm{diag}\left(|\mathbf{A}z|^{p_{91}-2}\circ\mathbf{A}z\right)$$
$$\mathrm{diag}\left(\frac{|b|^{p_{91}}}{\left\||\mathbf{A}z|^{p_{91}}\right\|_2\left\||b|^{p_{91}}\right\|_2} - \frac{|\mathbf{A}z|^{p_{91},\mathrm{T}}\,|b|^{p_{91}}\,|\mathbf{A}z|^{p_{91}}}{\left\||\mathbf{A}z|^{p_{91}}\right\|_2^2\left\||b|^{p_{91}}\right\|_2}\right) \tag{5.69}$$

$$\frac{\partial \overline{\mathcal{A}_9\left(z\right)}}{\partial z} = \overline{\frac{\partial \mathcal{A}_9\left(z\right)}{\partial z}} \tag{5.70} \qquad\qquad \left(\frac{\partial \overline{\mathcal{A}_9\left(z\right)}}{\partial z}\right)^{\mathrm{H}} = \overline{\left(\frac{\partial \mathcal{A}_9\left(z\right)}{\partial z}\right)^{\mathrm{H}}}. \tag{5.71}$$

A brief comparison of the scale-invariant formulation with the presented cosine-similarity formulation has been conducted for complex-valued normally distributed data and that stemming from the fields of a spherical multipole expansion sampled almost uniformly on a sphere with radius of $\lambda$. All solvers started from an initial guess computed via the optimal spectral method and at most performed $k_{\mathrm{max}} = 5 \times 10^3$ iterations. Here, $n = 10$ was considered and success was declared once $\epsilon_{c,\mathrm{dB}}\left(\mathbf{A}z, b\right) \leq -45\,\mathrm{dB}$ was obtained. The results are depicted in Fig. 5.13. For the cosine-similarity formulation, the parameter $p_{91} \in \{1, 2\}$ was chosen to either lead to a minimization in the magnitudes or the squared magnitudes. The remaining parameter, $p_{92}$, was set to unity.

When comparing the minimization in terms of magnitudes or squared magnitudes, both formulations are observed to perform similarly. This seems to confirm the observations made previously, where approaches working with the squared magnitudes have lead to a larger success rate compared to their counterparts working with the non-differentiable magnitude signals.

**Concluding Remarks — Cosine-Similarity Maximization** Motivated in the search for the optimal step length and descent direction when starting from a zero initial guess, the operator $\mathcal{A}_9$ was found. At its core, the cosine similarity is evaluated, rendering this formulation scale-invariant with respect to the unknown source coefficients — as it was the case with $\mathcal{A}_2$. Overall, the performance, the computational effort and the implementational complexity are seen to be on a similar level as that of $\mathcal{A}_2$.
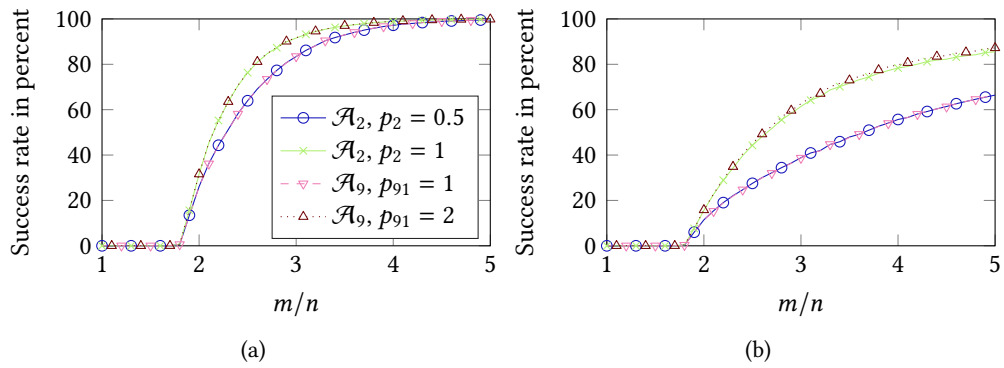
Fig. 5.13 Comparison of phase retrieval formulation based on $\mathcal{A}_9$ with that of $\mathcal{A}_2$. In all cases, $p_{92} = 1$ was set. In (a) and (b), the achievable success rate for $n = 10$ with complex-valued normally distributed data and NF data stemming from a spherical multipole expansion, respectively, is depicted. For each value of $m/n$, $5 \times 10^4$ repetitions have been run, where the algorithms have been started from an initial guess computed via the optimal spectral method. Success is declared, once $\epsilon_{c,\mathrm{dB}}(\mathbf{A}z, \mathbf{b}) \leq -45\,\mathrm{dB}$ is achieved.

## 5.5 Convex Phaseless Solvers

Aside the manifold of nonconvex phase retrieval algorithms, there exists a significantly smaller number of convex phase retrieval formulations. Among the most widely known algorithms, there are Phaselift [Candès et al. 2013], PhaseCut [Waldspurger et al. 2015] and PhaseMax [Goldstein and Studer 2018]. The basic idea of the latter seems to have been developed in parallel also by [Bahmani and Romberg 2017]. Note that there exist approaches trying to convexify nonconvex optimization problems, e.g., numerical continuation [Boykov et al. 2001; Fadili et al. 2004; Mobahi and Fisher III 2015; Trzasko and Manduca 2009; Xiao and Zhang 2012] or majorization-minimization [Qiu et al. 2016; Qiu and Palomar 2017; Sun et al. 2016], which, for the sake of brevity, will not be discussed here.

Despite their favorable convergence properties, convex algorithms have not been widely applied to phaseless problems in electromagnetics. Commonly, it is emphasized that PhaseLift and PhaseCut work with unknowns in the "lifted" problem space, requiring a drastic increase in computational effort and often also memory storage. Still and to name just a few examples, they have been employed for antenna diagnostics from phaseless FF measurements [Fuchs and Le Coq 2015], phaseless NFFFTs [Moretta and Pierri 2019; Paulus et al. 2017c] and X-ray crystallography [Candès et al. 2015a]. It is noteworthy that there exist approaches to work with first-order methods for the implementation of PhaseLift and PhaseCut [Frank and Wolfe 1956; Jaggi 2013; Odor et al. 2016; Yurtsever et al. 2015], potentially making these convex approaches applicable to large sized problems. Somehow differently, PhaseMax does not rely on a semidefinite relaxation and thus does not "lift" the problem dimensions. Instead, PhaseMax can be implemented via a basis pursuit [Boyd and Vandenberghe 2018; Chen et al. 2001; Foucart and Rauhut 2013], which should result in a more favorable computational complexity and memory requirements when compared to PhaseLift and PhaseCut.

So are these convex formulations the solution for phaseless NFFFTs that we are looking for? Do they allow us to reliably retrieve the phase of NF measurement data acquired via realistic

and feasible measurement setups? Before presenting results and allowing the reader to find an answer to this question on his/her own, the theoretical basis of the three convex methods is briefly summarized.

### 5.5.1 PhaseLift

Historically, PhaseLift [Candès et al. 2013] was the first convex phase retrieval algorithm to be reported and which is based on the principles of semidefinite programming. At its core, the phase retrieval problem is rewritten with bilinear forms [Cooperstein 2016; Milnor and Husemoller 1973; Shafarevich and Remizov 2013] and a semidefinite relaxation is applied.

We start by writing the phase retrieval task in the form of

$$|\boldsymbol{b}|^2 = |\mathbf{A}\boldsymbol{z}|^2 = \left| \begin{bmatrix} \boldsymbol{a}_1 & \dots & \boldsymbol{a}_m \end{bmatrix}^{\mathrm{T}} \boldsymbol{z} \right|^2 \tag{5.72}$$

with the rows of the forward operator $\boldsymbol{a}_i^{\mathrm{T}} \in \mathbb{C}^{1 \times n}$. Based on the bilinear form of the unknown vector, one can find

$$|[\boldsymbol{b}]_i|^2 = \boldsymbol{a}_i^{\mathrm{H}} \underbrace{\left( \boldsymbol{z}\boldsymbol{z}^{\mathrm{H}} \right)}_{\mathbf{Z} \in \mathbb{C}^{n \times n}} \boldsymbol{a}_i, \qquad i \in \{1, \dots, m\} . \tag{5.73}$$

The fundamental observation in (5.73) is that the magnitude of the measurement is nonlinear in the unknown vector $\boldsymbol{z}$, but is *linear* in the unknown, Hermitian matrix $\mathbf{Z}$ of rank one. So when writing

$$|\boldsymbol{b}|^2 = \mathscr{A}_{\mathrm{PL}}(\mathbf{Z}) = \begin{bmatrix} \boldsymbol{a}_1^{\mathrm{H}} \mathbf{Z} \boldsymbol{a}_1 \\ \vdots \\ \boldsymbol{a}_m^{\mathrm{H}} \mathbf{Z} \boldsymbol{a}_m \end{bmatrix}, \tag{5.74}$$

one can state the phase retrieval as the optimization problem

$$\begin{aligned} \min_{\mathbf{Z} \in \mathbb{C}^{n \times n}} \quad & \mathrm{rank}(\mathbf{Z}) \\ \text{s.t.} \quad & \mathscr{A}_{\mathrm{PL}}(\mathbf{Z}) = |\boldsymbol{b}|^2 \\ & \mathbf{Z} \succeq 0. \end{aligned} \tag{5.75}$$

Here, $\mathbf{Z} \succeq 0$ symbolizes that $\mathbf{Z}$ is positive semidefinite. By construction, it is known that there exists a solution to (5.75) with a rank of one. Since rank minimization is known to be an NP-hard problem, the rank is approximated by a trace-norm relaxation, resulting in the convex phase retrieval formulation

$$\begin{aligned} \min_{\mathbf{Z} \in \mathbb{C}^{n \times n}} \quad & \mathrm{Tr}(\mathbf{Z}) \\ \text{s.t.} \quad & \mathscr{A}_{\mathrm{PL}}(\mathbf{Z}) = |\boldsymbol{b}|^2 \\ & \mathbf{Z} \succeq 0, \end{aligned} \tag{5.76}$$

also called *PhaseLift*. The solution space is "lifted" as the unknowns now are bilinear forms of the original vector of unknowns.

## 5.5.2 PhaseCut

Closely following the line of thought in [Fuchs and Le Coq 2015] and [Waldspurger et al. 2015], a semidefinite relaxation can be utilized in order to rewrite (5.1) as a convex semidefinite optimization problem. This is done by first introducing unknown phases $\boldsymbol{u}$ which fulfill

$$\mathbf{A}\boldsymbol{z} = \operatorname{diag}\left(|\boldsymbol{b}|\right)\boldsymbol{u} \tag{5.77}$$

where

$$\boldsymbol{u} \in \mathbb{C}^{m \times 1}, \quad |[\boldsymbol{u}]_i| = 1. \tag{5.78}$$

The problem in (5.1) can then be rewritten as

$$\min_{\substack{\boldsymbol{z} \in \mathbb{C}^{n \times 1} \\ \boldsymbol{u} \in \mathbb{C}^{m \times 1}, |[\boldsymbol{u}]_i|=1}} \left\|\mathbf{A}\boldsymbol{z} - \operatorname{diag}\left(|\boldsymbol{b}|\right)\boldsymbol{u}\right\|^2. \tag{5.79}$$

Once a $\boldsymbol{u}$ has been found, $\boldsymbol{z}$ is obtained as the solution of a linear system of equations

$$\boldsymbol{z} = \mathbf{A}^{-1}\operatorname{diag}\left(|\boldsymbol{b}|\right)\boldsymbol{u}. \tag{5.80}$$

Combining (5.79) and (5.80) yields

$$\min_{\boldsymbol{u} \in \mathbb{C}^{m \times 1}, |[\boldsymbol{u}]_i|=1} \left\|\mathbf{A}\mathbf{A}^{-1}\operatorname{diag}\left(|\boldsymbol{b}|\right)\boldsymbol{u} - \operatorname{diag}\left(|\boldsymbol{b}|\right)\boldsymbol{u}\right\|^2 \tag{5.81}$$

which is an optimization in $m$ complex-valued unknowns. The idea of semidefinite programming is to rewrite (5.81) in a way that it leads to a linear dependency on an unknown matrix instead of a nonlinear dependence on the vector $\boldsymbol{u}$. Starting with

$$\left\|\mathbf{A}\mathbf{A}^{-1}\operatorname{diag}\left(|\boldsymbol{b}|\right)\boldsymbol{u} - \operatorname{diag}\left(|\boldsymbol{b}|\right)\boldsymbol{u}\right\|^2 = \boldsymbol{u}^{\mathrm{H}}\mathbf{M}\boldsymbol{u} \tag{5.82}$$

where

$$\mathbf{M} = \operatorname{diag}\left(|\boldsymbol{b}|\right)\left(\mathbf{I} - \mathbf{A}\mathbf{A}^{-1}\right)\operatorname{diag}\left(|\boldsymbol{b}|\right) \tag{5.83}$$

is a positive definite Hermitian matrix obtained by using the identity

$$\left(\mathbf{A}\mathbf{A}^{-1} - \mathbf{I}\right)^{\mathrm{H}}\left(\mathbf{A}\mathbf{A}^{-1} - \mathbf{I}\right) = \left(\mathbf{I} - \mathbf{A}\mathbf{A}^{-1}\right), \tag{5.84}$$

one can construct the Hermitian rank-one matrix

$$\mathbf{U} = \boldsymbol{u}\boldsymbol{u}^{\mathrm{H}} \tag{5.85}$$

resulting in $\boldsymbol{u}^{\mathrm{H}}\mathbf{M}\boldsymbol{u} = \mathrm{Tr}(\mathbf{M}\mathbf{U})$. The minimization of (5.81) can thus be written as

$$
\begin{aligned}
\min_{\mathbf{U}\in\mathbb{C}^{m\times m}} \quad & \mathrm{Tr}\,(\mathbf{M}\mathbf{U}) \\
\text{s.t.} \quad & \mathrm{diag}\,(\mathbf{U}) = \mathbf{1} \\
& \mathbf{U} \succeq 0 \\
& \mathrm{rank}\,(\mathbf{U}) = 1.
\end{aligned}
\tag{5.86}
$$

Since the rank-one matrix constraint is nonconvex [Fuchs and Le Coq 2015], one can obtain a convex relaxation as

$$
\begin{aligned}
\min_{\mathbf{U}\in\mathbb{C}^{m\times m}} \quad & \mathrm{Tr}\,(\mathbf{M}\mathbf{U}) \\
\text{s.t.} \quad & \mathrm{diag}\,(\mathbf{U}) = \mathbf{1} \\
& \mathbf{U} \succeq 0
\end{aligned}
\tag{5.87}
$$

where the solution will only be an approximation. As $\mathbf{U}$ is no longer of rank one, the reconstructed phase vector $\boldsymbol{u}$ is chosen as the eigenvector of $\mathbf{U}$ corresponding to the eigenvalue with the largest magnitude. Finally, one obtains an approximation of the unknown equivalent AUT representation from (5.80).

An imperfect realization of PhaseCut in terms of the optimization framework of this thesis is presented in Appendix A.7.

### 5.5.3 PhaseMax

The convex phase retrieval formulation *PhaseMax* has been proposed in [Goldstein and Studer 2018]. Different to other convex formulations, the problem is not linearized by a "lifting" procedure, instead, only the magnitude restriction is relaxed. The basic formulation is rather intuitive, when looking at the cosine similarity, e.g., defined in (5.8). PhaseMax looks for a vector that is as collinear as possible to a vector assumed to be very close to the true solution, while enforcing a convex condition on the resulting measurement magnitudes. Given the approximate solution vector $\boldsymbol{z}_{\mathrm{PM}}$, also called *anchor* vector in [Bahmani and Romberg 2017], the phase retrieval is written as the optimization problem

$$
\begin{aligned}
\max_{\boldsymbol{z}\in\mathbb{C}^{n\times 1}} \quad & \mathrm{Re}\,\left\{\boldsymbol{z}_{\mathrm{PM}}^{\mathrm{H}}\boldsymbol{z}\right\} \\
\text{s.t.} \quad & |\mathbf{A}\boldsymbol{z}| \leq |\boldsymbol{b}|\,.
\end{aligned}
\tag{5.88}
$$

According to [Goldstein and Studer 2018], this task can be rewritten as a basis pursuit problem [Boyd and Vandenberghe 2018; Chen et al. 2001; Foucart and Rauhut 2013]

$$
\begin{aligned}
\min_{\boldsymbol{z}\in\mathbb{C}^{m\times 1}} \quad & \|\boldsymbol{z}\|_1 \\
\text{s.t.} \quad & \boldsymbol{z}_{\mathrm{PM}} = \mathbf{A}^{\mathrm{H}}\mathrm{diag}(|\boldsymbol{b}|)^{-1}\boldsymbol{z}.
\end{aligned}
\tag{5.89}
$$

A rudimentary implementation of (5.89) via the optimization framework is discussed in Appendix A.8. One of the main results in [Goldstein and Studer 2018] is that PhaseMax is able to determine the correct solution with a linear sampling complexity $O(n)$, however, assuming

that the cosine similarity between the anchor vector and the true solution does not depend on the problem dimension. This may or may not hold true when picking the anchor vector by means of the procedures discussed in Section 5.3. As a reminder, refer to Fig. 5.3 for the achievable cosine similarity depending on the problem dimension for random and NF data.

### 5.5.4 Numerical Results

After having reviewed the basics of the convex formulations, there performance is to be evaluated empirically. Similar to the procedure used for the presented nonconvex techniques, random data is considered first. For the three algorithms there are convergence proofs based on random data which is why a similar behavior as for the non-convex solvers is expected. For all presented results, the implementation of PhaseCut is based on the code provided by the authors of PhaseCut in [Waldspurger et al. 2015], which is based on a procedure provided in [Helmberg et al. 1996] for an interior-point method. The PhaseLift and PhaseMax solvers are called via the Phasepack library [Chandra et al. 2019, 2017], which internally calls the FASTA solver [Goldstein et al. 2014] for the underlying convex problems.

#### Gaussian Data

The performance of the three convex phase retrieval algorithms PhaseLift, PhaseCut and PhaseMax for complex-valued normally distributed data is depicted in Fig. 5.14. Results for the scale-invariant, nonconvex method with $\mathcal{A}_2$ were added for reasons of comparability. The problem dimension is fixed to $n = 10$ and various sampling ratios have been tested. All solvers at most ran $5 \times 10^3$ iterations, starting from an initial guess computed via the optimal spectral method in (5.4). For each value of $m/n$, $1 \times 10^3$ repetitions were conducted. For PhaseMax, the initial guess was used as the anchor vector. As expected, all solvers are able to perform an accurate phase reconstruction once the number of measurements is sufficiently large. Based on the implementations at hand, PhaseCut seems to have the best performance in terms of the required number of measurements, however, also features the largest computational effort. In contrast, PhaseMax allows for a faster reconstruction, which is reliable when more than twice the number of measurements needed by PhaseCut are available. Here, PhaseLift is seen to be some kind of compromise between runtime and sampling effort. It should be kept in mind that PhaseCut is based on unknowns in the observation domain, causing the steep increase in computation time with larger $m/n$. In a similar way, it is expected that PhaseLift requires more computational effort when $n$ is increased. Since $m/n$ is always required to be larger than one, the computational effort and memory requirements of PhaseCut are expected to exceed that of PhaseLift for the same problem.

#### Near-Field Antenna Data — Quasi-Yagi Antenna

We continue our performance evaluation with a simple example of a synthetic NF antenna measurement setup. A typical spherical NF measurement is realized in terms of simulations of a planar quasi-Yagi-Uda antenna [Kaneda et al. 2002; Qian et al. 1999] in the CST Studio Suite [3DS Simulia 2019]. At 10 GHz, the AUT fits into a minimum sphere with a radius of approximately $0.83\lambda$ and the tangential electric field is sampled on a spherical surface with a radius of $2\lambda$, centered around the AUT. A CAD model of the simulation setup is depicted in Fig. 5.15(a), where the measurement surface is depicted in form of a gray sphere enclosing the AUT. For the purpose of illustration, the sphere is cut open, revealing the AUT inside. In order to equally distribute the measurement
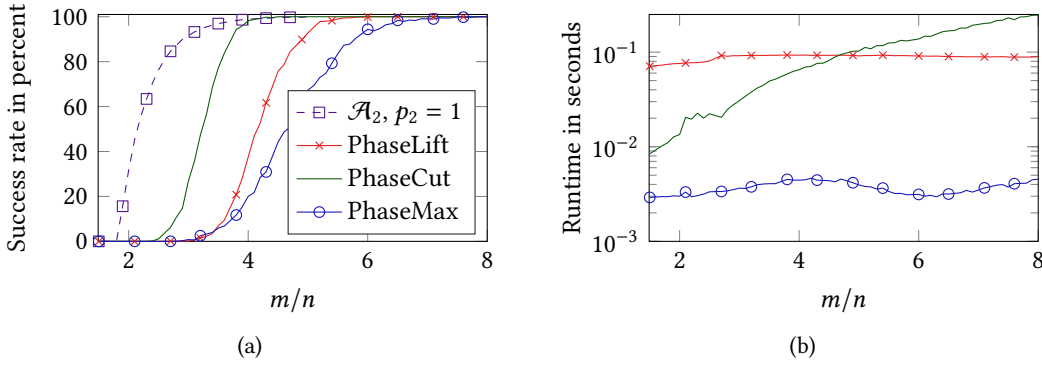
Fig. 5.14 Performance of convex phase retrieval algorithms for complex-valued random Gaussian distributed data for $n = 10$ and various sampling ratios $m/n$. (a) The success rate ($\epsilon_{c,\mathrm{dB}} \leq -45\,\mathrm{dB}$). (b) The average run time of the algorithms.

samples on the spherical surface, a Fibonacci mapping [Keinert et al. 2015] was employed. In total $m = 1 \times 10^4$ measurements and $n = 2 \times 10^3$ unknown electric and magnetic dipoles were utilized for modeling the problem. Despite the relatively large oversampling of $m/n = 5$, the measurement setup can be called "naive" or rather unsuitable for a phaseless transformation. No additional effort has been made to compensate for the lack of phase information, e.g., by sampling on multiple surfaces, with special probe antennas or combining broadband data. Except for the increased number of measurement samples, this simple synthetic example represents a typical NF measurement setup when full phase information is available. Ideally, we would like to have a phase retrieval algorithm which can accurately and reliably reconstruct the phase information from that minimalistic measurement.

The obtainable NF deviation of PhaseLift, PhaseMax and the nonconvex solver in (5.30) for NF data of the quasi-Yagi antenna is depicted in Fig. 5.15(b). The implementation of PhaseCut based on the interior-point method is excluded from the investigations as the required computational resources (time and memory) were considered to be too large. The remaining algorithms were allowed to perform at most $5 \times 10^3$ iterations and were started from an initial guess generated via the optimal spectral method. Out of the maximum number of $1 \times 10^4$ measurements, a varying number of samples were randomly picked, such that a range of $m/n \in [2, 5]$ could be investigated. The NF deviation was computed with respect to all $m = 1 \times 10^4$ measurement entries. As a reference, the NF deviation for a transformation with full phase information was added. It can be seen that the chosen AUT model can reproduce the NF data generated by CST up to a level of approximately $-59\,\mathrm{dB}$, a value that is mainly limited by the accuracy of the simulation model in CST. Non of the investigated phase retrieval methods comes close to the result of the transformation with phase knowledge, even for a decently large oversampling ratio of $m/n = 5$. The information contained in the provided magnitudes simply is insufficient. Solely a slight advantage of the nonconvex solver compared to the convex ones can be observed.

This leads us to a *rather general and preliminary conclusion*. The convexity of certain phase retrieval algorithms can not compensate for the potential lack of information in measurement data. In fact, convexity is often achieved at the expense of dropping nonconvex restrictions. In the regime where it is unclear whether or not the measurement data contains a sufficient amount of
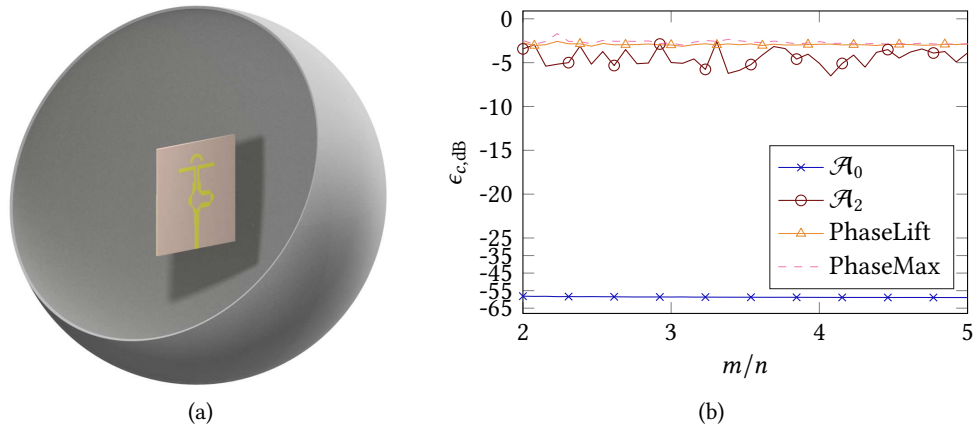
Fig. 5.15 (a) Geometry of a planar quasi-Yagi-Uda antenna [Kaneda et al. 2002; Qian et al. 1999], including the spherical measurement surface indicated by the gray sphere. For illustration purposes, part of the measurement sphere is cut away in order to reveal the AUT inside. The achievable NF deviation of a nonconvex and two convex phase retrieval algorithms in comparison of a fully coherent transformation is shown in (b).

information, these constraints can potentially allow nonconvex methods to obtain more accurate results than their convex alternatives.

Towards the application to phaseless field transformations, we can make a significant statement: Common NF antenna measurement setups provide magnitude data that is inappropriate for the task of phase retrieval. Solely increasing the sampling density does not solve the problem. Neither convex, nor nonconvex algorithms can perform an accurate and reliable phase reconstruction from the data provided by these measurements. Consequently, the main difficulty related to phaseless NFFFTs is not equivalent to picking the best existing phase retrieval algorithm. Instead, the real question to be asked is how to obtain phaseless data that allows a — possibly any — phase retrieval algorithm to perform well, just as most of them do for random normally distributed data.

**Near-Field Antenna Data — Horn Antenna Array**

Continuing with more relevant phaseless data, the $4 \times 4$ array consisting of horn antennas depicted in Fig. 5.16(a) is considered. At the operating frequency, only the fundamental waveguide mode is relevant and employed. All array elements colored in red are excited with a coefficient of one, only the antenna in blue color and green color have coefficients of 0.5 and $-1$, respectively. The antenna array was simulated in Feko and NF data of two orthogonal polarizations on two planes, indicated by black lines in Fig. 5.16(b), at distances of $2.9\lambda$ and $4.9\lambda$ was recorded. Within the NFFFT, the AUT was modeled by $n = 795$ Hertzian dipoles placed on a box closely confined to the antenna array, where the bottom surface of the box was removed (at the feed region of the horn antennas). The resulting equivalent model is thus well suited to describe the radiation of the horn array in direction of the main beam and the sides, while featuring a slightly reduced number of unknowns compared to using a fully closed Huygens surface. Keeping the number of unknowns at a minimum is especially important in case of the convex solvers based on lifting, as their computational effort increases drastically with larger problem dimensions. All solvers were allowed to perform at most

$5 \times 10^3$ iterations and were started from an initial guess computed via the optimal spectral method. The obtained NF deviations are depicted in Fig. 5.16(c), also including a fully coherent solver and the scale-invariant, nonconvex solver with $p_2 = 0.5$. Out of the $3 \times 10^4$ available probe samples, a certain portion was randomly picked, resulting in various oversampling values $m/n$. The NF deviation was computed with respect to all $m = 3 \times 10^4$ samples. Based on the performance of the solver with full phase information, one can conclude that the equivalent model can approximate the NF data from Feko up to around $-65$ dB, a value that is by far not achieved by any of the phaseless solvers. While the nonconvex solver of (5.30), in agreement with its nonconvexity, sporadically converges to a stationary point of decent accuracy, the convex solvers perform badly. For PhaseLift, a trend towards decreasing NF deviations for larger $m/n$ is visible, which can not be observed for PhaseMax in case of the considered oversampling values. In total, these results are unsatisfying, as the only potentially reliable algorithms (the convex ones) are not able to exploit the provided field variations between the two measurement surfaces and to retrieve the true phase distribution with sufficient accuracy. The varying performance of the nonconvex solver is caused by stagnation at local stationary points. The convergence is highly dependent on the initial guess as well as the different weighting of "information" in the measurement data. Both, the starting point and the weighting of the data may still differ for large ratios of $m/n$, while the overall restrictions implied by the acquired fields do not.

As a point of interest, the field distribution caused by the equivalent sources of the horn antenna array in a plane slightly above the apertures is depicted in Fig. 5.17. The results have been obtained when utilizing a ratio of $m/n \approx 12.6$ for the transformation with full phase information and for the nonconvex solver. The corresponding NF deviations are $\epsilon_{c,\text{dB}} \approx -62$ dB and $\epsilon_{c,\text{dB}} \approx -21$ dB, respectively. For the nonconvex solver, this corresponds to one of the better attempts, however, can not be interpreted as its typical performance. For completeness, the result obtainable with PhaseLift and $m/n = 20$ is shown. In the left and right columns of Fig. 5.17, the magnitude and phase of the dominant electric field component is drawn. The dashed boxes indicate the locations of the antenna apertures, where the green and blue rectangles mark the elements with 180° phase shift and with only half the excitation coefficient, respectively. Looking at the phase distribution, the phase shifted element can clearly be identified from the results of the solver with full phase and the nonconvex phaseless approach. For both solvers, there are slight variations in the magnitude of the field near the element with reduced excitation strength. Still, a clear detection of a "faulty" element can not be made. With a large NF deviation of approximately $-2.5$ dB, the result by PhaseLift does not allow for any kind of antenna diagnostics.

The resulting FF radiation behavior of the three results is shown in Fig. 5.18. Due to the truncated nature of the measurement setup, only the radiation within a limited angular range can be predicted by the equivalent sources. Here, only the dominant electric field component in the plane of $\varphi = 0°$ is drawn and the deviation with respect to the true FF obtained with a simulation in Feko is given. Overall, the FF discrepancies are proportional to the stated NF deviations, where the transformation with full phase performs best, followed by the nonconvex formulation. The result for PhaseLift does not provide meaningful information in the FF.

**Concluding Remarks — Convex Phase Retrieval**  Opposed to the abundance of nonconvex phase retrieval approaches, there exist only a few convex alternatives. Inherent to convexity, they do not suffer from the occurrence of local stationary points and are resistant to improper initial guesses, which are two severe issues of nonconvex methods and initialization techniques

when going to large-sized problems. In all cases, convexity is achieved at the cost of loosening restrictions and, thus, dropping *information* about the phases. Sometimes this involves "lifting" the problem dimensions, which increases the computational effort drastically. Consequently, the convex techniques can not be expected to exhibit best performance for small numbers of measurements and may be limited in their utilization for large tasks. However, in the regime where a decent amount of information is contained in the measured magnitudes — not enough to prevent the nonconvex solvers from getting stuck in local stationary points — convex techniques may be worth a try, even if they are just used to generate a more appropriate initial guess for their nonconvex colleagues. From the numerical examples presented here, no practical advantage of the convex methods on the nonconvex alternatives was visible for NF antenna data. The two convex techniques PhaseLift and PhaseMax will be briefly tested for a modified type of field data later on in Chapter 6.

(a)



(b)



(c)
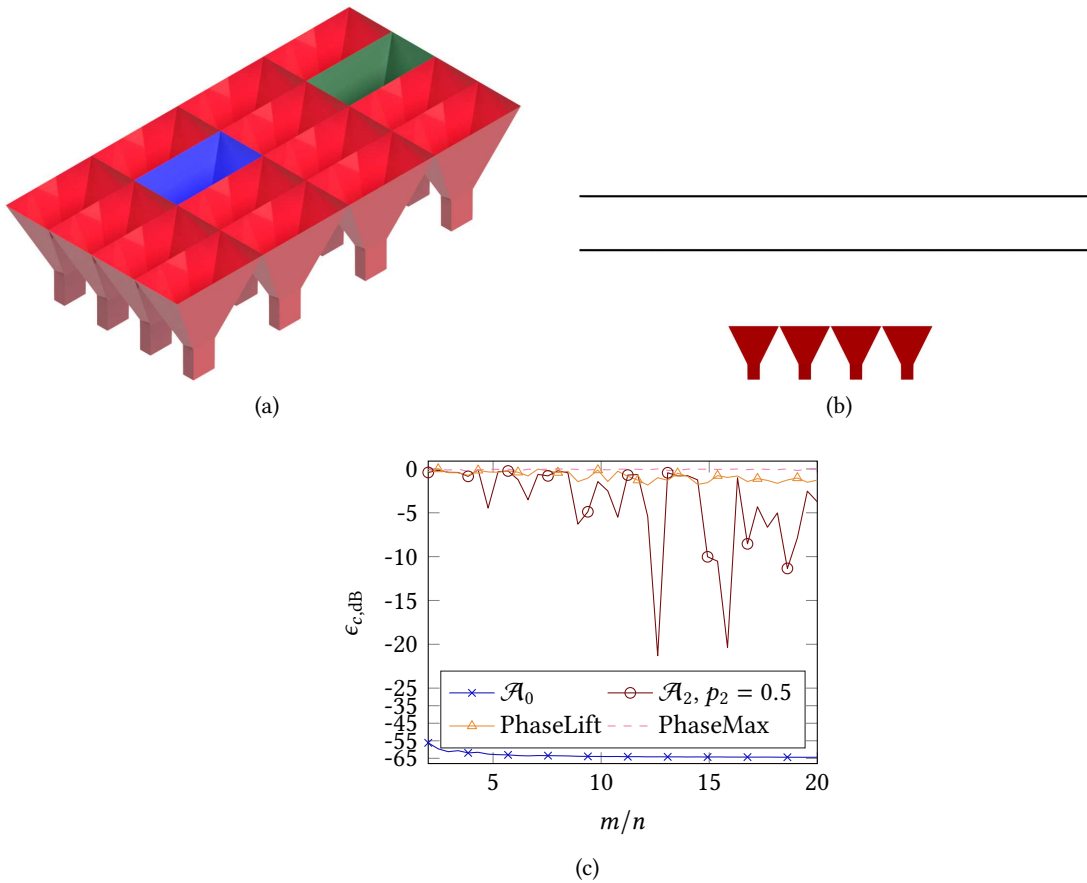
Fig. 5.16 (a) The geometry of a synthetic horn antenna array. The antenna marked in blue is excited with only half of value of the excitation coefficients of the red antennas. The antenna in green exhibits a phase shift of $180°$ with respect to the red antennas. NF samples are acquired on two planes in front of the aperture, indicated by the black lines in (b). (c) The obtained NF deviation for various phase retrieval algorithms and dependent on the oversampling ratio. The measurements have been randomly picked on the two measurement planes and the NF deviation is computed with respect to all $m = 3 \times 10^4$ probe signals. For the transformations, $n = 795$ Hertzian dipoles as unknowns were utilized.
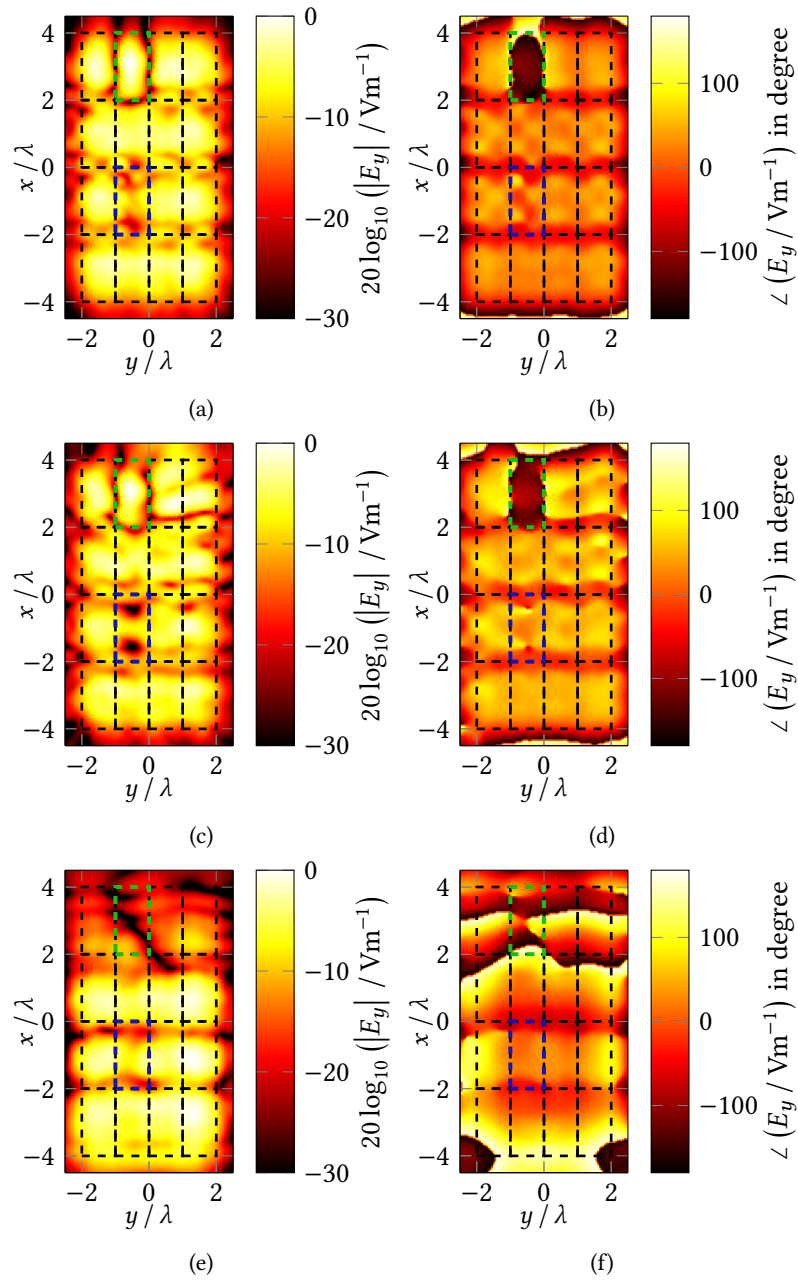
Fig. 5.17 Magnitude (left column) and phase (right column) of the dominant electric field component radiated by the reconstructed sources. The field is evaluated on a plane slightly above the aperture of the horn array. Dashed black lines indicate the location of the antenna apertures. The results in (a) and (b) were obtained via (4.4) assuming full phase information and $m/n \approx 12.6$, (c) and (d) via the nonconvex phaseless solver (5.30) with $m/n \approx 12.6$ and (e) and (f) via the convex formulation PhaseLift in (5.76) for $m/n = 20$. The NF deviations with respect to the fields in Feko read as $\epsilon_{c,\mathrm{dB}} \approx -62\,\mathrm{dB}$, $\epsilon_{c,\mathrm{dB}} \approx -21\,\mathrm{dB}$ and $\epsilon_{c,\mathrm{dB}} \approx -2.5\,\mathrm{dB}$, respectively.
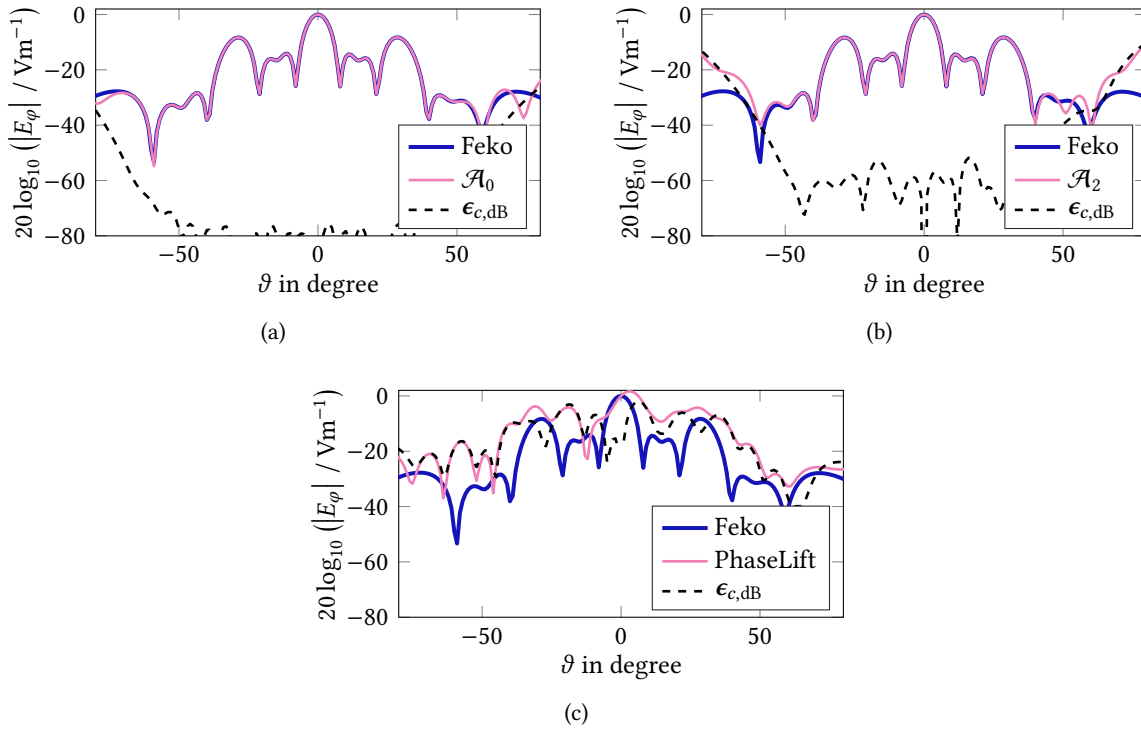
Fig. 5.18 Comparison of the reconstructed FF of the horn antenna array with true radiation characteristic obtained in Feko. Depicted is the dominant electric field component in the plane with $\varphi = 0°$. Due to the planar measurement setup, the valid region of the reconstructed fields is limited. (a) The transformation result when full phase information is available. (b) Transformation result with the nonconvex formulation in (5.30) with $p_2 = 0.5$, for $m/n \approx 12.6$. The result in (c) was computed with PhaseLift for $m/n = 20$. The corresponding NF deviations with respect to Feko read as $\epsilon_{c,\mathrm{dB}} \approx -62\,\mathrm{dB}$, $\epsilon_{c,\mathrm{dB}} \approx -21\,\mathrm{dB}$ and $\epsilon_{c,\mathrm{dB}} \approx -2.5\,\mathrm{dB}$, respectively.

## 5.6 Exact and Direct Phase Retrieval

Aside the plethora of phase retrieval algorithms relying on optimization, there exists an optimization-free and exact phase retrieval technique. Most of the theory of this chapter has been reported in [Knapp et al. 2019b] and, from another point of view and with different notation, has been discussed in [Balan et al. 2009]. At its core, the phase retrieval problem is rewritten with bilinear forms, which allow for a linear representation of previously nonlinear terms. The downside of using bilinear forms is the direct increase in the problem dimensions. The resulting computational effort is comparable to that observed with certain iterative convex phase retrieval algorithms [Candès et al. 2013; Waldspurger et al. 2015], which themselves rely on bilinear forms.

We start by introducing the general idea of the direct phase retrieval and afterwards derive an easy-to-use, trivial-to-implement and insightful formulation.

### 5.6.1 Reconstruction in Bilinear Forms

Consider the retrieval problem denoted in an element-wise fashion as

$$|[\boldsymbol{b}]_k|^2 = \boldsymbol{z}^{\mathrm{H}} \left( \overline{\boldsymbol{a}}_k \boldsymbol{a}_k^{\mathrm{T}} \right) \boldsymbol{z}, \qquad \text{with} \quad \mathbf{A} = \begin{bmatrix} \boldsymbol{a}_1 & \boldsymbol{a}_2 & \dots & \boldsymbol{a}_m \end{bmatrix}^{\mathrm{T}}, \qquad \text{for} \quad k \in \{1, ..., m\} \tag{5.90}$$

where $\boldsymbol{a}_k^{\mathrm{T}} \in \mathbb{C}^{1 \times n}$ is the $k$th row in the measurement matrix $\mathbf{A}$. Consequently, we can form linear combinations (LCs) of the measurements as

$$\alpha_{\mathrm{B}} \,|[\boldsymbol{b}]_k|^2 + \beta_{\mathrm{B}} \,|[\boldsymbol{b}]_l|^2 = \boldsymbol{z}^{\mathrm{H}} \left( \alpha_{\mathrm{B}} \overline{\boldsymbol{a}}_k \boldsymbol{a}_k^{\mathrm{T}} \right) \boldsymbol{z} + \boldsymbol{z}^{\mathrm{H}} \left( \beta_{\mathrm{B}} \overline{\boldsymbol{a}}_l \boldsymbol{a}_l^{\mathrm{T}} \right) \boldsymbol{z}$$

$$= \boldsymbol{z}^{\mathrm{H}} \left( \alpha_{\mathrm{B}} \overline{\boldsymbol{a}}_k \boldsymbol{a}_k^{\mathrm{T}} + \beta_{\mathrm{B}} \overline{\boldsymbol{a}}_l \boldsymbol{a}_l^{\mathrm{T}} \right) \boldsymbol{z} \tag{5.91}$$

for some coefficients $\alpha_{\mathrm{B}}$ and $\beta_{\mathrm{B}}$. Forming arbitrary LCs and collecting the coefficients in $\boldsymbol{\gamma}_b$, we can write

$$\boldsymbol{\gamma}_b^{\mathrm{T}} \,|\boldsymbol{b}|^2 = \boldsymbol{z}^{\mathrm{H}} \underbrace{\left( \mathrm{diag} \left( \boldsymbol{\gamma}_b \right) \sum_{i=1}^{m} \overline{\boldsymbol{a}}_i \boldsymbol{a}_i^{\mathrm{T}} \right)}_{\mathbf{C}_b \in \mathbb{C}^{n \times n}} \boldsymbol{z}. \tag{5.92}$$

Equation (5.92) lays the foundation for a direct solution of the phase retrieval problem. The idea is to construct the matrix $\mathbf{C}_b$, i.e., find the coefficients in $\boldsymbol{\gamma}_b$, such that we can directly compute the magnitude of the coefficients $\boldsymbol{z}$ and all necessary phase differences between the coefficients. Alternatively, one can try to find the coefficients such that the phase differences in the measurement vector can be computed. For the moment, we will follow the first approach and try to reconstruct the magnitude of the solution $\boldsymbol{z}$. We thus need to find the vectors $\boldsymbol{\gamma}_k$ and $\boldsymbol{\gamma}_l$ such that

$$\boldsymbol{\gamma}_k^{\mathrm{T}} \,|\boldsymbol{b}|^2 = \boldsymbol{z}^{\mathrm{H}} \left( \mathbf{C}_k \right) \boldsymbol{z} = |[\boldsymbol{z}]_k|^2 = w_1, \tag{5.93}$$

$$\boldsymbol{\gamma}_l^{\mathrm{T}} \,|\boldsymbol{b}|^2 = \boldsymbol{z}^{\mathrm{H}} \left( \mathbf{C}_l \right) \boldsymbol{z} = |[\boldsymbol{z}]_l|^2 = w_2, \tag{5.94}$$

which is obtained for sparse matrices $\mathbf{C}_{k/l}$ with a single scalar one on the main diagonal in the $k/l$th row. Analogous, we can design the matrix to generate two LCs of two source coefficients via

$$\boldsymbol{\gamma}_u^{\mathrm{T}} |\boldsymbol{b}|^2 = \boldsymbol{z}^{\mathrm{H}} (\mathbf{C}_u) \, \boldsymbol{z} = |[z]_k + [z]_l|^2 = w_3 \tag{5.95}$$

$$\boldsymbol{\gamma}_v^{\mathrm{T}} |\boldsymbol{b}|^2 = \boldsymbol{z}^{\mathrm{H}} (\mathbf{C}_v) \, \boldsymbol{z} = |[z]_k + \mathrm{j}[z]_l|^2 = w_4. \tag{5.96}$$

Combining $w_1$ to $w_4$ via the well known equation

$$\Delta\varphi = \angle([z]_k) - \angle([z]_l) = \mathrm{atan} \left[ \frac{w_4 - w_1 - w_2}{w_3 - w_1 - w_2} \right] \tag{5.97}$$

yields the phase difference $\Delta\varphi$ between the two source coefficients. By forming a chain of phase differences, the complete complex-valued source vector can be reconstructed up to a global phase shift.

With this procedure, we can exactly reconstruct the magnitude and the relative phases of the solution vector $\boldsymbol{z}$. The sampling complexity of this algorithm is $O(n^2)$, since in general we need to construct arbitrary matrices $\mathbf{C}_o \in \mathbb{C}^{n \times n}$ from weighted sums of the outer products of the rows of the forward operator. Only in case these outer products form a complete basis for the space $\mathbb{C}^{n \times n}$, arbitrary matrices can be formed. In total, in the order of $n$ linear systems of equations involving matrices approximately of the size of $\mathbb{C}^{n^2 \times n^2}$ need to be solved. The estimated computational complexity of this method thus is $O(n^5)$. However, the approach is of general validity and could in theory be applied independent of the underlying physical problem. The main drawback is that enough information has to be captured by the $m = O(n^2)$ measurements. Otherwise, a construction of the relevant matrices $\mathbf{C}_o$ may not be possible or inaccurate. Note that the computationally expensive part of the method only needs to be performed once per operator. Whenever the measurement vector changes, phase retrieval can be performed at the expenses of a single matrix-vector product with a worst-case complexity of $O(n^2)$. This is in strong contrast to phase retrieval algorithms based on optimization, as these approaches have to be applied with full complexity every time a new measurement vector $\boldsymbol{b}$ is considered.

With the specific procedure explained above, care has to be taken whenever a phase difference between source coefficients is to be calculated, where one coefficient has zero magnitude. As the phase difference is then not defined, the algorithm may fail. However, once the magnitudes have been computed, a chain of phase differences along nonzero coefficients can be chosen and computed. Further note, as the sampling complexity appears to be $O(n^2)$, it is wise to work with the minimum number of unknowns. In case of field transformation algorithms, a spherical multipole expansion or equivalent currents based on a SVD are thus recommendable.

Now that we have sketched the general idea of the direct phase retrieval method based on bilinear forms, let us investigate the formulation further in order to find an easy-to-use implementation.

## 5.6.2 Implementation of Direct Phase Retrieval

We start by defining our new vector of unknowns

$$\boldsymbol{z} = \begin{bmatrix} [z]_1 & [z]_2 & \dots & [z]_m \end{bmatrix}^{\mathrm{T}} \in \mathbb{C}^{m \times 1}, \tag{5.98}$$

which shall be chosen such that

$$\mathbf{W} = \sum_{i=1}^{m} [z]_i \left( \overline{a}_i a_i^{\mathrm{T}} \right), \tag{5.99}$$

where $\mathbf{W} \in \mathbb{C}^{n \times n}$ is an arbitrary and choosable matrix, in this application featuring a rank of one. We introduce the column-vector notation of the aforementioned matrices with

$$\mathbf{W} = \begin{bmatrix} w_1 & w_2 & \dots & w_n \end{bmatrix} \quad \text{and} \quad \left( \overline{a}_i a_i^{\mathrm{T}} \right) = \begin{bmatrix} v_{i,1} & v_{i,2} & \dots & v_{i,n} \end{bmatrix}, \tag{5.100}$$

where $w_i \in \mathbb{C}^{n \times 1}$, $v_{i,k} \in \mathbb{C}^{n \times 1}$ and, from some simplifications, we can find

$$v_{i,k} = [a_i]_k \, \overline{a_i}. \tag{5.101}$$

We can now vectorize (5.99) by stacking the vectors in larger column vectors and form a larger linear system of equations

$$\hat{w} = \underbrace{\begin{bmatrix} w_1 \\ w_2 \\ \vdots \\ w_n \end{bmatrix}}_{\in \mathbb{C}^{n^2 \times 1}} = \underbrace{\begin{bmatrix} \underbrace{\begin{bmatrix} v_{1,1} \\ v_{1,2} \\ \vdots \\ v_{1,n} \end{bmatrix}}_{q_1} & q_2 & \dots & q_m \end{bmatrix}}_{\mathbf{O} \in \mathbb{C}^{n^2 \times m}} z. \tag{5.102}$$

As $\mathbf{O}$ is not a square matrix, one may resort to solving the normal system of equations

$$\mathbf{O}^{\mathrm{H}} \mathbf{O} z = \mathbf{O}^{\mathrm{H}} \hat{w}. \tag{5.103}$$

Next, we try to simplify the equations further. We start by writing the matrix-matrix product in its explicit form

$$\begin{aligned} \mathbf{O}^{\mathrm{H}} \mathbf{O} &= \begin{bmatrix} a_1^{\mathrm{T}} \overline{[a_1]_1} & \dots & a_1^{\mathrm{T}} \overline{[a_1]_n} \\ \vdots & \ddots & \vdots \\ a_m^{\mathrm{T}} \overline{[a_m]_1} & \dots & a_m^{\mathrm{T}} \overline{[a_m]_n} \end{bmatrix} \begin{bmatrix} \overline{a_1} [a_1]_1 & \dots & \overline{a_m} [a_m]_1 \\ \vdots & \ddots & \vdots \\ \overline{a_1} [a_1]_n & \dots & \overline{a_m} [a_m]_n \end{bmatrix} \\ &= \begin{bmatrix} (a_1^{\mathrm{T}} \overline{a}_1) \overline{(a_1^{\mathrm{T}} \overline{a}_1)} & \dots & (a_1^{\mathrm{T}} \overline{a}_m) \overline{(a_1^{\mathrm{T}} \overline{a}_m)} \\ \vdots & \ddots & \vdots \\ (a_m^{\mathrm{T}} \overline{a}_1) \overline{(a_m^{\mathrm{T}} \overline{a}_1)} & \dots & (a_m^{\mathrm{T}} \overline{a}_m) \overline{(a_m^{\mathrm{T}} \overline{a}_m)} \end{bmatrix} = \left| \mathbf{A} \mathbf{A}^{\mathrm{H}} \right|^2 \in \mathbb{R}^{m \times m}. \end{aligned} \tag{5.104}$$

Note that the resulting matrix only contains real valued entries. Furthermore, the product

$$\mathbf{O}^{\mathrm{H}} \hat{w} = \begin{bmatrix} a_1^{\mathrm{T}} \overline{[a_1]_1} & \dots & a_1^{\mathrm{T}} \overline{[a_1]_n} \\ \vdots & \ddots & \vdots \\ a_m^{\mathrm{T}} \overline{[a_m]_1} & \dots & a_m^{\mathrm{T}} \overline{[a_m]_n} \end{bmatrix} \begin{bmatrix} w_1 \\ \vdots \\ w_n \end{bmatrix} = \begin{bmatrix} (a_1^{\mathrm{T}} \tilde{w}^{\mathrm{H}}) \overline{(a_1^{\mathrm{T}} \tilde{w}^{\mathrm{H}})} \\ \vdots \\ (a_m^{\mathrm{T}} \tilde{w}^{\mathrm{H}}) \overline{(a_m^{\mathrm{T}} \tilde{w}^{\mathrm{H}})} \end{bmatrix} = \left| \mathbf{A} \tilde{w}^{\mathrm{H}} \right|^2. \tag{5.105}$$

can be written in a simplified way, since $\mathbf{W}$ is commonly created as a rank-one matrix according to

$$\mathbf{W} = \tilde{\boldsymbol{w}}^{\mathrm{H}}\tilde{\boldsymbol{w}} = \begin{bmatrix} \tilde{\boldsymbol{w}}^{\mathrm{H}}[\tilde{\boldsymbol{w}}]_1 & \dots & \tilde{\boldsymbol{w}}^{\mathrm{H}}[\tilde{\boldsymbol{w}}]_n \end{bmatrix} = \begin{bmatrix} \boldsymbol{w}_1 & \dots & \boldsymbol{w}_n \end{bmatrix}. \tag{5.106}$$

Keep in mind that $\tilde{\boldsymbol{w}} \in \mathbf{C}^{1 \times n}$ basically represents *a row* of the forward operator, *to which we want to find the measured magnitude.*

Now, assume one wants to know the magnitudes of a collection of theoretically measurable signals

$$\tilde{\boldsymbol{b}} = \begin{bmatrix} [\tilde{\boldsymbol{b}}]_1 & \dots & [\tilde{\boldsymbol{b}}]_q \end{bmatrix}^{\mathrm{T}}, \tag{5.107}$$

which can for example be unknown values of the copolar component in the FF of the AUT. The according measurement rows, e.g., the known rows of a FF radiation operator, are stacked as columns in the matrix

$$\tilde{\mathbf{W}} = \begin{bmatrix} \tilde{\boldsymbol{w}}_1^{\mathrm{T}} & \tilde{\boldsymbol{w}}_2^{\mathrm{T}} & \dots & \tilde{\boldsymbol{w}}_q^{\mathrm{T}} \end{bmatrix}. \tag{5.108}$$

We can find the desired measurement signals via

$$\left| \tilde{\boldsymbol{b}} \right|^2 = \left[ \left( \left| \mathbf{A}\mathbf{A}^{\mathrm{H}} \right|^2 \right)^{-1} \left| \mathbf{A}\overline{\tilde{\mathbf{W}}} \right|^2 \right]^{\mathrm{T}} |\boldsymbol{b}|^2. \tag{5.109}$$

From (5.109) we can see that an exact phase retrieval is possible by solving a linear system of equations. Deriving (5.109) did not require any simplifications or approximations, thus, it represents an exact solution. As mentioned earlier, the major downside of the approach is the required worst-possible sampling complexity of $O(n^2)$, as otherwise no solution to the linear system may exist. At the core of the procedure, the linear system of equations with the matrix $|\mathbf{A}\mathbf{A}^{\mathrm{H}}|^2$ needs to be inverted. This particular matrix plays an essential role in the solution process. Only when it is of *full rank*, which requires $m \geq n^2$, the retrieval process is ensured to be successful. Consequently, $\mathrm{rank}(|\mathbf{A}\mathbf{A}^{\mathrm{H}}|^2)$ can be used as a crucial indicator for how much "information" is available in form of the magnitude measurements [Knapp et al. 2019b]. Here, we will utilize this figure in order to judge the suitability of forward operators and the underlying measurement setups. Even when the full-rank condition is not fulfilled, one can say that the larger the rank of this matrix, the higher the chance that an accurate phase reconstruction will be achieved. Opposite, a low rank indicates an inadequate measurement setup.

A simplistic implementation of the direct phase retrieval is stated in Alg. 13. Pseudo-code in Matlab [Matlab 2021] notation is given, essentially reconstructing the phase differences between the measurements with respect to the first entry in the measurement vector. In order for the algorithm to work, the first entry in the measurement vector has to feature a nonzero magnitude. Reconstruction of the phase differences is based on the interferometric relation in (5.97) and the related LCs.

**Numerical Results for Direct Phase Retrieval**

Figure 5.19(a) illustrates the performance of the direct phase retrieval method for complex-valued normally distributed data. The threshold for a successful transformation was set to a relatively low value of $\epsilon_{c,\mathrm{dB}} \leq -45\,\mathrm{dB}$, which should be the reason that a nonzero rate of success can be observed

---

**Algorithm 13** Exact Phase Retrieval (Matlab Code)

---

**Input:** $A = A$, $b = |\boldsymbol{b}|^2$
**Output:** complex measurement vector $\mathrm{br} = \boldsymbol{b}\mathrm{e}^{\mathrm{j}\varphi_0}$
    *Number of measurements* :
1: `m = size(A,1);`
    *Rows to be constructed* :
2: `W = [A;A(2:end,:)+A(1,:);...`
      `A(2:end,:)+1i*A(1,:)].';`
    **Solve linear systems (core of phase retrieval)** :
3: `bt = ...`
      `((abs(A*A').^2)\(abs(A*conj(W)).^2)).'*b;`
    *Compute phase differences* :
4: `dp = atan2((bt(2*m:end)-bt(1)-bt(2:m)),...`
      `(bt(m+1:2*m-1)-bt(1)-bt(2:m)));`
    *Construct complex signal* :
5: `br = sqrt(bt(1:m)).*exp(1i*[0;dp]);`
6: **return** `br`

---

for $m \leq n^2$ in some cases. For each ratio of $m/n^2$, $5 \times 10^3$ simulations were performed. The direct transformation in the form of that given in Alg. 13 was used. Note that a guaranteed success is observed for $m \geq n^2$ since in the case of Gaussian distributed rows in the forward operator, the information content in the magnitude measurement monotonically increases until the upper limit of $n^2$. In other words, every row added in $\mathbf{A}$ increases the $\mathrm{rank}(|\mathbf{A}\mathbf{A}^{\mathrm{H}}|^2)$ by one. This may not be observed for real-world applications, where additional measurements typically feature a certain degree of redundancy with existing ones.

The relation between the number of measurements and the rank of the relevant matrix for various measurement models is depicted in Fig. 5.19(b), where $n = 20$ was employed. As has been said, the information content (solid lines) for complex-valued normally distributed operators increases directly proportional with the number of measurements until at $m = n^2$ the maximum is reached. In contrast, models of real-world antenna measurements with electromagnetic radiation operators and probe antennas exhibit a saturation effect above certain sampling ratios. Here, the forward operator for NF measurements on a single spherical surface, for two spherical surfaces and with specialized probe antennas is considered. The specific details of the setups are not of interest here — it simply shall be seen that a real measurement setup will cause the rows of the forward operator to exhibit linear dependencies in their corresponding bilinear forms. As a result, adding more samples of the same measurement setup to an existing dense sampling, e.g., more measurement with the same probe antenna at the same measurement distance, will not add more information to the phase retrieval task — visible from the saturation of the rank-curves. In the same plot in Fig. 5.19(b), the success rate (dashed lines) of a phaseless transformation based on the occurring forward operators is depicted. The formulation in (5.16) with $p_1 = 1$ was used for this purpose. For each ratio of $m/n^2$ and the corresponding forward operator, a true solution vector was randomly picked from a complex-valued normal distribution and the resulting measurement vector was computed. Afterwards the phase retrieval problem was solved and declared to be successful
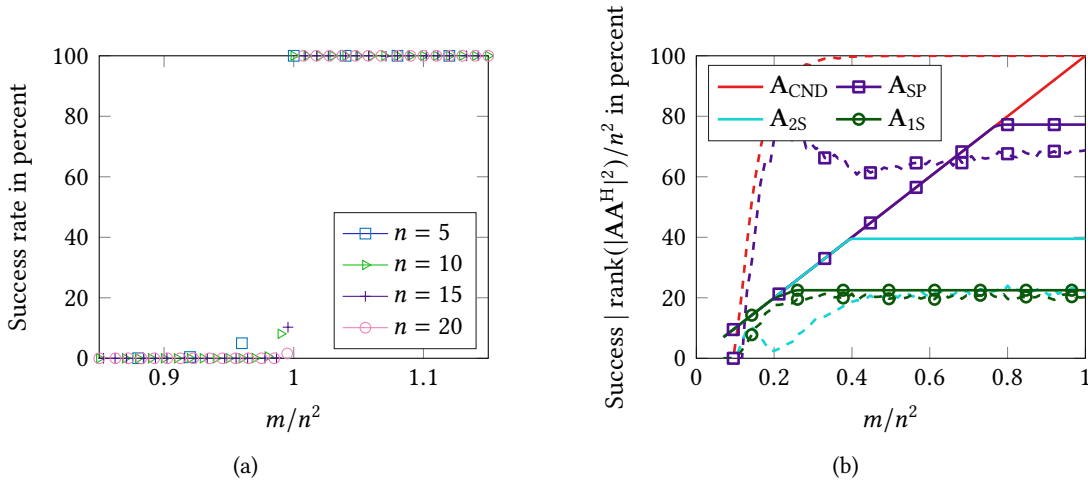
Fig. 5.19 (a) Success rate of the exact phase retrieval method for complex-valued normally distributed data. (b) Percentage of the achieved rank and the success rate of formulation (5.16) for various forward operators. $\mathbf{A}_{\text{CND}}$, $\mathbf{A}_{\text{SP}}$, $\mathbf{A}_{\text{2S}}$ and $\mathbf{A}_{\text{1S}}$ refer to complex-valued normally distributed data, a spherical NF measurement setup with "special" probe antennas on a single surface, a measurement with common probes on spherical surfaces of two different radii and on a single surface, respectively. Solid lines represent the rank while dashed lines refer to the success rate. The number of unknowns was set to $n = 20$. Spherical vector wave functions have been used for constructing the NF matrices.

once a complex NF deviation below $-45\,\text{dB}$ was achieved. For each ratio $m/n^2$, $5 \times 10^3$ solution vectors were considered per model. As can be seen from Fig. 5.19(b), there is a correlation between the success rate of the phase retrieval solver and the information content of the forward operator. As claimed, a larger rank seems to increase the chance of a successful transformation. Nevertheless, there is no simple relationship and the correlation should only be seen as a rule of thumb. Also, adding more measurements is seen to possibly reduce the chance of a successful transformation, probably because of improper weighting of strong and weak probe signal contributions. Note that the condition number of the occurring operators are quite similar throughout various ratios of $m/n^2$. No connection between well- or ill-conditioned matrices and the success rate for phase retrieval is evident from the presented results.

**Concluding Remarks — Exact and Direct Phase Retrieval** An exact and direct solution to the general phase retrieval problem can be computed via the linear formulation in (5.109). The procedure requires $m \geq n^2$ magnitudes to be available and, thus, features the worst-case sampling complexity of $O(n^2)$. The computational effort related to solving the linear system is correspondingly large, mainly due to the fact that $m = n^2 \gg n$ is commonly the case. As a consequence, the presented approach is limited to applications with few unknowns and where plenty of measurements can be conducted, providing enough information such that $\text{rank}(|\mathbf{A}\mathbf{A}^{\text{H}}|^2) = n^2$ is fulfilled. However, even if the condition on the rank is not fulfilled, the rank itself can be used as an indicator for the suitability of measurement setups for the task of phase retrieval. The larger the rank, the better the chances for common phase retrieval algorithms to successfully reconstruct the phase.

# 6. Near-Field Far-Field Transformation with Partially Coherent Observations

Similar to that the world is neither solely black nor solely white, an NFFFT can be performed with measurements that are neither fully coherent nor completely phaseless. This general class between absolute coherence and magnitude-only measurements is here referred to as *partially coherent observations*, meaning that certain "pieces" or "portions" of the measurement data contain reliable phase information in addition to the knowledge of magnitudes. For reasons of completeness, another class of retrieval problems — *magnitude retrieval* — is briefly discussed in Appendix A.9.

Throughout Section 6.1, we will discuss NF antenna measurement setups allowing for the acquisition of partially coherent probe signals. Two relevant measurement scenarios — multi-frequency and multi-channel setups — are identified, both of them requiring additional measurement equipment and the feasibility of the approaches needs to be checked dependent on the specific application. However, at least the multi-channel technique can be regarded as reasonable and of practical relevance in a wide range of phaseless measurement scenarios. After having discussed the measurement setups, Section 6.2 puts the focus on the algorithmic exploitation of partial coherence. Two distinct approaches are introduced, where both methods feature different downsides and benefits, which justify their parallel existence and favoring one or another method for a practical application at hand. More details are provided for the treatment of phase difference information stemming from multi-frequency data. Finally, the formulations and approaches are extensively tested in Section 6.3 for realistic NF antenna data.

## 6.1 Partial Coherence in Antenna Measurements

We have already seen an overview of a typical NF antenna measurement setup in Fig. 4.1(b) and its underlying model in terms of electromagnetic theory in Fig. 4.1(a). In Fig. 6.1, a closer view on the synchronization between the TX and the RX is given and the cases of fully coherent and fully phaseless measurements are repeated. With a direct synchronization between the LO of the TX and the LO of the RX, as depicted in Fig. 6.1(a), a stable phase relation between the transmitted and the received signals is ensured, resulting in reliable phase information throughout the complete measurement, i.e., among different frequencies and measurement locations. This synchronization needs to be "accurate at the LO frequency", which is usually close to the actual measurement frequency. By this we mean that independent from the frequency at which the actual synchronization is implemented, any phase errors in the synchronization will translate one-to-one to phase errors in the measurement signals. For example, when feeding both LOs with the same reference clock at 10 MHz, a phase error of 0.001° in the 10 MHz signal will cause a 1° phase error at a potential LO frequency of 10 GHz. The LO phase error then directly affects the phase of the measurement signals, again in this example, with a phase error of around 1° at the measured frequency. Thus, the phase stability of all components in the system has to be on a suitably high level.

The case of a completely phaseless measurement is illustrated in Fig. 6.1(b), where TX and RX are not synchronized at all. The received signal phase varies randomly and no coherence between successive measurements or different spectral components can be ensured.

One way of obtaining partially coherent measurements is depicted in Fig. 6.1(c). By synchronizing the TX and RX at the baseband frequencies, it is possible to obtain stable phase information *within the transmitted bandwidth.* As a consequence, the phase relation between the spectral components of the received signal at each measurement location is stable and reliable. However, when moving either TX or RX, no reliable phase information between spatially separated measurements is obtained. Due to the synchronization on baseband-level, the simultaneously acquired spectral portions of the TX signal are received coherently. As a result, phase differences among signal components at difference frequencies are available. Exploiting this kind of spectral coherence is not straightforward in NFFFTs, as commonly transformations at distinct frequencies are performed. Details on how to make use of such kind of multi-frequency information are given at a later point. More details about baseband synchronization and spectral coherence can be found in [Knapp et al. 2021].

A straightforward way of obtaining partially coherent observations is indicated in Fig. 6.1(d). Instead of establishing a synchronization of any kind between TX and RX, hardware complexity on the RX side is added. Note that the same principle holds true when making modifications on the TX side, which is not discussed here for reasons of brevity. Instead of measuring with a single RX antenna at two locations sequentially, a second antenna is added, which captures a signal at the second location *in parallel* to the first antenna. By down-converting both signals with the same LO signal, coherence among the resulting two baseband signals is obtained. Obviously, this principle can be extended to an arbitrary number of receive antennas, only limited by the availability of suitable hardware and space limitations in practice. Comparing this with the case of a completely phaseless measurement and assuming that the transmitting part represents the AUT, no modifications are required on the AUT side. As such, this approach is expected to be of high practical relevance as it should be applicable in a wide range of problem settings. Note that the multi-channel measurement principle can also be interpreted in a more general way than illustrated in the figure. There is no need for the second receive antenna to move together with the original RX. Antenna measurements with a stationary reference antenna have been proposed as a simple way of overcoming the problem of phaseless measurements [Castaldi and Pinto 2000; Laviada and Las-Heras 2013; Laviada Martinez et al. 2014; Sánchez et al. 2020b]. By "comparing" the measured signal at the first RX antenna (at the different measurement locations) with that of the stationary reference antenna, one obtains a stable phase relation among all measurements. This procedure is commonly known as holography [Gabor 1949] and can be interpreted as a special case of the setup in Fig. 6.1(d). As we will see soon, reliable phase retrieval is possible with this setup, even when the reference antenna is not stationary and when no special precautions regarding the arrangement of the multi-channel RX are taken. It is seen to be sufficient to perform phaseless multi-channel measurements in the same way as common fully coherent measurements are performed. Similar sampling densities are required and aside the multi-channel RX, no additional hardware is required.

Next, a mathematical description of partially coherent observations is introduced and two approaches for exploiting partial coherence in the measurement vector are presented.
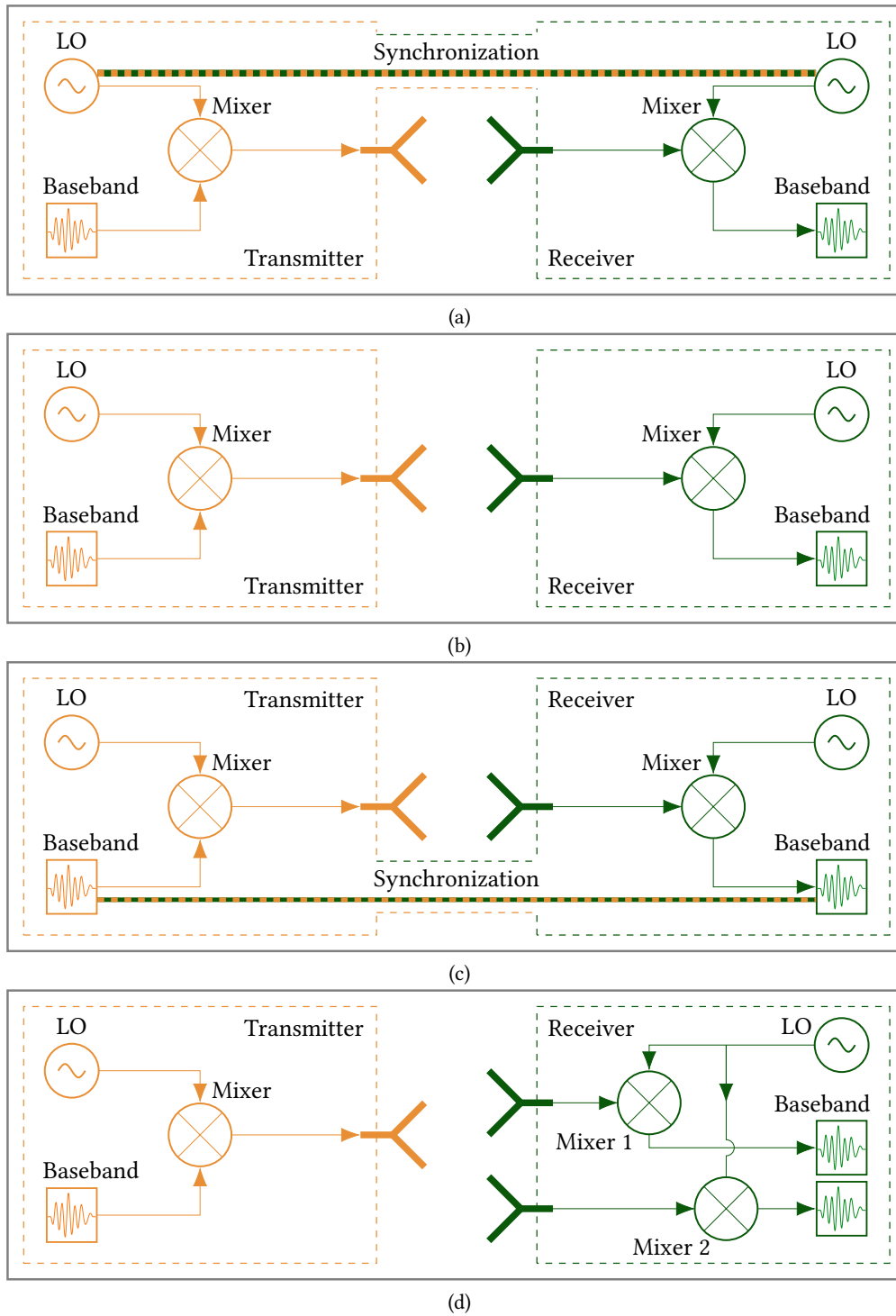
Fig. 6.1 Measurement scenarios for acquiring NF antenna data. (a) Fully-coherent data is acquired as the TX and RX LOs are synchronized. Breaking up the synchronization in (b) results in phaseless measurements. Adding a synchronization of the baseband signals in (c) allows for coherence among the spectral components of the received baseband signal. The multi-channel RX in (d) returns samples with local coherence without requiring synchronization between TX and RX.

## 6.2 Phase Retrieval with Partially Coherent Observations

Let us assume that data is available, which features distinct partial coherence. In Sections 6.2.1 and 6.2.2, two ways of exploiting that information in an otherwise phaseless field transformation are presented. Both techniques exhibit advantages and disadvantages, making each method suitable for a certain problem at hand. At the same time, the treatment of multi-frequency data with known phase differences requires some special attention, which is provided in Section 6.2.3.

### 6.2.1 Phase Differences in Form of Linear Combinations

As has been seen previously, it is possible to encode phase information in the form of magnitude measurements, where the phase can again be reconstructed analytically via (5.97). For a unique encoding of the information about the phase difference between two complex-valued scalar signals, the magnitudes of *four LCs* of the signals are required. In general, one can assume the LCs of the $i$th and the $k$th signal in the form

$$y_1 = |[x_{\mathrm{LC}}]_1 [b]_i + [x_{\mathrm{LC}}]_2 [b]_k|^2$$
$$y_2 = |[x_{\mathrm{LC}}]_3 [b]_i + [x_{\mathrm{LC}}]_4 [b]_k|^2$$
$$y_3 = |[x_{\mathrm{LC}}]_5 [b]_i + [x_{\mathrm{LC}}]_6 [b]_k|^2$$
$$y_4 = |[x_{\mathrm{LC}}]_7 [b]_i + [x_{\mathrm{LC}}]_8 [b]_k|^2 \tag{6.1}$$

for arbitrary complex-valued coefficients $x_{\mathrm{LC}} \in \mathbb{C}^{8 \times 1}$. From the investigations regarding the exact phase retrieval algorithm in Section 5.6, we can now pose a requirement on the coefficients, such that the phases of $[b]_i$ and $[b]_k$ can be retrieved up to an arbitrary phase shift — resulting in the correct phase difference between the signals. From theory, we expect the reconstruction of $n = 2$ unknowns to be possible via the exact phase retrieval method once $m = 4$, which is fulfilled by $y_1$ to $y_4$. What remains to be checked is the rank condition on the bilinear forms of the measurement rows, i.e.,

$$\mathrm{rank}\left(\left|\mathsf{A}_{\mathrm{LC}}\mathsf{A}_{\mathrm{LC}}^{\mathrm{H}}\right|^2\right) \stackrel{!}{=} 4, \quad \text{for } \mathsf{A}_{\mathrm{LC}} = \begin{bmatrix} [x_{\mathrm{LC}}]_1 & [x_{\mathrm{LC}}]_2 \\ [x_{\mathrm{LC}}]_3 & [x_{\mathrm{LC}}]_4 \\ [x_{\mathrm{LC}}]_5 & [x_{\mathrm{LC}}]_6 \\ [x_{\mathrm{LC}}]_7 & [x_{\mathrm{LC}}]_8 \end{bmatrix}. \tag{6.2}$$

All $x_{\mathrm{LC}}$ defining the LCs in (6.1) and fulfilling (6.2) allow for a reconstruction of the phase differences between two complex-valued signals $[b]_i$ and $[b]_k$ via (5.109). Thus, the coefficients $x'_{\mathrm{LC}} = [1\,0\,0\,1\,1\,1\,1\,\mathrm{j}]^{\mathrm{T}}$ required for (5.97) to be applicable are a special case. Due to the ease of phase retrieval for this case, it is often used representative for encoding phase information in the magnitudes of LCs.

If we are interested in determining

$$w'_1 = |[b]_i|^2, \quad w'_3 = |[b]_i + [b]_k|^2,$$
$$w'_2 = |[b]_k|^2, \quad w'_4 = |[b]_i + \mathrm{j}[b]_k|^2 \tag{6.3}$$

in order to apply (5.97) and compute the phase difference between the two complex-valued scalars $[\boldsymbol{b}]_i$ and $[\boldsymbol{b}]_k$, we can evaluate

$$
\begin{bmatrix} w_1' \\ w_2' \\ w_3' \\ w_4' \end{bmatrix} = \left[ \left( \left| \mathbf{A}_{\text{LC}} \mathbf{A}_{\text{LC}}^{\text{H}} \right|^2 \right)^{-1} \left| \mathbf{A}_{\text{LC}} \begin{bmatrix} 1 & 0 & 1 & 1 \\ 0 & 1 & 1 & -\text{j} \end{bmatrix} \right|^2 \right]^{\text{T}} \begin{bmatrix} y_1 \\ y_2 \\ y_3 \\ y_4 \end{bmatrix}
\tag{6.4}
$$

for the general LCs in (6.1). As such, (6.4) represents an analytic solution for determining the phase difference between two scalars once the rank condition in (6.2) is fulfilled.

So far, it has been seen that the knowledge of phase differences between measurement values can be represented in the form of the magnitudes of LCs of these measurements. Accordingly, we can exploit the knowledge of partial coherence among parts of the measurements by adding LCs to the forward operator.

Consider an example, where one has performed three sets of measurements $\boldsymbol{b}_1$ to $\boldsymbol{b}_3$ with their corresponding operators $\mathbf{A}_1$ to $\mathbf{A}_3$. Let us assume that the first measurement has been conducted independently from the second and third measurement set, such that no phase relation between $\boldsymbol{b}_1$ and $\boldsymbol{b}_{2/3}$ is known. Further assume that $\boldsymbol{b}_2$ and $\boldsymbol{b}_3$ have been acquired by a two-channel RX, resulting in element-wise coherence between the entries in $\boldsymbol{b}_2$ and $\boldsymbol{b}_3$, which both have the same number of entries. We can then define the standard phase retrieval problem as

$$
\left\| \begin{bmatrix} \mathbf{A}_1 \\ \mathbf{A}_2 \\ \mathbf{A}_3 \end{bmatrix} \boldsymbol{z} \right\| = \left\| \begin{bmatrix} \boldsymbol{b}_1 \\ \boldsymbol{b}_2 \\ \boldsymbol{b}_3 \end{bmatrix} \right\|
\tag{6.5}
$$

*ignoring* the knowledge of phase differences and which can be tackled by the previously presented approaches. Still based on the assumptions of this example, we may form $\boldsymbol{b}_2 + \boldsymbol{b}_3$ and $\boldsymbol{b}_2 + \text{j}\boldsymbol{b}_3$, for which we can correctly compute the magnitudes *but not the phases*.

We can thus *exploit the partial coherence* between $\boldsymbol{b}_2$ and $\boldsymbol{b}_3$ by solving

$$
\left\| \begin{bmatrix} \mathbf{A}_1 \\ \mathbf{A}_2 \\ \mathbf{A}_3 \\ \mathbf{A}_2 + \mathbf{A}_3 \\ \mathbf{A}_2 + \text{j}\mathbf{A}_3 \end{bmatrix} \boldsymbol{z} \right\| = \left\| \begin{bmatrix} \boldsymbol{b}_1 \\ \boldsymbol{b}_2 \\ \boldsymbol{b}_3 \\ \boldsymbol{b}_2 + \boldsymbol{b}_3 \\ \boldsymbol{b}_2 + \text{j}\boldsymbol{b}_3 \end{bmatrix} \right\| .
\tag{6.6}
$$

The nonlinear system of equations in (6.6) has the same outer shape as the standard phase retrieval problem, however, incorporates further knowledge about partially coherent measurements. For (6.6), the special case of the LCs $\boldsymbol{x}_{\text{LC}}'$ were used, nonetheless, any coefficients fulfilling (6.2) might be employed.

A few evident and less evident things should be said about (6.6). First, one has arrived at an easy-to-use formulation, which incorporates the *maximum amount of information* about the problem, i.e., considering all information about the magnitudes and partial coherence. The formulation requires only minor modifications of the original problem, and solvers which can efficiently solve the original phase retrieval problem can be used to solve (6.6). This formulation thus allows for a quick test on how the additional phase restrictions affect the phase retrieval result. Yet, while the formulation can directly be used in existing phase retrieval algorithms, all the downsides of

existing methods are also inherited, including local stationary points in case of nonconvex solvers. Further, there are plenty of choices for the coefficients of the LCs, where finding the optimal ones for a given task remains an open problem. Inappropriate coefficients can result in badly weighted measurements and, thus, may even worsen the result compared to that obtainable without the LCs.

**Concluding Remarks — Phase Differences via Linear Combinations**   According to the holographic relation in (5.97), a single phase difference between two scalars can be encoded into the magnitudes of four weighted sums of the scalars, which are here called LCs. The concept is of wide generality and allows to incorporate partial coherence into existing phase retrieval algorithms without the need of modifying the methods — causing existing issues like local stationary points to persist.

## 6.2.2  Linearized Formulation with Phase Differences

Partial coherence is here exploited in order to arrive at a linearized formulation. The fundamentals of the approach have essentially been reported in [Kornprobst et al. 2021b] and [Paulus et al. 2021b]. Related ideas have lead to a rudimentary approach for fully incoherent data in [Y. Sugimoto et al. 2021; Zhao et al. 2016].

**Derivation of a Linearized Phase Retrieval**

For simplicity, but without loss of generality, we consider a specific example and derive the general equations based on that model. Analogous to the example which lead to (6.6), assume that three measurement vectors have been acquired, $b_1 \in \mathbb{C}^{m_1 \times 1}$, $b_2 \in \mathbb{C}^{m_2 \times 1}$ and $b_3 \in \mathbb{C}^{m_3 \times 1}$. Here, we claim that $b_1$ has been acquired completely separately from $b_{2/3}$, but the second and third set of samples have been measured coherently, for example by a two-channel RX. The latter two sets thus feature the same number of entries, $m_2 = m_3$, and there are known phase differences between the $k$th entries in $b_2$ and $b_3$ for $k \in \{1, ..., m_2\}$.

In order to keep things simple, we set $m_1 = 1$ and $m_2 = 2 = m_3$, resulting in

$$b_1 = |[b_1]_1| \, \mathrm{e}^{\mathrm{j}[\varphi_1]_1}, \ b_2 = \begin{bmatrix} |[b_2]_1| \, \mathrm{e}^{\mathrm{j}[\varphi_2]_1} \\ |[b_2]_2| \, \mathrm{e}^{\mathrm{j}[\varphi_2]_2} \end{bmatrix}, \ b_3 = \begin{bmatrix} |[b_3]_1| \, \mathrm{e}^{\mathrm{j}[\varphi_3]_1} \\ |[b_3]_2| \, \mathrm{e}^{\mathrm{j}[\varphi_3]_2} \end{bmatrix}. \tag{6.7}$$

In line with [Paulus et al. 2021b], we can then write

$$
\begin{aligned}
\mathbf{A}z = b &= \begin{bmatrix} b_1^{\mathrm{T}} & b_2^{\mathrm{T}} & b_3^{\mathrm{T}} \end{bmatrix}^{\mathrm{T}} \\
&= \begin{bmatrix} |[b_1]_1| & 0 & 0 \\ 0 & |[b_2]_1| & 0 \\ 0 & 0 & |[b_2]_2| \\ 0 & |[b_3]_1| \, \mathrm{e}^{\mathrm{j}([\varphi_3]_1 - [\varphi_2]_1)} & 0 \\ 0 & 0 & |[b_3]_2| \, \mathrm{e}^{\mathrm{j}([\varphi_3]_2 - [\varphi_2]_2)} \end{bmatrix} \begin{bmatrix} \mathrm{e}^{\mathrm{j}[\varphi_1]_1} \\ \mathrm{e}^{\mathrm{j}[\varphi_2]_1} \\ \mathrm{e}^{\mathrm{j}[\varphi_2]_2} \end{bmatrix} \\
&= \mathrm{diag}\,(|b|) \begin{bmatrix} 1 & 0 & 0 \\ 0 & 1 & 0 \\ 0 & 0 & 1 \\ 0 & \mathrm{e}^{\mathrm{j}([\varphi_3]_1 - [\varphi_2]_1)} & 0 \\ 0 & 0 & \mathrm{e}^{\mathrm{j}([\varphi_3]_2 - [\varphi_2]_2)} \end{bmatrix} \boldsymbol{\psi}
\end{aligned}
$$

$$= \mathbf{BC}\boldsymbol{\psi}, \tag{6.8}$$

resulting in the linear formulation

$$\left(\mathbf{AP}_1 - \mathbf{BCP}_2\right)\tilde{z} = 0, \qquad \tilde{z} = \begin{bmatrix} z^{\mathrm{T}} & \boldsymbol{\psi}^{\mathrm{T}} \end{bmatrix}^{\mathrm{T}} \in \mathbb{C}^{n+q \times 1} \tag{6.9}$$

with the stacked vector of unknowns $\tilde{z}$ comprising the unknown AUT coefficients $z$ and $\boldsymbol{\psi}$, a vector containing all remaining unknown phase terms. The matrices $\mathbf{P}_{1/2}$ in (6.9) extract the respective parts from the stacked vector of unknowns and are defined via identity and zero matrices $\mathbf{I}$ and $\mathbf{0}$, respectively, as

$$\mathbf{P}_1\tilde{z} = \begin{bmatrix} \mathbf{I} & \mathbf{0} \end{bmatrix} \tilde{z} = z \in \mathbb{C}^{n \times 1} \tag{6.10}$$

$$\mathbf{P}_2\tilde{z} = \begin{bmatrix} \mathbf{0} & \mathbf{I} \end{bmatrix} \tilde{z} = \boldsymbol{\psi} \in \mathbb{C}^{q \times 1}. \tag{6.11}$$

The measured magnitudes comprise the diagonal matrix $\mathbf{B} \in \mathbb{R}^{m \times m}$, while the actual information about known phase differences is inside the sparse matrix $\mathbf{C} \in \mathbb{C}^{m \times q}$. One thing not explicitly mentioned in (6.9) is the condition $|\mathbf{P}_2\tilde{z}| = \mathbf{1}$, which is required to ensure a correct solution. This condition, however, is nonconvex. In order to avoid potential local stationary points, one can utilize a relaxed and linear version of that by writing

$$\left(\mathbf{AP}_1 - \mathbf{BCP}_2\right)\tilde{z} = 0 \tag{6.12}$$
$$\text{s.t.} \quad [\boldsymbol{\psi}]_s = 1,$$

which only enforces the magnitude constraint on a single, possibly arbitrarily picked, $s$th phase unknown. The approach in (6.9) is a linear and, thus, convex phase retrieval formulation for the case of partially coherent observations.

Based on (6.8), one can easily derive an alternative formulation. Essentially, we have replaced the true and unknown measurement vector $b$ in (6.8) by a formulation exploiting *some* known phase differences and requiring to solve for the remaining phase terms. Still, as soon as the measurement vector with absolute phase has been restored, one can determine the source coefficients by solving a linear system of equations. Effectively, this means one can write

$$\mathbf{BC}\boldsymbol{\psi} = b = \mathbf{A}z = \mathbf{AA}^{-1}b = \mathbf{AA}^{-1}\mathbf{BC}\boldsymbol{\psi}, \tag{6.13}$$

resulting in

$$\left(\mathbf{I} - \mathbf{AA}^{-1}\right)\mathbf{BC}\boldsymbol{\psi} = 0 \tag{6.14}$$
$$\text{s.t.} \quad |\boldsymbol{\psi}| = \mathbf{1},$$

or, correspondingly, in the linearized version

$$\left(\mathbf{I} - \mathbf{AA}^{-1}\right)\mathbf{BC}\boldsymbol{\psi} = 0 \tag{6.15}$$
$$\text{s.t.} \quad [\boldsymbol{\psi}]_s = 1.$$

Comparing the formulations (6.12) and (6.15), we can see that the latter requires a larger computational effort per matrix-vector product, though, at the benefit of a reduced number of unknowns.

Numerical experiments have shown that (6.15) in general exhibits a favorable convergence behavior and a slightly superior robustness with respect to noise.

It should be mentioned that a minor modification of the presented formulations can be employed to allow for a simpler theoretical treatment in some cases. Namely, again utilizing the example in (6.8), it is possible to write

$$
\mathbf{BC} = \text{diag}\left(|\boldsymbol{b}|\right)
\begin{bmatrix}
1 & 0 & 0 \\
0 & 1 & 0 \\
0 & 0 & 1 \\
0 & e^{j([\boldsymbol{\varphi}_3]_1 - [\boldsymbol{\varphi}_2]_1)} & 0 \\
0 & 0 & e^{j([\boldsymbol{\varphi}_3]_2 - [\boldsymbol{\varphi}_2]_2)}
\end{bmatrix}
= \text{diag}\left(\boldsymbol{b}\right)
\begin{bmatrix}
1 & 0 & 0 \\
0 & 1 & 0 \\
0 & 0 & 1 \\
0 & 1 & 0 \\
0 & 0 & 1
\end{bmatrix}
= \mathbf{B}'\mathbf{C}', \qquad (6.16)
$$

where now $\mathbf{B}' \in \mathbb{C}^{m \times 1}$ and $\mathbf{C}' \in \mathbb{R}^{m \times q}$ instead of $\mathbf{B} \in \mathbb{R}^{m \times 1}$ and $\mathbf{C} \in \mathbb{C}^{m \times q}$ are utilized. The only difference between both formulations is the quantity, in which the information about the phase differences is stored. In terms of practicability, the notation with $\mathbf{B}'\mathbf{C}'$ is experienced to be superior as the construction of the matrix $\mathbf{C}'$ is trivially simple and only the phase values in $\boldsymbol{b}$, which belong to the phase differences previously defined in $\mathbf{C}$, are employed. Basically, all phases in the vector $\boldsymbol{b}$, except for the phase differences to be utilized, may be arbitrarily set to zero.

**Linearized Formulations — Solvers**   There are several ways of solving the homogeneous problem in (6.15), where two possibilities are discussed here. First, removing one unknown, i.e., one column of the total matrix $(\mathbf{I} - \mathbf{A}\mathbf{A}^{-1})\mathbf{BC}$, leads to an inhomogeneous system of equations that can be tackled with the solvers discussed in Section 4.3. Second, one can artificially add a measurement and its corresponding row, resulting in a nonzero entry on the right-hand side, which in turn allows solvers for inhomogeneous system to be applied. Both approaches essentially fix one of the unknown phase terms and will be explained for the exemplary homogeneous linear system of equations with a single magnitude constraint

$$
\mathbf{G}\boldsymbol{v} = \mathbf{0}, \quad \text{s.t.} \ \ [\boldsymbol{v}]_k = 1, \ \ k \in \{1, ..., n\} \qquad (6.17)
$$

with $\mathbf{G} \in \mathbb{C}^{m \times n}$ and $\boldsymbol{v} \in \mathbb{C}^{n \times 1}$.

The first approach can be implemented by defining

$$
\boldsymbol{b}_1 = \mathbf{G}\boldsymbol{v}_0, \quad \text{e.g.,} \ \ \boldsymbol{v}_0 = \begin{bmatrix} 0 & \ldots & 0 & 1 & 0 & \ldots & 0 \end{bmatrix}^{\mathsf{T}}, \qquad (6.18)
$$

which essentially fixes the $k$th entry in $\boldsymbol{v}$. Instead of solving $\mathbf{G}\boldsymbol{v} = \mathbf{0}$, one then solves $\mathbf{G}_1\boldsymbol{v}_1 = \boldsymbol{b}_1$, where the matrix $\mathbf{G}_1 \in \mathbb{C}^{m \times n-1}$ equals $\mathbf{G}$, except that the $k$th column has been removed. Accordingly, $\boldsymbol{v}_1 \in \mathbb{C}^{q-1 \times 1}$ features one entry less.

The second approach requires the addition of one measurement row to the original homogeneous system, resulting in

$$
\begin{bmatrix} \mathbf{G} \\ \begin{bmatrix} 0 & \ldots & 0 & 1 & 0 & \ldots & 0 \end{bmatrix} \end{bmatrix} \boldsymbol{v} = \begin{bmatrix} 0 & \ldots & 0 & 1 \end{bmatrix}^{\mathsf{T}} = \boldsymbol{b}_2. \qquad (6.19)
$$

The new, inhomogeneous linear system of equations $\mathbf{G}_2\boldsymbol{v} = \boldsymbol{b}_2$ with $\mathbf{G}_2 \in \mathbb{C}^{m+1 \times n}$ and $\boldsymbol{b}_2 \in \mathbb{R}^{m+1 \times 1}$ needs to be solved. Downside of this method is the potentially inappropriate weighting of the

additional row with respect to the original matrix $\mathbf{G}$. This difficulty is not encountered when removing a single row as explained before.

**Linearized Formulations — Necessary Condition**   An important question is under which circumstances do the linearized formulations in (6.12) and (6.15) yield a correct solution with respect to the original nonlinear task. Let us take a closer look at the homogeneous linear system of equations in (6.15), which is given by

$$\underbrace{\left(\mathbf{I} - \mathbf{A}\mathbf{A}^{-1}\right)}_{\mathbf{P} \in \mathbb{C}^{m \times m}} \underbrace{\mathbf{B}}_{\in \mathbb{R}^{m \times m}} \underbrace{\mathbf{C}}_{\in \mathbb{C}^{m \times q}} \underbrace{\boldsymbol{\psi}}_{\in \mathbb{C}^{q \times 1}} = \mathbf{0} \tag{6.20}$$

with the projection matrix $\mathbf{P}$. A *square* matrix is a projection matrix *if and only if* it is an *idempotent* matrix [Leon 2015]. Idempotent matrices fulfill the condition

$$\mathbf{A}^2 = \mathbf{A}. \tag{6.21}$$

For the matrices involved above, one can see that

$$\left(\mathbf{A}\mathbf{A}^{-1}\right)^2 = \mathbf{A}\mathbf{A}^{-1} \tag{6.22}$$

$$\mathbf{P}^2 = \mathbf{P} \tag{6.23}$$

are both idempotent matrices, and since these matrices are square matrices, they both are projection matrices. In the following, we will only utilize the idempotent property.

In order to find a unique solution to (6.20), the null space of the product of matrices on the left-hand side in (6.20) must have a dimension of one. Equivalently, we can require

$$\operatorname{rank}\left(\mathbf{PBC}\right) \overset{!}{=} q - 1. \tag{6.24}$$

The rank of a product of matrices is bounded via

$$\operatorname{rank}\left(\mathbf{PBC}\right) \leq \min\left(\operatorname{rank}\left(\mathbf{P}\right), \operatorname{rank}\left(\mathbf{B}\right), \operatorname{rank}\left(\mathbf{C}\right)\right). \tag{6.25}$$

Utilizing that for idempotent matrices

$$\operatorname{rank}\left(\mathbf{A}\right) = \operatorname{Tr}\left(\mathbf{A}\right) \tag{6.26}$$

and that

$$\operatorname{Tr}\left(\mathbf{A} + \mathbf{B}\right) = \operatorname{Tr}\left(\mathbf{A}\right) + \operatorname{Tr}\left(\mathbf{B}\right) \tag{6.27}$$

is valid in general, we can find

$$\operatorname{rank}\left(\mathbf{P}\right) \overset{(6.26)}{=} \operatorname{Tr}\left(\mathbf{P}\right) = \operatorname{Tr}\left(\mathbf{I} - \mathbf{A}\mathbf{A}^{-1}\right) \overset{(6.27)(6.26)}{=} m - \operatorname{rank}\left(\mathbf{A}\mathbf{A}^{-1}\right) \geq m - \operatorname{rank}\left(\mathbf{A}\right) \tag{6.28}$$

$$\operatorname{rank}\left(\mathbf{B}\right) = m^1 \tag{6.29}$$

$$\operatorname{rank}\left(\mathbf{C}\right) = \min\left(m, q\right) = q. \tag{6.30}$$

For the rank of **C** we have used that $m \geq q$. Furthermore, it was assumed that there are no nonzero entries in the measurement vector $\boldsymbol{b}$. Yet, it can be shown that the necessary condition derived in the following holds as long as at least $q - 1$ entries in the measurement vector are nonzero. As we will see in a moment, measurements with zero magnitude do not obstruct the formulation, instead they may even lower the following bound.

Putting everything together, we obtain

$$\text{rank}\,(\mathbf{PBC}) \leq \min\,(m - \text{rank}\,(\mathbf{A})\,, m, q) = \min\,(m - \text{rank}\,(\mathbf{A})\,, q)\,. \tag{6.31}$$

Since (6.31) only features an upper bound for the rank, we obtain the *necessary condition*

$$m - \text{rank}\,(\mathbf{A}) \geq q - 1. \tag{6.32}$$

This requirement holds as long as there are at least $q - 1$ nonzero entries in the measurement vector $\boldsymbol{b}$. If this is not the case, then the less intuitive but potentially lower bound

$$m - \text{rank}\,(\mathbf{A}) \geq \text{rank}\,(\mathbf{BC}) - 1 \tag{6.33}$$

holds true. Since the matrix **B** is a diagonal matrix containing the measurement entries, the right-hand side of the bound in (6.33) can only be lowered if zero entries in $\boldsymbol{b}$ coincide with the structure of **C**, such that the total rank of **BC** is reduced. In particular, whenever all entries in $\boldsymbol{b}$ associated with the same unknown phase in $\boldsymbol{\psi}$ are zero, the rank of **BC** is reduced. In that case, the number of measurements required to resolve the remaining phase terms is even lower.

As an example, consider antenna measurement setups with multi-probes, which have been investigated in [Kornprobst et al. 2021b], where a necessary condition for this particular case was derived. We assume a multi-probe setup with $C$ elements and $C$ coherent RX channels, which are placed at in total $M$ measurement locations. The total number of recorded measurements then is $m = CM$ and we further require that $\text{rank}(\mathbf{A}) = N$, i.e., the number of unknowns is smaller or equal to the number of measurements. With $q = M$, one obtains

$$m - \text{rank}\,(\mathbf{A}) = CM - N \geq M - 1$$
$$\Rightarrow \quad M\,(C - 1) \geq N - 1. \tag{6.34}$$

The result in (6.34) is identical to that stated in (15) of [Kornprobst et al. 2021b].

**Linearized Formulations — Noise Analysis**

The presented linear phase retrieval algorithms at their core require that a particular matrix only features a null space containing a single non-trivial vector. A "unique" null space may exist when the model perfectly matches the measurement data, however, this is not guaranteed in case the measurement process is affected by noise of any kind. The measurement vector may be distorted by noise as part of the measurement process, whereas the model underlying the measurement matrix may be inaccurate due to its discrete nature or inadequacy to describe the measurement environment. Consequently, the practical relevance of the presented formulations is highly dependent on the

---

[1]Assuming that there are $m$ nonzero measurement entries. This requirement allows for simplifications, however, does not impose any limitations on the final result. In fact and as shown, zero measurements can only have a beneficial effect of reducing the required amount of measurements.

behavior of the methods when working with imperfect and noise affected measurement data and models.

In the following, a noise analysis of linear systems of equations [Demmel 1997] based on perturbation theory is employed for the investigation of the formulation in (6.15). Utilizing the notation of (6.20) and (6.16) with $\mathbf{N} = \mathbf{PB'C'}$, one can start with

$$(\mathbf{N} + \delta\mathbf{N})\,(\boldsymbol{\psi} + \delta\boldsymbol{\psi}) = \mathbf{0} \tag{6.35}$$

leading to

$$\delta\boldsymbol{\psi} = -\mathbf{N}^{-1}\delta\mathbf{N}\boldsymbol{\psi} \tag{6.36}$$

when the second-order term $\delta\mathbf{N}\delta\boldsymbol{\psi}$ is assumed to be negligible and where $\mathbf{N}\boldsymbol{\psi} = \mathbf{0}$ has been inserted. Here, we assume $\mathbf{N}^{-1}$ to be a pseudoinverse of the matrix $\mathbf{N}$. Consequently one can take an arbitrary vector norm on both sides and exploit the triangle equation to obtain a first upper bound on the relative error in the solution vector as

$$\frac{\|\delta\boldsymbol{\psi}\|}{\|\boldsymbol{\psi}\|} \leq \left\|\mathbf{N}^{-1}\right\| \|\delta\mathbf{N}\| \,. \tag{6.37}$$

It might be confusing that the right-hand side of (6.37) does only feature a perturbation in terms of a matrix and not a measurement vector. Still, remember that all the partially coherent measurements are incorporated inside the $\mathbf{B'}$ matrix, which is part of $\mathbf{N}$. The remaining and difficult task is to rewrite the right-hand side of (6.37) explicitly dependent on a perturbation in the measurement vector $\delta\boldsymbol{b}$.

One attempt in this direction can be made by choosing the Frobenius norm, for which one can find

$$\frac{\|\delta\boldsymbol{b}\|_{\mathrm{F}}}{\|\boldsymbol{b}\|_{\mathrm{F}}} \leq c_{\mathrm{F}} \quad \Longrightarrow \quad \frac{\|\delta\mathbf{B'}\|_{\mathrm{F}}}{\|\mathbf{B'}\|_{\mathrm{F}}} = \frac{\|\mathrm{diag}\left(\delta\boldsymbol{b}\right)\|_{\mathrm{F}}}{\|\mathrm{diag}\left(\boldsymbol{b}\right)\|_{\mathrm{F}}} = \frac{\|\delta\boldsymbol{b}\|_{\mathrm{F}}}{\|\boldsymbol{b}\|_{\mathrm{F}}} \leq c_{\mathrm{F}}, \tag{6.38}$$

meaning that whenever the relative noise in the measurement vector is bounded by some constant $c_{\mathrm{F}}$, then also the relative perturbation in the $\mathbf{B'}$ matrix is bounded by the same constant. Furthermore, we know that the matrix $\mathbf{C'} \in \mathbb{R}^{m \times q}$ contains at most $qm$ nonzero entries with unit magnitude resulting in $\|\mathbf{C'}\|_{\mathrm{F}} \leq \sqrt{qm}$. One can then state

$$\frac{\|\delta\boldsymbol{\psi}\|_{\mathrm{F}}}{\|\boldsymbol{\psi}\|_{\mathrm{F}}} \leq \left\|(\mathbf{PB'C'})^{-1}\right\|_{\mathrm{F}} \|\mathbf{P}\|_{\mathrm{F}} \sqrt{qm}\, \|\delta\boldsymbol{b}\|_{\mathrm{F}}, \tag{6.39}$$

which shows that the relative deviation in the solution vector is limited as long as the perturbation in the measurement vector as well as the relevant Frobenius norms are finite. Remember that this estimate is only a first-order bound, requiring the second-order term $\delta\mathbf{N}\delta\boldsymbol{\psi}$ to be negligible. This should in general hold true when encountering relatively small perturbations.

The bound in (6.39) is exemplarily applied to a complex-valued normally distributed measurement matrix and solution vector for various instances of white noise realizations of different signal-to-
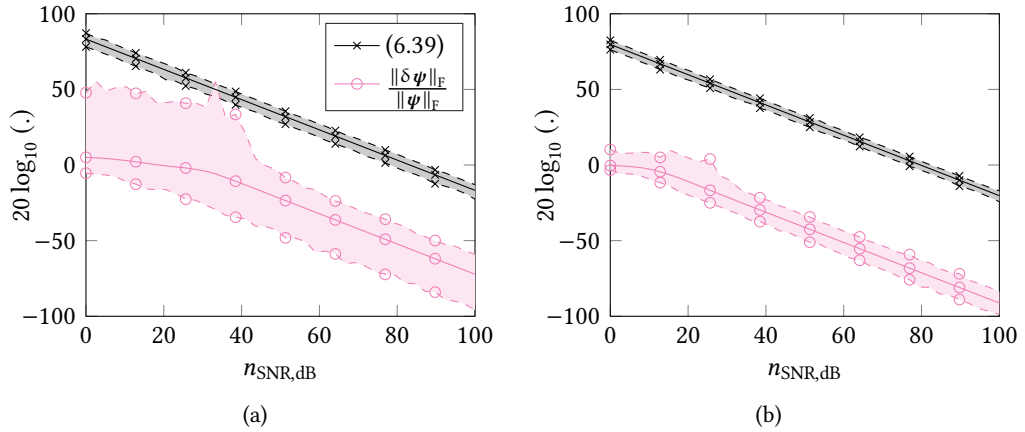
Fig. 6.2 Investigation of the relative error in the solution vector of formulation (6.15) when the measurement vector is affected with Gaussian distributed noise. Complex-valued normally distributed measurement matrices and solution vectors with $n = 10$ are employed and a two-channel RX is assumed. (a) With $m = 18$, i.e., $q = 9$. (b) $m = 36$, i.e., $q = 18$. The range of observable errors in the solution vector and the right-hand side of the upper bound in (6.39) is drawn. Minimum and maximum values are indicated by the dashed lines. For each value of the SNR, $5 \times 10^4$ noise realizations have been considered and the average results are drawn with solid lines.

noise ratios (SNRs). In this work, we define the SNR as

$$n_{\mathrm{SNR}} = \left[ \frac{\max \left( |\boldsymbol{b}| \right)}{\mathrm{std} \left( \boldsymbol{n} \right)} \right]^2 \quad \text{and} \quad n_{\mathrm{SNR,dB}} = 10 \log_{10} \left( n_{\mathrm{SNR}} \right) \tag{6.40}$$

for a complex-valued measurement signal $\boldsymbol{b}$ and a complex-valued noise signal $\boldsymbol{n}$. The function $\mathrm{std}(\boldsymbol{x})$ returns the standard deviation of a vector $\boldsymbol{x}$.

For $n = 10$, Fig. 6.2 illustrates the obtained true deviation in the solution vector when solving with (6.15). In most cases for $m = 18$, i.e., $q = 9$ in Fig. 6.2(a) and in all cases for $m = 36$, i.e., $q = 18$ in Fig. 6.2(b), the observable error is below that estimated by the first-order bound. For each value of the SNR, $5 \times 10^4$ random noise realizations have been considered. Overall, the estimate provides a rather loose barrier on the resulting error, however, it clearly indicates the limited effect of small perturbations in the measurement vector. As such, the presented linear phase retrieval formulations for partially coherent observations are regarded to be stable with respect to noise influence. Whether or not this results in a *sufficient robustness* against noise when it comes to real-world applications remains to be investigated. Nonetheless, comparing Fig. 6.2(a) and Fig. 6.2(b), it becomes clear that a larger oversampling may reduce the average and maximum relative errors—identical to the behavior of a solver with full coherence. A practical recommendation may therefore be to increase the sampling density and thus the noise robustness at the expense of longer measurement times.

**Concluding Remarks—Linearized Phase Retrieval with Partial Coherence** Partial coherence in measurement data can be exploited to derive a linearized representation of the underlying phase retrieval task. Linearity comes at the cost of dropping magnitude constraints and, thus,

information about the problem — exhibiting similarities with the convex algorithms, in particular with PhaseMax. The solution of the linearized and approximate task remains meaningful under a given necessary condition, which certifies the presented algorithms a linear sampling complexity. Independent of the various ways of implementing the formulations, general stability with respect to noise was shown.

### 6.2.3 Phase Differences in Frequency Domain

So far, partial coherence in measurements belonging to the same vector of unknown coefficients has been considered. Things get more complicated when utilizing partially coherent NF antenna data from the measurement setup indicated in Fig. 6.1(c). In essence, partial coherence is here only ensured within the bandwidth of the frequency spectrum of the measurement signal, which potentially reduces the requirements on the quality of the synchronization between TX and RX. However, as the vector of AUT coefficients changes over frequency, phase differences between measurement vectors stemming from different vectors of unknowns have to be incorporated. This prohibits the direct application of the concepts of LCs and the linearized formulations presented in Sections 6.2.1 and 6.2.2. Nevertheless, two possible formulations for the utilization of this particular multi-frequency data are presented — the theory of one of them has in detail been discussed in [Knapp et al. 2021].

The main assumption is that information about phase differences between measurements at the same spatial location but for different frequencies is available. For $l$ frequencies one has $l$ measurement vectors $\boldsymbol{b}_1$ to $\boldsymbol{b}_l$, all acquired at the same set of measurement locations and thus having the same number of entries $m$. In this case, we can relate equivalent sources and phaseless measurements at all frequencies separately, i.e.,

$$\left[|\boldsymbol{b}_1|^\mathrm{T} \quad \ldots \quad |\boldsymbol{b}_l|^\mathrm{T}\right]^\mathrm{T} = \left[|\mathbf{A}_1\boldsymbol{z}_1|^\mathrm{T} \quad \ldots \quad |\mathbf{A}_l\boldsymbol{z}_l|^\mathrm{T}\right]^\mathrm{T} \tag{6.41}$$

while knowing the phase differences between the signals with the $k$th and the $l$th frequency

$$\boldsymbol{\varphi}_k - \boldsymbol{\varphi}_l = \angle(\boldsymbol{b}_k \circ \overline{\boldsymbol{b}_l}), \tag{6.42}$$

where all operations are performed element-wise.

**Multi-Frequency Formulation for Classical Phase Retrieval Algorithms**   Leaving aside the magnitude operations for a moment and knowing the spectral phase differences with respect to some reference frequency with the index $p$, one may write

$$\begin{bmatrix} \boldsymbol{b}_1 \\ \vdots \\ \boldsymbol{b}_p \\ \vdots \\ \boldsymbol{b}_l \end{bmatrix} = \begin{bmatrix} \mathbf{A}_1\mathbf{A}_1^{-1}\mathrm{diag}\left(\dfrac{|\boldsymbol{b}_1|}{|\boldsymbol{b}_p|} \circ \mathrm{e}^{\mathrm{j}\left(\boldsymbol{\varphi}_1 - \boldsymbol{\varphi}_p\right)}\right)\mathbf{A}_p\boldsymbol{z}_p \\ \vdots \\ \mathbf{A}_p\boldsymbol{z}_p \\ \vdots \\ \mathbf{A}_l\mathbf{A}_l^{-1}\mathrm{diag}\left(\dfrac{|\boldsymbol{b}_l|}{|\boldsymbol{b}_p|} \circ \mathrm{e}^{\mathrm{j}\left(\boldsymbol{\varphi}_l - \boldsymbol{\varphi}_p\right)}\right)\mathbf{A}_p\boldsymbol{z}_p \end{bmatrix}, \tag{6.43}$$

where the division by the magnitudes at the reference frequency is the key step in order to map signals generated by the forward operator at the reference frequency to any other frequency at hand. It can be easily verified that the equality in (6.43) holds once a $z_p$ which fulfills $A_p z_p = b_p$ is inserted. While the phase differences between the signals at different frequencies are required and ensure that the resulting phase values are correct, the final projectors $A_i A_i^{-1}$ are necessary in order to remove improper contributions of the magnitudes.

Finally, one can stack all relevant quantities in the form

$$|\tilde{b}| = \begin{bmatrix} |b_1| \\ \vdots \\ |b_p| \\ \vdots \\ |b_p| \end{bmatrix} = \left| \begin{bmatrix} A_1 A_1^{-1} \text{diag}\left( \dfrac{|b_1|}{|b_p|} \circ e^{j(\varphi_1 - \varphi_P)} \right) A_p \\ \vdots \\ A_p \\ \vdots \\ A_l A_l^{-1} \text{diag}\left( \dfrac{|b_l|}{|b_l|} \circ e^{j(\varphi_l - \varphi_P)} \right) A_p \end{bmatrix} z_p \right| = \left| \tilde{A} x_p \right| \in \mathbb{R}^{lm \times 1} \qquad (6.44)$$

and obtain a single, concatenated nonlinear system of equations for the task of phase retrieval containing more measurements while keeping the number of unknowns the same as at the reference frequency. As the structure of (6.44) equals that of a common phase retrieval task, any existing phase retrieval algorithm can directly be applied, making (6.44) a versatile way of exploiting multi-frequency data.

What is the working principle of (6.44)? Essentially, the division with the magnitude at an arbitrarily chosen reference frequency and multiplication with the relevant phase differences allows to map the sources at the reference frequency to the signals at another frequency. As part of the process and, to be precise, caused by the division, physically incorrect signal contributions may arise. That is why the projectors $A_i A_i^{-1}$ are required, which filter out signal portions that are not supported by the operators and the underlying model. Thus, a physically meaningful solution is ensured at all frequencies. This filter property works well once a sufficiently large number of measurements $m$ in the spatial domain has been acquired. Commonly, higher frequencies correspond to electrically larger AUTs, which require more spatial samples. When combining frequencies over a broad bandwidth, the highest frequency component essentially dictates the sampling density to be applied at all other frequencies. This may cause an increased measurement effort in practice. As another downside of (6.44), the computational effort increases drastically. For every matrix-vector product of $\tilde{A}x$, $(l-1)$ linear systems of equations need to be solved. However, as long as the full operator $\tilde{A}$ fits into the memory, it may be computed explicitly and reused on demand, or a fast inversion algorithm can be employed.

In the limit of a vanishing bandwidth the diversity among the operators and measurements will decrease, while the vector of phase differences will go to zero. Thus, as expected new information is only added as long as the measurement setup or the measurement signals exhibit a sufficiently large frequency variation over the considered bandwidth. As long as this condition is met, the formulation with $\tilde{A}$ features new and uncorrelated rows with respect to the forward operator at the reference frequency.

Note that one does not have to stop after constructing (6.44). Partial coherence was the key ingredient for combining signals at different frequencies and allowing to stack the operators and the measurement vectors. Still, when solving (6.44) with a standard phase retrieval algorithm,

knowledge of the phase differences is only *inherently* exploited. It is highly recommended to furthermore utilize a phase retrieval algorithm, which explicitly enforces knowledge on partial coherence in the final problem in (6.44). As such, (6.44) can be expanded to incorporate the phase differences in the form of LCs as additional rows. Alternatively, the linearized phase retrieval algorithms for the case of partially coherent observations can be applied. Nonetheless note that the results in [Knapp et al. 2021] have been obtained by the standard phase retrieval formulation (5.30).

**Linear Multi-Frequency Formulation** Based on the linearized formulations in Section 6.2.2, a simple linear formulation for NF data at multiple frequencies can be derived. While the approaches in (6.12) and (6.15) could be applied to (6.44), we here present a more convenient method for the general case of partial coherence among measurements belonging to different linear systems of equations.

Essentially, one can consider a generalization of (6.41) consisting of $l$ linear operators $\mathbf{A}_i \in \mathbb{C}^{m_i \times n_i}$, $i \in \{1, ..., l\}$, each potentially featuring a variable number of rows and columns. Associated with the operators, there are the vectors of unknowns $z_i \in \mathbb{C}^{n_i \times 1}$ and the measurement vectors $b_i \in \mathbb{C}^{m_i \times 1}$. Whenever there exist known phase relations within or among the measurement vectors $b_i$, it may make sense to formulate the corresponding partially coherent systems

$$\underbrace{\left(\mathbf{I} - \mathbf{A}_i \mathbf{A}_i^{-1}\right) \operatorname{diag}\left(b_i\right) \mathbf{C}_i'}_{\mathbf{P}_i} \psi = 0, \quad [\psi]_k = 1, \tag{6.45}$$

where for the sake of simplicity, the notation from (6.16) is employed. In this notation, the occurring matrices defining the phase relations $\mathbf{C}_i' \in \mathbb{R}^{m_i \times q}$ already feature columns according to the *overall* number $q$ of remaining phase unknowns, which are related to *all* $l$ operators and measurements. When combining all the $i \in \{1, ..., l\}$ systems, one obtains

$$\underbrace{\begin{bmatrix} \mathbf{P}_1 & 0 & \ldots & \ldots & 0 \\ 0 & \ddots & 0 & \ldots & \vdots \\ \vdots & 0 & \mathbf{P}_i & 0 & \vdots \\ \vdots & \ldots & 0 & \ddots & 0 \\ 0 & \ldots & \ldots & 0 & \mathbf{P}_l \end{bmatrix}}_{\mathbf{P}_{\text{LMF}} \in \mathbb{C}^{m \times m}} \operatorname{diag}\underbrace{\left(\begin{bmatrix} b_1 \\ \vdots \\ b_i \\ \vdots \\ b_l \end{bmatrix}\right)}_{\mathbf{B}_{\text{LMF}}' \in \mathbb{C}^{m \times m}} \underbrace{\begin{bmatrix} \mathbf{C}_1' \\ \vdots \\ \mathbf{C}_i' \\ \vdots \\ \mathbf{C}_l' \end{bmatrix}}_{\mathbf{C}_{\text{LMF}}' \in \mathbb{C}^{m \times q}} \psi = 0, \quad [\psi]_k = 1, \tag{6.46}$$

when $m = \sum_{i=1}^{l} m_i$. One can derive the necessary condition

$$\sum_{i=1}^{l} \left[m_i - \operatorname{rank}\left(\mathbf{A}_i\right)\right] \geq \operatorname{rank}\left(\mathbf{B}_{\text{LMF}}' \mathbf{C}_{\text{LMF}}'\right) - 1, \tag{6.47}$$

for (6.46) to return a meaningful solution when measurements of zero magnitude occur. Analogous to (6.32), the potentially more intuitive relation

$$\sum_{i=1}^{l} \left[m_i - \operatorname{rank}\left(\mathbf{A}_i\right)\right] \geq q - 1 \tag{6.48}$$

is obtained when at least $q - 1$ nonzero magnitudes are available. While the new and highly general system in (6.46) seems to be similar to the previous formulations, there are drastic limitations associated with it when compared to (6.15) and (6.12). The single projector, e.g., in (6.15), is replaced by a block-diagonal arrangement of projection matrices. Inherent to its structure, the resulting matrix $\mathbf{P}_{\mathrm{LMF}}$ can exhibit a null space that *may* contaminate the null space of the overall matrix system. Whether or not this is the case highly depends on the structure of the matrix $\mathbf{C}'_{\mathrm{LMF}}$ at hand. Whenever a set of measurements $\boldsymbol{b}_i$ is not related to any of the other sets via at least one phase difference, it is essentially decoupled from the rest and has to fulfill the condition (6.32) "on its own". Then, this set does not contribute to the solution of the other measurement sets.

Let us now specialize (6.46) for the case of multi-frequency data, where all sets feature the same number of measurements, $m = m_i \ \forall i \in \{1, ..., l\}$ and phase differences are known between the $k$th entry of $\boldsymbol{b}_1$ and $\boldsymbol{b}_i$ for all $k \in \{1, ..., m\}$ and all $i \in \{2, ..., l\}$. The total number of measurements in this case is $lm$. The resulting partially coherent system is found as

$$\left[[\mathbf{P}_1 \mathrm{diag}\,(\boldsymbol{b}_1)]^{\mathrm{T}} \quad ... \quad [\mathbf{P}_i \mathrm{diag}\,(\boldsymbol{b}_i)]^{\mathrm{T}} \quad ... \quad [\mathbf{P}_l \mathrm{diag}\,(\boldsymbol{b}_l)]^{\mathrm{T}}\right]^{\mathrm{T}} \boldsymbol{\psi} = \mathbf{0}, \quad [\boldsymbol{\psi}]_k = 1, \tag{6.49}$$

which is seen to not suffer from an additional null space, as all projectors occurring in the partial-coherence system are coupled via the element-wise phase differences between the measurements at multiple frequencies. Assuming $\mathrm{rank}(\mathbf{A}_i) = n_i$, the necessary condition of (6.48) can here be found to read

$$(l - 1)\,m \geq \left(\sum_{i=1}^{l} n_i\right) - 1, \tag{6.50}$$

or, further assuming $n_i = n \ \forall i$,

$$\frac{(l - 1)\,m}{ln - 1} \geq 1. \tag{6.51}$$

**Concluding Remarks — Phase Differences in Frequency Domain**   With a synchronization of TX and RX hardware in the baseband frequency range, phase differences within a corresponding bandwidth can be obtained. This kind of partial coherence is fundamentally different to that of RXs with multiple coherent channels. While in the latter case the phase information is essentially stemming from single unknown vector of AUT coefficients, coherence among broadband data is imposing relations between multiple unknown source vectors. Still, two possible formulations for the utilization of partial coherence of multi-frequency data have been described, both exploiting projectors at the expense of increased computational costs. One conserves the original nonlinear problem formulation and can be solved via existing general purpose phase retrieval algorithms — again inheriting the same benefits and drawbacks of these techniques. The second method follows the approximation made by the single-frequency linearized phase retrieval formulations, dropping most magnitude restrictions in exchange of linearity. Again the approximation is found to return meaningful results under a necessary condition proving a linear sampling complexity for this approach.

# 6.3  Transformation Results

The presented methods for partially coherent observations are here tested extensively with realistic NF antenna data. A differentiation is done regarding spatial phase differences measurable with a setup illustrated in Fig. 6.1(d) and those in frequency domain, which could be acquired with a synchronization as indicated in Fig. 6.1(c).

## 6.3.1  Phase Differences in Spatial Domain

### Field Data of a Planar Array — Linear Combinations

The knowledge of partial coherence, or in other words the knowledge of phase differences, can be encoded in the form of magnitudes of LCs. In the same way as this has been done for a particular example in (6.6), these LCs can be incorporated to form a modified forward operator and measurement vector for almost arbitrary and incomplete phase information. The resulting operators and measurement vectors can be fed to all previously discussed convex and nonconvex phase retrieval algorithms.

In order to evaluate the performance gain by the LCs, NF data on two measurement planes in front of a horn antenna array was generated. The antenna array including the measurement planes is illustrated in Figs. 5.16(a) and 5.16(b) and has already been described in the discussion thereof. For the analysis here, a three-channel RX was assumed, which allows to coherently acquire three NF samples at a time. This leads to the additional knowledge of two phase differences at each location on the measurement grid. The three channels were connected to an "L"-shaped, three-element array of identical probe antennas of identical polarization. The measurement grid including the three-element probe array and the three RX channels is illustrated in Fig. 6.3(a). The RX channels are marked by different colors and the locations of the respective NF samples are drawn with circles. The lines connecting the circles indicate the employed phase differences, each of them realized via two LCs of the relevant measurement signals. For this particular measurement setup with $m$ measurements, there are $2/3\,m$ available phase differences, which are incorporated in the form of $4/3\,m$ additional magnitudes of LCs of the measurements. In summary, a phase retrieval algorithm applied to this particular partially coherent problem has in total $7/3\,m$ magnitude measurements available, in contrast to the $m$ measurements of the original and completely phaseless problem. For all presented results, the horizontal and vertical distance between the elements in the "L"-shaped probe array was set to $\lambda/2$.

For the introduced planar NF measurement setup, transformation results for the nonconvex formulation in (5.30) with $p_2 = 0.5$, for PhaseLift and for PhaseMax are discussed. All solvers are applied to the original phaseless measurement problem and to that where LCs are added, corresponding to a measurement with partial coherence. Starting from an initial guess computed via the spectral method, at most $5 \times 10^3$ iterations were performed. The achieved NF deviation is depicted in Fig. 6.3(b). Be aware of the nonlinear $y$-axis. Similar to the previously obtained results in Fig. 5.16(c) for the same measurement setup, both convex algorithms struggle to obtain accurate results from the measurement data on the two planes. In contrast, the nonconvex solver is a paramount example of an unpredictable phase retrieval algorithm and returns accurate as well as highly inaccurate results for various ratios of $m/n$. When adding the LCs, the performance of the nonconvex algorithm improves further, nonetheless, it can also be worse, as seen in certain cases of $m/n$. Opposite to that, PhaseMax does not seem to be able to exploit the additional information in the
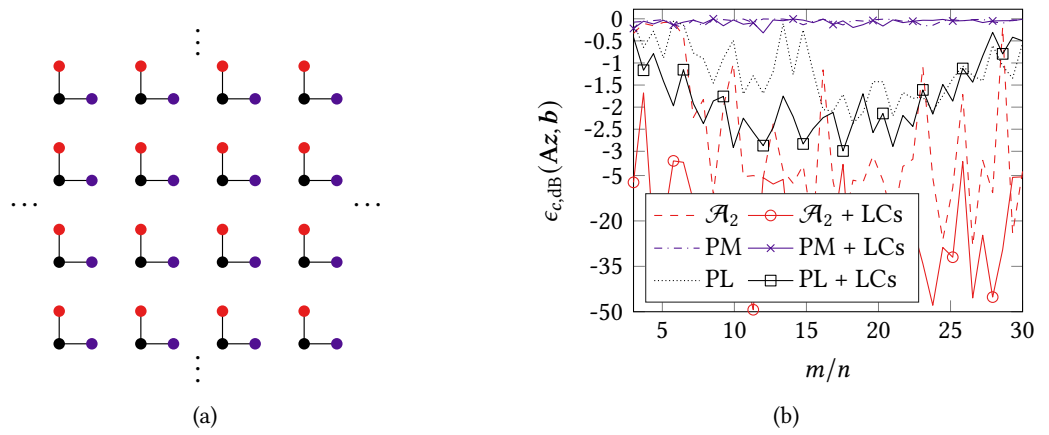
Fig. 6.3 (a) Illustration of the planar measurement grid employed for sampling the NF of the horn antenna array depicted in Fig. 5.16. The described "L"-shaped probe arrangement is employed on both measurement surfaces. The NF samples acquired with the three RX channels on regular grids are indicated by dots, where the colors refer to the different channels. The black lines represent the utilized phase differences, which, for the results in (b), have been exploited in the form of linear combinations (LCs) similar to the example given in (6.6). Accordingly, the transformation results in (b) are differentiated in terms of whether or not the LCs have been added ("+ LCs"). Note that the oversampling ratio $m/n$ does not consider the LCs. Consequently, results marked with "+ LCs" are effectively obtained with $7/3\,m$ rows in the corresponding operator. All solvers were allowed to at most perform $5 \times 10^3$ iterations, starting from an initial guess generated via the optimal spectral method. PhaseLift and PhaseMax are abbreviated as PL and PM.

LCs. Among the considered convex algorithms, solely PhaseLift slightly improves its performance on average, still, returns unsatisfactory results.

Based on the results, two major statements can safely be made. The performance improvement of phase retrieval algorithms to be expected when employing information about partial coherence *in the form of LCs* does vary significantly dependent on the algorithm at hand. Even though nonconvex phase retrieval algorithms are in general observed to perform favorably when adding LCs, *they remain unpredictable, unreliable and may fail.*

**Field Data of a Planar Array — Linearized Formulation**

The planar NF antenna measurement setup employed in Fig. 6.3 is considered again. The geometry of the AUT and the measurement planes can be seen in Figs. 5.16(a) and 5.16(b). For more details about the AUT, the reader is referred to the related discussion in the previous section.

In contrast to exploiting the knowledge of phase differences in the form of LCs, as was done for the results in Fig. 6.3(b), the available partial coherence is now utilized by the formulations in (6.12) and (6.15). Both concepts lead to homogeneous linear systems of equations with a linear side constraint, which can be reformulated as inhomogeneous linear systems by either adding an additional row or by removing one column, as already mentioned in the form of (6.19) and (6.18), respectively. The resulting inhomogeneous systems can either be solved directly, e.g., by a **QR**-

decomposition, or iteratively, e.g., by the formulation (4.4) or another solver like GMRES [Saad and Schultz 1986]. In total, this brings us to eight possible implementations, all of which have been applied to the NF data of the horn antenna array. The achievable NF deviation of the eight implementations is depicted in Fig. 6.4(a). Note that the same range of oversampling ratios $m/n$ has been used as for the results based on LCs in Fig. 6.3(b), making both figures comparable. Results for the direct solution via a **QR**-decomposition and via iterative solvers are marked by the superscripts "d" and "i", respectively. When a row has been added or a column has been removed, the superscripts "a" and "r" are added accordingly. As a reference, the result obtainable with a transformation exploiting full phase information is drawn. The iterative solvers applied to (6.12) and (6.15) were allowed to at most perform 1900 and $5 \times 10^2$ iterations, respectively. In practice the formulation in (6.12) leads to a highly ill-conditioned system while (6.15) exhibits reasonable condition numbers. Thus, more iterations are commonly necessary. Ideally, a well regularized solver should be employed, e.g., the GMRES. All iterative implementations except (6.12)$^{\text{ia}}$ rely on the linear solver of the formulation in (4.4), which previously in this work was seen to perform very similar compared to GMRES. For (6.12)$^{\text{ia}}$ the GMRES was employed. It should be mentioned that (6.12)$^{\text{ir}}$ exhibited the most unstable behavior of all iterative implementations, in a way that the formulation in its original form did not converge with neither of the linear solvers. Only when scaling **A** and **BC** in (6.12) by the inverse of the respective largest singular values, the condition number of the combined matrix $(\mathbf{AP}_1 - \mathbf{BCP}_2) = [\mathbf{A} \quad -\mathbf{BC}]$ was reduced by several orders of magnitude, allowing the solvers to converge within the considered 1900 iterations. Scaling of these sub-parts of the complete matrix is possible due to the decoupling of the contribution belonging to the source coefficients and the portion associated with the unknown phase terms via the matrices $\mathbf{P}_{1/2}$.

Let us first have a look at the overall performance of the linear phase retrieval algorithms for partially coherent data when varying the available number of measurement signals. As a reminder, results for existing approaches exploiting the phase differences in terms of LCs are visible in Fig. 6.3(b). For these approaches, slight improvements with increasing $m/n$ are visible. This is rather not the case in Fig. 6.4(a) for the linear formulations. Looking at the results obtained with the direct **QR**-decomposition, the achievable NF deviation is at around $-35$ dB and almost independent of $m/n$. There is no difference in terms of which variant is directly being solved, i.e., either adding a row or removing a column in order to obtain an inhomogeneous linear system. While the nonconvex solver performed best when exploiting the LCs in Fig. 6.3(b), its performance is of stochastic nature and in general unreliable, though, there were cases where accurate solutions with an NF deviation of as low as $-50$ dB were obtained. In contrast to that, the new formulations here reliably return a solution of decent accuracy. There is no danger of randomly obtaining a highly inaccurate result, however, the best accuracy seems to be limited by the numerical noise present in the simulation data as well as that added due to the discrete nature of the equivalent AUT representation. There also is a dependency of the noise robustness (numerical as well as measurement noise) on the geometrical properties of the probe antenna array, e.g., the spatial separation among the array elements. A more detailed investigation on the noise robustness is provided later.

When looking at the iterative implementations, a minor advantage of the formulation (6.12) over (6.15) can be identified. However, the difference could potentially be attributed to the different numbers of iterations performed. Comparing the approaches of adding a row or removing one column in order to obtain an inhomogeneous linear system, there is no difference to be observed for the method in (6.15), while for (6.12) removing one column seems to perform better. As mentioned previously, the specific implementation of (6.12)$^{\text{ir}}$ had to be modified by an improved weighting of
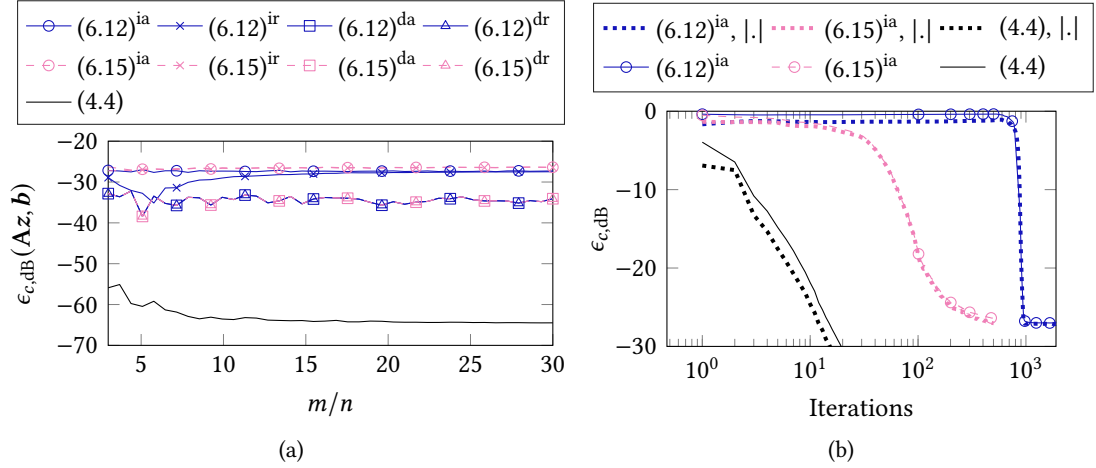
Fig. 6.4 Performance of the linear phase retrieval algorithms for the NF data of the horn antenna (Fig. 5.16) which was employed for the results of Fig. 6.3. Direct and iterative implementations of (6.12) and (6.15) are considered and indicated by the superscript "d" and "i". Further differentiation is done in terms of how the inhomogeneous system is obtained, either based on adding a row to, or removing one column from the homogeneous systems, see (6.19) and (6.18), respectively. The superscripts "a" and "r" are added accordingly. (a) The solver performance for various oversampling ratios. (b) Solver convergence for $m/n = 3$. As a reference, the result of a transformation with full phase information is drawn.

the portions of the relevant matrix in order to achieve stable convergence, which was not necessary and has not been done for $(6.12)^{\text{ia}}$. The larger discrepancy between both versions is thus highly likely to be caused by the additional weighting and does not reveal any substantial advantages or disadvantages of the add-row and remove-column approaches.

As a last point of interest, the convergence behavior of $(6.12)^{\text{ia}}$ and $(6.15)^{\text{ia}}$ as well as the reference solver is drawn in Fig. 6.4(b) for $m/n = 3$. Clearly, the projector-based formulation exhibits a relatively fast and desirable convergence. Here, both solvers are seen to simultaneously minimize the deviation in the magnitude-only ($\epsilon_{c,\text{dB}}(|\mathbf{A}\mathbf{z}|, |\mathbf{b}|)$, indicated by "$|.|$") as well as the complex-valued measurement vector ($\epsilon_{c,\text{dB}}(\mathbf{A}\mathbf{z}, \mathbf{b})$). This is another highly beneficial property, which has not always been observed to hold true for the formulation with source coefficients and unknown phases in (6.12). It may happen that this approach does exhibit a steep convergence in terms of the magnitude deviation, but a delayed or flat convergence in terms of the true, complex NF deviation. As a consequence, when working with the variants of (6.15), a low observable $\epsilon_{c,\text{dB}}(|\mathbf{A}\mathbf{z}|, |\mathbf{b}|)$ strongly indicates that an accurate solution has been found. Something that does not hold true when working with variants of (6.12). For the latter, convergence is in general observed after a larger number of iterations, stemming from the fact that the underlying linear operator is ill-conditioned. The convergence behavior of the solver with full phase information is by far preferable, as the solver achieves an NF deviation of around $-30\,\text{dB}$ after roughly 15 iterations. For reasons of completeness, it should be mentioned that the linearized formulations may here be adversely affected by an artificial null space emerging from the truncated and incomplete measurement setup. Improved accuracy for these approaches is expected when applying the modification mentioned in the results section about "Synthetic Data on a Real-World Drone Trajectory".

**Field Data of a Reflector Antenna**

A synthetic reflector antenna model simulated in Feko was employed to provide NF data on a planar measurement surface in the main beam direction of a parabolic reflector. Feeding of the model was done by means of a $z$-oriented Hertzian dipole placed approximately $1.67\lambda$ in front of the reflector, which has radius and focal length of $\approx 1.67\lambda$. The tangential components, in $y$- and $z$-direction, of the radiated electric field were sampled on a square shaped measurement plane with $\approx 50\lambda$ side length at a distance of around $16\lambda$ from the AUT. In total $n = 1 \times 10^3$ Hertzian dipoles were employed as an equivalent model of the reflector arrangement as part of the field transformation. In addition to samples on the measurement plane, which is illustrated in Fig. 6.5(a), four distinct observation points on the left and right side of the measurement plane were added. These locations, at which only the $z$-component of the electric field was acquired, were intended to represent the positions of reference antennas employed during the acquisition of each of the four sub-planes. In total $m = 5004$ measurement samples were utilized, including 1250 probe signals per square-shaped sub-region, which are indicated by different colors in Fig. 6.5(a). The four signals associated with the reference positions were added, however, assuming that the reference antennas do only provide a phase connection and no explicit measurement samples, they could have been dropped with negligible impact on the transformation results. Care was taken, such that the sub-regions on the measurement planes did not overlap or touch, resulting in four separate regions where the phase relation between these regions is unknown.

In the following, each reference antenna is assigned to its respective quadrant of the measurement square, for which it is assumed to provide a stable phase reference. In essence, the described setup reassembles that of a potentially realistic holographic NF antenna measurement with multiple reference antennas, or a single moving one. Based on classical holography, it is not directly possible to reconstruct the global phase, i.e., including the phase relation between the four quadrants in Fig. 6.5(a), as there is no overlap between the regions of local coherence. As will be shown in a moment, the previously introduced linear phase retrieval algorithms for partially coherent data allow to reliably reconstruct the global phase distribution without the need for additional holographic measurements. In a classical holographic setup, overlaps between the sub-regions of local coherence would be required to finally obtain *full coherence* among all samples. Note that in practice it may be necessary or beneficial to position the reference antenna at more than four locations, e.g., for reasons of shadowing and limited dynamic range. The measurement effort associated with ensuring a sufficient overlap between an increasing number of sub-regions is expected to grow rapidly — as well as the danger of accumulating phase errors due to inaccuracies in the overlaps. Consequently, methods based on classical holography quickly become impractical as more sub-areas are required.

Since previous tests have shown the feasibility of the linear formulations for partially coherent observations, focus is here put on the noise robustness of the methods. Therefore, a noise analysis is performed, where the SNR according to the definition in (6.40) is employed. Based on Fig. 6.5(b), the performance of various methods for noisy NF data can be estimated. Here, complex-valued normally distributed noise was added to the synthetic measurement data and the resulting NF deviation was recorded. For each value of the SNR and for each solver, 20 noise realizations were considered. The mean, minimum and maximum NF deviations are drawn in Fig. 6.5(b), where the latter two deviations are indicated by dashed lines. The solver exploiting full phase information is seen to achieve the most consistent NF deviations throughout the whole range of SNR values. With a similar performance, the transformation based on the nonconvex formulation and exploiting the phase differences in the form of LCs exhibits a good noise robustness, even achieving the lowest best-case

deviation of all solvers. Within the limited number of trials, no convergence to a suboptimal solution is observed, however, suboptimal solutions may still occur in an unlucky case. For larger SNR values, the linear phase retrieval algorithms based on partial coherence asymptotically come closer to the performance of the latter two algorithms and almost no difference between the two variants is visible. Still, the formulation based on the projector is observed to be slightly more noise-robust compared to the projector-free variant. For the particular example, the performance of the two variants varies the most around $n_{\mathrm{SNR,dB}} \approx 10\,\mathrm{dB}$ to $30\,\mathrm{dB}$ with deviations of up to a few dB. As mentioned, the linearized formulations may here be adversely affected by an artificial null space emerging from the truncated measurement setup. This issue is more severe for non-regularized direct implementations of the solvers than for iterative realizations. As the **QR**-decomposition was employed for the transformation with full phase, its performance has also been deteriorated slightly. Improved accuracy for the linear approaches as well as $\mathcal{A}_0$ is expected when applying the modification mentioned in the results section about "Synthetic Data on a Real-World Drone Trajectory".

Based on the discussed results, at least three statements can be made. First, the investigated linear phase retrieval algorithms for partially coherent data can directly be applied to holographic measurement setups. By employing the algorithms in a post-processing step, a wide range of limitations and restrictions of typical holographic measurements can be mitigated, e.g., allowing for a moving reference antenna. Second, the algorithms perform robust in the presence of noise, where their overall behavior for varying SNR values is comparable to that of field transformations with full phase information. Still, switching from full-phase to partial-phase information increases the sensitivity of the transformation with respect to measurement noise. Lastly, even nonconvex phase retrieval algorithms — when provided with suitable data — may exhibit a convex behavior and reliably return accurate results. Yet, the investigated example with its holographic background represents a rather extreme case, where almost full coherence is available. The observation is simply in line with the fact that the phase retrieval problem becomes convex once sufficient data is available [Sun et al. 2018].
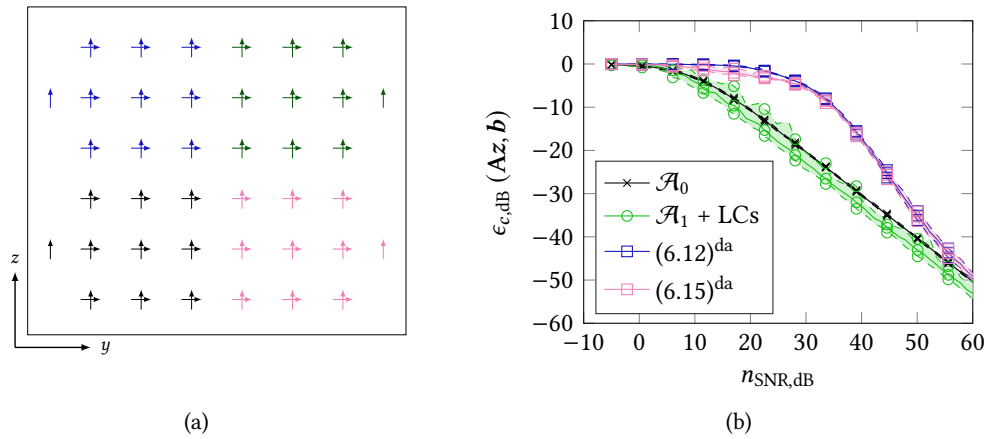
(a)

(b)

Fig. 6.5 Illustration of a planar measurement arrangement of a parabolic reflector fed by a Hertzian dipole in (a) and the achieved NF deviation of various transformation algorithms in (b). The colored arrows in (a) indicate regions of partial coherence and the acquired polarization. The measurement plane is split into four quadrants, each of which is assumed to feature *full coherence* among all field samples drawn with the same color and *unknown phase relations* to differently colored regions. Local coherence is assumed to be provided by the placement of respective reference antennas, which are indicated by the single, vertically oriented arrows at the sides of the quadrants. The illustration is not up to scale and does not depict all measurement locations on the measurement plane. For the results in (b), 20 transformations with random noise realizations were conducted for each solver and SNR and the mean, minimum and maximum NF deviations are drawn. The latter two are indicated by dashed lines.

### Logarithmic-Periodic Antenna—Single Frequency

A logarithmic-periodic dipole antenna was simulated in Feko and NF data on the lateral surface of a cylinder was acquired and fed to the phase retrieval algorithms. The model of the dipole antenna was constructed according to the Altair Feko 2019.1 Example Guide [Altair Engineering Inc. 2019] and the simulations where performed within the frequency range of 35 MHz to 60 MHz. A top-down view of the measurement setup is depicted in Fig. 6.6(a), where the measurement cylinder with a radius of 30 m shifted in $-x$-direction by 8 m is indicated by the solid red circle and the AUT dipoles are illustrated by black lines. The minimum sphere of the AUT is depicted by the dashed blue circle with a radius of roughly 7 m and its center shifted to $x = -6.2$ m. The smallest rod of the logarithmic-periodic antenna is centered in the origin of the coordinate system. The height of the measurement cylinder was set to 100 m, enabling a reconstruction of the AUT FF in almost the complete elevation plane.

For a first investigation at 60 MHz, a bent "L"-shaped probe antenna array was utilized for the acquisition of the tangential electric field on the lateral surface of the measurement cylinder. Partial coherence was assumed to be available among the elements of the probe array. Note that two orthogonal polarizations have been recorded in order to fully characterize the AUT, where no phase differences between the polarizations were exploited. The assignment of the probe array elements to the corresponding RX channels is illustrated in Fig. 6.6(b). All dots of the same color are assumed

to be acquired sequentially by one of the probe elements connected to its corresponding RX channel, resulting in local coherence between three measurement signals at each measurement location. The known phase differences are indicated by black lines, which connect the elements of the probe array. For the vertical separation of the probe elements a value of 2.5 m and for the horizontal separation, an angle of 5° was chosen — corresponding to a spacing of roughly 2.6 m. Results for the linear phase retrieval algorithms for data with partial coherence are depicted in Fig. 6.6(c), for which the AUT was modeled by $n = 646$ spherical vector wave functions. As a reference, the achievable NF deviation with a transformation utilizing full phase information was added. Also, a nonconvex phase retrieval algorithm exploiting the local coherence in the form of LCs has been applied to the NF data, where its initial guess was computed via the optimal spectral method and at most $2 \times 10^3$ iterations were allowed for the solver to converge. Despite the relatively low oversampling ratio $m/n$, the linear solvers are able to accurately determine the AUT coefficients, while the nonconvex solver does only sometimes return a solution with an NF deviation of around $-20$ dB. In fact, the behavior of the linear phase retrieval algorithms is observed to be very similar to that of the transformation with full phase information. For the latter, a low error can be achieved for $m/n \geq 1$, i.e., once the system is no longer underdetermined. For the linear phase retrieval algorithms for partially coherent data to obtain similar levels of NF deviation, the condition in (6.32) needs to be fulfilled. For a $C$-channel RX, i.e., a RX with $C$ coherent channels, this bound can be rewritten as

$$\frac{m}{n} \geq \frac{C\,(n-1)}{n\,(C-1)} \overset{C=3,n=646}{\approx} 1.498, \tag{6.52}$$

which exactly corresponds to the point of sudden drop in the NF deviation in Fig. 6.6(c). Similar to the transformation with full phase information, adding more measurements than required by the bound further reduces the NF deviation. While this trend continues for the full-phase solver over the complete range of $m/n$, the performance of the partial-coherence solvers stagnates for $m/n > 2.5$ at an NF deviation of around $-80$ dB. Evidently, the phase retrieval algorithms for partially coherent observations are in general more sensitive to noise than their full-phase counterparts. Since the NF data is not contaminated by any kind of measurement noise, the accuracy limitation could be caused by numerical noise, e.g., the discrete nature of the AUT model, round-off effects when storing and reading data from text files as well as computations with limited numerical precision. Due to the missing field samples on the top and bottom of the measurement cylinder, the forward operator may furthermore contain an artificial null space, which can adversely affect the linearized solvers.
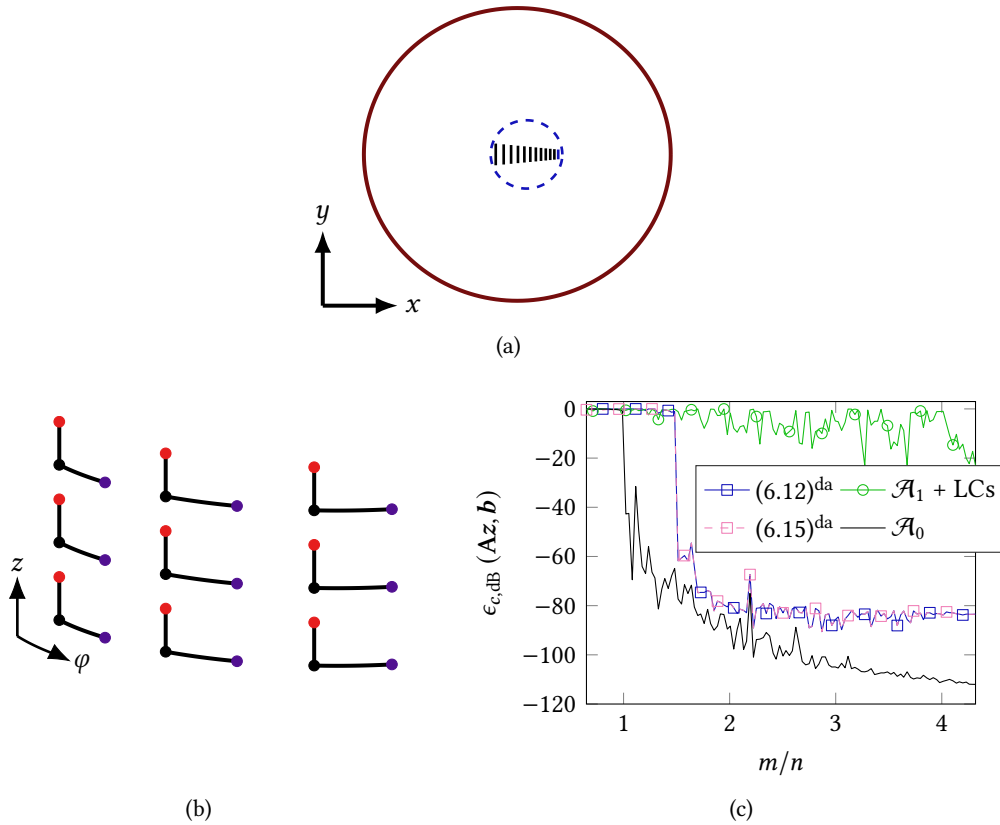
Fig. 6.6 (a) Illustration of the measurement setup of the logarithmic-periodic antenna. For the single-frequency case, local phase differences among the "L"-shape probe array depicted in (b) are assumed to be known. (c) The phase retrieval results for four transformation algorithms when fed with a varying amount of NF samples.

## Synthetic Data on a Real-World Drone Trajectory

A dual-polarized broadband Vivaldi antenna with a low back-lobe level has been proposed and investigated in [Azhar and Eibert 2021]. The design is intended to exhibit a decent mechanical stability while featuring a low weight due to an optimized all-aluminum construction. A digitally rendered image of the aluminum tapered-slot antenna (ALUTSA) is given in Fig. 6.7(a). The radiator is fed by two coaxial lines located on the front sides of two neighboring fins.

**ALUTSA — Near-Field Data Generation**   Based on a MoM simulation of the ALUTSA at 6 GHz in Feko, an equivalent Hertzian dipole representation on a box surface was determined and utilized to generate realistic NF data for measurement locations on a real-world drone trajectory. The employed multicopter and positioning system is described in [Mauermayer et al. 2019] whereas the truncated cylindrical flight path is indicated in Fig. 6.7(b). In particular, Fig. 6.7(b) depicts the dominant field component radiated by the equivalent ALUTSA dipoles on the box drawn in red.

For the given AUT, measurement locations and probe orientations, a multi-channel probe model is applied for data generation. As part of the field transformation algorithms, equivalent sources in the form of $n = 3 \times 10^3$ Hertzian dipoles on the surface of the blue sphere, as transparently drawn
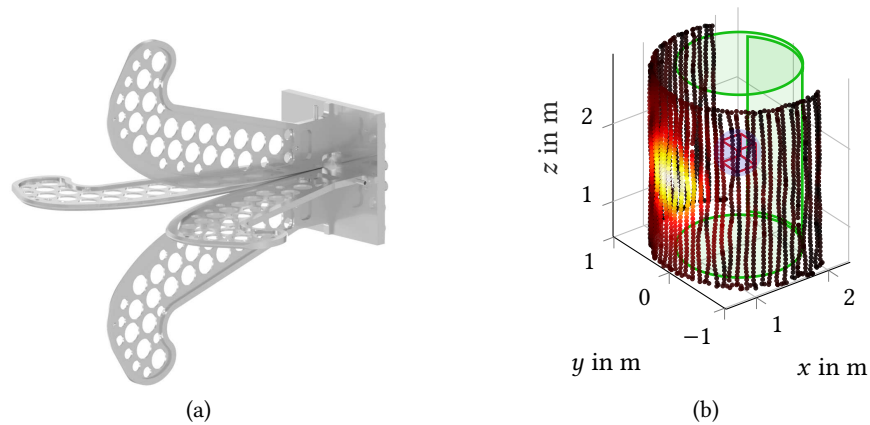
Fig. 6.7 Geometry of the ALUTSA in (a) and a synthetic NF antenna measurement setup combining the ALUTSA as an AUT with a real-world drone trajectory for the definition of the measurement locations and probe orientations in (b). The ALUTSA currents for NF generation are located on the red box, whereas for the field transformations equivalent surface current densities on an enclosing sphere, indicated in blue, are assumed. The green areas mark regions which have not been sampled and which may require special treatment within the phaseless transformation process.

in Fig. 6.7(b), are assumed. The areas drawn in green are not sampled by the probe at any time, so the reconstructed fields at these locations can have arbitrary values. When not taking care of this additional DoF, certain transformations algorithms are observed to be affected adversely.

The original ALUTSA sources on the red box in Fig. 6.7(b) and the measurement locations on the real-world drone trajectory are now utilized for the NF data generation with two different probe antenna arrays. The two-dimensional planar probe arrangements are illustrated in Figs. 6.8(a) and 6.8(b). Both arrays consist of four Hertzian dipoles, which are rotated and translated, effectively acquiring two field polarizations indicated by the red for horizontal and the green color for vertical polarization. The olive-colored elements in Fig. 6.8(a) receive an equally weighted sum of both field components. For the two probe arrays, the horizontal as well as the vertical separation between the elements was set to $\approx \lambda$.

**ALUTSA — Varying the Number of Measurements**    The resulting two sets of NF data have been processed assuming full coherence — as a reference — and only partial coherence among the four elements of each probe array. When varying the available number of measurements $m$, the NF deviations reported in Figs. 6.8(c) and 6.8(d) are obtained. Besides the reference, three different phase retrieval formulations have been applied. The scale-invariant, nonconvex solver has been utilized with $p_2 = 0.5$ and $p_2 = 1$, indicated by $\mathcal{A}_2^{0.5}$ and $\mathcal{A}_2^1$, respectively, as well as the linearized formulations with an added row and a direct solver, denoted by $(6.12)^{\text{da}}$ and $(6.15)^{\text{da}}$. For the nonlinear formulation, at most $5 \times 10^3$ iterations were performed and the knowledge of phase differences was incorporated in terms of LCs. As indicated by the green areas in Fig. 6.7(b), the measurement surface is not closed for the considered example, allowing for the rise of nonradiating sources, i.e., an artificial null space in the forward operator, when performing the field transformation without a proper regularization. Dependent on the severity of this effect, numerical issues may

result and deteriorate the accuracy of the transformation. One way of suppressing these undesired source contributions is to enforce zero field values outside the measurement surface. Therefore, an additional number of $2 \times 10^3$ measurements belonging to sample locations on the green areas featuring a magnitude of zero have been considered in the transformations marked with "+0s". Note that compared to the following results, similar improvements have been achieved by solving the linearized formulations with a sufficiently regularized solver, e.g., GMRES. Alternatively, only solving for source distributions that can be observed within the measurement region, e.g., in terms of a change of basis via a truncated SVD, is expected to eliminate the effect of the truncated measurement region.

In Figs. 6.8(c) and 6.8(d), the following observations can be made. The nonconvex and nonlinear formulation can not reliably provide decent results for the investigated range of $m/n$. Only the minimization in terms of the squared magnitudes, i.e., $p_1 = 1$, returns decent results in rare cases. No significant improvement is caused by adding the zero measurements with the nonlinear solver. In contrast, both linearized formulations exhibit a significant accuracy boost when suppressing nonradiating source contributions. This is mainly caused by the utilization of a direct solver and, as mentioned, could also be accomplished via a regularized iterative solver or by a proper choice of basis functions. In total, the linearized formulations are seen to outperform the nonlinear approach in terms of accuracy and reliability for the considered amount of NF data.

For reasons of completeness, the corresponding FF deviations within the valid region of $\vartheta \in [55°, 130°]$ with $\varphi \in [90°, 270°]$ are depicted in Figs. 6.8(e) and 6.8(f). The overall trend continues, however, a slight *processing gain* for all transformations can be observed. Here, $\mathbf{A}_{FF}$ and $\boldsymbol{b}_{FF}$ refer to the FF radiation operator and the true reference FF determined by the original ALUTSA sources.

The results in Fig. 6.8 may be compared to those obtainable with an unsuitable choice for a probe antenna array depicted in Fig. 6.9(a). Phase difference information among each polarization is only available in one (vertical) direction, whereas for the probes in Figs. 6.8(a) and 6.8(b) variation in both directions is revealed. As a result, the NF and FF deviations in Figs. 6.9(c) and 6.9(d), respectively, are considerably increased for all solvers working with partially coherent data. Still, slight improvements for the linearized solvers are observable when adding the synthetic measurements of zero magnitude.
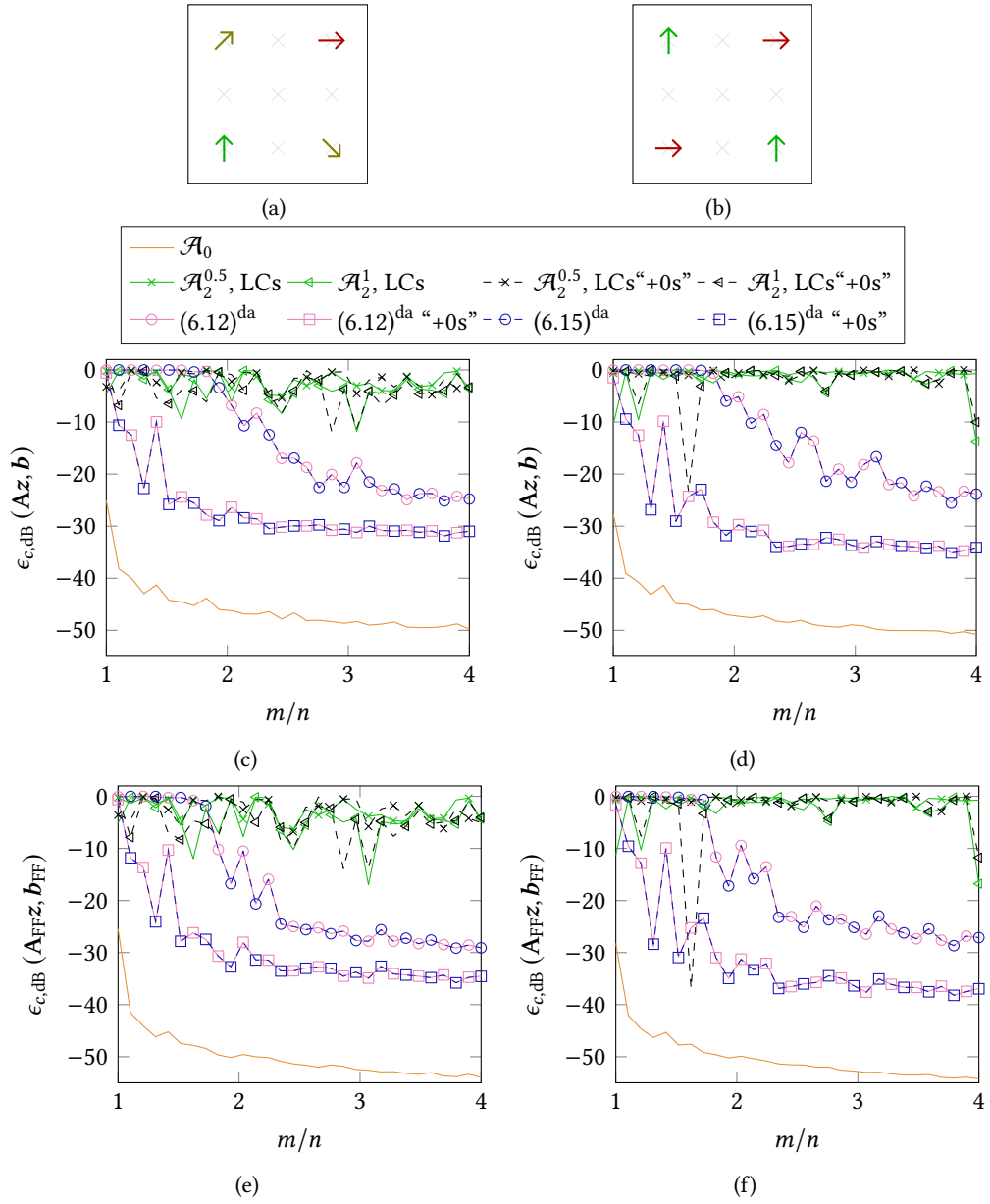
Fig. 6.8 Two probe arrangements, in (a) and (b), employed in combination with the virtual measurement setup of Fig. 6.7(b). Each two-dimensional probe array consists of four Hertzian dipoles, which sample the tangential electric field within the plane of the probe. Green colored elements extract the vertical polarization, red elements the horizontal polarization and the olive-green ones an equally weighted sum of both polarizations. The horizontal as well as vertical spacing between the elements is $\approx \lambda$. Noise according to $n_{\mathrm{SNR,dB}} = 60\,\mathrm{dB}$ was added to the NF data. The NF deviation achieved for various solvers when applied to the two probe arrangements of (a) and (b) is given in (c) and (d), respectively. The average relative FF deviation within the angular region of $\vartheta \in [55°, 130°]$ with $\varphi \in [90°, 270°]$ is depicted in (e) and (f).
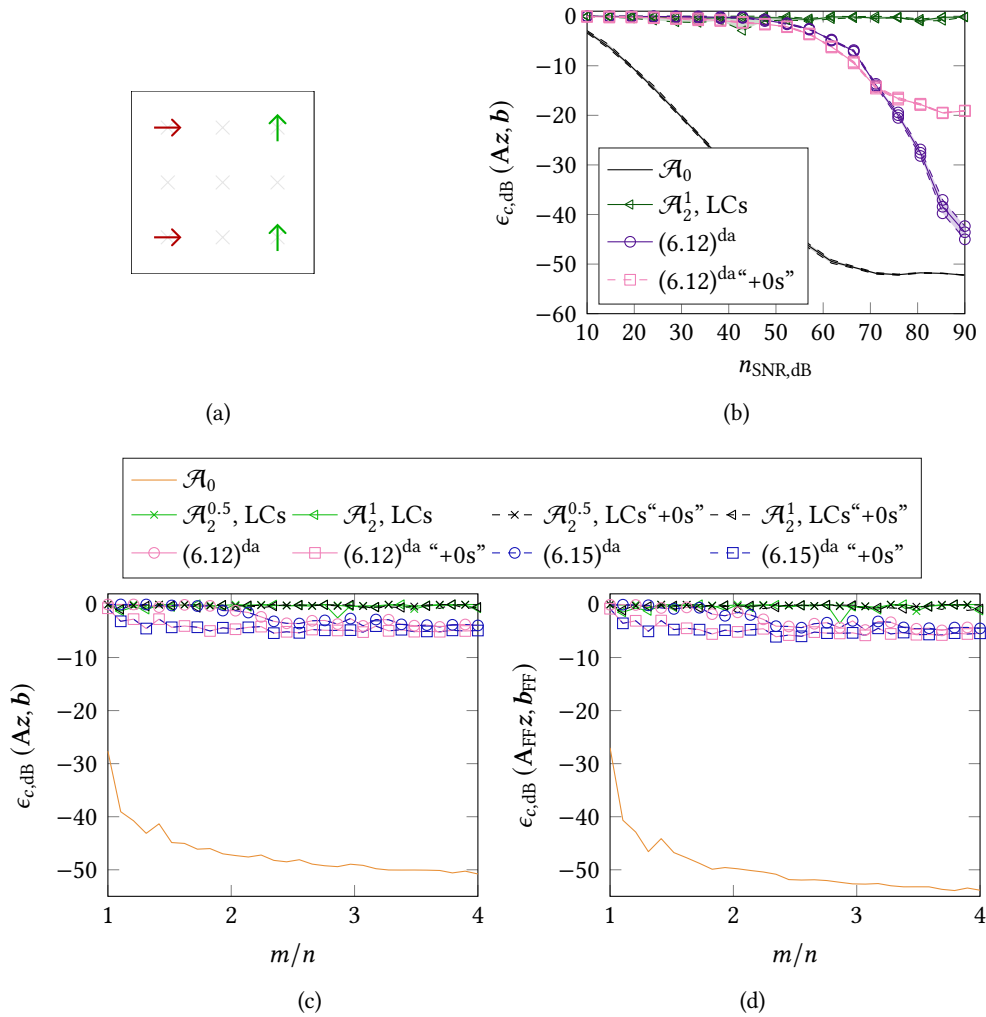
Fig. 6.9 (a) Improper choice of a probe antenna array employed in combination with the virtual measurement setup of Fig. 6.7(b). The two-dimensional probe array consists of four Hertzian dipoles sampling the tangential electric field within the plane of the probe. Green colored elements extract the vertical polarization, red elements the horizontal polarization. The horizontal and vertical spacing between the elements is $\approx \lambda$. (b) Achievable NF deviation for varying SNR values when $m/n \approx 3$. For each SNR value 20 repetitions with random noise realizations were conducted. The NF deviation achieved for various solvers is given in (c), where noise according to $n_{\text{SNR,dB}} = 60$ dB was added to the NF data. The average relative FF deviation within the angular region of $\vartheta \in [55°, 130°]$, $\varphi \in [90°, 270°]$ is depicted in (d).

**ALUTSA — Varying the SNR**   For a fixed oversampling ratio of $m/n \approx 3$, the SNR was swept from $n_{\text{SNR,dB}} = 10\,\text{dB}$ to $90\,\text{dB}$ and for each SNR value 20 repetitions with random noise realizations were performed. Figure 6.10 summarizes the results obtained with representative solvers — the performance of the linearized formulations has already been observed to be almost identical as part of Fig. 6.8 and only the best performing nonlinear formulation employing LCs was considered. The shaded regions indicate the variation of the results over the 20 runs, where the minimum, maximum and average NF deviation in decibels is drawn. The minimal achievable NF deviation can be deduced from the result of the reference solver based on $\mathcal{A}_0$ with full phase information, which stagnates below $\epsilon_{c,\text{dB}}(\mathbf{A}\mathbf{z}, \mathbf{b}) \approx -50\,\text{dB}$. With the employed probe antennas, any variation of the noise, even for the low-SNR regime, does not lead to any significant variations of the results obtained with the reference formulation. In contrast, the nonlinear formulation exhibits strong variations throughout most SNR regions. Only in rare cases, it can reconstruct the phase distribution more accurately than the linearized formulation employing the zero-measurements. Without these additional measurements, the linearized formulation is more susceptible to noise and shows more variation throughout all SNR values. However, in the high-SNR regime the artificial suppression of the forward operator null space is seen to limit the maximum accuracy. Shrinking the null-measurement region for larger values of the SNR would loosen the restrictions on the fields and help to avoid this stagnation of the NF deviation. Indicated by the results of the linearized formulation without the zero-measurements, similar levels of accuracy as with complete phase information can be achieved with the linearized formulations in the limit of high SNR values.

As expected, worse results are obtained and depicted in Fig. 6.9(b) when employing the unsuitable probe arrangement of Fig. 6.9(a). Essentially, the information encoded in the LCs, which could smooth out the nonconvexity and reduce the number of local stationary points, is obscured by the noise. The noise robustness is only slightly improved by adding the zero measurements and overall far larger SNR values are required for the linearized formulation to be able to determine an accurate solution. Still, the nonlinear solver based on $\mathcal{A}_2$ performs worse and was not able to find a mediocre quality solution even once.

**Concluding Remarks — Results with Phase Differences in Spatial Domain**   Either in the form of LCs or via linearized formulations, spatial phase differences have been observed to significantly improve the accuracy and success rate of phase retrieval algorithms. While incorporating LCs in existing general purpose reconstruction methods is straightforward, all positive as well as negative attributes of these algorithms persist — including the potentially unpredictable behavior of nonconvex methods. Existing formulations incorporating LCs steadily become more reliable and accurate in the regime of abundant numbers of measurements and phase differences. In contrast, far less measurements — deterministically predictable via (6.32) — are required by the linearized algorithms for spatial phase differences in order to work accurately and reliably. As such, the linearized methods behave similar to a fully coherent transformation, however, with an increased sensitivity for measurement inaccuracies and noise.
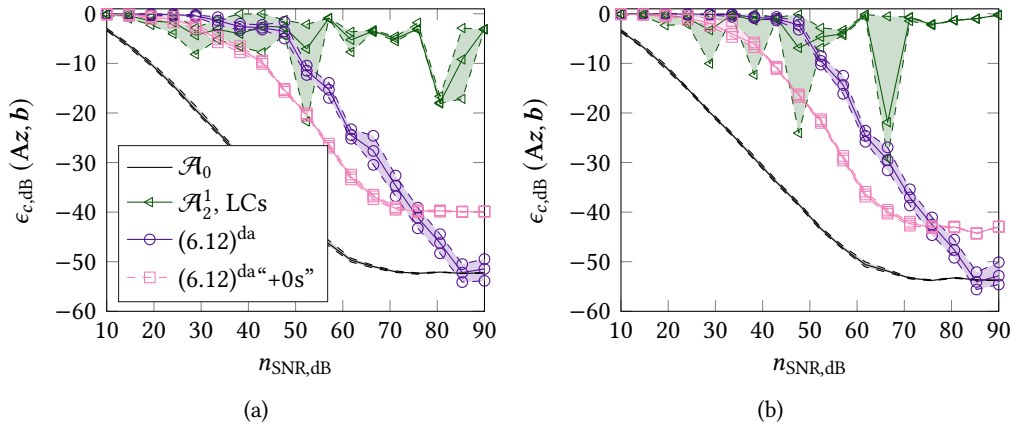
Fig. 6.10 Achievable NF deviation for varying SNR values. For each SNR value 20 repetitions with random noise realizations and with $m/n \approx 3$ were conducted. The results in (a) and (b) are based on the probe antenna array of Figs. 6.8(a) and 6.8(b).

## 6.3.2 Phase Differences in Frequency Domain

### Logarithmic-Periodic Antenna — Broadband Data

Broadband NF data of the already introduced logarithmic-periodic antenna depicted in Fig. 6.6(a) is employed for the task of phase retrieval from phase differences among probe signals at the same spatial location, but with varying frequency. NF measurements on a single cylindrical surface are considered, where the measurement cylinder features a radius of 20 m and is centered at $x = -8$ m. The height of the cylinder was set to 70 m and its lateral surface is discretized by 31 points in vertical and by 81 points in angular direction, resulting in a total of $m = 5022$ measurement signals comprising two polarizations. For the frequency range of interest from 35 MHz to 60 MHz, a varying number of coefficients of spherical multipole expansions ranging from $n = 336$ to $n = 576$ were chosen such that each frequency could separately (with full phase information) be solved up to an accuracy of $\epsilon_{c,dB} \approx -100$ dB. In total six frequency samples, in steps of 5 MHz, are considered and were transformed with the presented partially coherent formulations. As a parallel proof of concept, the same algorithms were also tested with random generated data, i.e., complex-valued normally distributed forward operators and source coefficients. White Gaussian noise was added to the corresponding measurement vectors such that a similar $\epsilon_{c,dB} \approx -100$ dB could be achieved (with full phase) for each of the six underlying linear systems. As a figure of merit for the performance of the considered algorithms, the maximum observable NF deviation of all of the frequencies was evaluated. The results for the simulated NF data and for fully-random data are stated in the first two rows of Tab. 6.1. The fully incoherent solver with $\mathcal{A}_2$ was applied to each frequency separately, as well as to the combined formulation in (6.44), without and with explicitly employing LCs similar to the way presented in (6.6). The linearized multi-frequency formulation (6.49) and, for reasons of comparison, the fully coherent solver applied to (6.43) were also included. For solvers working with $\mathcal{A}_0$ and $\mathcal{A}_2$, $5 \times 10^2$ and $5 \times 10^3$ iterations were allowed, respectively. The initial guess for all nonlinear solvers was computed via the optimal spectral method. The linearized multi-frequency formulation was

145

Tab. 6.1 Application of multi-frequency phase retrieval formulations to synthetic NF, random and mixed data. Spherical multipoles are employed as equivalent sources.

| $\mathbf{A}_i$ | $\boldsymbol{z}_i$ | $\max\limits_{i\in\{1,\,...,\,6\}} \epsilon_{c,\mathrm{dB}}\left(\mathbf{A}_i\boldsymbol{z}_i, \boldsymbol{b}_i\right)$ | | | | |
|---|---|---|---|---|---|---|
| | | $\mathscr{A}_2 \to \lvert\boldsymbol{b}_i\rvert$ | $\mathscr{A}_2 \to$ (6.44) | $\mathscr{A}_2 \to$ (6.44)+LCs | (6.49) | $\mathscr{A}_0 \to$ (6.43) |
| NF[1] | NF | $0\,\mathrm{dB}$ | $-0.4\,\mathrm{dB}$ | $-0.1\,\mathrm{dB}$ | $-8.3\,\mathrm{dB}$ | $-102\,\mathrm{dB}$ |
| rand[2] | rand | $-77.8\,\mathrm{dB}$ | $-95.2\,\mathrm{dB}$ | $-92.6\,\mathrm{dB}$ | $-104\,\mathrm{dB}$ | $-112\,\mathrm{dB}$ |
| rand | NF | $-91.3\,\mathrm{dB}$ | $-96.6\,\mathrm{dB}$ | $-93.6\,\mathrm{dB}$ | $-107\,\mathrm{dB}$ | $-111\,\mathrm{dB}$ |
| NF | rand | $0\,\mathrm{dB}$ | $-0.4\,\mathrm{dB}$ | $-0.1\,\mathrm{dB}$ | $-102\,\mathrm{dB}$ | $-110\,\mathrm{dB}$ |

[1] "NF": Forward operator and measurement vectors according to the multi-frequency NF measurement setup.

[2] "rand": Complex-valued normally distributed operators and solution vectors.

directly solved with Matlab's [Matlab 2021] **QR**-decomposition where the homogeneous system was transformed to a linear one by adding one row[2].

Based on Tab. 6.1, one can make multiple observations. Fully incoherent single-frequency NF antenna measurements on single surfaces do not provide sufficient information for a successful transformation with phase retrieval algorithms — again random data does work. Improvements can *potentially* be made when exploiting phase differences in multi-frequency measurements, and that is where again major differences dependent on the data models occur. This is visible when comparing the first and second row in Tab. 6.1, where all phaseless formulations, especially those utilizing multi-frequency information, show drastic improvements for random data compared to NF data. When it comes to comparing the incoherent/partially incoherent formulations for randomly drawn operators and source coefficients, only the multi-frequency approaches come close to the results of a fully coherent transformation. In addition, the linearized formulation is able to obtain slightly more accurate results than the nonlinear formulations.

The first two rows in Tab. 6.1 reveal severe doubts for the feasibility of the multi-frequency formulations applied to real-world NF antenna data. By alternately replacing either the operators or the true source coefficients of the random setup with that from the NF model, the results in the third and forth row of Tab. 6.1 can be obtained. In both cases, the measurement vectors were computed with the forward operator and source coefficients at hand and adding the same amount of noise to the measurement vectors as done previously in the case of random data. By looking at the performance of the linearized formulation, one can conclude that the multi-frequency formulations require a decent amount of "independence" of *either* the underlying radiating sources *or* the operators at the different frequencies. At least for the linearized formulation, there does not seem to be an issue with the slightly more ill-conditioned operators and potential similarity of those within the considered bandwidth. For the example of the logarithmic-periodic antenna, all nonlinear methods fail whenever NF-related forward operators are involved.

As a point of interest, the NF-related computations have been repeated with Hertzian dipoles placed tangentially on an AUT-enclosing box as equivalent sources. Slight improvements for the nonlinear formulations at the expense of strongly deteriorated accuracy of the linearized formulation is observed and reported in Tab. 6.2. The more stringent source localization of current-based AUT representations may be beneficial for general-purpose phase retrieval algorithms. The decreased

---

[2]See Fig. 6.4 and the description thereof for more details on how to solve the linearized formulations.

Tab. 6.2 Application of multi-frequency phase retrieval formulations to synthetic NF, random and mixed data. Hertzian dipoles as equivalent sources.

| $\mathbf{A}_i$ | $z_i$ | $\max\limits_{i\in\{1,...,6\}} \epsilon_{c,\mathrm{dB}}(\mathbf{A}_i z_i, \boldsymbol{b}_i)$ | | | | |
|---|---|---|---|---|---|---|
| | | $\mathscr{A}_2 \to |\boldsymbol{b}_i|$ | $\mathscr{A}_2 \to$ (6.44) | $\mathscr{A}_2 \to$ (6.44)+LCs | (6.49) | $\mathscr{A}_0 \to$(6.43) |
| NF[1] | NF | $-5.6\,\mathrm{dB}$ | $-14.1\,\mathrm{dB}$ | $-7.3\,\mathrm{dB}$ | $-3.7\,\mathrm{dB}$ | $-103\,\mathrm{dB}$ |
| rand[2] | rand | $-77.8\,\mathrm{dB}$ | $-95.2\,\mathrm{dB}$ | $-92.6\,\mathrm{dB}$ | $-104\,\mathrm{dB}$ | $-112\,\mathrm{dB}$ |
| rand | NF | $-5.6\,\mathrm{dB}$ | $-14.1\,\mathrm{dB}$ | $-7.3\,\mathrm{dB}$ | $-3.7\,\mathrm{dB}$ | $-103\,\mathrm{dB}$ |
| NF | rand | $-5.6\,\mathrm{dB}$ | $-15.6\,\mathrm{dB}$ | $-8.3\,\mathrm{dB}$ | $-7.5\,\mathrm{dB}$ | $-101\,\mathrm{dB}$ |

[1] "NF": Forward operator and measurement vectors according to the multi-frequency NF measurement setup, however, with equivalent Hertzian dipoles on an AUT-enclosing box.

[2] "rand": Complex-valued normally distributed operators and solution vectors.

performance of the linearized formulation is likely to be caused by the highly ill-conditioned forward operators often encountered with such kind of more redundant equivalent sources.

**Near-Field Data of a Triple-Horn Arrangement**

Broadband simulation data of an irregular three-element horn antenna arrangement was simulated in Feko. An illustration of the simulation model is given in Fig. 6.11(a). With strongly varying excitation coefficients of the antennas, the radiated NF was expected to feature more pronounced differences over frequency than in the previous example based on the logarithmic-periodic dipole array. The relevant tangential electric field components were acquired on two spherical surfaces with radii of 7 m and 9 m, indicated by the gray spherical shells in Fig. 6.11(a). The antennas were simulated at four discrete frequencies ranging from 150 MHz to 300 MHz in steps of 50 MHz. At each frequency $m_i = 4 \times 10^3$ $\forall i \in \{1, ..., 4\}$ measurement signals were randomly picked out of all available field values, resulting in $m = 16 \times 10^3$ known magnitudes in total. At each sampling location, the phase difference between probe signals (for each polarization separately) of different frequencies was assumed to be known. Inside the phaseless transformation algorithms, the horn antennas were then modeled by vector spherical wave functions with $n_1 = 720$, $n_2 = 966$, $n_3 = 1248$ and $n_4 = 1456$ at the frequencies $f_1 = 150\,\mathrm{MHz}$, $f_2 = 200\,\mathrm{MHz}$, $f_3 = 250\,\mathrm{MHz}$ and $f_4 = 300\,\mathrm{MHz}$, respectively. Table 6.3 summarizes the obtainable maximum NF deviation among all frequencies for various algorithms. More details on the comparison with random data models can be found in the description of Tab. 6.1 in the previous section. All nonlinear methods were started from an initial guess computed via the optimal spectral method.

With more variation over frequency, the considered NF data allows for the linearized formulation to yield a solution with better accuracy than when trying to solve each frequency separately. Again, the same setup, i.e., with the same number of unknowns and measurements, fully based on randomly distributed solution vectors and forward operators also allows all nonlinear approaches to find a precise solution. The third and forth row in Tab. 6.3 are examples of how the nonconvexity of the nonlinear solvers may affect the transformation results. The nonconvex formulation based on explicitly enforcing the phase differences with LCs is able to yield accurate results whenever either the operators or the source coefficients are randomly drawn. In contrast and probably due to bad luck, the remaining nonlinear solvers provide far worse results for the model in the fourth row.

Tab. 6.3 Application of multi-frequency phase retrieval formulations to synthetic NF data of an irregular horn array. Spherical multipoles are employed as equivalent sources.

| $\mathbf{A}_i$ | $\boldsymbol{z}_i$ | $\max\limits_{i \in \{1,...,6\}} \epsilon_{c,\mathrm{dB}} (\mathbf{A}_i \boldsymbol{z}_i, \boldsymbol{b}_i)$ | | | | |
|---|---|---|---|---|---|---|
| | | $\mathcal{A}_2 \rightarrow \lvert\boldsymbol{b}_i\rvert$ | $\mathcal{A}_2 \rightarrow$ (6.44) | $\mathcal{A}_2 \rightarrow$ (6.44)+LCs | (6.49) | $\mathcal{A}_0 \rightarrow$(6.43) |
| $\mathrm{NF}^1$ | NF | $-2.7\,\mathrm{dB}$ | $-1.3\,\mathrm{dB}$ | $-2.1\,\mathrm{dB}$ | $-17.9\,\mathrm{dB}$ | $-62.0\,\mathrm{dB}$ |
| $\mathrm{rand}^2$ | rand | $-60.1\,\mathrm{dB}$ | $-63.5\,\mathrm{dB}$ | $-63.4\,\mathrm{dB}$ | $-60.9\,\mathrm{dB}$ | $-63.7\,\mathrm{dB}$ |
| rand | NF | $-53.4\,\mathrm{dB}$ | $-63.2\,\mathrm{dB}$ | $-63.0\,\mathrm{dB}$ | $-58.8\,\mathrm{dB}$ | $-63.7\,\mathrm{dB}$ |
| NF | rand | $-1.8\,\mathrm{dB}$ | $-14.2\,\mathrm{dB}$ | $-61.0\,\mathrm{dB}$ | $-56.5\,\mathrm{dB}$ | $-62.1\,\mathrm{dB}$ |

[1] "NF": Forward operator and measurement vectors according to the multi-frequency NF measurement setup.

[2] "rand": Complex-valued normally distributed operators and solution vectors.

For reasons of completeness, the obtainable FF radiation characteristic after a phaseless transformation is shown in Fig. 6.11(b). The dominant electric field component in the $\varphi = 0°$ plane, containing the main beam, at a frequency of 150 MHz is drawn. In line with the numbers mentioned in Tab. 6.3, a single-frequency phaseless approach yields inaccurate FF results. Some degree of accuracy can be observed when applying the linearized MF formulation. Both results are compared to the FF resulting from a fully coherent NFFFT.

**Concluding Remarks — Results with Phase Differences in Frequency Domain**   While the concepts of how to exploit partial coherence in the spectral domain, i.e., phase differences in broadband signals, have been made clear, the insufficient diversity of realistic multi-frequency NF antenna data impedes their practical application. A stronger variation of either the forward operators or the equivalent source coefficients was seen to have a beneficial effect on the performance of all nonlinear and nonconvex but also the linearized formulations. Consequently, there may be potential use cases for antennas and measurement arrangements exhibiting a more pronounced frequency dependency. In all other cases, e.g., for narrowband AUTs, the utilization of spatial phase differences via multi-channel measurements is recommended.
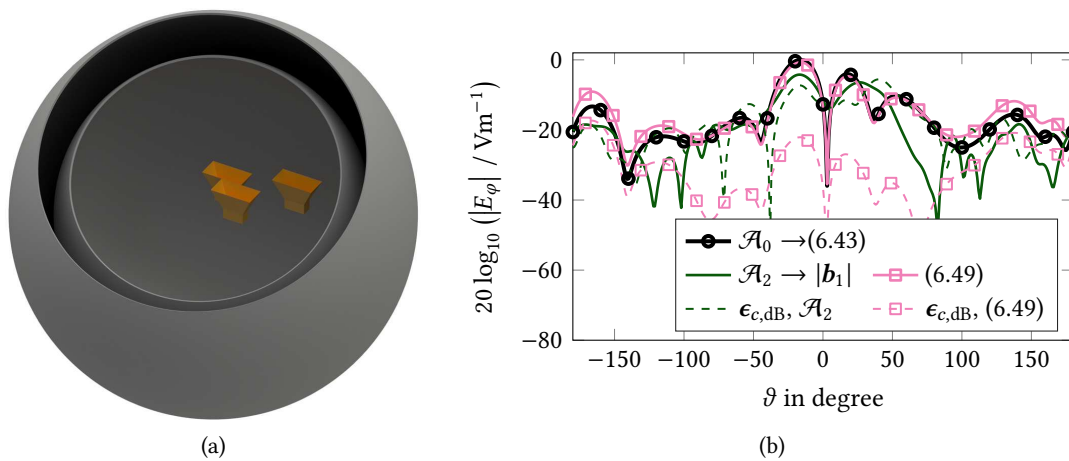
Fig. 6.11 (a) Illustration of the synthetic NF measurement setup consisting of three horn antennas
with strongly varying excitation coefficients. NF samples are acquired on two closed
spherical surfaces indicated by the gray shells. For the purpose of clearness, some part
of the measurement spheres is removed. (b) The obtainable FF radiation characteristic of
the dominant field component when performing the phaseless NFFFT for each frequency
separately or with the linearized MF approach. The deviation curves are computed with
respect to the result obtainable with full phase information. Only the field in the plane
with $\varphi = 0°$ for a frequency of 150 MHz is depicted.

# 7. Near-Field Far-Field Transformation with Obstacle Modeling

Real-world NF antenna measurements can not be conducted under idealized free-space conditions and are affected by various environmental influences, e.g., radiation from outside or material inhomogeneities within the measurement volume. In fact, great effort is spent on emulating a homogeneous disturbance-free environment in anechoic chambers of finite size, filled with additional hardware for positioning and moving the AUT as well as measurement probes. Despite the utilization of expensive wideband absorbers covering the walls and most of the auxiliary measurement components, experience shows that there may remain significant echo sources in the vicinity of the AUT. Strict requirements in terms of reliability, mechanical stiffness and loading capacity often require the mounting structures for the AUT to be made of metal or other electrically dense materials, which may give rise to significant echo contributions [Quijano et al. 2011]. When performing an NFFFT, the resulting FF is altered by the presence of these echoes in the NF data. Dependent on the relative distance between the AUT and the obstacles, the dominant coupling mechanism and, thus, the most appropriate echo suppression technique varies. Closely spaced objects will likely cause coupling in the reactive NF of the AUT, while objects further away will lead to the scattering of the AUT radiation.

In the following, source localization approaches for the compensation of echo sources in NF antenna measurements are presented. To a certain extent, the discussion follows the line of thought in [Paulus et al. 2019]. A possible extension of this work can be found in [Kornprobst et al. 2019]. After a brief overview on existing echo suppression techniques in Section 7.1, the concept of source localization is introduced in Section 7.2. In particular, three approaches based on source localization are discussed and applied to simulation data with full coherence in Section 7.3 and partial coherence in Section 7.4.

## 7.1 Overview of Echo Suppression Techniques

The possibility of echo suppression emerges from the assumption that signals stemming from the AUT and from the disturbing objects can be *differentiated*. Since radiators of finite size can only excite fields of limited DoFs, electromagnetic fields emerging from sufficiently spatially separated sources can theoretically be distinguished. Consequently, field transformation algorithms based on equivalent sources can exploit a-priori information about the AUT, for example in the form of inherent spatial filtering that comes from the localized model of the AUT, or by utilizing given properties of the modal spectrum of the AUT radiation [Cappellin and Pivnenko 2014; Eibert et al. 2015; Foged et al. 2013; Gregson et al. 2012; Hess 2010; Jorgensen et al. 2012; Kozan et al. 2014; Quijano et al. 2011; Quijano and Vecchi 2010]. Still, the performance obtainable with these techniques may not be sufficient for applications requiring high accuracy. Typically, techniques like time gating [Mauermayer and Eibert 2016, 2017], virtual beamforming [Knapp and Eibert 2018], scattering source localization [Araque Quijano et al. 2010; Quijano et al. 2011; Yinusa and Eibert 2013; Yinusa et al. 2012a; Yinusa et al. 2012b], low-pass filtering [Kozan et al. 2014; Mauermayer et al. 2013], modified Green's functions [Mauermayer and Eibert 2018], and scatterer modeling via

the uniform theory of diffraction (UTD) [Mauermayer and Eibert 2015] are thus applied in addition, when the AUT and the scattering object exhibit a sufficient spatial separation.

However, for closely spaced objects the measurement bandwidth required by time gating techniques in order to obtain a sufficient spatial resolution for separating the AUT and the scatterer may be unfeasible. Similarly, virtual beamforming requires an increasing number of measurements when the distance between AUT and scattering object decreases. In order to be able to create a decently steep transition between the nonzero fields at the AUT location and the (ideally zero) low field values at the scatterer geometry, virtual probe combinations with larger directivity are required. Effectively, this may render the approach useless for closely spaced obstacles in practice. Lastly, the conditions for ray-based techniques like the UTD are not fulfilled for this case. Thus, having considered most of the existing techniques for echo suppression, only source localization with its low-pass filter property seems to be applicable to remove, or at least reduce, the effect of obstacles close to the AUT. With more information about the measurement environment, echo objects can also be included in the form of a forward problem inside the original inverse source formulation. This has been done for dielectric bodies in [Mitharwal and Andriulli 2015; Omi et al. 2019].

In the following, two source localization methods removing the influence of perfectly electrically conducting (PEC) obstacles in the vicinity of the AUT as part of NF antenna measurements are presented. Both approaches can be interpreted as simple modifications to inverse-source based NFFFTs and are applicable to a variety of transformation algorithms.

## 7.2  Echo Suppression via Source Localization

Consider the two NF antenna measurement setups indicated in Fig. 7.1. In the reference case shown in Fig. 7.1(a), the AUT is assumed to be in free space, whereas in the second case in Fig. 7.1(b) a PEC obstacle is located nearby. In the latter case, the total fields collected by probe antennas at the measurement locations, indicated by the dashed contour, can be interpreted to consist of two portions, the signal directly coming from the geometry or location of the AUT and a disturbing portion stemming from the spatial region of the echo object. Note that there are further ways of classifying the contributions to the total received signal. However, in this way it is emphasized that the effect of the echo can be partially compensated by filtering out fields not being emitted by equivalent sources modeling the AUT — which is the task that we want to solve. Not only are the received NF signals distorted by the obstacle, but also the resulting equivalent sources and associated FF. Only when removing the echo influence, we are able to gain information about the free-space radiation characteristic of the AUT. It is important to notice that potential distortions of the equivalent sources of the AUT caused by the presence of the echo objects, often referred to as *mutual coupling*, can not be filtered out in this way. Once the current distribution on the AUT is altered, it can not be reversed or reconstructed in its original form with the methods discussed in this work.

An echo removal can now be tackled in various ways, where three possible attempts are illustrated in Fig. 7.2. The simplest approach, visible in Fig 7.2(a), is to ignore the PEC obstacle and only model the AUT in terms of equivalent sources. As the spatially restricted AUT representation can not fully account for the echo contributions to the probe signal, a relatively large NF deviation in (4.14) may be expected. This inherent low-pass filtering characteristic of source-based NFFFTs may be
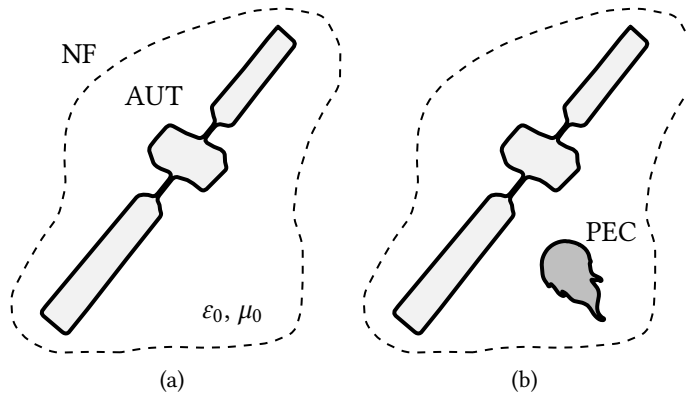
Fig. 7.1 NF antenna measurement setup without (a) and with (b) a PEC obstacle in the proximity of the AUT. The tangential AUT fields are sampled on an enclosing measurement surface indicated by the dashed contour.

sufficient for weak echo contributions, however, can be improved by modeling the echo objects as indicated in Figs. 7.2(b) and 7.2(c).

### 7.2.1 Source Localization of the Scatterer

In the second case, as shown in Fig. 7.2(b), equivalent sources are replacing the AUT and the echo object. Thus, in the last step of the NFFFT when the FF is computed from the equivalent sources, only the sources representing the original AUT are considered, potentially removing a large portion of the echo contribution. Effectively, the additional unknowns employed for the obstacle can be interpreted as belonging to a larger, extended AUT. With increasing AUT size, a larger number of NF samples is required in order to determine the unknown coefficients correctly [Hansen 2008]. In practice, this echo suppression method directly translates into longer measurement times. To a large degree, this methodology is identical to that discussed in [Araque Quijano et al. 2010; Quijano et al. 2011; Yinusa et al. 2012a; Yinusa et al. 2012b].

### 7.2.2 Scatterer Localization via Boundary Integral Equation

While the previous approach introduces certain knowledge on the echo objects in terms of their locations, it does not include the actual material properties. The supplementary measurement effort due to the larger number of equivalent sources can be avoided by taking into account the material properties in the form of a boundary condition (BC) on the obstacle surfaces. Here for reasons of simplicity, we will only consider PEC objects with the condition

$$\underline{n} \times \underline{E} = \underline{0}, \tag{7.1}$$

such that the tangential electric field has to vanish on the surface of PEC objects. Here, $\underline{n}$ is the normal vector pointing to the exterior of the respective object. Despite solving the inverse problem including the BC for the sources of the AUT and the obstacles, the desired FF is computed from the equivalent sources of the AUT only.
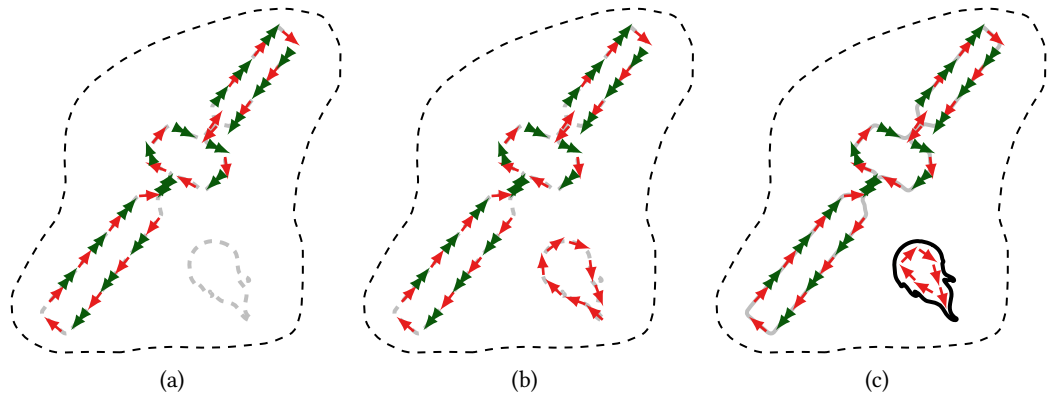
Fig. 7.2 Three equivalent models for the obstructed setup in Fig. 7.1(b). In (a), only equivalent sources for the AUT are employed, while in (b) the PEC obstacle is considered in terms of its own sources. In (c), the PEC BC on the surface of the obstacle is incorporated.

## 7.3 Source Localization — Full Phase Information

The three echo suppression methods based on source localization, as collected in Fig. 7.2, have been applied to simulation data obtained with the commercial simulation software Altair Feko [Altair Engineering Inc. 2018]. The two considered measurement scenarios are illustrated in Fig. 7.3, consisting of a horn antenna and a PEC sphere or PEC ellipsoid. For both cases, the reference FF was computed by simulating the horn antenna in free space with no obstacle present. For the transformation of the NF data contaminated by the echoes from the PEC objects, a dipole code accelerated by computations on GPUs was employed [Paulus and Eibert 2018a,b]. Hertzian dipoles [Schmidt et al. 2011] were used as equivalent sources and the PEC BC was incorporated by means of the method of auxiliary sources (MAS) [Anastassiu et al. 2002; Eisler and Leviatan 1989; Hassan and Kishk 2018; Heretakis et al. 2005; Kaklamani and Anastassiu 2002; Kouroublakis et al. 2021; Leviatan 1990; Moharram and Kishk 2015a,b; Petoev et al. 2015; Zaridze et al. 1998]. Similar to the method of the dipole moment (DM) [Mittra et al. 2011; Panayappan and Mittra 2015], MAS represents an alternative to the classical MoM [Harrington and Harrington 1996] used to solve electromagnetic problems. Though often falsely claimed, MAS does not feature a lower computational complexity than MoM, however, as its core benefit it does not require the treatment of singularities in the underlying integral equations. Identical to the DM approach, MAS avoids singularities by offsetting test and basis functions. The radiation operators utilized in NFFFTs, which are commonly applied to problems where sources and observation locations are spatially separated, can thus directly be applied to construct the relevant impedance matrix. As a downside, MAS is often observed to exhibit a limited accuracy, not comparable to a full MoM with singularity treatment, especially if the objects to be modeled have sharp corners or edges. Still, for the PEC sphere and PEC ellipsoid in Fig. 7.3, MAS has shown to be a suitable and easy-to-implement alternative to MoM for incorporating the BC in (7.1).

All occurring linear systems of equations related to the dipole-NFFFT have been solved via the fully coherent solver based on $\mathcal{A}_0$, such that a relative NF deviation of $\epsilon_{c,\mathrm{dB}} = -45\,\mathrm{dB}$ is achieved, or, at most $5 \times 10^2$ iterations have been performed. The dipole representation of the horn antenna
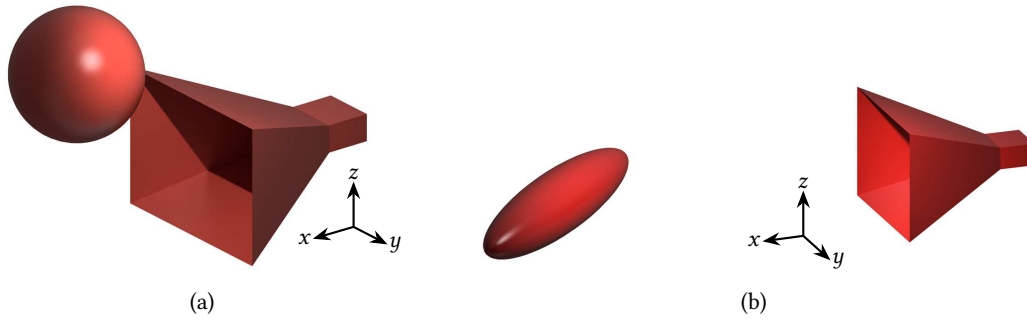
Fig. 7.3 (a) A PEC sphere with a diameter of $2\lambda$ in front of the horn aperture, which is at $x = 0.9\lambda$. The center of the sphere is located at $[3, 0, 2]\lambda$. (b) A PEC ellipsoid is placed at a distance of about $7.5\lambda$ in front of the horn. © IEEE 2019.

in free space was observed to achieve a maximum relative FF error of around $-55\,\text{dB}$ compared to the FF in Feko.

The two scattering scenarios illustrated in Fig. 7.3 are considered. In Fig. 7.3(a), a PEC sphere obstacle is placed in front of the horn antenna. The sphere has a diameter of $2\lambda$ and is located $3\lambda$ and $2\lambda$ apart the horn aperture in $x$-and $z$-direction, respectively. With an approximately closest distance of $\lambda$, the sphere is expected to be in the reactive NF of the AUT. The second example depicted in Fig. 7.3(b) features a PEC ellipsoid. The minimal distance between the horn aperture and the obstacle is around $6.6\lambda$, whereas the length and width of the ellipsoid are $6\lambda$ and $1.2\lambda$.

In a first step, the influence of mutual coupling between the echo objects and the antenna is estimated. Due to the presence of the obstacle, the current distribution on the AUT is modified, causing errors in the computed FF when only evaluating the equivalent sources for the horn antenna as part of the NFFFT later on. Thus, two simulations in Feko are performed for each scenario. Firstly, the FF of the horn antenna in free space is calculated and secondly, the current distribution on the horn is determined under the influence of the PEC object. In Fig. 7.4(a), the dominant FF component in the plane with $\varphi = 0°$ through the main beam of the horn antenna is depicted. In addition, the echo-perturbed simulation model is used to determine the FF only caused by the currents on the horn antenna and the results are added with the label "AUT". The ideal reference FF in free space is label with "Free space" and the fully-perturbed FF, including the effect of the obstacle, here a sphere, is denoted as "AUT+O". As can be seen, the presence of the PEC sphere does alter the FF characteristic in this plane up to a relative level of $-10\,\text{dB}$, whereas the mutual coupling modifies the currents on the horn antenna, such that a FF error of $-26\,\text{dB}$ is observed. It is this difference between the totally distorted FF with $-10\,\text{dB}$ deviation and that solely affected by mutual coupling up to $-26\,\text{dB}$, which one wants to exploit with the source-localization based echo suppression methods. It should be kept in mind that the presented methods can not overcome the limitations related to mutual coupling, as there is no simple way of recovering the original current distribution on the horn antenna. Figure 7.4(b) showcases the mutual coupling analysis for the case of the ellipsoidal scattering object. Here, the FF in the plane with $\vartheta = 90°$ cutting through the main beam is depicted. As the separation between the AUT and the ellipsoidal obstacle is considerably larger than in the example of the sphere, a lower distortion of up to $-15\,\text{dB}$ and a mutual coupling of below $-39\,\text{dB}$ is observable.
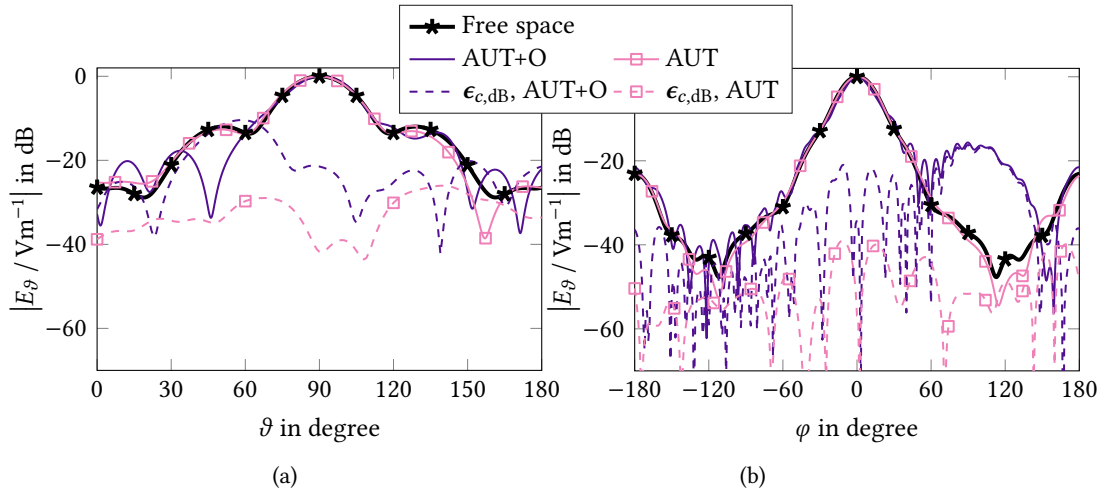
Fig. 7.4 In (a) and (b), the mutual coupling effect of the PEC sphere and ellipsoid on the FF pattern of the horn antenna is illustrated. Here, "AUT+O" refers to the fields caused by the AUT sources as well as the currents on the PEC object. For the PEC sphere, the plane $\varphi = 0°$ is considered while for the ellipsoid the $\vartheta = 90°$ plane is drawn. The field deviations are evaluated with respect to the free-space curves decorated with stars. (a) © IEEE 2019.

In the second step, the three discussed approaches are applied in order to remove the FF distortions up to the contribution of mutual coupling. As such, the mutual-coupling affected curves labeled with "AUT" in Figs. 7.4(a) and 7.4(b) are now considered the references and are denoted as "AUT only" in Figs. 7.5(a) and 7.5(b). For the sphere and the ellipsoid, ignoring the presence of the scatterer and solely modeling the AUT, one can obtain the curves labeled with "Ignore". Adding equivalent sources for the sphere but not including the BC, results in the curves denoted with "No BC". Finally, including the BC yields the best results named with "BC". Only the model including the PEC BC is able to achieve a reasonable error level of below $-50$ dB for the case of the PEC sphere in Fig. 7.5(a). The other methods yield FF errors on the order of $-10$ dB and $-15$ dB, respectively. It should be kept in mind that the NF sampling density in this particular example was set according to the minimum sphere of the AUT. Increasing the number of measurement samples, i.e., allowing to resolve all modes present in the fields, lets both methods, which model the obstacle with and without BC, perform on the same level. For the case of the ellipsoid, the results in Fig. 7.5(b) show that both methods, with and without considering the BC, drastically improve the FF accuracy when compared to ignoring the scatterer. To be more precise, the observable maximum FF errors are $-47$ dB, $-60$ dB and $-16$ dB when not using the BC, using the BC and ignoring the obstacle, respectively.

Focusing on the approach enforcing the BC, a core question arises. How accurately does one need to know the position and shape of the PEC scatterer such that modeling the BC improves the transformation quality? In Fig. 7.6, the influence of positioning inaccuracies in terms of the PEC sphere is illustrated. Typically, the location of scatterers is required to be known up to $\lambda/25$ when only the direct path (scatterer to RX) is considered. Multiple paths and reflections may even worsen this requirement, such that the location of the relevant surfaces may need to be known up to $\lambda/50$ or $\lambda/100$. As in this particular example mutual coupling already accounts for FF errors around $-26$ dB, a less stringent positioning accuracy is necessary. In the $y$-direction, shifts of around $\pm0.1\lambda$
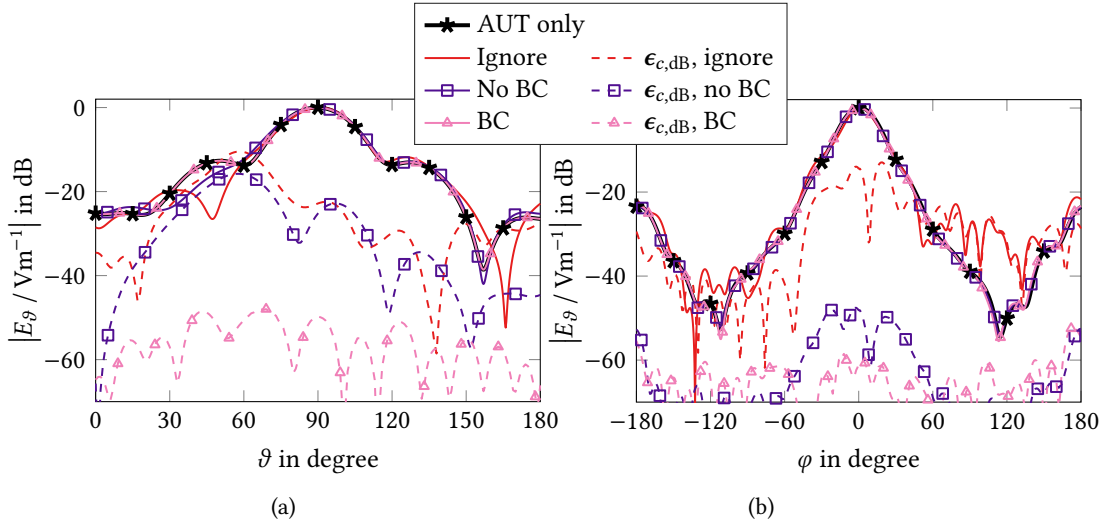
Fig. 7.5 In (a) and (b), the FF transformation results for the synthetic NF measurements including the PEC sphere and PEC ellipsoid are shown. For the PEC sphere, the plane $\varphi = 0°$ is considered while for the ellipsoid the $\vartheta = 90°$ plane is drawn. The field deviations are evaluated with respect to the AUT-only curves decorated with stars. (a) and (b) © IEEE 2019.
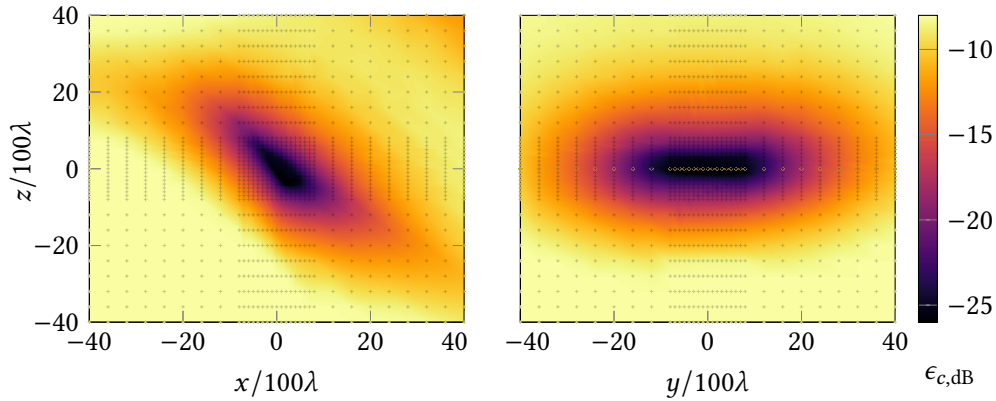


Fig. 7.6 A solution deterioration analysis assuming a wrong scatterer position inside the NFFFT with included PEC BC according to (7.1). The maximum FF deviation is shown. © IEEE 2019.

are not expected to cause errors exceeding those of the mutual coupling effect. On the other side, the distance to the AUT in $x$-direction is observed to be more sensitive to positioning mistakes.

In Fig. 7.7, the NF of the horn antenna in free space can be compared to the field distribution when solving for the equivalent sources of the AUT and the currents on the PEC ellipsoid. Extracting and evaluating only the AUT currents from the latter, the field distribution in Fig. 7.7(c) can be obtained. The result comes visually close to that of the free-space reference in Fig. 7.7(a).

**Concluding Remarks — Fully Coherent Source Localization** Obstacles in the close proximity of the AUT affect the collected NF data and, thus, the transformed FF via two disturbance
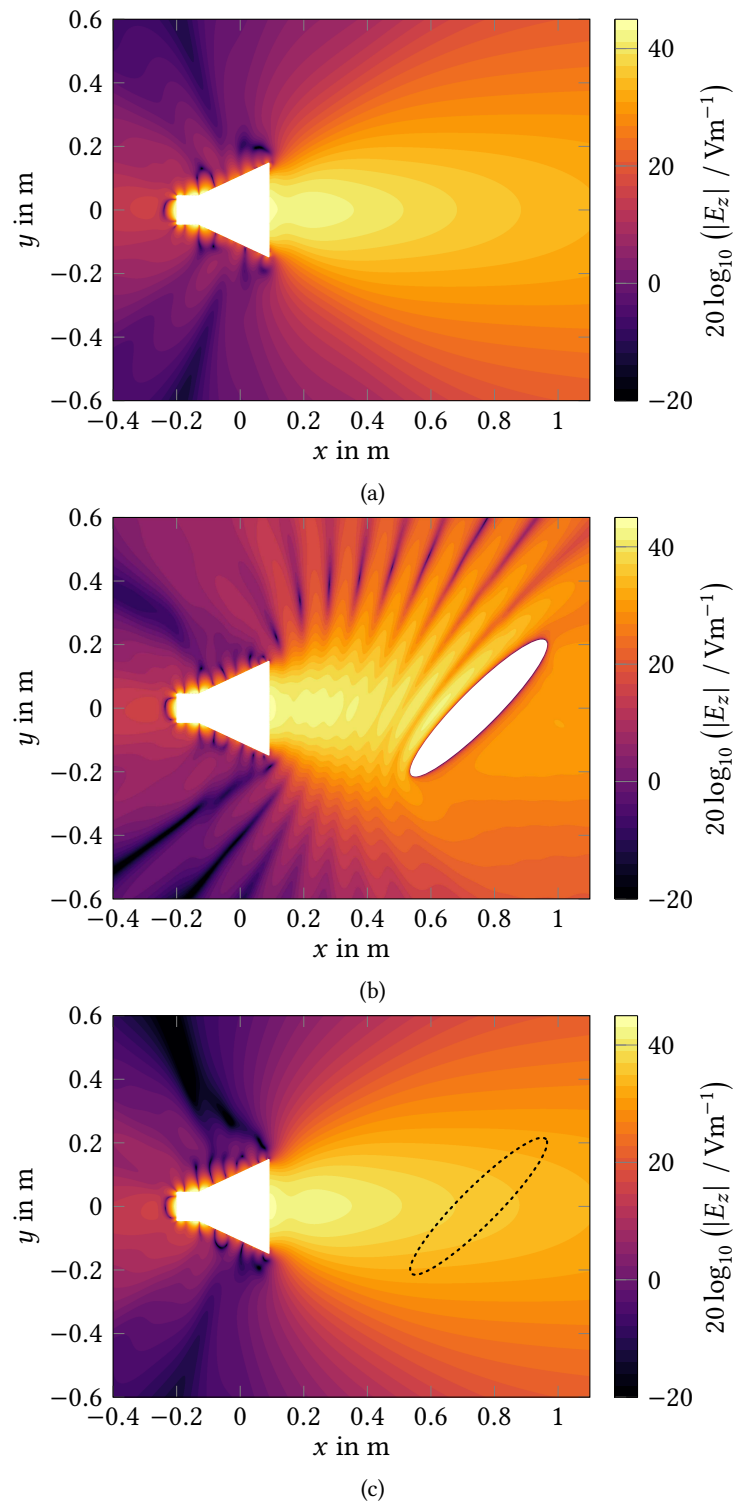
Fig. 7.7 Magnitude of the electric NF in the $z = 0\,\mathrm{m}$ plane. (a) Caused by the free-space solution. (b) The solution including the PEC ellipsoid. (c) The extracted AUT currents. © IEEE 2019.

mechanisms. First, fields radiated by the AUT are scattered at the object, yielding a modified field distribution at the probe locations. Second, the presence of the obstacle modifies the currents on the AUT itself, which then exhibits a different radiation behavior. Source localization methods are able to partially compensate for the first mechanism, however, they can not remove the effect of the latter disturbance — also called *mutual coupling*. In particular, modeling the scatterer in terms of additional equivalent sources is seen to remove the scattering contribution of obstacles to a large degree. Less NF measurement samples are required in case the material properties of the obstacle are considered additionally, e.g., in the form of BCs.

## 7.4  Source Localization — Partially Coherent Data

So far, the capabilities of the three source-localization based echo suppression methods illustrated in Fig. 7.2 have been applied to fully coherent data. However, the same principles are expected to hold true for phaseless or partially coherent measurement data. In the following, a simulation setup similar to that depicted in Fig. 7.3(a) is considered. Both the horn antenna and the PEC sphere feature a slightly different geometry, where the diameter of the sphere was kept at $2\lambda$. The surface of the sphere is located roughly $2.3\lambda$ away from the aperture of the horn, in the main beam direction. The model was again simulated in Feko [Altair Engineering Inc. 2018] and the currents on the horn antenna were evaluated, as well as NF data on a spherical surface with a radius of $10\lambda$ was computed. In order to also provide NF data with *partial coherence*, a three-element probe antenna array with an "L"-shaped arrangement was employed. The inter-array element separation in both directions of the array was set to $0.5\lambda$ and the elements were modeled as Hertzian dipoles. The received signals for two polarizations were obtained by rotating the "L"-probe by $90°$. The 1500 sample locations on the spherical surface were determined according to a Fibonacci mapping [Keinert et al. 2015], effectively resulting in an almost uniform distribution on the measurement sphere. In total, $3 \times 2 \times 1500 = 6 \times 10^3$ measurement entries related to NF data have been utilized. The AUT was represented by $8 \times 10^2$ Hertzian dipoles and the PEC sphere was modeled with $3 \times 10^3$ Hertzian dipoles as sources and 3200 BC field values were tested, corresponding to two tangential field components at 1600 locations.

In a first step, the effect of the mutual coupling between the PEC sphere and the horn antenna was estimated by comparing the FF of the horn antenna in free space and that obtained from the simulation in the presence of the obstacle. Based on the latter simulation, only the surface currents on the AUT geometry were used to compute the "AUT only" FF pattern depicted in Fig. 7.8. The free-space pattern were computed from the NF data exported from Feko, evaluated first with full phase information ("Coherent") and secondly assuming the partial coherence between the probe array elements ("Part. coh."). As expected, and due to the sufficient number of measurement samples utilized, both transformations return an almost identical result with a maximum FF deviation of around $-23.5\,\mathrm{dB}$ with respect to the FF affected by the mutual coupling. For the transformation with partial coherence the formulation in (6.15) was employed.

In the next step, the FF distorted by the mutual coupling was taken as a reference for the results obtained with the three source-localization methods. All three methods were applied to the fully coherent and the partially coherent simulation data. The results are collected in Fig. 7.9, where for the curves in Fig. 7.9(a) full phase information was utilized and for Fig. 7.9(b) only the partial coherence between the probe array elements was exploited. Independent of the phase information, the transformation results obtained when not actively modeling but instead "ignoring"
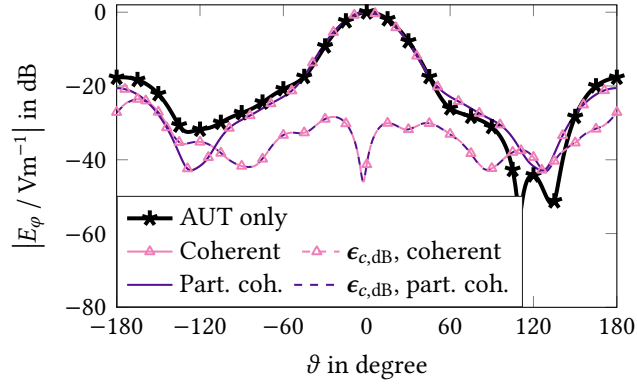
Fig. 7.8 Radiation characteristic of a horn antenna distorted by an obstructing PEC sphere in the vicinity of the horn aperture. For the FF computation, only the AUT currents have been evaluated. For comparison, the FFs obtained via a fully coherent and a partially coherent NFFFT, via (6.15), from NF data of the horn antenna in free space are depicted. Only the dominant field component of the AUT in the $\varphi = 0°$ plane is drawn.

the PEC scatterer are distorted to a very large degree. In this case, the inherent low-pass filtering of the equivalent sources of the AUT is insufficient to separate the fields caused by the AUT and the obstacle. Improved performance for this approach is expected when utilizing a simplified representation of the AUT featuring less unknowns, i.e., less DoFs, and thus stronger filtering properties. More accurate results can be obtained by modeling the scattering object, either with or without enforcing the BC on the surface of the PEC obstacle. While the results in Fig. 7.9(a) with fully coherent data are relatively similar in both cases, stronger discrepancies are visible for partial phase knowledge and the results thereof in Fig. 7.9(b). The explanation of this effect is based on two facts. First, for the same number of measurements, partial coherence provides less information than full coherence. Second, adding more measurements, e.g., in the form of a BC, improves the noise robustness of field transformation algorithms — known as *processing gain.* For the fully coherent results in Fig. 7.9(a), sufficient information was provided with and without BC, such that the results are mainly bound by the accuracy limitations of the equivalent AUT representation. The same limit is only reached with the additional BC measurements in Fig. 7.9(b). As a consequence, the partially coherent results without BC could be improved by providing more measurement data, leading to a more pronounced processing gain and noise robustness. In other words, the results with and without BC for fully coherent data as well as the results for partial coherence with the BC are bound by the equivalent model. Without the BC, the results for partially coherent data are noise bound. Nevertheless, the NFFFT for partially coherent data in the form of (6.15) is well suited for the application in echo suppression techniques via source localization.

**Concluding Remarks — Partially Coherent Source Localization**   The concept of source and scatterer localization for echo suppression in field transformation remains applicable for phaseless and partially coherent data. In particular, a promising agreement of the performance of source localization methods with fully and partially coherent data was observed. In practice, care should be taken to ensure a sufficient amount of measurement samples, especially when not incorporating knowledge about the material properties of the scatterer, e.g., in the form of BCs. It should also
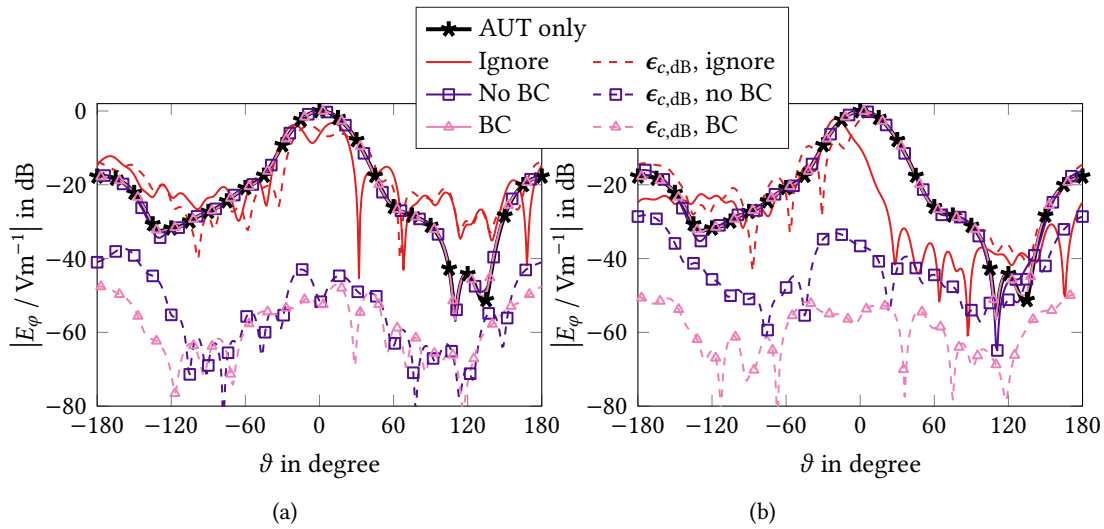
Fig. 7.9 Radiation characteristics obtained from NFFFTs employing the three source-localization based echo suppression methods illustrated in Fig. 7.3. As the effect of mutual coupling can not be removed in any case, the FF obtained from only the true AUT currents (distorted by the PEC object) is taken as a reference. Results for an NFFFT with full phase information in (a). In (b), only the partial coherence among the three elements of an "L"-shaped probe antenna array is assumed and processed via (6.15).

be kept in mind that the partially coherent approaches require a linear amount of additional measurements in order to achieve the same level of accuracy as the fully coherent solvers.

# 8. Summary and Conclusion

Electromagnetic field transformations working with a variable amount of phase information have been investigated. The problem statement requires knowledge in the regimes of electromagnetics and optimization theory. First, the theoretical foundations for electromagnetic transformations with complete phase information in the form of the uniqueness and the equivalence principle have been reviewed. Simple yet powerful and highly-parallelized radiation operators were provided for the description of the electromagnetic fields. Second, the rudimentary principles of nonconvex, non-linear, unconstrained and multivariate optimization of complex-valued quantities via the Wirtinger calculus have been discussed. A flexible optimization framework intended for the treatment of a variety of electromagnetic problems was presented.

In a first step, the tools and procedures from the fields of electromagnetics and optimization theory have been utilized to perform *phase retrieval* from fully incoherent data. Routines for the generation of initial guesses, nonconvex and convex algorithms have been observed to perform far inferior when provided with realistic near-field (NF) antenna data instead of complex-valued normally distributed data, which is mainly utilized as a baseline for comparisons in literature. At this point, phase retrieval for random normally distributed data can be considered as solved once a sufficient number of measurement samples is available. In essence, measurements belonging to a random data model have only a minimum degree of redundancy, so each additional measurement adds information to the problem. In contrast, phase retrieval remains challenging in most applications of practical relevance, where successive measurements show redundancy due to the underlying physical process. The issue can not be evaded by simply employing an increased number of measured magnitudes, instead, the arrangement of the measurement setups need to be modified in order to provide more restrictions on the phases and, thus, increase the chance of a successful phase retrieval. Aside the data dependency, various phase retrieval formulations for fully incoherent data have been seen to perform similarly. In practice, the required computational resources are expected to be the main reason for favoring one or another method. It should be stressed that the strong data dependency was also encountered with convex algorithms, which in this work have not been observed to perform better than their nonconvex counterparts when treating NF data.

Aside numerous iterative algorithms, a direct phase retrieval formulation — of striking simplicity – has been discussed. The main drawbacks are its quadratic sampling complexity, i.e., requiring the largest number of magnitude measurements among all existing methods, and its large computational complexity, which is comparable to that of most convex methods. Once a sufficient number of suitable measurements are available, this approach returns the unknown phase distribution at the expense of solving multiple linear systems of equations. However, as the main accomplishment of this method, it can be utilized to roughly judge the suitability of a forward operator or, equivalently, a measurement setup for the task of phase retrieval. Overall, unsatisfactory results have been reported for any of the investigated phase retrieval methods or approaches, when working with *conventional* phaseless NF antenna data.

This shortcoming of typical electromagnetic field data was the starting point for phase retrieval from *partially coherent* measurements. As has been motivated, realistic antenna measurement setups often allow the acquisition of incomplete knowledge of phase differences, either in the frequency or spatial domain. These potentially tiny portions of phase information can have drastic impact on the performance of phase retrieval algorithms, enabling for the first time reliable and predictable

field transformations based on magnitude-only information. Phase differences were shown to be utilizable with existing nonlinear retrieval algorithms via interferometric equivalences, i.e., in the form of magnitudes of linear combinations (LCs), as well as exploitable in linearized formulations. Especially the latter outperform existing approaches based on LCs in terms of the required number of measurements — predictable via a deterministic necessary condition — , and more importantly, in terms of reliability. Only in the regime of a large number of available phase differences with low signal-to-noise ratio (SNR) should the existing techniques with LCs be preferred over the linearized methods. This may be subject to changes in the near future as more knowledge and improvements are gained for the linearized formulations.

Promising results have been obtained when applying the concept of partial coherence to echo suppression techniques for NF antenna measurements based on source localization. Except for disturbances in the current distribution of the antenna under test (AUT) due to mutual coupling, the presented methods were able to significantly suppress echo contributions of a closely located object made of perfectly electrically conducting (PEC) material — with full or partial coherence. In particular, knowledge of the scatterer material was exploited to reduce the required number of measurements, which were expectedly larger with incomplete phase information than with full coherence.

In the context of NF antenna measurements, phase retrieval remains a difficult task. For well suited models, e.g., random normally distributed forward operators, a phase reconstruction is already feasible with existing techniques, which then behave quite similarly. As such, the various general purpose phase retrieval approaches published in the past decades have provided negligible improvements for treating real-world phaseless problems. More benefits are to be expected from highly specialized formulations, customized to the problems at hand and, most importantly, which are able to incorporate as much knowledge on the problem statement as possible. Phase retrieval is all about finding a formulation which represents the best compromise of mathematical elegance (simplicity) and favorable properties (linearity, convexity, ...), while still enforcing as many restrictions on the problem as possible (all magnitudes, phase differences, bandlimitedness, ...). Since real-world problems vary in terms of available knowledge and side constraints, the optimal formulation changes from application to application and there is no ideal approach that fits perfectly for all problems. A first step in the direction of *specialization* has here been taken with the concept of *partially coherent* measurements. With a slightly reduced generality, i.e., requiring the knowledge of a certain portion of phases, the phase retrieval problem was seen to become solvable via linearized formulations with reasonable computational effort and a linear sampling complexity, i.e., requiring a similar number of measurements as a fully coherent approach. The concept is well applicable to a variety of NF antenna measurements and may prove feasible in other fields of research. It is expected that the maturity of the presented linearized algorithms will improve over the coming years, providing better noise robustness and improved handling of artificial null spaces in the operators.

# A. Appendix

## A.1 Electric Field of Current Densities in Free Space

The two equations (2.26) and (2.27) stating the electric field radiated by electric and magnetic current densities in free space are briefly derived here.

### Magnetic Current Density

We start from the two fundamental equations

$$\underline{E}\left(\underline{r}\right) = -\frac{1}{\varepsilon}\nabla \times \underline{F} \tag{A.1}$$

$$\underline{F}\left(\underline{r}\right) = \frac{\varepsilon}{4\pi} \iiint \frac{e^{-jkR}}{R}\underline{M}\left(\underline{r}'\right)\mathrm{d}V' \tag{A.2}$$

relating the electric vector potential with the electric field, where $R = \left\|\underline{R}\right\|_2$ and $\underline{R} = \underline{r} - \underline{r}'$. The vectors $\underline{r}$ and $\underline{r}'$ describe the observation and source location. With the spatial derivative with respect to the observation location

$$\nabla \stackrel{\wedge}{=} \frac{\partial}{\partial \underline{r}} \quad \text{and} \quad \frac{\partial R}{\partial \underline{r}} = \frac{\partial}{\partial \underline{r}}\left(\underline{R}^{\mathrm{T}}\underline{R}\right)^{\frac{1}{2}} = \frac{1}{R}\underline{R} \tag{A.3}$$

one can write

$$\underline{E}\left(\underline{r}\right) = -\frac{1}{4\pi}\iiint \nabla \times \frac{e^{-jkR}}{R}\underline{M}\left(\underline{r}'\right)\mathrm{d}V' \tag{A.4}$$

$$= -\frac{1}{4\pi}\iiint \nabla\left(\frac{e^{-jkR}}{R}\right) \times \underline{M}\left(\underline{r}'\right)\mathrm{d}V' \tag{A.5}$$

$$\underline{E}\left(\underline{r}\right) = -\frac{1}{4\pi}\iiint \underline{M}\left(\underline{r}'\right) \times \underline{R}\frac{e^{-jkR}}{R^3}\left(jkR+1\right)\mathrm{d}V', \tag{A.6}$$

which equals the formula stated in (2.27). For (A.5) we used the identity

$$\nabla \times \left(x\left(\underline{r}\right)\underline{A}\left(\underline{r}'\right)\right) = x\left(\underline{r}\right)\nabla \times \underline{A}\left(\underline{r}'\right) - \underline{A}\left(\underline{r}'\right) \times \nabla x\left(\underline{r}\right) \tag{A.7}$$

for a scalar field $x\left(\underline{r}\right)$ and a vector field $\underline{A}\left(\underline{r}'\right)$, which simplifies to

$$\nabla \times \left(x\left(\underline{r}\right)\underline{A}\left(\underline{r}'\right)\right) = \nabla x\left(\underline{r}\right) \times \underline{A}\left(\underline{r}'\right) \tag{A.8}$$

when $\underline{A}(\underline{r}')$ is not dependent on the spatial coordinate $\underline{r}$ relevant for taking the derivative. Furthermore,

$$\nabla \frac{e^{-jkR}}{R} = -\frac{e^{-jkR}}{R^3}\left(1+jkR\right)\underline{R} \tag{A.9}$$

has been utilized.

## Electric Current Density

The analogous case of radiation caused by electric current densities can be derived when starting with the relations

$$\underline{E}\left(\underline{r}\right) = \frac{1}{\mathrm{j}\omega\mu\varepsilon}\nabla \times \nabla \times \underline{A}\left(\underline{r}\right) \tag{A.10}$$

$$\underline{A}\left(\underline{r}\right) = \frac{\mu}{4\pi}\iiint \frac{\mathrm{e}^{-\mathrm{j}kR}}{R}\underline{J}\left(\underline{r}'\right)\mathrm{d}V' \tag{A.11}$$

involving the magnetic vector potential. The electric field is here evaluated at source-free locations, i.e., where $\underline{J}\left(\underline{r}\right) = \underline{0}$. Again utilizing the steps in (A.8) and (A.9), one can find

$$\underline{E}\left(\underline{r}\right) = \frac{1}{\mathrm{j}4\pi\omega\varepsilon}\iiint \underbrace{\nabla \times \left(\frac{\mathrm{e}^{-\mathrm{j}kR}}{R^3}\left(1 + \mathrm{j}kR\right)\underline{J}\times\underline{R}\right)}_{\nabla\times\left(P\underline{c}\times\underline{R}\right)}\mathrm{d}V'. \tag{A.12}$$

Continuing with

$$\nabla \times \left(P\underline{c}\times\underline{R}\right) = P\underbrace{\nabla\times\left(\underline{c}\times\underline{R}\right)}_{I.} - \underbrace{\left(\underline{c}\times\underline{R}\right)\times\nabla P}_{II.} \tag{A.13}$$

$$I. = -\left(\underline{c}\cdot\nabla\right)\underline{R} + \underline{c}\underbrace{\nabla\underline{R}}_{=3} = -\underline{c} + 3\underline{c} = 2\underline{c} \tag{A.14}$$

$$II. = \nabla P \times \left(\underline{c}\times\underline{R}\right) = \left(\underline{R}\cdot\nabla P\right)\underline{c} - \left(\underline{c}\cdot\nabla P\right)\underline{R} \tag{A.15}$$

one finds

$$\underline{E}\left(\underline{r}\right) = \frac{1}{\mathrm{j}4\pi\omega\varepsilon}\iiint \left[2P\underline{c} + \left(\underline{R}\cdot\nabla P\right)\underline{c} - \left(\underline{c}\cdot\nabla P\right)\underline{R}\right]\mathrm{d}V'. \tag{A.16}$$

With

$$\nabla\left(\frac{\mathrm{e}^{-\mathrm{j}kR}}{R^3}\left(1 + \mathrm{j}kR\right)\right) = -\frac{\mathrm{e}^{-\mathrm{j}kR}}{R^3}\left(\frac{3}{R^2} + \frac{3\mathrm{j}k}{R} - k^2\right)\underline{R} \tag{A.17}$$

we then write

$$\underline{E}\left(\underline{r}\right) = \frac{1}{\mathrm{j}4\pi\omega\varepsilon}\iiint \left[2\frac{\mathrm{e}^{-\mathrm{j}kR}}{R^3}\left(1 + \mathrm{j}kR\right)\underline{J} - \left(\underline{R}\cdot\underline{R}\frac{\mathrm{e}^{-\mathrm{j}kR}}{R^3}\left(\frac{3}{R^2} + \frac{3\mathrm{j}k}{R} - k^2\right)\right)\underline{J}\right.$$
$$\left. + \left(\underline{J}\cdot\underline{R}\frac{\mathrm{e}^{-\mathrm{j}kR}}{R^3}\left(\frac{3}{R^2} + \frac{3\mathrm{j}k}{R} - k^2\right)\right)\underline{R}\right]\mathrm{d}V' \tag{A.18}$$

$$= \frac{1}{\mathrm{j}4\pi\omega\varepsilon}\iiint \left[2\frac{\mathrm{e}^{-\mathrm{j}kR}}{R^3}\left(1 + \mathrm{j}kR\right)\underline{J} - \left(\frac{\mathrm{e}^{-\mathrm{j}kR}}{R}\left(\frac{3}{R^2} + \frac{3\mathrm{j}k}{R} - k^2\right)\right)\underline{J}\right.$$
$$\left. + \left(\underline{J}\cdot\underline{R}\frac{\mathrm{e}^{-\mathrm{j}kR}}{R^3}\left(\frac{3}{R^2} + \frac{3\mathrm{j}k}{R} - k^2\right)\right)\underline{R}\right]\mathrm{d}V'. \tag{A.19}$$

Next, one obtains

$$\underline{E}\,(\underline{r}) = -\frac{1}{4\pi}\sqrt{\frac{\mu}{\varepsilon}}\frac{\mathrm{j}}{k}\iiint \underline{J}\cdot\left[\left(k^2R-\frac{1}{R}-\mathrm{j}k\right)\underline{\mathbf{I}}+\left(\frac{3}{R^3}+\frac{3\mathrm{j}k}{R^2}-\frac{k^2}{R}\right)\underline{RR}\right]\frac{\mathrm{e}^{-\mathrm{j}kR}}{R^2}\mathrm{d}V' \tag{A.20}$$

and thus finally

$$\underline{E}\,(\underline{r}) = -\frac{1}{4\pi}\sqrt{\frac{\mu}{\varepsilon}}\iiint \underline{J}\,(\underline{r}')\cdot\left[\left(1+\mathrm{j}kR+\frac{1}{\mathrm{j}kR}\right)\underline{\mathbf{I}}+\left(\frac{k}{\mathrm{j}R}-\frac{3}{R^2}-\frac{3}{\mathrm{j}kR^3}\right)\underline{RR}\right]\frac{\mathrm{e}^{-\mathrm{j}kR}}{R^2}\mathrm{d}V', \tag{A.21}$$

which is identical to (2.26).

## A.2  Mean-Squared Deviation — Optimal Scaling

Consider the task of determining the optimal complex-valued scaling factor $c \in \mathbb{C}$ such that the mean-squared error between to complex-valued vectors $\boldsymbol{v}_{1/2} \in \mathbb{C}^{n\times 1}$ is minimal. The problem can be written as

$$\arg\min_{c\in\mathbb{C}}\frac{\|c\boldsymbol{v}_1-\boldsymbol{v}_2\|_2}{\|\boldsymbol{v}_2\|_2} \equiv \arg\min_{c\in\mathbb{C}}\|c\boldsymbol{v}_1-\boldsymbol{v}_2\|_2^2. \tag{A.22}$$

We can find the solution by rewriting the squared norm as

$$\|c\boldsymbol{v}_1-\boldsymbol{v}_2\|_2^2 = (c\boldsymbol{v}_1-\boldsymbol{v}_2)^{\mathrm{H}}(c\boldsymbol{v}_1-\boldsymbol{v}_2) \tag{A.23}$$

$$= c\bar{c}\boldsymbol{v}_1^{\mathrm{H}}\boldsymbol{v}_1 - \bar{c}\boldsymbol{v}_1^{\mathrm{H}}\boldsymbol{v}_2 - c\boldsymbol{v}_2^{\mathrm{H}}\boldsymbol{v}_1 + \boldsymbol{v}_2^{\mathrm{H}}\boldsymbol{v}_2. \tag{A.24}$$

The consideration of a complex-valued scaling factor makes this task slightly more complicated. However, it can be treated by replacing the complex-valued optimal scaling by separated variables for its magnitude and phase, written as $c = c_1 c_2$, where $c_1 \in \mathbb{R}$ and $|c_2| = 1$, $c_2 \in \mathbb{C}$. One can then continue to write

$$\|c\boldsymbol{v}_1-\boldsymbol{v}_2\|_2^2 = c_1^2\boldsymbol{v}_1^{\mathrm{H}}\boldsymbol{v}_1 - c_1\left(\bar{c}_2\boldsymbol{v}_1^{\mathrm{H}}\boldsymbol{v}_2 + c_2\boldsymbol{v}_2^{\mathrm{H}}\boldsymbol{v}_1\right) + \boldsymbol{v}_2^{\mathrm{H}}\boldsymbol{v}_2 \tag{A.25}$$

$$= c_1^2\boldsymbol{v}_1^{\mathrm{H}}\boldsymbol{v}_1 - 2c_1\mathrm{Re}\left\{c_2\boldsymbol{v}_2^{\mathrm{H}}\boldsymbol{v}_1\right\} + \boldsymbol{v}_2^{\mathrm{H}}\boldsymbol{v}_2. \tag{A.26}$$

In search for a stationary point, setting the first-order derivative with respect to the magnitude of the scaling factor to zero yields

$$0 \stackrel{!}{=} 2c_1\boldsymbol{v}_1^{\mathrm{H}}\boldsymbol{v}_1 - 2\mathrm{Re}\left\{c_2\boldsymbol{v}_2^{\mathrm{H}}\boldsymbol{v}_1\right\}, \tag{A.27}$$

leading to

$$c_1 = \frac{\mathrm{Re}\left\{c_2\boldsymbol{v}_2^{\mathrm{H}}\boldsymbol{v}_1\right\}}{\boldsymbol{v}_1^{\mathrm{H}}\boldsymbol{v}_1}. \tag{A.28}$$

A quick check of the second-order derivative reveals that (A.28) belongs to a minimum. Looking back at (A.26) it is also clear that $\mathrm{Re}\{c_2\boldsymbol{v}_2^{\mathrm{H}}\boldsymbol{v}_1\}$ has to be the most positive value possible in order

minimize the mean-squared difference further, for which the maximum

$$\max_{c_2 \in \mathbb{C}, |c_2|=1} \text{Re}\{c_2 \boldsymbol{v}_2^{\text{H}} \boldsymbol{v}_1\} = \max_{c_2 \in \mathbb{C}, |c_2|=1} \left| \boldsymbol{v}_2^{\text{H}} \boldsymbol{v}_1 \right| \cos \left( \angle (c_2) + \angle \left( \boldsymbol{v}_2^{\text{H}} \boldsymbol{v}_1 \right) \right) \tag{A.29}$$

is achieved when

$$c_2 = e^{-j\angle \left( \boldsymbol{v}_2^{\text{H}} \boldsymbol{v}_1 \right)}. \tag{A.30}$$

Multiplying (A.28) with $c_2$ while inserting (A.30), one obtains

$$c = \frac{\boldsymbol{v}_1^{\text{H}} \boldsymbol{v}_2}{\boldsymbol{v}_1^{\text{H}} \boldsymbol{v}_1} \tag{A.31}$$

to be the solution to and thus the optimal scaling for the problem in (A.22).

## A.3 Derivation of the Spatial Derivative of Magnitude Signals

The spatial derivative of the magnitude of probe signals in (5.48) is derived. Without loss of generality, we state the derivation for the spatial derivative in $x'$-direction which yields

$$\begin{aligned} \mathscr{A}^{x'}(z) = \frac{\partial |\mathbf{A}z|}{\partial x'} &= \frac{\partial}{\partial x'} \left( \mathbf{A}z \circ \frac{\overline{\mathbf{A}z}}{|\mathbf{A}z|} \right) = \frac{\overline{\mathbf{A}z}}{|\mathbf{A}z|} \circ \frac{\partial \mathbf{A}}{\partial x'} z + \mathbf{A}z \circ \left( \frac{\partial}{\partial x'} \frac{\overline{\mathbf{A}z}}{|\mathbf{A}z|} \right) \\ &= \mathbf{A}^{x'} z \circ e^{-j\varphi^{x'}} + \mathbf{A}z \circ \frac{\overline{\mathbf{A}^{x'}z} \circ |\mathbf{A}z| - \overline{\mathbf{A}z} \circ \frac{\partial |\mathbf{A}z|}{\partial x'}}{|\mathbf{A}z|^2} \\ &= \mathbf{A}^{x'} z \circ e^{-j\varphi^{x'}} + \overline{\mathbf{A}^{x'}z} \circ e^{j\varphi^{x'}} - \frac{\partial |\mathbf{A}z|}{\partial x'} \\ &= \text{Re} \left\{ \left( \mathbf{A}^{x'}z \right) \circ e^{-j\varphi^{x'}} \right\}. \end{aligned} \tag{A.32}$$

The complete three-directional derivative is again obtained by stacking the derivatives in $x'$-, $y'$- and $z'$-direction, as given in (5.48) with the stacked vector $\boldsymbol{\varphi}^{r'}$ in (5.49).

In a slightly different manner we can derive (5.50), the spatial derivative of the real-valued phase of the received probe signal. Again, we here present the derivative in $x'$-direction and the other directions follow by variable substitution. We find that

$$\begin{aligned} \frac{\partial \angle (\mathbf{A}z)}{\partial x'} &= \frac{\partial \text{atan2} (\text{Im} \{\mathbf{A}z\}, \text{Re} \{\mathbf{A}z\})}{\partial x'} = \frac{\partial \text{atan} \left( \frac{\text{Im}\{\mathbf{A}z\}}{\text{Re}\{\mathbf{A}z\}} \right)}{\partial x'} \\ &= \frac{1}{1 + \left( \frac{\text{Im}\{\mathbf{A}z\}}{\text{Re}\{\mathbf{A}z\}} \right)^2} \frac{\frac{\partial \text{Im}\{\mathbf{A}z\}}{\partial x'} \circ \text{Re} \{\mathbf{A}z\} - \text{Im} \{\mathbf{A}z\} \circ \frac{\partial \text{Re}\{\mathbf{A}z\}}{\partial x'}}{\text{Re} \{\mathbf{A}z\}^2} \\ &= \frac{1}{|\mathbf{A}z|^2} \left( \text{Im} \left\{ \mathbf{A}^{x'}z \right\} \circ \text{Re} \{\mathbf{A}z\} - \text{Im} \{\mathbf{A}z\} \circ \text{Re} \left\{ \mathbf{A}^{x'}z \right\} \right) \\ &= \frac{1}{|\mathbf{A}z|^2} \text{Im} \left\{ \mathbf{A}^{x'}z \circ \frac{1}{2} \left( \mathbf{A}z - \overline{\mathbf{A}z} \right) - \mathbf{A}z \circ \frac{1}{2} \left( \mathbf{A}^{x'}z + \overline{\mathbf{A}^{x'}z} \right) \right\} \end{aligned}$$

$$= \frac{1}{2\left|\mathbf{A}z\right|}\text{Im}\left\{\mathbf{A}^{x'}z \circ \left(\mathrm{e}^{\mathrm{j}\angle \mathbf{A}z} - \mathrm{e}^{-\mathrm{j}\angle \mathbf{A}z}\right) - \mathrm{e}^{\mathrm{j}\angle \mathbf{A}z} \circ \left(\mathbf{A}^{x'}z + \overline{\mathbf{A}^{x'}z}\right)\right\}$$

$$= \frac{1}{\left|\mathbf{A}z\right|}\text{Im}\left\{-\left(\overline{\mathbf{A}^{x'}z}\right) \circ \mathrm{e}^{\mathrm{j}\angle \mathbf{A}z}\right\} = \frac{1}{\left|\mathbf{A}z\right|}\text{Im}\left\{\left(\mathbf{A}^{x'}z\right) \circ \mathrm{e}^{-\mathrm{j}\angle \mathbf{A}z}\right\}, \tag{A.33}$$

which corresponds to (5.50) with the additional variable $M$ defined in (5.51).

## A.4 Normal Error System in Phase Retrieval

When looking at (4.3), one can see that formulation (5.16) can be modified as

$$\mathcal{A}_3 = \left[\left(\mathbf{A}\mathbf{A}^{\mathrm{H}}z\right) \circ \left(\overline{\mathbf{A}\mathbf{A}^{\mathrm{H}}z}\right)\right]^{p_3} = \left|\mathbf{A}\mathbf{A}^{\mathrm{H}}z\right|^{2p_3} \quad \text{with} \quad d_3 = |b|^{2p_3}. \tag{A.34}$$

This corresponds to employing the normal error system of equations, as thoroughly investigated in [Kornprobst et al. 2021a] for NFFFTs with full phase information, in the context of phase retrieval. Effectively, this requires to insert $\mathbf{A}\mathbf{A}^{\mathrm{H}}z$ instead of $\mathbf{A}z$ into the optimization framework. Note that the normal residual system of equations can not be applied, as the computation of the corresponding right-hand side would require the knowledge of the complex-valued measurement vector, including its phase. Analogous, one can make the same modification to (5.30).

The derivatives of formulation (5.16) consequently apply when using $\mathbf{A} \leftarrow \mathbf{A}\mathbf{A}^{\mathrm{H}}$ and are thus omitted.

It is obvious that the formulations (5.16) and (A.34) deviate in the shape of the forward operator, where for the second case the additional constraint of the adjoint operator $\mathbf{A}^{\mathrm{H}}$ is enforced on the unknowns. In case only function handles to the forward and the adjoint operator are available, the second formulation requires four matrix-vector multiplications per iteration of the solver, whereas the first formulation only requires two. The main difference between the formulations is that (A.34) shifts the space of unknowns into the domain of the measurement signal. As we usually have $m > n$ or even $m \gg n$, this may be a disadvantage — in contrast to the possibly beneficial effect of the additional filtering with $\mathbf{A}^{\mathrm{H}}$.

In order to compare the formulations, the success rates for both algorithms have been evaluated for complex-valued normally distributed matrices. A successful transformation is said to be achieved once a complex error in (4.14) below $-45\,\mathrm{dB}$ is obtained. In Fig. A.1 a comparison of the formulations (5.16) and (A.34) can be seen. Again, the parameter $p_{1/3} \in \{0.5, 1\}$ was set to result in a minimization of the magnitude or the squared magnitude, respectively. The results indicate that there is no benefit in applying the adjoint operator in the form of (A.34). Independent of $p_{1/3}$, the success rate and the average number of iterations required until convergence are inferior when using (A.34) compared to (5.16).

## A.5 Phase-Invariant Source Reconstruction

Consider the formulation

$$\mathcal{A}_4 = \mathbf{A}z - |b|\,\mathrm{e}^{\mathrm{j}\angle(\mathbf{A}z)} \quad \text{with} \quad d_4 = 0 \tag{A.35}$$

which maps complex-valued source coefficients $z$ to a complex-valued difference of vectors. Essentially, the formulation searches for source coefficients, while automatically adjusting the phase
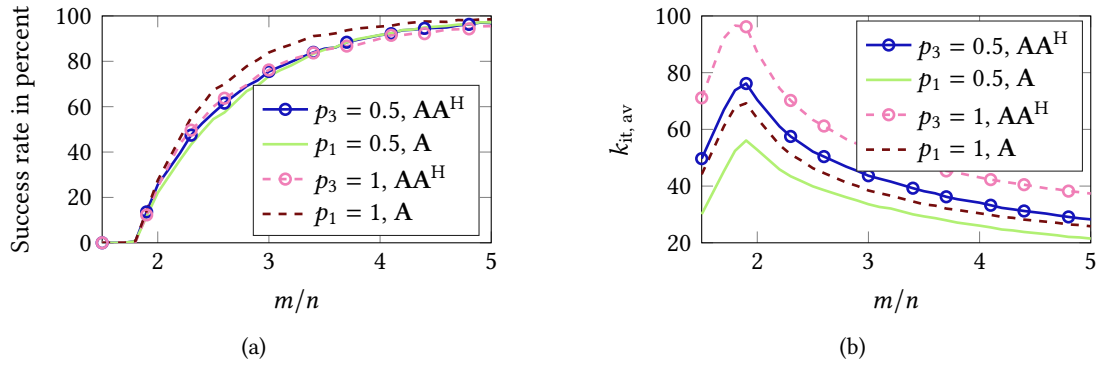
Fig. A.1 Comparison of formulations (5.16) and (A.34) for complex-valued normally distributed data. All solvers were limited to $k_{\mathrm{max}} = 5 \times 10^2$ iterations. For every ratio $m/n$, where $n = 10$, $5 \times 10^3$ runs were performed and the initial guess is computed via 40 power iterations of a spectral initialization. (a) Success rate, where success is declared once $\epsilon_{c,\mathrm{dB}} \leq -45\,\mathrm{dB}$ is achieved. (b) Average number of iterations $k_{\mathrm{av, it}}$ performed.

of the measurement vector to fit to the current solution. Thus, no restrictions on the phases are enforced. Due to the occurrence of the phase term $\angle (\mathbf{A}\boldsymbol{z})$, the formulation exhibits "more nonlinearity" than for example the formulation in (5.16). While the working principle is resemblant to that of the standard formulations, the nonlinear operator $\mathcal{A}_4$ returns complex-valued vectors instead of real-valued ones, e.g., as in the case of $\mathcal{A}_1$.

The required derivatives yield

$$\frac{\partial \mathcal{A}_4}{\partial \boldsymbol{z}} = \mathrm{diag}\left(\mathbf{1} - \frac{1}{2}\frac{|\boldsymbol{b}|}{|\mathbf{A}\boldsymbol{z}|}\right)\mathbf{A} \qquad (A.36)$$

$$\left(\frac{\partial \mathcal{A}_4}{\partial \boldsymbol{z}}\right)^{\mathrm{H}} = \mathbf{A}^{\mathrm{H}}\mathrm{diag}\left(\mathbf{1} - \frac{1}{2}\frac{|\boldsymbol{b}|}{|\mathbf{A}\boldsymbol{z}|}\right) \qquad (A.38)$$

$$\frac{\partial \overline{\mathcal{A}}_4}{\partial \boldsymbol{z}} = \frac{1}{2}\mathrm{diag}\left(\frac{|\boldsymbol{b}|\,\mathrm{e}^{-2\mathrm{j}\angle(\mathbf{A}\boldsymbol{z})}}{|\mathbf{A}\boldsymbol{z}|}\right)\mathbf{A} \qquad (A.37)$$

$$\left(\frac{\partial \overline{\mathcal{A}}_4}{\partial \boldsymbol{z}}\right)^{\mathrm{H}} = \frac{1}{2}\mathbf{A}^{\mathrm{H}}\mathrm{diag}\left(\frac{|\boldsymbol{b}|\,\mathrm{e}^{2\mathrm{j}\angle(\mathbf{A}\boldsymbol{z})}}{|\mathbf{A}\boldsymbol{z}|}\right). \qquad (A.39)$$

Due to the similarity with the standard approach in (5.16), the success rates reported for random and for NF data in Fig. A.2 are of no surprise. Despite the larger computational burden, the performance of (A.35) can not be distinguished from that of (5.16) for $p_1 = 0.5$.

## A.6 Enforcement of Phase Differences with Partial Knowledge of Magnitudes

In Section 5.4.5, the case may arise where partial information is available on two linear measurements of the same unknown quantity. To be more precise, consider the case with the known linear operators $\mathbf{A}_{1/2} \in \mathbb{C}^{m \times n}$ and the unknowns in $\boldsymbol{z} \in \mathbb{C}^{n \times 1}$, for which $|\mathbf{A}_1\boldsymbol{z}| = |\boldsymbol{b}_1|$ and $\angle(\mathbf{A}_1\boldsymbol{z} \circ \mathbf{A}_2\boldsymbol{z})$ are *available* and $|\mathbf{A}_2\boldsymbol{z}| = |\boldsymbol{b}_2|$ and $\angle(\mathbf{A}_{1/2}\boldsymbol{z})$ are *unknown*. As in particular $|\mathbf{A}_2\boldsymbol{z}|$ is not given, the phase retrieval algorithms in Chapter 6 for partially coherent data can not be applied.
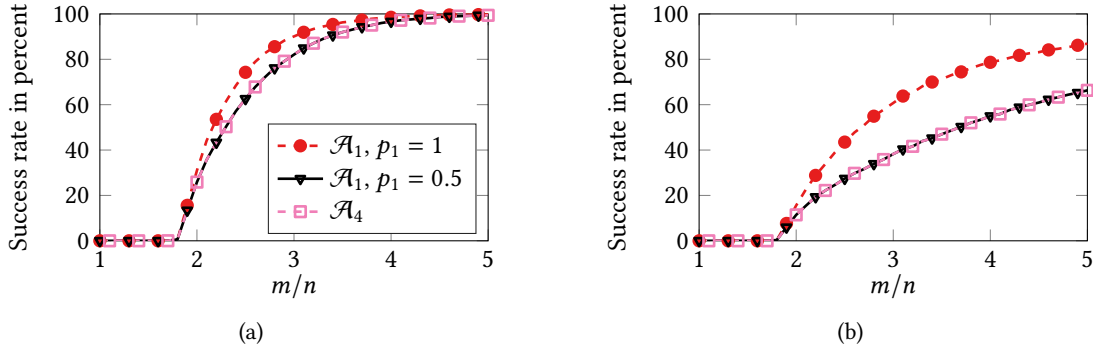
(a)



(b)

Fig. A.2 Success rate of the phase retrieval formulations (5.16) and (A.35) for complex-valued normally distributed data, in (a), and NF data on a synthetic measurement sphere, generated by spherical vector wave functions, in (b). All solvers were limited to $k_{\max} = 5 \times 10^3$ iterations. For each ratio $m/n$, where $n = 10$, $50 \times 10^3$ runs were performed and the initial guess is computed via the optimal spectral method. Success is declared once $\epsilon_{c,\mathrm{dB}} \leq -45$ dB is achieved.

We can enforce the knowledge of the phase differences as part of the optimization framework via

$$\mathcal{A}_{11} = \frac{\mathbf{A}_2 z \circ \overline{\mathbf{A}_1 z}}{|\mathbf{A}_2 z| \circ g_{11}(z)} \quad \text{with} \quad d_{11} = e^{j\angle\left(\mathbf{A}_2 z \circ \overline{\mathbf{A}_1 z}\right)}, \tag{A.40}$$

where $g_{11}(z) \in \mathbb{R}^{m \times 1}$ represents the magnitude of the measurement with $\mathbf{A}_1$. In particular, $g_{11}$ can either be set to $|\mathbf{A}_1 z|$, dependent on $z$, or independent of $z$, as $|b_1|$.

The required derivatives are found as

$$\frac{\partial \mathcal{A}_{11}(z)}{\partial z} = \frac{\mathrm{diag}\left(\overline{\mathbf{A}_1 z} \circ |\mathbf{A}_2 z| \circ g_{11}(z)\right) \mathbf{A}_2}{(|\mathbf{A}_2 z| \circ g_{11}(z))^2}$$

$$- \frac{\mathrm{diag}\left(\mathbf{A}_2 z \circ \overline{\mathbf{A}_1 z}\right)\left[\mathrm{diag}\left(g_{11}(z) \circ e^{-j\angle(\mathbf{A}_2 z)}\right) \mathbf{A}_2 + \mathrm{diag}(|\mathbf{A}_2 z|) \dfrac{\partial g_{11}(z)}{\partial z}\right]}{2\left(|\mathbf{A}_2 z| \circ g_{11}(z)\right)^2} \tag{A.41}$$

$$\left(\frac{\partial \mathcal{A}_{11}(z)}{\partial z}\right)^{\mathrm{H}} = \mathbf{A}_2^{\mathrm{H}} \frac{\mathrm{diag}\left(\mathbf{A}_1 z \circ |\mathbf{A}_2 z| \circ g_{11}(z)\right)}{(|\mathbf{A}_2 z| \circ g_{11}(z))^2}$$

$$- \mathbf{A}_2^{\mathrm{H}} \frac{\mathrm{diag}\left(\mathbf{A}_1 z \circ \overline{\mathbf{A}_2 z} \circ g_{11}(z) \circ e^{j\angle(\mathbf{A}_2 z)}\right)}{2\left(|\mathbf{A}_2 z| \circ g_{11}(z)\right)^2}$$

$$+ \frac{\left(\dfrac{\partial g_{11}(z)}{\partial z}\right)^{\mathrm{H}} \mathrm{diag}\left(\mathbf{A}_1 z \circ \overline{\mathbf{A}_2 z} \circ |\mathbf{A}_2 z|\right)}{2\left(|\mathbf{A}_2 z| \circ g_{11}(z)\right)^2} \tag{A.42}$$

$$\frac{\partial \overline{\mathcal{A}_{11}(z)}}{\partial z} = \frac{\mathrm{diag}\left(\overline{\mathbf{A}_2 z} \circ |\mathbf{A}_2 z| \circ g_{11}(z)\right) \mathbf{A}_1}{(|\mathbf{A}_2 z| \circ g_{11}(z))^2}$$

$$-\frac{\text{diag}\left(\mathbf{A}_1 z \circ \overline{\mathbf{A}_2 z}\right)\left[\text{diag}\left(\boldsymbol{g}_{11}\left(z\right)\circ \mathrm{e}^{-\mathrm{j}\angle(\mathbf{A}_2 z)}\right)\mathbf{A}_2 + \text{diag}\left(|\mathbf{A}_2 z|\right)\frac{\partial \boldsymbol{g}_{11}\left(z\right)}{\partial z}\right]}{2\left(|\mathbf{A}_2 z| \circ \boldsymbol{g}_{11}\left(z\right)\right)^2} \tag{A.43}$$

$$\left(\frac{\partial \overline{\mathcal{A}_{11}\left(z\right)}}{\partial z}\right)^{\mathrm{H}} = \mathbf{A}_1^{\mathrm{H}}\frac{\text{diag}\left(\mathbf{A}_2 z \circ |\mathbf{A}_2 z| \circ \boldsymbol{g}_{11}\left(z\right)\right)}{\left(|\mathbf{A}_2 z| \circ \boldsymbol{g}_{11}\left(z\right)\right)^2}$$

$$-\mathbf{A}_2^{\mathrm{H}}\frac{\text{diag}\left(\mathbf{A}_2 z \circ \overline{\mathbf{A}_1 z} \circ \boldsymbol{g}_{11}\left(z\right)\circ \mathrm{e}^{-\mathrm{j}\angle(\mathbf{A}_2 z)}\right)}{2\left(|\mathbf{A}_2 z| \circ \boldsymbol{g}_{11}\left(z\right)\right)^2}$$

$$+\frac{\left(\frac{\partial \boldsymbol{g}_{11}\left(z\right)}{\partial z}\right)^{\mathrm{H}}\text{diag}\left(\mathbf{A}_2 z \circ \overline{\mathbf{A}_1 z} \circ |\mathbf{A}_2 z|\right)}{2\left(|\mathbf{A}_2 z| \circ \boldsymbol{g}_{11}\left(z\right)\right)^2}. \tag{A.44}$$

Note that if $\boldsymbol{g}_{11}\left(z\right) = |\mathbf{A}_1 z|$, we have

$$\frac{\partial \boldsymbol{g}_{11}\left(z\right)}{\partial z} = \frac{1}{2}\text{diag}\left(\mathrm{e}^{-\mathrm{j}\angle(\mathbf{A}_1 z)}\right)\mathbf{A}_1 \quad \text{(A.45)} \qquad \left(\frac{\partial \boldsymbol{g}_{11}\left(z\right)}{\partial z}\right)^{\mathrm{H}} = \frac{1}{2}\mathbf{A}_1^{\mathrm{H}}\text{diag}\left(\mathrm{e}^{\mathrm{j}\angle(\mathbf{A}_1 z)}\right), \quad \text{(A.46)}$$

or when $\boldsymbol{g}_{11}\left(z\right) = |\boldsymbol{b}_1|$,

$$\frac{\partial \boldsymbol{g}_{11}\left(z\right)}{\partial z} = \mathbf{0} \quad \text{(A.47)} \qquad\qquad \left(\frac{\partial \boldsymbol{g}_{11}\left(z\right)}{\partial z}\right)^{\mathrm{H}} = \mathbf{0}. \quad \text{(A.48)}$$

A simple verification of the approach has been conducted with complex-valued normally distributed data, where $\boldsymbol{g}_{11}(z) = |\boldsymbol{b}_1|$ and $n = 10$. Three approaches have been compared. First, solely applying the formulation in (A.40), which effectively only utilizes the phase difference information. Second, the phase retrieval formulation in (5.30) applied *only to* $|\mathbf{A}_1 z| = |\boldsymbol{b}_1|$, and, third, a combination of both, where both cost functions are minimized in parallel with equal weighting. In all three cases, the initial guess is computed via the optimal spectral method applied to $|\mathbf{A}_1 z| = |\boldsymbol{b}_1|$. All solvers were allowed to at most perform $5 \times 10^2$ iterations. A transformation was said to be successful, once $\epsilon_{c,\mathrm{dB}}(\mathbf{A}_1 z, \boldsymbol{b}_1) \leq -45\,\mathrm{dB}$ was obtained. The results are depicted in Fig. A.3, where the success rate versus the oversampling ratio $m/n$ is depicted.

The formulation with $\mathcal{A}_{11}$ can be interpreted as a particular case of the magnitude retrieval problem briefly discussed in Appendix A.9, only featuring knowledge of phase differences and no absolute phases. As such, and as indeed can be seen in Fig. A.3, it should perform somehow worse than the magnitude retrieval in Fig. A.6 for the same number of unknowns. Keep in mind that $\mathcal{A}_{11}$ in Fig. A.3 actually exploits twice the number of measurements as available for the solvers in Fig. A.6, since a second linear measurement operator is considered. Thus, it seems reasonable that nonzero success rates can be observed starting at $m/n \approx 1$, while $m/n \approx 2$ are required in Fig. A.6. Still, the overall number of measurements required for $\mathcal{A}_{11}$ to reach reasonable success rates is quite large compared to case of magnitude retrieval from absolute phase knowledge. Finally, a combination of $\mathcal{A}_{11}$ with the classical phase retrieval formulation via $\mathcal{A}_2$ is seen to feature a decent improvement compared to a separate minimization of the cost functions. As is seen throughout this dissertation, adding information to the original phase retrieval problem is mainly seen to improve the obtainable results — the opposite is rarely observed.
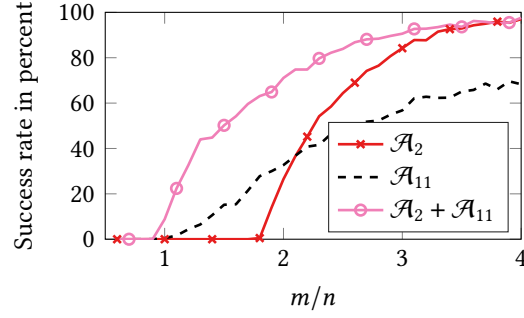
Fig. A.3 Success rate of phase retrieval algorithms for partially coherent observations with limited knowledge of magnitudes. Here for $n = 10$ and complex-valued normally distributed data. For each ratio of $m/n$, $1 \times 10^3$ trials were performed. The formulation with $\mathcal{A}_2$ only utilizes $|\mathbf{A}_1 \boldsymbol{z}|$, while $\mathcal{A}_{11}$ only exploits $\angle(\mathbf{A}_2 \boldsymbol{z} \circ \overline{\mathbf{A}_1 \boldsymbol{z}})$. Consequently, the combination of both cost functions makes use of magnitudes and phase differences, simultaneously.

## A.7 PhaseCut via the Optimization Framework

Consider the convex formulation of the phase retrieval problem called PhaseCut [Waldspurger et al. 2015]

$$
\min_{\mathbf{U} \in \mathbb{C}^{m \times m}} \quad \mathrm{Tr}\,(\mathbf{MU})
$$
$$
\text{s.t.} \quad \mathrm{diag}\,(\mathbf{U}) = \mathbf{1}
$$
$$
\mathbf{U} \succeq 0, \tag{A.49}
$$

where

$$
\mathbf{M} = \mathrm{diag}\,(|\boldsymbol{b}|)\left(\mathbf{I} - \mathbf{AA}^{-1}\right)\mathrm{diag}\,(|\boldsymbol{b}|) \tag{A.50}
$$

is a positive definite Hermitian matrix.

We can implement this minimization in form of our framework, with

$$
\mathcal{A}_{\mathrm{PC}} = \begin{bmatrix} \mathrm{Tr}\,(\mathbf{MX}^{\mathrm{H}}\mathbf{X}) \\ \mathrm{diag}\,(\mathbf{X}^{\mathrm{H}}\mathbf{X}) \end{bmatrix}, \quad \mathbf{X} \in \mathbb{C}^{m \times m} \text{ with } \boldsymbol{d}_{\mathrm{PC}} = \underbrace{\begin{bmatrix} \mathbf{0} \\ \mathbf{1} \end{bmatrix}}_{\in \mathbb{R}^{m+1 \times 1}}, \tag{A.51}
$$

where the positive semidefiniteness of the unknown $\mathbf{U} = \mathbf{X}^{\mathrm{H}}\mathbf{X}$ is enforced by solving for a upper triangular matrix $\mathbf{X}$.

The required derivatives can be found as

$$
\overbrace{\frac{\partial \mathcal{A}_{\mathrm{PC}}\,(\mathbf{X})}{\partial \mathbf{X}}}^{\in \mathbb{C}^{1+m \times (m \times m)}} \overbrace{(\mathbf{Y})}^{\in \mathbb{C}^{(m \times m)}} = \overbrace{\begin{bmatrix} \mathrm{Tr}\,(\mathbf{MX}^{\mathrm{H}}\mathbf{Y}) \\ \mathrm{diag}\,(\mathbf{X}^{\mathrm{H}}\mathbf{Y}) \end{bmatrix}}^{\in \mathbb{C}^{m+1 \times 1}} \quad \frac{\partial \overline{\mathcal{A}_{\mathrm{PC}}\,(\mathbf{X})}}{\partial \mathbf{X}}\,(\mathbf{Y}) = \begin{bmatrix} \mathrm{Tr}\,(\mathbf{M}^{\mathrm{H}}\mathbf{X}^{\mathrm{H}}\mathbf{Y}) \\ \mathrm{diag}\,(\mathbf{X}^{\mathrm{H}}\mathbf{Y}) \end{bmatrix} \tag{A.52}
$$

$$\underbrace{\left(\frac{\partial \mathcal{A}_{\mathrm{PC}}(\mathbf{X})}{\partial \mathbf{X}}\right)^{\mathrm{H}}}_{\in \mathbb{C}^{(m \times m) \times 1+m}} \underbrace{(\boldsymbol{y})}_{\in \mathbb{R}^{m+1 \times 1}} = \underbrace{\mathbf{X}\mathbf{M}^{\mathrm{H}}[\boldsymbol{y}]_1}_{\in \mathbb{C}^{(m \times m) \times 1}} + \underbrace{\mathbf{X}\mathrm{diag}\left([\boldsymbol{y}]_{2:m}\right)}_{\in \mathbb{C}^{(m \times m) \times 1}} \tag{A.53}$$

and

$$\left(\overline{\frac{\partial \overline{\mathcal{A}_{\mathrm{PC}}(\mathbf{X})}}{\partial \mathbf{X}}}\right)^{\mathrm{H}} (\boldsymbol{y}) = \mathbf{X}\mathbf{M}[\boldsymbol{y}]_1 + \mathbf{X}\mathrm{diag}\left([\boldsymbol{y}]_{2:m}\right). \tag{A.54}$$

Dimensions in brackets are here treated as a single dimension, i.e., for $\mathbf{U}_1 \in \mathbb{C}^{q \times (m \times m)}$ and $\mathbf{U}_2 \in \mathbb{C}^{(m \times m) \times 1}$, the product $\mathbf{U}_1 \mathbf{U}_2 = \mathbf{U}_3$ leads to $\mathbf{U}_3 \in \mathbb{C}^{q \times 1}$. The rather abusive notation $[\boldsymbol{y}]_{k:l}$ extracts the elements with the indices $k$ to $l$ from the vector $\boldsymbol{y}$. Furthermore, the framework operates on vector unknowns and not on matrices, thus, the entries of the upper triangular matrix $\mathbf{X}$ are represented as vector entries $\boldsymbol{x} \in \mathbb{C}^{m(m+1)/2 \times 1}$.

A comparison of the implementation by [Waldspurger et al. 2015] based on the interior-point method [Helmberg et al. 1996] and the formulation in (A.51) can be drawn from the results in Fig. A.4. Complex-valued normally distributed data for $n = 10$ was used to determine the success rate of both implementations dependent on the oversampling ratio $m/n$ in Fig. A.4(a). Both algorithms were allowed to at most perform $5 \times 10^2$ iterations. The initial guess was computed via the optimal spectral method. Success was declared once $\epsilon_{c,\mathrm{dB}} \leq -45$ dB was obtained. Both implementations are observed to perform differently, where the formulation based on (A.51) requires fewer measurement samples for the same success rate. In contrast to that, Fig. A.4(b) draws a rather negative picture of the presented formulation. For a single transformation example, the solvers were started from $1 \times 10^2$ randomly picked initial guesses and the cosine similarity between the transformation results of all $i \in \{1, ..., 1 \times 10^2\}$ runs was compared to that of the first run, $i = 1$. On the $x$-axis, the cosine similarity of the initial guess with respect to the true solution is drawn, where larger values close to unity indicate a superior initial guess and smaller values represent larger distances to the correct solution. It can be seen that the implementation by [Waldspurger et al. 2015] does always converge to the same solution within at most $1 \times 10^2$ iterations, whereas the proposed implementation, even for a very large number of iterations of $5 \times 10^3$, converges to different solutions. Consequently, the presented formulation does not exhibit the positive convex property that would have been expected by the PhaseCut approach. This is likely to be attributed to the direct enforcement of the positive semidefiniteness as well as the entries on the diagonal of $\mathbf{U}$ with a magnitude of one.
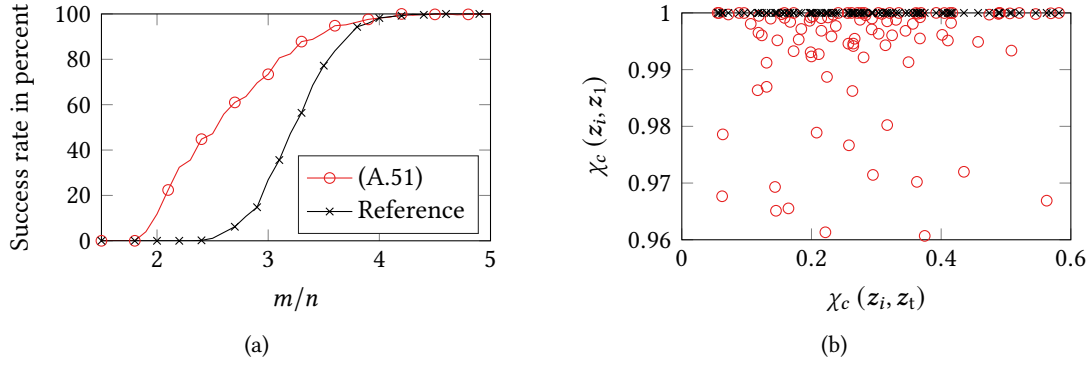
Fig. A.4 Performance metrics of the PhaseCut implementation via the optimization framework in comparison to the reference by [Waldspurger et al. 2015] based on the interior-point method in [Helmberg et al. 1996]. Complex-valued normally distributed data with $n = 10$ was employed. (a) The success rate. (b) The cosine similarity between the first returned solution $z_1$ and all other solutions $z_i$ for $m/n = 3$ and $i \in \{1, ..., 1 \times 10^2\}$. On the $x$-axis, the cosine similarity of the initial guess with respect to the true solution is drawn. At most $5 \times 10^3$ and $1 \times 10^2$ iterations were allowed for the optimization framework and the interior-point method, respectively.

## A.8  PhaseMax via the Optimization Framework

The basis pursuit formulation of PhaseMax in (5.89) consists of an $\ell_1$-minimization as well as a linear side constraint. Both contributions can be modeled via the optimization framework, where the linear constraint, i.e., the linear system of equations $z_{\mathrm{PM}} = \mathbf{A}^{\mathrm{H}}\mathrm{diag}(|\boldsymbol{b}|)^{-1}z$, is treated via an appropriate operator $\mathcal{A}_0$ and the derivatives thereof. The operator for an $\ell_{2p_{\mathrm{PM}}}$-norm can be found as

$$\mathcal{A}_{\mathrm{PM}} = \left[ \mathbf{1}^{\mathrm{T}} \left( z \circ \overline{z} \right)^{p_{\mathrm{PM}}} \right]^{q_{\mathrm{PM}}}, \quad z \in \mathbb{C}^{m \times 1} \quad \text{with } d_{\mathrm{PM}} = 0 \tag{A.55}$$

and $q_{\mathrm{PM}} = 1/(2p_{\mathrm{PM}})$. The corresponding derivatives are given by

$$\frac{\partial \mathcal{A}_{\mathrm{PM}}}{\partial z} = c_{\mathrm{PM}} \mathbf{1}^{\mathrm{T}} \mathrm{diag} \left( \overline{z} \circ (z \circ \overline{z})^{p_{\mathrm{PM}}-1} \right) \quad \text{(A.56)} \qquad \frac{\partial \overline{\mathcal{A}}_{\mathrm{PM}}}{\partial z} = \frac{\partial \mathcal{A}_{\mathrm{PM}}}{\partial z} \tag{A.58}$$

$$\left( \frac{\partial \mathcal{A}_{\mathrm{PM}}}{\partial z} \right)^{\mathrm{H}} = c_{\mathrm{PM}} \mathrm{diag} \left( z \circ (z \circ \overline{z})^{p_{\mathrm{PM}}-1} \right) \mathbf{1} \quad \text{(A.57)} \qquad \left( \frac{\partial \overline{\mathcal{A}}_{\mathrm{PM}}}{\partial z} \right)^{\mathrm{H}} = \left( \frac{\partial \mathcal{A}_{\mathrm{PM}}}{\partial z} \right)^{\mathrm{H}} \tag{A.59}$$

with $c_{\mathrm{PM}} = p_{\mathrm{PM}} q_{\mathrm{PM}} (\mathbf{1}^{\mathrm{T}} (z \circ \overline{z})^{p_{\mathrm{PM}}})^{q_{\mathrm{PM}}-1} \in \mathbb{R}$. For an $\ell_1$-norm, $p_{\mathrm{PM}} = 0.5$ has to be set.

The performance of the PhaseMax implementation via the optimization framework compared to that of the PhasePack library [Chandra et al. 2019, 2017] is illustrated in Fig. A.5. The PhasePack implementation employs the FASTA [Goldstein et al. 2014] for solving the corresponding basis pursuit problem. The success rate for complex-valued normally distributed data with $n = 10$ unknowns and a variable number of measurements is shown in Fig. A.5(a). Both algorithms were allowed to at most perform $5 \times 10^2$ iterations and the initial guess was computed via the optimal spectral method, which was also utilized as the anchor vector. The cost functions were minimized in
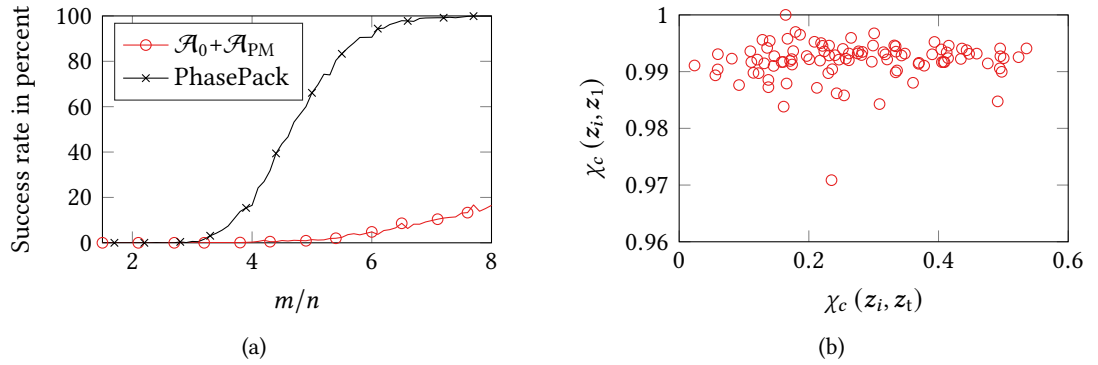
Fig. A.5 Performance metrics of the PhaseMax implementation via the optimization framework in comparison to that in the PhasePack library [Chandra et al. 2019, 2017] based on the FASTA [Goldstein et al. 2014]. Complex-valued normally distributed data with $n = 10$ was employed. (a) The success rate. (b) The cosine similarity between the first returned solution $z_1$ and all other solutions $z_i$ for $m/n = 5$ and $i \in \{1, ..., 1 \times 10^2\}$. On the $x$-axis, the cosine similarity of the initial guess with respect to the true solution is drawn.

parallel and the weightings were set as $\alpha_{\mathrm{OF},0} = 3 \times 10^3$ for $\mathcal{A}_0$ and $\alpha_{\mathrm{OF,PM}} = 1$ for $\mathcal{A}_{\mathrm{PM}}$. Empirically, these particular weightings were observed to yield rather satisfactory results for $n = 10$ and the given data. In practice, adaptive weightings are recommendable, such that good results can be obtained for arbitrary values of $n$. Figure A.5(a) reveals that the implementation via the optimization framework is functioning, however, it is far inferior to that of PhasePack. As a second test, a single transformation example of normally distributed data with $n = 10$ and $m/n = 5$ was considered. The framework solver was started from $1 \times 10^2$ randomly picked initial guesses and the cosine similarity between the transformation results of all $i \in \{1, ..., 1 \times 10^2\}$ runs was compared to that of the first run, i.e., $i = 1$. On the $x$-axis of Fig. A.5(b), the cosine similarity of the initial guess with respect to the true solution is drawn, where larger values close to unity indicate a superior initial guess and smaller values represent larger distances to the correct solution. Convex algorithms are expected to always return an identical solution, independent of the quality and location of the starting point. This statement holds true as long as the allowed number of iterations (here $k_{\max} = 1 \times 10^3$) is sufficiently large and the solver is able to converge. In case any nonconvexity is encountered, different starting points may lead to varying solutions at local stationary points. Consequently, the similarity drawn on the $y$-axis in Fig. A.5(b) should be identical to unity for a convex algorithm and may vary with nonconvexity. For this particular investigation, the anchor vector was set to the true solution and only the initial guess was varied. Results for the PhasePack library where not included as it was not possible to set anchor vector and initial guess independent from each other. The reported similarity values in Fig. A.5(b) indicate moderate deviations among the solutions, which might have been caused by inaccuracies in the line search process. The current implementation can not said to be truly convex, however, it has the potential for convexity once more effort is spent on numerical aspects, e.g., the line search. Furthermore, drastic improvements in the achievable success rate of the implementation are expected from a proper adaptive weighting of the cost functions.

## A.9 Magnitudeless Near-Field Far-Field Transformation

For reasons of completeness and hoping to obtain more insights, we here discuss the complementary case to phaseless transformations, the phase-only transformation. While there is an obvious relation to the task of phase retrieval, *magnitude retrieval* has received less attention so far [Mc Donald 2004; Olfat and Soltanian-Zadeh 2001]. Still, one may have to determine a complex-valued source vector $z$, such that

$$\angle\left(\mathbf{A}z\right) = \angle\left(b\right), \tag{A.60}$$

where the $\angle(.)$ operator element-wise extracts the phase from a complex-valued vector, e.g., in the form of complex numbers with unit magnitude. We know that a complex signal is completely described by its magnitude and phase. From the results for the phaseless formulations, we may have gotten the intuition that the information content of the phase and the magnitude parts of a signal are not equal, instead, the magnitude seems to carry less restrictions than the phase. Thus, one can expect the problem of magnitude retrieval to be somehow easier to solve than the task of phase retrieval. In the following, a simple optimization-based attempt is made to solve the magnitude retrieval problem.

In terms of the proposed framework, one can formulate the problem via

$$\mathcal{A}_{12} = \frac{\mathbf{A}z}{|\mathbf{A}z|} = e^{j\angle(\mathbf{A}z)} \quad \text{with } d_{12} = e^{j\angle(b)}. \tag{A.61}$$

The required derivatives can be found as

$$\frac{\partial \mathcal{A}_{12}\left(z\right)}{\partial z} = \tfrac{1}{2}\mathrm{diag}\left(\frac{1}{|\mathbf{A}z|}\right)\mathbf{A} \qquad \text{(A.62)} \qquad \frac{\partial \overline{\mathcal{A}_{12}\left(z\right)}}{\partial z} = -\tfrac{1}{2}\mathrm{diag}\left(\frac{e^{-2j\angle(\mathbf{A}z)}}{|\mathbf{A}z|}\right)\mathbf{A} \qquad \text{(A.64)}$$

$$\left(\frac{\partial \mathcal{A}_{12}\left(z\right)}{\partial z}\right)^{\mathrm{H}} = \tfrac{1}{2}\mathbf{A}^{\mathrm{H}}\mathrm{diag}\left(\frac{1}{|\mathbf{A}z|}\right) \qquad \text{(A.63)} \qquad \left(\frac{\partial \overline{\mathcal{A}_{12}\left(z\right)}}{\partial z}\right)^{\mathrm{H}} = -\tfrac{1}{2}\mathbf{A}^{\mathrm{H}}\mathrm{diag}\left(\frac{e^{2j\angle(\mathbf{A}z)}}{|\mathbf{A}z|}\right). \qquad \text{(A.65)}$$

Now, let us draw a quick comparison between phase and magnitude retrieval. In Fig. A.6 the chance for a successful retrieval for both methods is depicted. The forward operator and the true solution vector were both drawn from a complex-valued normal distribution. Phase retrieval was performed via the formulation in (5.30). At each ratio of $m/n$, $5 \times 10^2$ random instances of the forward operator and the solution vector were considered and a retrieval was counted as successful, once a complex error according to (4.14) below $-70\,\mathrm{dB}$ was achieved. At each instance, the same random initial guess was provided to the retrieval algorithms. The simulation was performed for rather small sized problems with $n = 10$, $n = 20$, $n = 30$ and $n = 40$. The overall trend shows that magnitude retrieval requires less measurements in order to achieve a reasonable chance of success, indicating that more information is contained in the phase of a signal than in its magnitude. Due to the nonconvexity of both formulations, a success rate of 100% is rarely observed.
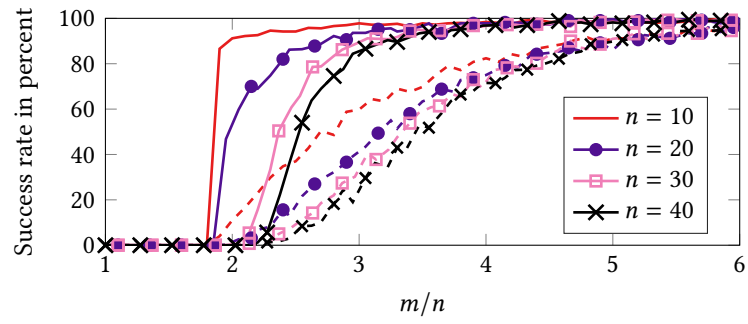
Fig. A.6 Comparison of phase retrieval (dashed lines) and magnitude retrieval (solid lines) for complex-valued normal distribution data. Phase and magnitude retrieval are performed via the formulations in (5.30) and (A.61).

# Important Variables and Symbols

| Symbol | Unit | Description |
|---|---|---|
| *Physical quantities* | | |
| $\underline{E}$ | $\text{Vm}^{-1}$ | electric field |
| $\underline{H}$ | $\text{Am}^{-1}$ | magnetic field |
| $\underline{D}$ | $\text{Asm}^{-2}$ | electric flux density |
| $\underline{B}$ | $\text{Vsm}^{-2}$ | magnetic flux density |
| $\underline{J}$ | $\text{Am}^{-1}$ / $\text{Am}^{-2}$ | electric surface/volume current density |
| $\underline{M}$ | $\text{Vm}^{-1}$ / $\text{Vm}^{-2}$ | magnetic surface/volume current density |
| $\underline{F}$ | $\text{Asm}^{-1}$ | electric vector potential |
| $\underline{A}$ | $\text{Vsm}^{-1}$ | magnetic vector potential |
| $\underline{E}_\text{H}$ | $\text{Vm}^{-1}$ | electric field radiated by a Hertzian dipole, see (2.29) |
| $\underline{E}_\text{F}$ | $\text{Vm}^{-1}$ | electric field radiated by a Fitzgerald dipole, see (2.30) |
| $\underline{H}_\text{H}$ | $\text{Am}^{-1}$ | magnetic field radiated by a Hertzian dipole |
| $\underline{H}_\text{F}$ | $\text{Am}^{-1}$ | magnetic field radiated by a Fitzgerald dipole |
| $\underline{n}$ | m | unit normal vector pointing to the exterior |
| $\underline{r}$ | m | observation location |
| $\underline{r}'$ | m | source location |
| $\underline{R}$ | m | relative separation between source and observation point |
| $f$ | $\text{s}^{-1}$ | frequency |
| $k$ | $\text{m}^{-1}$ | wavenumber |
| $Q_{smn}$ | $\sqrt{\text{VA}}$ | coefficients of a spherical vector wave expansion |
| $r_0$ | m | minimum-sphere radius in (2.18) |
| $R$ | m | distance between source and observation location |
| $Z_\text{F0}$ | $\Omega$ | free-space wave impedance |
| $\varepsilon$ | $\text{AsV}^{-1}\text{m}^{-1}$ | permittivity |
| $\varepsilon_0$ | $\text{AsV}^{-1}\text{m}^{-1}$ | vacuum permittivity |
| $\mu$ | $\text{VsA}^{-1}\text{m}^{-1}$ | permeability |
| $\mu_0$ | $\text{VsA}^{-1}\text{m}^{-1}$ | vacuum permeability |
| $\rho_\text{e}$ | $\text{Asm}^{-3}$ | electric charge density |
| $\rho_\text{m}$ | $\text{Vsm}^{-3}$ | magnetic charge density |
| $\sigma$ | $\Omega\text{m}$ | electric conductivity |
| $\omega$ | $\text{s}^{-1}$ | angular frequency |

| Symbol | Description |
|---|---|
| *Matrix and vector operations* | |
| $\overline{\mathbf{A}}$, $\overline{z}$ | complex conjugate of a matrix or vector |
| $\mathbf{A}^{\mathrm{T}}$, $z^{\mathrm{T}}$ | transpose of a matrix or vector |
| $\mathbf{A}^{\mathrm{H}}$, $z^{\mathrm{H}}$ | Hermitian/conjugate transpose of a matrix or vector |
| $\mathbf{A}^{-1}$ | inverse/pseudo-inverse of a matrix |
| $\nabla$ | del operator |
| $\nabla\times$ | rotation |
| $\nabla\cdot$ | divergence |
| $\Delta$ | Laplace operator |
| $\boldsymbol{\nabla}_x$, $\nabla_x^2$ | gradient and Hessian operator with respect to the real-valued vector $\boldsymbol{x}$, see (3.4) |
| $\boldsymbol{\nabla}_c$, $\nabla_c^2$ | gradient and Hessian operator defined in terms of the conjugate coordinates $\boldsymbol{c}$, see (3.27) and (3.28) |
| $\boldsymbol{\nabla}_z$ | gradient with respect to the complex-valued vector $\boldsymbol{z}$, valid for real-valued cost functions, see (3.50) |
| *Matrices* | |
| $\mathbf{A}$ | linear forward operator, also called measurement matrix |
| $\mathbf{A}_{\mathrm{H/F}\to\mathrm{H/F}}$ | dipole-dipole interaction matrices between Hertzian and Fitzgerald dipoles, see (2.40), (2.41), (2.43) and (2.42) |
| $\mathbf{A}^{r'}$ | spatially-differentiated forward operator, see (2.48) |
| $\mathbf{A}_{\mathrm{H/F}\to\mathrm{H/F}}^{x'}$ | in $x'$-direction spatially-differentiated interaction matrices for Hertzian and Fitzgerald dipoles, see (2.49) and (2.54) |
| $\mathbf{B}$ | diagonal matrix of measured magnitudes, see (6.8) |
| $\mathbf{B}'$ | diagonal matrix of the complex-valued measurement vector, see (6.16) |
| $\mathbf{B}'_{\mathrm{LMF}}$ | diagonal matrix of complex-valued measurement signals for the multi-frequency case, see (6.46) |
| $\mathbf{C}$ | matrix of known phase differences, see (6.8) |
| $\mathbf{C}'$ | matrix mapping the remaining phase unknowns to entries in the measurement vector, see (6.16) |
| $\mathbf{C}'_{\mathrm{LMF}}$ | matrix mapping the remaining phase unknowns to entries in the measurement vector in the multi-frequency case, see (6.46) |
| $\mathbf{C}_8$ | matrix allowing for a linear phase retrieval update rule in (5.62), leading to the linearized Alg. 12 |
| $\mathbf{J}$ | transformation matrix from real and imaginary parts to conjugate coordinates, see (3.15), (3.19) and (3.24) |
| $\mathbf{M}$ | positive definite Hermitian matrix, see (5.83) |
| $\mathbf{O}$ | system matrix for direct phase retrieval, see (5.102) |
| $\mathbf{P}$ | idempotent projection matrix, see (6.20) |

| Symbol | Description |
|---|---|
| $\mathbf{P}_1$ | matrix picking the source coefficients from the combined vector of unknowns, see (6.9) |
| $\mathbf{P}_2$ | matrix picking the remaining phase unknowns from the combined vector of unknowns, see (6.9) |
| $\mathbf{P}_{\mathrm{LMF}}$ | projection matrix for the multi-frequency case, see (6.46) |
| $\mathbf{Q}, \mathbf{R}$ | orthogonal and upper triangular matrices, belonging to a $\mathbf{QR}$-decomposition |
| $\mathbf{U}$ | bilinear form of unknown phase terms, see (5.85) |
| $\mathbf{W}$ | target bilinear matrix for direct phase retrieval, see (5.99) and (5.106) |
| $\tilde{\mathbf{W}}$ | collection of desired measurement rows, see (5.108) |
| $\mathbf{X}$ | matrix of unknowns, part of a PhaseCut implementation based on the presented optimization framework, see (A.51) |
| $\mathbf{Y}$ | square matrix employed in spectral initialization methods, see (5.2) |
| $\mathbf{Z}$ | bilinear form of unknown source coefficients, see (5.73) |

*Vectors*

| Symbol | Description |
|---|---|
| $\boldsymbol{b}$ | complex-valued measurement vector |
| $\tilde{\boldsymbol{b}}$ | measurements belonging to the matrix $\tilde{\mathbf{W}}$, see (5.107) and (5.109) |
| $\boldsymbol{d}$ | vector of known information, part of cost functions, e.g., see (3.67) |
| $\boldsymbol{I}^\star, \boldsymbol{r}^\star, \boldsymbol{p}^\star$ | collection of source dipole coefficients, orientations and locations, see (2.33) |
| $\boldsymbol{I}', \boldsymbol{r}', \boldsymbol{p}'$ | collection of observation dipole coefficients, orientations and locations, see (2.34) |
| $\boldsymbol{M}$ | vector of stacked reciprocal probe signal magnitudes, see (5.50) and (5.51) |
| $\boldsymbol{p}$ | descent direction, e.g., see (3.52) and (3.55) |
| $\boldsymbol{s}_i, \boldsymbol{y}_i$ | quantities stored as part of the L-BFGS method, see Alg. 1 |
| $\boldsymbol{t}$ | vector defining the matrix $\mathbf{Y}$ dependent on the specific initialization method, see (5.3) to (5.7) |
| $\boldsymbol{u}$ | complex-valued vector of unknown phase terms as defined in (5.77) |
| $\boldsymbol{v}_{i,j}$ | $j$th column of the bilinear form of the $i$th column of $\mathbf{A}$, see (5.101) |
| $\boldsymbol{w}_i$ | columns of $\mathbf{W}$, see (5.106) |
| $\hat{\boldsymbol{w}}$ | vectorized bilinear form of $\mathbf{W}$, see (5.102) |
| $\boldsymbol{q}_i$ | columns of $\mathbf{O}$, see (5.102) |
| $\boldsymbol{z}$ | vector of unknowns |
| $\tilde{\boldsymbol{z}}$ | combined vector of unknowns consisting of the source coefficients and the remaining unknown phase terms, see (6.9) |
| $\boldsymbol{z}_{\mathrm{i/t}}$ | initial/true solution vector |
| $\boldsymbol{z}_{\mathrm{PM}}$ | anchor vector required by PhaseMax, see (5.88) |
| $\boldsymbol{\epsilon}_c, \boldsymbol{\epsilon}_{c,\mathrm{dB}}$ | scale-invariant normalized vector of deviations, see (4.15) |
| $\boldsymbol{\varphi}_z$ | phase vector in the source domain, e.g., see (5.11) |
| $\boldsymbol{\varphi}_b$ | phase vector in the observation domain, e.g., see (5.10) |
| $\boldsymbol{\psi}$ | vector of remaining unknown phase terms, see (6.8) |

| Symbol | Description |
|---|---|
| *Scalars* | |
| $c_{1/2}$ | parameters of the (strong) Wolfe conditions, see (3.58) and (3.59) |
| $c_{\text{si}}$ | factor adjusting the scaling in $\mathcal{A}_2$, see (5.31) |
| $C$ | number of coherent channels of a multi-channel receiver |
| $J$ | number of spherical vector wave functions associated with a certain multipole order, see (2.25) |
| $k_{\text{it}}$ | number of iterations performed |
| $k_{\text{max}}$ | maximum number of iterations allowed |
| $l$ | number of frequencies considered with multi-frequency data |
| $L_{\text{mem}}$ | number of previous iterations considered in the L-BFGS method |
| $m$ | number of observation entries |
| $n$ | number of source coefficients |
| $n_{\text{SNR}}, n_{\text{SNR,dB}}$ | SNR in linear and logarithmic scale, see (6.40) |
| $N_0$ | multipole order according to (2.18) |
| $p_{1/2/3}$ | exponent parameters of $\mathcal{A}_{1/2/3}$ |
| $p_{\text{PM}}, q_{\text{PM}}$ | parameters required for a PhaseMax implementation based on the presented optimization framework, see (A.55) |
| $p_{91}, p_{92}$ | exponent parameters as part of (5.67) |
| $q$ | number of unknown phase terms in the presence of partial coherence |
| $\alpha$ | step length, e.g., see (3.52) |
| $\alpha_{\text{i/m}}$ | initial/maximum step length |
| $\alpha_{\text{OF}}, p_{\text{OF}}$ | weighting and exponent of cost functions, e.g., see (3.67) |
| $\alpha_{\text{opt}}$ | optimal step length in the context of $\mathcal{A}_0$, see (4.12) |
| $\beta$ | conjugate gradient weighting, see Tab. 3.2 |
| $\epsilon_c, \epsilon_{c,\text{dB}}$ | scale-invariant relative NF deviation in linear and logarithmic scale, see (4.14) |
| $\Phi(\alpha)$ | one-dimensional representation of a cost function along a descent direction dependent on the step length, e.g., see (3.57) |
| $\chi, \chi_c$ | cosine similarity and scale-invariant cosine similarity, see (5.8) and (5.9) |
| *Cost function operators* | |
| $\mathcal{A}$ | nonlinear operator essentially defining a cost function, e.g., see (3.67) |
| $\mathcal{A}_0$ | operator related to solving the fully coherent problem, see (4.4) |
| $\mathcal{A}_1$ | nonlinear operator related to a standard phase retrieval approach, see (5.16) |
| $\mathcal{A}_2$ | scale-invariant nonlinear operator for phase retrieval, see (5.30) |
| $\mathcal{A}_3$ | operator defining a cost function in terms of the normal error system of equations, see (A.34) |
| $\mathcal{A}_4$ | operator defining a phase-invariant cost function, see (A.35) |
| $\mathcal{A}_5$ | projector-based phase retrieval operator employing real-valued unknowns, see (5.38) |

| Symbol | Description |
|--------|-------------|
| $\mathcal{A}_6$ | projector-based phase retrieval operator employing complex-valued unknowns, see (5.43) |
| $\mathcal{A}_7$ | nonlinear operator containing the spatial derivative of the magnitude of probe signals, see (5.48) |
| $\mathcal{A}_9$ | nonlinear operator implementing a cosine-similarity maximization, see (5.67) |
| $\mathcal{A}_{\text{PL}}$ | nonlinear forward operator of PhaseLift, see (5.74) |
| $\mathcal{A}_{\text{PC}}$ | operator of a PhaseCut implementation based on the presented optimization framework, see (A.51) |
| $\mathcal{A}_{\text{PM}}$ | operator of a PhaseMax implementation based on the presented optimization framework, see (A.55) |
| $\mathcal{A}_{11}$ | operator defining a cost function for phase retrieval from incomplete magnitude and phase measurements, see (A.40) |
| $\mathcal{A}_{12}$ | operator required for a magnitude retrieval algorithm implemented via the presented optimization framework, see (A.61) |

# Abbreviations

AUT       antenna under test
AWS       Amazon Web Services
CPU       central processing unit
DM        dipole moment
DoF       degree of freedom
FF        far field
FIAFTA    fast irregular antenna field transformation algorithm
GMRES     generalized minimal residual
GPU       graphics processing unit
L-BFGS    memory-limited Broyden-Fletcher-Goldfarb-Shanno
LC        linear combination
LO        local oscillator
LSQR      least squares
MLFMM     multi-level fast-multipole method
MoM       method of moments
NF        near field
NFFFT     near-field far-field transformation
NP-hard   non-deterministic polynomial-time hard
PEC       perfect electric conductor or perfectly electrically conducting
QMR       quasi-minimal residual
RX        receiver
SVD       singular value decomposition
TX        transmitter
UTD       uniform theory of diffraction

# Bibliography

3DS Simulia (2019), *CST Studio Suite*, Dassault Systems, Vélizy-Villacoublay, France, URL: https://www.3ds.com/products-services/simulia/products/cst-studio-suite/.

Abramowitz, M. and I. A. Stegun, eds. (2013), *Handbook of Mathematical Functions: With Formulas, Graphs, and Mathematical Tables*, 9th ed., Dover Books on Mathematics, New York, NY, USA: Dover Publishing, URL: https://www.cs.bham.ac.uk/~aps/research/projects/as/.

Altair Engineering Inc. (2018), *Altair® Feko®*, URL: https://www.altair.com/feko/.

– (2019), *Altair Feko 2019.1 examples guide*.

Álvarez-Narciandi, G., J. Laviada, Y. Álvarez-López, G. Ducournau, C. Luxey, C. Belem-Goncalves, F. Gianesello, N. Nachabe, C. Del Rio, and F. Las-Heras (2021), "Freehand system for antenna diagnosis based on amplitude-only data", *IEEE Transactions on Antennas and Propagation*, vol. 69, no. 8, pp. 4988–4998.

Amazon Web Services Inc. (n.d.), URL: https://aws.amazon.com.

Ambrosio et al., M. (2002), "Final results of magnetic monopole searches with the MACRO experiment", *The European Physical Journal C*, vol. 25, no. 4, pp. 511–522.

Anastassiu, H. T., D. I. Kaklamani, D. P. Economou, and O. Breinbjerg (2002), "Electromagnetic scattering analysis of coated conductors with edges using the method of auxiliary sources (MAS) in conjunction with the standard impedance boundary condition (SIBC)", *IEEE Transactions on Antennas and Propagation*, vol. 50, no. 1, pp. 59–66.

Andrei, N. (2010), "Accelerated scaled memoryless BFGS preconditioned conjugate gradient algorithm for unconstrained optimization", *European Journal of Operational Research*, vol. 204, no. 3, pp. 410–420.

Araque Quijano, J. L., G. Vecchi, L. Li, M. Sabbadini, L. Scialacqua, B. Bencivenga, F. Mioc, and L. Foged (2010), "3D spatial filtering applications in spherical near field antenna measurements", *33th Meeting and Symposium of the Antenna Measurement Techniques Association (AMTA)*, Atlanta, GA, USA.

Asmundis, R. de, D. Di Serafino, F. Riccio, and G. Toraldo (2013), "On spectral properties of steepest descent methods", *IMA Journal of Numerical Analysis*, vol. 33, no. 4, pp. 1416–1435.

Azhar, A. and T. F. Eibert (2021), "A dual-polarized tapered slot antenna for UAV-Based collection of locally coherent field data", *15th European Conference on Antennas and Propagation (EuCAP)*, Düsseldorf, Germany.

Babaie-Kafaki, S., R. Ghanbari, and N. Mahdavi-Amiri (2010), "Two new conjugate gradient methods based on modified secant equations", *Journal of Computational and Applied Mathematics*, vol. 234, no. 5, pp. 1374–1386.

Bacca, J., S. Pinilla, and H. Arguello (2019), "Super-resolution phase retrieval from designed coded diffraction patterns", *IEEE Transactions on Image Processing*, vol. 29, pp. 2598–2609.

Baechler, G., M. Krekovic, J. Ranieri, A. Chebira, Y. M. Lu, and M. Vetterli (2019), "Super resolution phase retrieval for sparse signals", *IEEE Transactions on Signal Processing*, vol. 67, no. 18, pp. 4839–4854.

Bahmani, S. and J. Romberg (2017), "Phase retrieval meets statistical learning theory: A flexible convex relaxation", *20th International Conference on Artificial Intelligence and Statistics (AISTATS)*, vol. 54, Fort Lauderdale, FL, USA, pp. 252–260.

*Bibliography*

Balan, R., B. G. Bodmann, P. G. Casazza, and D. Edidin (2009), "Painless reconstruction from magnitudes of frame coefficients", *Journal of Fourier Analysis and Applications*, vol. 15, no. 4, pp. 488–501.

Balan, R., P. Casazza, and D. Edidin (2006), "On signal reconstruction without phase", *Applied and Computational Harmonic Analysis*, vol. 20, no. 3, pp. 345–356.

Bandeira, A., J. Cahill, D. G. Mixon, and A. Nelson (2013), "Fundamental limits of phase retrieval", *10th International Conference on Sampling Theory and Applications (SampTA)*, Bremen, Germany, pp. 77–80.

Bangun, A., A. Behboodi, and R. Mathar (2019a), "Signal recovery from phaseless measurements of spherical harmonics expansion", *27th European Signal Processing Conference (EUSIPCO)*, A Coruna, Spain.

Bangun, A., C. Culotta-López, A. Behboodi, R. Mathar, and D. Heberling (2019b), "On phaseless spherical near-field antenna measurements", *13th European Conference on Antennas and Propagation (EuCAP)*, Krakow, Poland.

Bao, S., D. Wang, Y. Mo, S. Hu, J. Gu, and W. Tang (2020), "Fully analytical evaluation of singular integrals with RWG and rooftop basis functions", *IEEE Journal on Multiscale and Multiphysics Computational Techniques*, vol. 5, pp. 217–226.

Bates, R. H. (1982), "Fourier phase problems are uniquely solvable in more than one dimension. I: Underlying theory", *Optik (Stuttgart)*, vol. 61, no. 3, pp. 247–262.

Bauschke, H. H., P. L. Combettes, and D. R. Luke (2002), "Phase retrieval, error reduction algorithm, and Fienup variants: A view from convex optimization", *Journal of the Optical Society of America A (JOSA)*, vol. 19, no. 7, pp. 1334–1345.

Bendory, T., R. Beinert, and Y. C. Eldar (2017), "Fourier phase retrieval: Uniqueness and algorithms", *Compressed Sensing and its Applications*, ed. by H. Boche, G. Caire, R. Calderbank, M. März, G. Kutyniok, and R. Mathar, Applied and Numerical Harmonic Analysis, Cham: Birkhäuser, pp. 55–91.

Berlt, P., C. Bornkessel, and M. A. Hein (2020), "Accurate 3D phase recovery of automotive antennas through LTE power measurements on a cylindrical surface", *14th European Conference on Antennas and Propagation (EuCAP)*, Copenhagen, Denmark.

Birgin, E. G. (2001), "A spectral conjugate gradient method for unconstrained optimization", *Applied Mathematics and Optimization*, vol. 43, no. 2, pp. 117–128.

Bodmann, B. G. and N. Hammen (2015), "Stable phase retrieval with low-redundancy frames", *Advances in Computational Mathematics*, vol. 41, no. 2, pp. 317–331.

Borwein, J., K. Dilcher, and A. Lewis (2006), *Convex Analysis and Nonlinear Optimization*, New York, NY, USA: Springer New York.

Bovet, D. P. and P. Crescenzi (1993), *Introduction to the Theory of Complexity*, Upper Saddle River, NJ, USA: Prentice Hall.

Boyd, S. P. and L. Vandenberghe (2018), *Convex Optimization*, 22nd ed., Cambridge, UK: Cambridge University Press.

Boykov, Y., O. Veksler, and R. Zabih (2001), "Fast approximate energy minimization via graph cuts", *IEEE Transactions on Pattern Analysis and Machine Intelligence*, vol. 23, no. 11, pp. 1222–1239.

Brandwood, D. H. (1983), "A complex gradient operator and its application in adaptive array theory", *IEE Proceedings H-Microwaves, Optics and Antennas*, vol. 130, no. 1, pp. 11–16.

Breinbjerg, O. and J. F. Alvarez (2019), "Mathematical formulation of phase retrieval for phaseless spherical near-field antenna measurements with probe correction", *URSI International Symposium on Electromagnetic Theory (EMTS)*, San Diego, CA, USA.

Bucci, O. M., G. D'Elia, and M. D. Migliore (1999), "An effective near-field far-field transformation technique from truncated and inaccurate amplitude-only data", *IEEE Transactions on Antennas and Propagation*, vol. 47, no. 9, pp. 1377–1385.

Bucci, O. M., C. Gennarelli, and C. Savarese (1991), "Fast and accurate near-field-far-field transformation by sampling interpolation of plane-polar measurements", *IEEE Transactions on Antennas and Propagation*, vol. 39, no. 1, pp. 48–55.

Cai, J.-F., H. Liu, and Y. Wang (2019), "Fast rank-one alternating minimization algorithm for phase retrieval", *Journal of Scientific Computing*, vol. 79, no. 1, pp. 128–147.

Candès, E. J. and X. Li (2014), "Solving quadratic equations via PhaseLift when there are about as many equations as unknowns", *Foundations of Computational Mathematics*, vol. 14, no. 5, pp. 1017–1026.

Candès, E. J., X. Li, and M. Soltanolkotabi (2015a), "Phase retrieval from coded diffraction patterns", *Applied and Computational Harmonic Analysis*, vol. 39, no. 2, pp. 277–299.

– (2015b), "Phase retrieval via Wirtinger flow: Theory and algorithms", *IEEE Transactions on Information Theory*, vol. 61, no. 4, pp. 1985–2007.

Candès, E. J., T. Strohmer, and V. Voroninski (2013), "Phaselift: Exact and stable signal recovery from magnitude measurements via convex programming", *Communications on Pure and Applied Mathematics*, vol. 66, no. 8, pp. 1241–1274.

Capoglu, İ. R., A. Taflove, and V. Backman (2012), "A frequency-domain near-field-to-far-field transform for planar layered media", *IEEE Transactions on Antennas and Propagation*, vol. 60, no. 4, pp. 1878–1885.

Cappellin, C. and S. Pivnenko (2014), "Filtering of measurement noise with the 3D reconstruction algorithm", *36th Meeting and Symposium of the Antenna Measurement Techniques Association (AMTA)*, Boston, MA, USA.

Castaldi, G. and I. M. Pinto (2000), "Well-posed well-conditioned phase retrieval technique using a known reference source", *APS International Symposium on Antennas and Propagation & USNC/URSI National Radio Science Meeting*, Salt Lake City, UT, USA, pp. 1780–1782.

Cauchy, A. (1847), "Méthode générale pour la résolution des systemes d'équations simultanées", *Comptes Rendus de l'Académie des Sciences*, vol. 25, no. 1847, pp. 536–538.

Chandra, R., T. Goldstein, and C. Studer (2019), "PhasePack: A phase retrieval library", *13th International Conference on Sampling Theory and Applications (SampTA)*, Bordeaux, France.

Chandra, R., Z. Zhong, J. Hontz, V. McCulloch, C. Studer, and T. Goldstein (2017), "PhasePack: A phase retrieval library", *51st Asilomar Conference on Signals, Systems, and Computers (ACSSC)*, Pacific Grove, CA, USA, pp. 1617–1621.

Chen, P., A. Fannjiang, and G.-R. Liu (2018), "Phase retrieval with one or two diffraction patterns by alternating projections with the null initialization", *Journal of Fourier Analysis and Applications*, vol. 24, no. 3, pp. 719–758.

Chen, S. S., D. L. Donoho, and M. A. Saunders (2001), "Atomic decomposition by basis pursuit", *SIAM Review*, vol. 43, no. 1, pp. 129–159.

Chen, Y. and E. J. Candès (2017), "Solving random quadratic systems of equations is nearly as easy as solving linear systems", *Communications on Pure and Applied Mathematics*, vol. 70, no. 5, pp. 822–883.

Chew, W. C., E. Michielssen, J. M. Song, and J.-M. Jin (2001), *Fast and Efficient Algorithms in Computational Electromagnetics*, London, UK: Artech House, Inc.

Clarke, F. H. (1989), *Optimization and Nonsmooth Analysis*, Montreal, Canada: Les Publications CRM, Université de Montréal.

Clerc, M. (2006), *Particle Swarm Optimization*, London, UK: ISTE.

Coene, W., G. Janssen, M. op de Beeck, and D. van Dyck (1992), "Phase retrieval through focus variation for ultra-resolution in field-emission transmission electron microscopy", *Physical Review Letters*, vol. 69, no. 26, pp. 3743–3746.

Conca, A., D. Edidin, M. Hering, and C. Vinzant (2015), "An algebraic characterization of injectivity in phase retrieval", *Applied and Computational Harmonic Analysis*, vol. 38, no. 2, pp. 346–356.

Cooperstein, B. (2016), *Advanced Linear Algebra*, Boca Raton, FL, USA: CRC Press.

Cornelius, R. and D. Heberling (2017), "Correction of non-ideal probe orientations for spherical near-field antenna measurements", *39th Meeting and Symposium of the Antenna Measurement Techniques Association (AMTA)*, Atlanta, GA, USA.

Cornelius, R., D. Heberling, N. Koep, A. Behboodi, and R. Mathar (2016), "Compressed sensing applied to spherical near-field to far-field transformation", *10th European Conference on Antennas and Propagation (EuCAP)*, Davos, Switzerland.

Costanzo, S., G. Di Massa, and M. D. Migliore (2001), "Integrated microstrip probe for phaseless near-field measurements on plane-polar geometry", *Electronics Letters*, vol. 37, no. 16, pp. 1018–1020.

– (2005), "A novel hybrid approach for far-field characterization from near-field amplitude-only measurements on arbitrary scanning surfaces", *IEEE Transactions on Antennas and Propagation*, vol. 53, no. 6, pp. 1866–1874.

Costanzo, S. and G. Di Massa (2001), "An integrated probe for phaseless plane-polar near-field measurements", *Microwave and Optical Technology Letters*, vol. 30, no. 5, pp. 293–295.

– (2008), "Wideband phase retrieval technique from amplitude-only near-field data", *Radioengineering*, vol. 17, no. 4, pp. 8–12.

Costanzo, S. and G. Lopez (2020), "Phaseless approach to microwave biomedical imaging: System requirements towards clinical applications", *14th European Conference on Antennas and Propagation (EuCAP)*, Copenhagen, Denmark.

Dai, Y. H. and Y. Yuan (1999), "A nonlinear conjugate gradient method with a strong global convergence property", *SIAM Journal on Optimization*, vol. 10, no. 1, pp. 177–182.

Davis, L. (1990), *Genetic Algorithms and Simulated Annealing*, Reprint, Research Notes in Artificial Intelligence, London, UK: Pitman.

Demmel, J. W. (1997), *Applied Numerical Linear Algebra*, Philadelphia, PA, USA: Society for Industrial and Applied Mathematics.

Devaney, A. J. and R. Chidlaw (1978), "On the uniqueness question in the problem of phase retrieval from intensity measurements", *Journal of the Optical Society of America A (JOSA)*, vol. 68, no. 10, pp. 1352–1354.

Donoho, D. L. (2006), "Compressed sensing", *IEEE Transactions on Information Theory*, vol. 52, no. 4, pp. 1289–1306.

Dudeja, R., M. Bakhshizadeh, J. Ma, and A. Maleki (2020), "Analysis of spectral methods for phase retrieval with random orthogonal matrices", *IEEE Transactions on Information Theory*, vol. 66, no. 8, pp. 5182–5203.

Eibert, T. F. (2007), "Some scattering results computed by surface-integral-equation and hybrid finite-element-boundary-integral techniques, accelerated by the multilevel fast multipole method", *IEEE Antennas and Propagation Magazine*, vol. 49, no. 2, pp. 61–69.

Eibert, T. F. and V. Hansen (1995), "On the calculation of potential integrals for linear source distributions on triangular domains", *IEEE Transactions on Antennas and Propagation*, vol. 43, no. 12, pp. 1499–1502.

Eibert, T. F., Ismatullah, E. Kaliyaperumal, and C. H. Schmidt (2010), "Inverse equivalent surface current method with hierarchical higher order basis functions, full probe correction and multilevel fast multipole acceleration [Invited paper]", *Progress In Electromagnetics Research*, vol. 106, pp. 377–394.

Eibert, T. F., E. Kilic, C. Lopez, R. A. Mauermayer, O. Neitz, and G. Schnattinger (2015), "Electromagnetic field transformations for measurements and simulations [Invited paper]", *Progress In Electromagnetics Research*, vol. 151, pp. 127–150.

Eibert, T. F. and C. H. Schmidt (2009), "Multilevel fast multipole accelerated inverse equivalent current method employing Rao–Wilton–Glisson discretization of electric and magnetic surface currents", *IEEE Transactions on Antennas and Propagation*, vol. 57, no. 4, pp. 1178–1185.

Eisler, S. and Y. Leviatan (1989), "Analysis of electromagnetic scattering from metallic and penetrable cylinders with edges using a multifilament current model", *IEE Proceedings H-Microwaves, Antennas and Propagation*, vol. 136, no. 6, pp. 431–438.

Elser, V. (2003), "Phase retrieval by iterated projections", *Journal of the Optical Society of America A (JOSA)*, vol. 20, no. 1, pp. 40–55.

Estatico, C., A. Fedeli, M. Pastorino, A. Randazzo, and E. Tavanti (2020), "A phaseless microwave imaging approach based on a Lebesgue-space inversion algorithm", *IEEE Transactions on Antennas and Propagation*, vol. 68, no. 12, pp. 8091–8103.

Fadili, M.-J., M. Melkemi, and A. Elmoataz (2004), "Non-convex onion-peeling using a shape hull algorithm", *Pattern Recognition Letters*, vol. 25, no. 14, pp. 1577–1585.

Faulkner, H. M. L. and J. M. Rodenburg (2004), "Movable aperture lensless transmission microscopy: A novel phase retrieval algorithm", *Physical Review Letters*, vol. 93, no. 2, p. 023903.

Fienup, J. R. (1982), "Phase retrieval algorithms: A comparison", *Applied Optics*, vol. 21, no. 15, pp. 2758–2769.

Fletcher, R. and C. M. Reeves (1964), "Function minimization by conjugate gradients", *The Computer Journal*, vol. 7, no. 2, pp. 149–154.

Foged, L. J., L. Scialacqua, F. Mioc, F. Saccardi, P. O. Iversen, L. Shmidov, R. Braun, J. L. A. Quijano, and G. Vecchi (2013), "Echo suppression by spatial-filtering techniques in advanced planar and spherical near-field antenna measurements [AMTA corner]", *IEEE Antennas and Propagation Magazine*, vol. 55, no. 5, pp. 235–242.

Fogel, F., I. Waldspurger, and A. d'Aspremont (2016), "Phase retrieval for imaging problems", *Mathematical Programming Computation*, vol. 8, no. 3, pp. 311–335.

Foucart, S. and H. Rauhut (2013), *A Mathematical Introduction to Compressive Sensing*, New York, NY, USA: Springer New York.

Frank, M. and P. Wolfe (1956), "An algorithm for quadratic programming", *Naval Research Logistics Quarterly*, vol. 3, no. 1-2, pp. 95–110.

Freund, R. W. and N. M. Nachtigal (1991), "QMR: A quasi-minimal residual method for non-Hermitian linear systems", *Numerische Mathematik*, vol. 60, no. 1, pp. 315–339.

Fuchs, B. and L. Le Coq (2015), "Excitation retrieval of microwave linear arrays from phaseless far-field data", *IEEE Transactions on Antennas and Propagation*, vol. 63, no. 2, pp. 748–754.

Fuchs, B., M. Mattes, S. Rondineau, and L. Le Coq (2020), "Phaseless near-field antenna measurements from two surface scans — numerical and experimental investigations", *IEEE Transactions on Antennas and Propagation*, vol. 68, no. 3, pp. 2315–2322.

Gabor, D. (1949), "Microscopy by reconstructed wave-fronts", *Proceedings of the Royal Society of London A: Mathematical, Physical and Engineering Sciences*, vol. 197, pp. 454–487.

*Bibliography*

Gerchberg, R. W. and W. O. Saxton (1972), "A practical algorithm for the determination of phase from image and diffraction plane pictures", *Optik*, vol. 35, pp. 237–246.

Gilbert, J. C. and J. Nocedal (1992), "Global convergence properties of conjugate gradient methods for optimization", *SIAM Journal on Optimization*, vol. 2, no. 1, pp. 21–42.

Goldstein, T. and C. Studer (2018), "PhaseMax: Convex phase retrieval via basis pursuit", *IEEE Transactions on Information Theory*, vol. 64, no. 4, pp. 2675–2689.

Goldstein, T., C. Studer, and R. Baraniuk (2014), "A field guide to forward-backward splitting with a FASTA implementation", *arXiv preprint arXiv: 1411.3406*, URL: https://arxiv.org/abs/1411.3406.

Gregson, S. F., A. C. Newell, and G. E. Hindman (2012), "Examination of far-field mathematical absorber reflection suppression through computational electromagnetic simulation", *International Journal of Antennas and Propagation*, vol. 2012, no. 623268.

Gross, D., F. Krahmer, and R. Kueng (2015), "A partial derandomization of PhaseLift using spherical designs", *Journal of Fourier Analysis and Applications*, vol. 21, no. 2, pp. 229–266.

Guizar-Sicairos, M. and J. R. Fienup (2008), "Phase retrieval with transverse translation diversity: A nonlinear optimization approach", *Optics Express*, vol. 16, no. 10, pp. 7264–7278.

Gunther, J., S. Popov, H.-P. Seidel, and P. Slusallek (2007), "Realtime ray tracing on GPU with BVH-based packet traversal", *2nd Symposium on Interactive Ray Tracing*, Ulm, Germany, pp. 113–118.

Hager, W. W. and H. Zhang (2005), "A new conjugate gradient method with guaranteed descent and an efficient line search", *SIAM Journal on Optimization*, vol. 16, no. 1, pp. 170–192.

– (2006), "A survey of nonlinear conjugate gradient methods", *Pacific journal of Optimization*, vol. 2, no. 1, pp. 35–58.

Hansen, J. E. (2008), *Spherical Near-Field Antenna Measurements*, Reprinted, vol. 26, Stevenage, UK: The Institute of Engineering and Technology.

Hansen, R. C. (1981), "Fundamental limitations in antennas", *Proceedings of the IEEE*, vol. 69, no. 2, pp. 170–182.

Hansen, T. B., A. Paulus, and T. F. Eibert (2019), "On the condition number of a normal matrix in near-field to far-field transformations", *IEEE Transactions on Antennas and Propagation*, vol. 67, no. 3, pp. 2028–2033.

Hansen, W. W. and J. R. Woodyard (1938), "A new principle in directional antenna design", *Proceedings of the IRE*, vol. 26, no. 3, pp. 333–345.

Harrington, R. F. (2001), *Time-Harmonic Electromagnetic Fields*, 2nd ed., New York, NY, USA: John Wiley & Sons.

Harrington, R. F. and J. L. Harrington (1996), *Field Computation by Moment Methods*, New York, NY, USA: Oxford University Press.

Harrison, R. W. (1993), "Phase problem in crystallography", *Journal of the Optical Society of America A (JOSA)*, vol. 10, no. 5, pp. 1046–1055.

Hassan, M. A. M. and A. A. Kishk (2018), "Solutions for general-purpose electromagnetic problems using the random auxiliary sources method", *IEEE Transactions on Antennas and Propagation*, vol. 66, no. 4, pp. 1947–1956.

Helmberg, C., F. Rendl, R. J. Vanderbei, and H. Wolkowicz (1996), "An interior-point method for semidefinite programming", *SIAM Journal on Optimization*, vol. 6, no. 2, pp. 342–361.

Heretakis, I. I., P. J. Papakanellos, and C. N. Capsalis (2005), "A stochastically optimized adaptive procedure for the location of MAS auxiliary monopoles: The case of electromagnetic scattering by dielectric cylinders", *IEEE Transactions on Antennas and Propagation*, vol. 53, no. 3, pp. 938–947.

Hess, D. W. (2010), "The IsoFilter technique: A method of isolating the pattern of an individual radiator from data measured in a contaminated environment", *IEEE Antennas Propagation Magazine*, vol. 52, no. 1, pp. 174–181.

Hestenes, M. R. and E. Stiefel (1952), "Methods of conjugate gradients for solving linear systems", *Journal of Research of the National Bureau of Standards*, vol. 49, no. 6, pp. 409–436.

Holloway, J., M. S. Asif, M. K. Sharma, N. Matsuda, R. Horstmeyer, O. Cossairt, and A. Veeraraghavan (2016), "Toward long-distance subdiffraction imaging using coherent camera arrays", *IEEE Transactions on Computational Imaging*, vol. 2, no. 3, pp. 251–265.

Huang, K., Y. C. Eldar, and N. D. Sidiropoulos (2016), "Phase retrieval from 1D Fourier measurements: Convexity, uniqueness, and algorithms", *IEEE Transactions on Signal Processing*, vol. 64, no. 23, pp. 6105–6117.

Hwang, C.-R. (1988), "Simulated annealing: Theory and applications", *Acta Applicandae Mathematicae*, vol. 12, no. 1, pp. 108–111.

Inan, K. and R. E. Diaz (2011), "On the uniqueness of the phase retrieval problem from far field amplitude-only data", *IEEE Transactions on Antennas and Propagation*, vol. 59, no. 3, pp. 1053–1057.

Intel Corporation (2018), *Intel C++ compiler version 19.0.*

Isernia, T., G. Leone, and R. Pierri (1996a), "Radiation pattern evaluation from near-field intensities on planes", *IEEE Transactions on Antennas and Propagation*, vol. 44, no. 5, pp. 701–710.

Isernia, T., F. Soldovieri, G. Leone, and R. Pierri (1996b), "On the local minima in phase reconstruction algorithms", *Radio Science*, vol. 31, no. 6, pp. 1887–1899.

Jaganathan, K., S. Oymak, and B. Hassibi (2013), "Sparse phase retrieval: Convex algorithms and limitations", *International Symposium on Information Theory (ISIT)*, Istanbul, Turkey, pp. 1022–1026.

Jaggi, M. (2013), "Revisiting Frank-Wolfe: Projection-free sparse convex optimization", *30th International Conference on Machine Learning (ICML)*, vol. 28, 1, Atlanta, GA, USA, pp. 427–435.

Järvenpää, S., M. Taskinen, and P. Ylä-Oijala (2003), "Singularity extraction technique for integral equation methods with higher order basis functions on plane triangles and tetrahedra", *International Journal for Numerical Methods in Engineering*, vol. 58, no. 8, pp. 1149–1165.

Ji, L. and Z. Tie (2016), "On gradient descent algorithm for generalized phase retrieval problem", *13th International Conference on Signal Processing (ICSP)*, Chengdu, China, pp. 320–325.

Ji, X., X. Liu, and B. Zhang (2019), "Phaseless inverse source scattering problem: Phase retrieval, uniqueness and direct sampling methods", *Journal of Computational Physics: X*, vol. 1, p. 100003.

Jin, B. and P. Maass (2012), "Sparsity regularization for parameter identification problems", *Inverse Problems*, vol. 28, no. 12, p. 123001.

Jin, J.-M. (2015), *Theory and Computation of Electromagnetic Fields*, 2nd ed., Piscataway, NJ and Hoboken, NJ, USA: IEEE Press and Wiley.

Jorgensen, E., D. W. Hess, P. Meincke, O. Borries, C. Cappellin, and J. Fordham (2012), "Antenna diagnostics on planar arrays using a 3D source reconstruction technique and spherical near-field measurements", *6th European Conference on Antennas and Propagation (EUCAP)*, Prague, Czech Republic, pp. 2547–2550.

Kaklamani, D. I. and H. T. Anastassiu (2002), "Aspects of the method of auxiliary sources (MAS) in computational electromagnetics", *IEEE Antennas and Propagation Magazine*, vol. 44, no. 3, pp. 48–64.

Kaneda, N., W. R. Deal, Y. Qian, R. Waterhouse, and T. Itoh (2002), "A broadband planar quasi-Yagi antenna", *IEEE Transactions on Antennas and Propagation*, vol. 50, no. 8, pp. 1158–1160.

Katz, V. J. (1979), "The history of Stokes' theorem", *Mathematics Magazine*, vol. 52, no. 3, pp. 146–156.

Keinert, B., M. Innmann, M. Sänger, and M. Stamminger (2015), "Spherical Fibonacci mapping", *ACM Transactions on Graphics*, vol. 34, no. 6, 193:1–193:7.

Kennedy, J. and R. Eberhart (1995), "Particle swarm optimization", *International Conference on Neural Networks (ICNN)*, Perth, WA, Australia, pp. 1942–1948.

Khan, H. N., D. A. Hounshell, and E. R. H. Fuchs (2018), "Science and research policy at the end of Moore's law", *Nature Electronics*, vol. 1, no. 1, pp. 14–21.

Klinkenbusch, L. (2008), "Brief review of spherical-multipole analysis in radio science", *URSI Radio Science Bulletin*, vol. 2008, no. 324, pp. 5–16.

Knapp, J. and T. F. Eibert (2018), "Accurate determination of radiation patterns from near-field measurements in highly reflective environments", *12th European Conference on Antennas and Propagation (EuCAP)*, London, UK.

Knapp, J., A. Paulus, and T. F. Eibert (2017a), "Implementation and evaluation of the utilization of partial knowledge of phase differences in magnitude only near-field far-field transformations", *Progress In Electromagnetics Research Symposium (PIERS)*, St. Petersburg, Russia.

– (2019a), "Investigation on diversity effects for phaseless near-field far-field transformations", *13th European Conference on Antennas and Propagation (EuCAP)*, Krakow, Poland.

– (2019b), "Reconstruction of squared field magnitudes and relative phases from magnitude-only near-field measurements", *IEEE Transactions on Antennas and Propagation*, vol. 67, no. 5, pp. 3397–3409.

Knapp, J., A. Paulus, J. Kornprobst, U. Siart, and T. F. Eibert (2021), "Multi-frequency phase retrieval for antenna measurements", *IEEE Transactions on Antennas and Propagation*, vol. 69, no. 1, pp. 488–501.

Knapp, J., A. Paulus, C. Lopez, and T. F. Eibert (2017b), "Comparison of non-convex cost functionals for the consideration of phase differences in phaseless near-field far-field transformations of measured antenna fields", *Advances in Radio Science (ARS)*, vol. 15, pp. 11–19.

Kornprobst, J., J. Knapp, R. A. M. Mauermayer, O. Neitz, A. Paulus, and T. F. Eibert (2021a), "Accuracy and conditioning of surface-source based near-field to far-field transformations", *IEEE Transactions on Antennas and Propagation*, vol. 69, no. 8.

Kornprobst, J., A. Paulus, T. F. Eibert, and R. A. M. Mauermayer (2019), "Method-of-moments modeling of conducting objects within the fast irregular antenna field transformation algorithm", *41st Antenna Measurement Techniques Association Symposium (AMTA)*, San Diego, CA, USA.

Kornprobst, J., A. Paulus, J. Knapp, and T. F. Eibert (2021b), "Phase retrieval for partially coherent observations", *IEEE Transactions on Signal Processing*, vol. 69, pp. 1394–1406.

Kou, S. S., L. Waller, G. Barbastathis, and C. J. R. Sheppard (2010), "Transport-of-intensity approach to differential interference contrast (TI-DIC) microscopy for quantitative phase imaging", *Optics Letters*, vol. 35, no. 3, pp. 447–449.

Kouroublakis, M., N. L. Tsitsas, and G. Fikioris (2021), "Mode analysis by the method of auxiliary sources with an excitation source", *IEEE Transactions on Microwave Theory and Techniques*, vol. 69, no. 6, pp. 2960–2971.

Kozan, T., S. Burgos, L. J. Foged, F. Saccardi, and P. O. Iversen (2014), "Comparison of a direct low-pass filtering technique with spherical modal filtering applied to the suppression of range reflections in antenna measurements", *8th European Conference on Antennas and Propagation (EuCAP)*, The Hague, The Netherlands, pp. 2481–2485.

Kreutz-Delgado, K. (2009), "The complex gradient operator and the CR-calculus", *arXiv preprint arXiv: 0906.4835,* URL: https://arxiv.org/abs/0906.4835.

Kudielka, K. H. and W. Klaus (1999), "Optical homodyne PSK receiver: Phase synchronization by maximizing baseband signal power", *12th Annual Meeting of the Lasers and Electro-Optics Society (LEOS)*, San Francisco, CA, USA, pp. 295–296.

Laitinen, T. A., S. Pivnenko, and O. Breinbjerg (2005), "Iterative probe correction technique for spherical near-field antenna measurements", *Antennas and Wireless Propagation Letters*, vol. 4, pp. 221–223.

Lane, R., W. Fright, and R. Bates (1987), "Direct phase retrieval", *IEEE Transactions on Acoustics, Speech, and Signal Processing*, vol. 35, no. 4, pp. 520–526.

Larsson, C. (2016), "Near to far field transformation of RCS using a compressive sensing method", *38th Meeting and Symposium of the Antenna Measurement Techniques Association (AMTA)*, Austin, TX, USA.

Las-Heras, F., Y. Álvarez-López, J. Laviada, A. Arboleya-Arboleya, M. García-Fernández, and G. Álvarez-Narciandi (2020), "Antenna measurements and signal processing techniques", *14th European Conference on Antennas and Propagation (EuCAP)*, Copenhagen, Denmark.

Laviada, J. and F. Las-Heras (2013), "Phaseless antenna measurement on non-redundant sample points via Leith-Upatnieks holography", *IEEE Transactions on Antennas and Propagation*, vol. 61, no. 8, pp. 4036–4044.

Laviada Martinez, J., A. Arboleya-Arboleya, Y. Álvarez-López, C. Garcia-Gonzalez, and F. Las-Heras (2014), "Phaseless antenna diagnostics based on off-axis holography with synthetic reference wave", *Antennas and Wireless Propagation Letters*, vol. 13, pp. 43–46.

Lee, H., A. Battle, R. Raina, and A. Y. Ng (2007), "Efficient sparse coding algorithms", *Advances in Neural Information Processing Systems (NIPS)*, pp. 801–808.

Leibfritz, M. M. and P. M. Landstorfer (2006), "Full probe-correction for near-field antenna measurements", *11th APS International Symposium on Antennas and Propagation*, Albuquerque, NM, USA, pp. 437–440.

Leon, S. J. (2015), *Linear Algebra with Applications*, 9th ed., Always Learning, Boston, MA, USA: Pearson.

Leone, G. (1997), "On the performances of two algorithms in phaseless antenna measurements", *10th International Conference on Antennas and Propagation (ICAP)*, Edinburgh, UK, pp. 136–141.

Leviatan, Y. (1990), "Analytic continuation considerations when using generalized formulations for scattering problems", *IEEE Transactions on Antennas and Propagation*, vol. 38, no. 8, pp. 1259–1263.

Li, H. and T. Adalı (2008), "Complex-valued adaptive signal processing using nonlinear functions", *EURASIP Journal on Advances in Signal Processing*, vol. 2008, no. 1, p. 765615.

Li, L.-W., X.-K. Kang, and M.-S. Leong (2004), *Spheroidal Wave Functions in Electromagnetic Theory*, 1st ed., vol. 1, Wiley Series in Microwave and Optical Engineering, New York, NY, USA: John Wiley & Sons.

Liu, D. C. and J. Nocedal (1989), "On the limited memory BFGS method for large scale optimization", *Mathematical Programming*, vol. 45, no. 1, pp. 503–528.

Liu, K., Z. Xing, L. Yang, and L. Wan (2018), "Phase retrieval via a modified null vector estimator", *10th International Conference on Wireless Communications and Signal Processing (WCSP)*, Hangzhou, China.

Liu, Y. and C. Storey (1991), "Efficient generalized conjugate gradient algorithms, part 1: Theory", *Journal of Optimization Theory and Applications*, vol. 69, no. 1, pp. 129–137.

Luo, Q., H. Wang, and S. Lin (2020), "Phase retrieval via smoothed amplitude flow", *Signal Processing*, vol. 177, p. 107719.

Luo, W., W. Alghamdi, and Y. M. Lu (2019), "Optimal spectral initialization for signal recovery with applications to phase retrieval", *IEEE Transactions on Signal Processing*, vol. 67, no. 9, pp. 2347–2356.

Macready, W. G. and D. H. Wolpert (1996), "What makes an optimization problem hand?", *Complexity*, vol. 1, no. 5, pp. 40–46.

Matlab (2021), *9.10.0.1602886 (R2021a)*, Natick, MA, USA.

Mauermayer, R. A. M. and T. F. Eibert (2015), "Combining the fast irregular antenna field transformation algorithm with asymptotic high frequency methods", *9th European Conference on Antennas and Propagation (EuCAP)*, Lisbon, Portugal.

– (2016), "Time gating based on sparse time domain signal reconstruction from limited frequency domain information", *39th Meeting and Symposium of the Antenna Measurement Techniques Association (AMTA)*, Austin, TX, USA.

– (2017), "Sparse time domain signal representation for echo suppression in antenna measurements", *19th International Conference on Electromagnetics in Advanced Applications (ICEAA)*, Verona, Italy, pp. 1247–1249.

– (2018), "Spherical field transformation above perfectly electrically conducting ground planes", *IEEE Transactions on Antennas and Propagation*, vol. 66, no. 3, pp. 1465–1478.

Mauermayer, R. A. M., G. Schnattinger, and T. F. Eibert (2013), "Antenna diagnostic, echo suppression and equivalent sources representation capabilities of the fast irregular antenna field transformation algorithm", *35th Meeting and Symposium of the Antenna Measurement Techniques Association (AMTA)*, Columbus, OH, USA.

Mauermayer, R. A. M., J. Kornprobst, and T. Fritzel (2019), "A low-cost multicopter based near-field antenna measurement system employing software defined radio and 6-D laser metrology", *41st Antenna Measurement Techniques Association Symposium (AMTA)*, San Diego, CA, USA.

Mc Donald, J. N. (2004), "Phase retrieval and magnitude retrieval of entire functions", *Journal of Fourier Analysis and Applications*, vol. 10, no. 3, pp. 259–267.

Miao, J., T. Ishikawa, Q. Shen, and T. Earnest (2008), "Extending X-ray crystallography to allow the imaging of noncrystalline materials, cells, and single protein complexes", *Annual Review of Physical Chemistry*, vol. 59, no. 1, pp. 387–410.

Miao, J., R. L. Sandberg, and C. Song (2012), "Coherent X-ray diffraction imaging", *IEEE Journal of Selected Topics in Quantum Electronics*, vol. 18, no. 1, pp. 399–410.

Microsoft Corporation (2021), *logman performance monitor*, URL: https://docs.microsoft.com/en-us/windows-server/administration/windows-commands/logman (visited on 2021).

Milnor, J. and D. Husemoller (1973), *Symmetric Bilinear Forms*, Berlin and Heidelberg, Germany: Springer Berlin Heidelberg.

Mises, R. V. and H. Pollaczek-Geiringer (1929), "Praktische Verfahren der Gleichungsauflösung", *ZAMM - Zeitschrift für Angewandte Mathematik und Mechanik*, vol. 9, no. 2, pp. 152–164.

Mitharwal, R. and F. P. Andriulli (2015), "A regularised boundary element formulation for contactless SAR evaluations within homogeneous and inhomogeneous head phantoms", *Comptes Rendus Physique*, vol. 16, no. 9, pp. 776–788.

Mittra, R., C. Pelletti, K. Panyappan, and A. Monorchio (2011), "The dipole moment (DM) and recursive update in frequency domain (RUFD) methods: Two novel techniques in computational electromagnetics", *URSI Radio Science Bulletin*, vol. 2011, no. 338, pp. 7–24.

Mobahi, H. and J. W. Fisher III (2015), "A theoretical analysis of optimization by Gaussian continuation", *Association for the Advancement of Artificial Intelligence (AAAI)*, Austin, TX, USA, pp. 1205–1211.

Moharram, M. A. and A. A. Kishk (2015a), "Efficient electromagnetic scattering computation using the random auxiliary sources method for multiple composite 3-D arbitrary objects", *IEEE Transactions on Antennas and Propagation*, vol. 63, no. 8, pp. 3621–3633.

– (2015b), "Electromagnetic scattering from two-dimensional arbitrary objects using random auxiliary sources", *IEEE Antennas and Propagation Magazine*, vol. 57, no. 1, pp. 204–216.

Mondelli, M. and A. Montanari (2019), "Fundamental limits of weak recovery with applications to phase retrieval", *Foundations of Computational Mathematics*, vol. 19, no. 3, pp. 703–773.

Moore, G. E. et al. (1975), "Progress in digital integrated electronics", *Electron devices meeting*, vol. 21, Maryland, pp. 11–13.

Moretta, R. and R. Pierri (2019), "Performance of phase retrieval via Phaselift and quadratic inversion in circular scanning case", *IEEE Transactions on Antennas and Propagation*, vol. 67, no. 12, pp. 7528–7537.

Mroueh, Y. and L. Rosasco (2014), "On efficiency and low sample complexity in phase retrieval", *International Symposium on Information Theory (ISIT)*, Honolulu, HI, USA, pp. 931–935.

Nagy, J. G. and K. M. Palmer (2003), "Steepest descent, CG, and iterative regularization of ill-posed problems", *BIT Numerical Mathematics*, vol. 43, no. 5, pp. 1003–1017.

Netrapalli, P., P. Jain, and S. Sanghavi (2015), "Phase retrieval using alternating minimization", *IEEE Transactions on Signal Processing*, vol. 63, no. 18, pp. 4814–4826.

Newell, A. C. (1988), "Error analysis techniques for planar near-field measurements", *IEEE Transactions on Antennas and Propagation*, vol. 36, no. 6, pp. 754–768.

Nocedal, J. and S. J. Wright (2006), *Numerical Optimization*, 2nd ed., Springer Series in Operations Research and Financial Engineering, New York, NY, USA: Springer Science+Business Media LLC.

Nvidia Corporation (2016a), *Nvidia DGX-1 artifical intelligence system*, URL: https://www.nvidia.com/en-us/data-center/dgx-systems/.

– (2016b), *Nvidia GeForce GTX 1080*, URL: https://www.nvidia.com/en-us/geforce/10-series/.

– (2017), *Nvidia CUDA compiler version 8.0*, URL: http://docs.nvidia.com/cuda/cuda-compiler-driver-nvcc/index.html.

– (2020a), *CUDA, release: 10.2.89*, URL: https://developer.nvidia.com/cuda-toolkit.

– (2020b), *Nvidia GeForce RTX 3090*, URL: https://www.nvidia.com/en-us/geforce/graphics-cards/30-series/rtx-3090/.

– (2021), *Nvidia CUDA compiler version 11.3*, URL: http://docs.nvidia.com/cuda/cuda-compiler-driver-nvcc/index.html.

Odor, G., Y.-H. Li, A. Yurtsever, Y.-P. Hsieh, Q. Tran-Dinh, M. E. Halabi, and V. Cevher (2016), "Frank-Wolfe works for non-Lipschitz continuous gradient objectives: Scalable poisson phase retrieval", *41st International Conference on Acoustics, Speech and Signal Processing (ICASSP)*, Shanghai, China, pp. 6230–6234.

Olfat, A. and H. Soltanian-Zadeh (2001), "A neural network approach to magnitude retrieval", *Signal Processing*, vol. 81, no. 9, pp. 1879–1888.

Omi, S., T. Uno, T. Arima, and J. Wiart (2019), "Reconstruction of internal field of dielectric objects for noninvasive SAR measurement using boundary integral equation", *IEEE Transactions on Electromagnetic Compatibility*, vol. 61, no. 1, pp. 48–56.

OpenMP Architecture Review Board (2020), *OpenMP application program interface version 5.1*, URL: https://www.openmp.org/wp-content/uploads/OpenMP-API-Specification-5-1.pdf.

*Bibliography*

Oseen, C. W. (1922), "Die Einsteinsche Nadelstichstrahlung und die Maxwellschen Gleichungen", *Annalen der Physik*, vol. 374, no. 19, pp. 202–204.

Osipov, A., H. Kobayashi, and H. Suzuki (2013), "An improved image-based circular near-field-to-far-field transformation", *IEEE Transactions on Antennas and Propagation*, vol. 61, no. 2, pp. 989–993.

Paige, C. C. and M. A. Saunders (1982), "LSQR: An algorithm for sparse linear equations and sparse least squares", *ACM Transactions on Mathematical Software*, vol. 8, no. 1, pp. 43–71.

Panayappan, K. and R. Mittra (2015), "A singularity free MoM-type of formulation using the dipole-moment-based approach", *Progress In Electromagnetics Research*, vol. 151, pp. 33–54.

Paris, D., W. Leach, and E. Joy (1978), "Basic theory of probe-compensated near-field measurements", *IEEE Transactions on Antennas and Propagation*, vol. 26, no. 3, pp. 373–379.

Park, M. Y. and T. Hastie (2007), "L1-regularization path algorithm for generalized linear models", *Journal of the Royal Statistical Society: Series B (Statistical Methodology)*, vol. 69, no. 4, pp. 659–677.

Paulus, A., J. Knapp, and T. F. Eibert (2018a), "Nonconvex phaseless near-field far-field transformation for electrically large problems", *12th European Conference on Antennas and Propagation (EuCAP)*, London, UK.

Paulus, A. and T. F. Eibert (2018a), "Parallel brute-force evaluation of dipole radiation operators on GPUs", *Progress In Electromagnetics Research Symposium (PIERS)*, Toyama, Japan.

– (2018b), "Brute-force GPU accelerated evaluation of dipole-dipole interactions", *23th APS International Symposium on Antennas and Propagation & USNC/URSI National Radio Science Meeting*, Boston, MA, USA, pp. 1839–1840.

– (2019), "Reliable multi-frequency phase retrieval in near-field far-field transformations", *Kleinheubacher Tagung*, Miltenberg, Germany.

– (2020), "Exploiting spatial derivative information in phaseless near-field far-field transformations", *14th European Conference on Antennas and Propagation (EuCAP)*, Copenhagen, Denmark.

Paulus, A., J. Knapp, and T. F. Eibert (2016a), "Nahfeld-Fernfeld Transformation von phasenlosen Nahfeldmessungen", *ITG Workshop Antennen-Messtechnik für zukünftige Funksysteme: "Aktiv, Phasenlos, Automobil"*, Munich, Germany.

– (2016b), "Phasenlose Nahfeld-Fernfeld Transformation von gemessenen Antennenfeldern über nicht-konvexe Optimierung", *Kleinheubacher Tagung*, Miltenberg, Germany.

– (2017a), "Phaseless near-field far-field transformation utilizing combinations of probe signals", *IEEE Transactions on Antennas and Propagation*, vol. 65, no. 10, pp. 5492–5502.

– (2017b), "Phaseless near-field measurements and transformation for electrically large antennas", *5. Nationale Konferenz Satellitenkommunikation in Deutschland*, Bonn, Germany.

– (2017c), "Utilizing partial knowledge of phase differences in convex optimization for amplitude-only near-field far-field transformation", *11th European Conference on Antennas and Propagation (EuCAP)*, Paris, France, pp. 3766–3770.

– (2018b), "Phasenlose Nahfeld-Fernfeld Transformation mit Neuronalen Netzen", *Kleinheubacher Tagung*, Miltenberg, Germany.

Paulus, A., J. Knapp, J. Kornprobst, and T. F. Eibert (2020), "Improved-reliability phase-retrieval with broadband antenna measurements", *14th European Conference on Antennas and Propagation (EuCAP)*, Copenhagen, Denmark.

– (2022, early access), "Reliable linearized phase retrieval for near-field antenna measurements with truncated measurement surfaces", *IEEE Transactions on Antennas and Propagation*.

Paulus, A., J. Kornprobst, J. Knapp, and T. F. Eibert (2021a), "Linear phase retrieval for near-field measurements with locally known phase relations", *15th European Conference on Antennas and Propagation (EuCAP)*.

– (2021b), "Linear phase retrieval for near-field measurements with locally known phase relations", *15th European Conference on Antennas and Propagation (EuCAP)*, Düsseldorf, Germany.

Paulus, A., J. Kornprobst, R. A. M. Mauermayer, and T. F. Eibert (2019), "Comparison of source localization and scatterer modeling in near-field antenna measurements", *13th European Conference on Antennas and Propagation (EuCAP)*, Krakow, Poland.

Pauwels, E. J. R., A. Beck, Y. C. Eldar, and S. Sabach (2018), "On Fienup methods for sparse phase retrieval", *IEEE Transactions on Signal Processing*, vol. 66, no. 4, pp. 982–991.

Pelland, P., G. Hindman, and A. Newell (2013), "Advances in automated error assessment of spherical near-field antenna measurements", *7th European Conference on Antennas and Propagation (EuCAP)*, pp. 793–797.

Petoev, I., V. Tabatadze, and R. Zaridze (2015), "The method of auxiliary sources for eigen frequencies and eigen fields determination", *XXth IEEE International Seminar/Workshop on Direct and Inverse Problems of Electromagnetic and Acoustic Wave Theory (DIPED)*, Lviv, Ukraine, pp. 13–17.

Petre, P. and T. K. Sarkar (1992), "Planar near-field to far-field transformation using an equivalent magnetic current approach", *IEEE Transactions on Antennas and Propagation*, vol. 40, no. 11, pp. 1348–1356.

Pfeiffer, F., T. Weitkamp, O. Bunk, and C. David (2006), "Phase retrieval and differential phase-contrast imaging with low-brilliance X-ray sources", *Nature Physics*, vol. 2, no. 4, pp. 258–261.

Pierri, R., G. D'Elia, and F. Soldovieri (1999), "A two probes scanning phaseless near-field far-field transformation technique", *IEEE Transactions on Antennas and Propagation*, vol. 47, no. 5, pp. 792–802.

Pierri, R. and R. Moretta (2020), "On data increasing in phase retrieval via quadratic inversion: Flattening manifold and local minima", *IEEE Transactions on Antennas and Propagation*, vol. 68, no. 12, pp. 8104–8113.

Pinilla, S., J. Bacca, and H. Arguello (2018), "Phase retrieval algorithm via nonconvex minimization using a smoothing function", *IEEE Transactions on Signal Processing*, vol. 66, no. 17, pp. 4574–4584.

Poincaré, H. (1899), "Sur les propriétés du potentiel et sur les fonctions Abéliennes", *Acta Mathematica*, vol. 22, pp. 1–18.

Polak, E. and G. Ribiere (1969), "Note sur la convergence de méthodes de directions conjuguées", *ESAIM: Mathematical Modelling and Numerical Analysis - Modélisation Mathématique et Analyse Numérique*, vol. 3, no. R1, pp. 35–43.

Poli, R., J. Kennedy, and T. Blackwell (2007), "Particle swarm optimization", *Swarm Intelligence*, vol. 1, no. 1, pp. 33–57.

Polimeridis, A. G. and J. R. Mosig (2010), "Complete semi-analytical treatment of weakly singular integrals on planar triangles via the direct evaluation method", *International Journal for Numerical Methods in Engineering*, vol. 83, no. 12, pp. 1625–1650.

Polyak, B. T. (1969), "The conjugate gradient method in extremal problems", *USSR Computational Mathematics and Mathematical Physics*, vol. 9, no. 4, pp. 94–112.

Popov, S., J. Günther, H.-P. Seidel, and P. Slusallek (2007), "Stackless KD-tree traversal for high performance GPU ray tracing", *Computer Graphics Forum*, vol. 26, no. 3, pp. 415–424.

Powell, M. J. D. (1976), "Some convergence properties of the conjugate gradient method", *Mathematical Programming*, vol. 11, no. 1, pp. 42–49.

Preskill, J. (1984), "Magnetic monopoles", *Annual Review of Nuclear and Particle Science*, vol. 34, no. 1, pp. 461–530.

Press, W. H. (2003), *Numerical Recipes in Fortran 77: The Art of Scientific Computing*, 2nd ed., Cambridge, UK: Cambridge University Press.

Qian, Y., W. R. Deal, N. Kaneda, and T. Itoh (1999), "A uniplanar quasi-Yagi antenna with wide bandwidth and low mutual coupling characteristics", *4th APS International Symposium on Antennas and Propagation & USNC/URSI National Radio Science Meeting*, pp. 924–927.

Qiu, T., P. Babu, and D. P. Palomar (2016), "PRIME: Phase retrieval via majorization-minimization", *IEEE Transactions on Signal Processing*, vol. 64, no. 19, pp. 5174–5186.

Qiu, T. and D. P. Palomar (2017), "Undersampled sparse phase retrieval via majorization–minimization", *IEEE Transactions on Signal Processing*, vol. 65, no. 22, pp. 5957–5969.

Quijano, J. L. A., L. Scialacqua, J. Zackrisson, L. J. Foged, M. Sabbadini, and G. Vecchi (2011), "Suppression of undesired radiated fields based on equivalent currents reconstruction from measured data", *IEEE Antennas Wireless Propagation Letters*, vol. 10, pp. 314–317.

Quijano, J. L. A. and G. Vecchi (2010), "Field and source equivalence in source reconstruction on 3D surfaces", *Progress In Electromagnetics Research*, vol. 103, pp. 67–100.

Qureshi, M. A., C. H. Schmidt, and T. F. Eibert (2013), "Efficient near-field far-field transformation for nonredundant sampling representation on arbitrary surfaces in near-field antenna measurements", *IEEE Transactions on Antennas and Propagation*, vol. 61, no. 4, pp. 2025–2033.

Rajantie, A. (2012), "Introduction to magnetic monopoles", *Contemporary Physics*, vol. 53, no. 3, pp. 195–211.

Ramos, T., B. E. Grønager, M. S. Andersen, and J. W. Andreasen (2019), "Direct three-dimensional tomographic reconstruction and phase retrieval of far-field coherent diffraction patterns", *Physical Review A*, vol. 99, no. 2, p. 023801.

Rao, S., A. Glisson, D. Wilton, and B. Vidula (1979), "A simple numerical solution procedure for statics problems involving arbitrary-shaped surfaces", *IEEE Transactions on Antennas and Propagation*, vol. 27, no. 5, pp. 604–608.

Rao, S., D. Wilton, and A. Glisson (1982), "Electromagnetic scattering by surfaces of arbitrary shape", *IEEE Transactions on Antennas and Propagation*, vol. 30, no. 3, pp. 409–418.

Razavi, S. F. and Y. Rahmat-Samii (2008), "On the uniqueness of planar near-field phaseless antenna measurements based on two amplitude-only measurements", *13th APS International Symposium on Antennas and Propagation & USNC/URSI National Radio Science Meeting*, San Diego, CA, USA.

Razavi, S. F. and Y. Rahmat-Samii (2010), "Phaseless diagnostics for non-rectangular near-field antenna measurement systems", *4th European Conference on Antennas and Propagation (EuCAP)*, Barcelona, Spain.

Remmert, R. (1991), *Theory of Complex Functions*, vol. 122, New York, NY, USA: Springer Science & Business Media.

Rohde & Schwarz GmbH & Co. KG (n.d.), *Double-Ridged Waveguide Horn Antenna*, URL: https://www.rohde-schwarz.com/us/product/hf907-productstartpage_63493-7982.html?.

Rossi, L. and P. J. Cullen (1999), "On the fully numerical evaluation of the linear-shape function times the 3D Green's function on a plane triangle", *IEEE Transactions on Microwave Theory and Techniques*, vol. 47, no. 4, pp. 398–402.

Saad, Y. and M. H. Schultz (1986), "GMRES: A generalized minimal residual algorithm for solving nonsymmetric linear systems", *SIAM Journal on scientific and statistical computing*, vol. 7, no. 3, pp. 856–869.

Sánchez, R. T. and M. S. Castañer (2018), "Evaluation of software defined radio receiver for phaseless near-field measurements", *40th Meeting and Symposium of the Antenna Measurement Techniques Association (AMTA)*, Williamsburg, VA, USA.

Sánchez, R. T., M. S. C. Castañer, and L. Foged (2020a), "Relative phase reconstruction based on multiprobe solutions and post-processing techniques", *14th European Conference on Antennas and Propagation (EuCAP)*, Copenhagen, Denmark.

Sánchez, R. T., M. Sierra Castaner, and L. J. Foged (2020b), "A referenceless antenna measurement system based on software-defined radio [measurements corner]", *IEEE Antennas and Propagation Magazine*, vol. 62, no. 5, pp. 108–118.

Schmidt, C. H., M. M. Leibfritz, and T. F. Eibert (2008), "Fully probe-corrected near-field far-field transformation employing plane wave expansion and diagonal translation operators", *IEEE Transactions on Antennas and Propagation*, vol. 56, no. 3, pp. 737–746.

Schmidt, C. H. and Y. Rahmat-Samii (2009), "Phaseless spherical near-field antenna measurements: Concept, algorithm and simulation", *13th APS International Symposium on Antennas and Propagation*, North Charleston, SC, USA.

Schmidt, C. H., D. T. Schobert, and T. F. Eibert (2011), "Electric dipole based synthetic data generation for probe-corrected near-field antenna measurements", *5th European Conference on Antennas and Propagation (EuCAP)*, Rome, Italy, pp. 3269–3273.

Schmidt, M., G. Fung, and R. Rosales (2007), "Fast optimization methods for l1 regularization: A comparative study and two new approaches", *18th European Conference on Machine Learning (ECML)*, Springer, Warsaw, Poland, pp. 286–297.

Schnattinger, G., C. Lopez, E. Kılıç, and T. F. Eibert (2014), "Fast near-field far-field transformation for phaseless and irregular antenna measurement data", *Advances in Radio Science (ARS)*, vol. 12, pp. 171–177.

Seldin, J. H. and J. R. Fienup (1990), "Numerical investigation of the uniqueness of phase retrieval", *Journal of the Optical Society of America A (JOSA)*, vol. 7, no. 3, pp. 412–427.

Shafarevich, I. R. and A. O. Remizov (2013), *Linear Algebra and Geometry*, Berlin and Heidelberg, Germany: Springer Berlin Heidelberg.

Shechtman, Y., A. Beck, and Y. C. Eldar (2014), "GESPAR: Efficient phase retrieval of sparse signals", *IEEE Transactions on Signal Processing*, vol. 62, no. 4, pp. 928–938.

Sievers, D., T. F. Eibert, and V. Hansen (2005), "Correction to "On the calculation of potential integrals for linear Source distributions on triangular domains"", *IEEE Transactions on Antennas and Propagation*, vol. 53, no. 9, p. 3113.

Soldovieri, F., A. Liseno, G. D'Elia, and R. Pierri (2005), "Global convergence of phase retrieval by quadratic approach", *IEEE Transactions on Antennas and Propagation*, vol. 53, no. 10, pp. 3135–3141.

Sorber, L., M. van Barel, and L. D. Lathauwer (2012), "Unconstrained optimization of real functions in complex variables", *SIAM Journal on Optimization*, vol. 22, no. 3, pp. 879–898.

Steinkraus, D., I. Buck, and P. Y. Simard (2005), "Using GPUs for machine learning algorithms", *8th International Conference on Document Analysis and Recognition (ICDAR)*, vol. 2, Seoul, South Korea, pp. 1115–1120.

Sun, J., Q. Qu, and J. Wright (2018), "A geometric analysis of phase retrieval", *Foundations of Computational Mathematics*, vol. 18, no. 5, pp. 1131–1198.

Sun, M. and J. Liu (2015), "Three modified Polak-Ribière-Polyak conjugate gradient methods with sufficient descent property", *Journal of Inequalities and Applications*, vol. 2015, no. 1, p. 125.

Sun, Y., P. Babu, and D. Palomar (2016), "Majorization-minimization algorithms in signal processing, communications, and machine learning", *IEEE Transactions on Signal Processing*, vol. 65, no. 3, pp. 794–816.

Sunada, S., K. Arai, K. Yoshimura, and M. Adachi (2014), "Optical phase synchronization by injection of common broadband low-coherent light", *Physical Review Letters*, vol. 112, no. 20.

Tai, C.-T. (1994), *Dyadic Green Functions in Electromagnetic Theory*, 2nd ed., IEEE Series on Electromagnetic Waves, New York, NJ, USA: IEEE Press.

Taylor, D. J. (2003), "Accurate and efficient numerical integration of weakly singular integrals in galerkin EFIE solutions", *IEEE Transactions on Antennas and Propagation*, vol. 51, no. 7, pp. 1630–1637.

Theis, T. N. and H.-S. P. Wong (2017), "The end of Moore's law: A new beginning for information technology", *Computing in Science & Engineering*, vol. 19, no. 2, pp. 41–50.

Tian, L. and L. Waller (2015), "3D intensity and phase imaging from light field measurements in an LED array microscope", *Optica*, vol. 2, no. 2, pp. 104–111.

Tihon, D. and C. Craeye (2018), "All-analytical evaluation of the singular integrals involved in the method of moments", *IEEE Transactions on Antennas and Propagation*, vol. 66, no. 4, pp. 1925–1936.

Trzasko, J. and A. Manduca (2009), "Highly undersampled magnetic resonance image reconstruction via homotopic $\ell_0$-minimization", *IEEE Transactions on Medical Imaging*, vol. 28, no. 1, pp. 106–121.

van den Bos, A. (1994), "Estimation of complex parameters", *IFAC Proceedings Volumes*, vol. 27, no. 8, pp. 1429–1433.

Varela, F. R., J. F. Alvarez, B. G. Iraguen, M. S. Castaner, and O. Breinbjerg (2021), "Numerical and experimental investigation of phaseless spherical near-field antenna measurements", *IEEE Transactions on Antennas and Propagation (early access)*.

Varela, F. R., B. G. Iraguen, M. S. Castaner, J. F. Alvarez, M. Mattes, and O. Breinbjerg (2019), "Combination of spherical and planar scanning for phaseless near-field antenna measurements", *41st Meeting and Symposium of the Antenna Measurement Techniques Association (AMTA)*, San Diego, CA, USA.

Vipiana, F., D. R. Wilton, and W. A. Johnson (2013), "Advanced numerical schemes for the accurate evaluation of 4-D reaction integrals in the method of moments", *IEEE Transactions on Antennas and Propagation*, vol. 61, no. 11, pp. 5559–5566.

Waldspurger, I., A. d'Aspremont, and S. Mallat (2015), "Phase recovery, MaxCut and complex semidefinite programming", *Mathematical Programming*, vol. 149, no. 1, pp. 47–81.

Wang, G., G. B. Giannakis, and J. Chen (2017), "Solving large-scale systems of random quadratic equations via stochastic truncated amplitude flow", *25th European Signal Processing Conference (EUSIPCO)*, Kos, Greece, pp. 1420–1424.

Wang, G., G. B. Giannakis, and Y. C. Eldar (2018a), "Solving systems of random quadratic equations via truncated amplitude flow", *IEEE Transactions on Information Theory*, vol. 64, no. 2, pp. 773–794.

Wang, G., G. B. Giannakis, Y. Saad, and J. Chen (2018b), "Phase retrieval via reweighted amplitude flow", *IEEE Transactions on Signal Processing*, vol. 66, no. 11, pp. 2818–2833.

Wang, G., L. Zhang, G. B. Giannakis, M. Akcakaya, and J. Chen (2018c), "Sparse phase retrieval via truncated amplitude flow", *IEEE Transactions on Signal Processing*, vol. 66, no. 2, pp. 479–491.

Wang, K., A. Paulus, T. J. Wachter, U. Siart, and T. F. Eibert (2014), "Compact CW radar transceiver antennas with novel decoupling technique based on neutralization", *8th European Conference on Antennas and Propagation (EuCAP)*, The Hague, Netherlands, pp. 1309–1312.

Wang, L., Y. Zhang, F. Han, J. Zhou, and Q. H. Liu (2020a), "A phaseless inverse source method (PISM) based on near-field scanning for radiation diagnosis and prediction of PCBs", *IEEE Transactions on Microwave Theory and Techniques*, vol. 68, no. 10, pp. 4151–4160.

Wang, W., Y. Han, H. Gao, Y. Wu, Z. Lai, and Y. Liu (2020b), "An improved method of reducing SWE order for phaseless spherical near-field antenna measurement", *AEÜ - International Journal of Electronics and Communications*, vol. 120, p. 153199.

Weiner, J. M., K. C. Cox, J. G. Bohnet, and J. K. Thompson (2017), "Phase synchronization inside a superradiant laser", *Physical Review A*, vol. 95, no. 3.

Williams, R. S. (2017), "What's next? [The end of Moore's law]", *Computing in Science & Engineering*, vol. 19, no. 2, pp. 7–13.

Wilton, D., S. Rao, A. Glisson, D. Schaubert, O. Al-Bundak, and C. Butler (1984), "Potential integrals for uniform and linear source distributions on polygonal and polyhedral domains", *IEEE Transactions on Antennas and Propagation*, vol. 32, no. 3, pp. 276–281.

Wirtinger, W. (1927), "Zur formalen Theorie der Funktionen von mehr komplexen Veränderlichen", *Mathematische Annalen*, vol. 97, no. 1, pp. 357–375.

Wolpert, D. H. and W. G. Macready (1997), "No free lunch theorems for optimization", *IEEE Transactions on Evolutionary Computation*, vol. 1, no. 1, pp. 67–82.

Xiao, L. and T. Zhang (2012), "A proximal-gradient homotopy method for the $\ell_1$-regularized least-squares problem", *29th International Conference on Machine Learning (ICML)*, Edinburgh, UK, pp. 839–846.

Y. Sugimoto, K. Sakakibara, and N. Kikuma (2021), "Iteration-free phase retrieval method using phaseless single-plane near-field", *25th International Symposium on Antennas and Propagation (ISAP)*, Osaka, Japan, pp. 253–254.

Yaccarino, R. G. and Y. Rahmat-Samii (1995), "Phaseless bi-polar near-field measurements using a two-plane squared amplitude interpolation algorithm", *APS International Symposium on Antennas and Propagation*, Newport Beach, CA, USA, pp. 248–251.

– (1997), "Microwave antenna imaging, diagnostics, and phaseless reconstructions", *International Journal of Imaging Systems and Technology*, vol. 8, no. 4, pp. 396–406.

– (1999), "Phaseless bi-polar planar near-field measurements and diagnostics of array antennas", *IEEE Transactions on Antennas and Propagation*, vol. 47, no. 3, pp. 574–583.

Yaghjian, A. (1986), "An overview of near-field antenna measurements", *IEEE Transactions on Antennas and Propagation*, vol. 34, no. 1, pp. 30–45.

Ye, J., H. Schnatz, and L. W. Hollberg (2003), "Optical frequency combs: From frequency metrology to optical phase control", *IEEE Journal of Selected Topics in Quantum Electronics*, vol. 9, no. 4, pp. 1041–1058.

Yinusa, K. A. and T. F. Eibert (2013), "A multi-probe antenna measurement technique with echo suppression capability", *IEEE Transactions on Antennas and Propagation*, vol. 61, no. 10, pp. 5008–5016.

Yinusa, K. A., C. H. Schmidt, and T. F. Eibert (2012a), "Modeling of unknown echoic measurement facilities with equivalent scattering centers", *6th European Conference on Antennas and Propagation (EuCAP)*, Prague, Czech Republic, pp. 2104–2108.

Yinusa, K. A., C. H. Schmidt, and T. F. Eibert (2012b), "Scattering centers modeling of non-anechoic measurement environments", *Advances in Radio Science (ARS)*, vol. 10, pp. 69–73.

Yuan, Z. and H. Wang (2017), "Phase retrieval via reweighted Wirtinger flow", *Applied Optics*, vol. 56, no. 9, pp. 2418–2427.

*Bibliography*

Yurtsever, A., Y.-P. Hsieh, and V. Cevher (2015), "Scalable convex methods for phase retrieval", *6th International Workshop on Computational Advances in Multi-Sensor Adaptive Processing (CAMSAP)*, Cancun, Mexico, pp. 381–384.

Zangwill, A. (2013), *Modern Electrodynamics*, Cambridge, UK: Cambridge University Press.

Zaridze, R. S., R. Jobava, G. Bit-Banik, D. Karkasbadze, D. P. Economou, and N. K. Uzunoglu (1998), "The method of auxiliary sources and scattered field singularities (caustics)", *Journal of Electromagnetic Waves and Applications*, vol. 12, no. 11, pp. 1491–1507.

Zhang, H., Y. Han, and G. Han (2007), "Expansion of the electromagnetic fields of a shaped beam in terms of cylindrical vector wave functions", *Journal of the Optical Society of America B*, vol. 24, no. 6, pp. 1383–1391.

Zhang, H. and Y. Liang (2016), "Reshaped Wirtinger flow for solving quadratic system of equations", *Advances in Neural Information Processing Systems (NIPS)*, vol. 29, pp. 2622–2630.

Zhang, H., Y. Zhou, Y. Liang, and Y. Chi (2017), "A nonconvex approach for phase retrieval: Reshaped Wirtinger flow and incremental algorithms", *The Journal of Machine Learning Research*, vol. 18, no. 1, pp. 5164–5198.

Zhao, H., Y. Zhang, J. Hu, and E.-P. Li (2016), "Iteration-free-phase retrieval for directive radiators using field amplitudes on two closely separated observation planes", *IEEE Transactions on Electromagnetic Compatibility*, vol. 58, no. 2, pp. 607–610.

# Publications of the Author

Hansen, T. B., A. Paulus, and T. F. Eibert (2019), "On the condition number of a normal matrix in near-field to far-field transformations", *IEEE Transactions on Antennas and Propagation*, vol. 67, no. 3, pp. 2028–2033.

Knapp, J., A. Paulus, and T. F. Eibert (2017a), "Implementation and evaluation of the utilization of partial knowledge of phase differences in magnitude only near-field far-field transformations", *Progress In Electromagnetics Research Symposium (PIERS)*, St. Petersburg, Russia.

– (2019a), "Investigation on diversity effects for phaseless near-field far-field transformations", *13th European Conference on Antennas and Propagation (EuCAP)*, Krakow, Poland.

– (2019b), "Reconstruction of squared field magnitudes and relative phases from magnitude-only near-field measurements", *IEEE Transactions on Antennas and Propagation*, vol. 67, no. 5, pp. 3397–3409.

Knapp, J., A. Paulus, J. Kornprobst, U. Siart, and T. F. Eibert (2021), "Multi-frequency phase retrieval for antenna measurements", *IEEE Transactions on Antennas and Propagation*, vol. 69, no. 1, pp. 488–501.

Knapp, J., A. Paulus, C. Lopez, and T. F. Eibert (2017b), "Comparison of non-convex cost functionals for the consideration of phase differences in phaseless near-field far-field transformations of measured antenna fields", *Advances in Radio Science (ARS)*, vol. 15, pp. 11–19.

Kornprobst, J., J. Knapp, R. A. M. Mauermayer, O. Neitz, A. Paulus, and T. F. Eibert (2021a), "Accuracy and conditioning of surface-source based near-field to far-field transformations", *IEEE Transactions on Antennas and Propagation*, vol. 69, no. 8.

Kornprobst, J., A. Paulus, T. F. Eibert, and R. A. M. Mauermayer (2019), "Method-of-moments modeling of conducting objects within the fast irregular antenna field transformation algorithm", *41st Antenna Measurement Techniques Association Symposium (AMTA)*, San Diego, CA, USA.

Kornprobst, J., A. Paulus, J. Knapp, and T. F. Eibert (2021b), "Phase retrieval for partially coherent observations", *IEEE Transactions on Signal Processing*, vol. 69, pp. 1394–1406.

Paulus, A., J. Knapp, and T. F. Eibert (2018a), "Nonconvex phaseless near-field far-field transformation for electrically large problems", *12th European Conference on Antennas and Propagation (EuCAP)*, London, UK.

Paulus, A. and T. F. Eibert (2018a), "Parallel brute-force evaluation of dipole radiation operators on GPUs", *Progress In Electromagnetics Research Symposium (PIERS)*, Toyama, Japan.

– (2018b), "Brute-force GPU accelerated evaluation of dipole-dipole interactions", *23rd APS International Symposium on Antennas and Propagation & USNC/URSI National Radio Science Meeting*, Boston, MA, USA, pp. 1839–1840.

– (2019), "Reliable multi-frequency phase retrieval in near-field far-field transformations", *Kleinheubacher Tagung*, Miltenberg, Germany.

– (2020), "Exploiting spatial derivative information in phaseless near-field far-field transformations", *14th European Conference on Antennas and Propagation (EuCAP)*, Copenhagen, Denmark.

Paulus, A., J. Knapp, and T. F. Eibert (2016a), "Nahfeld-Fernfeld Transformation von phasenlosen Nahfeldmessungen", *ITG Workshop Antennen-Messtechnik für zukünftige Funksysteme: "Aktiv, Phasenlos, Automobil"*, Munich, Germany.

– (2016b), "Phasenlose Nahfeld-Fernfeld Transformation von gemessenen Antennenfeldern über nicht-konvexe Optimierung", *Kleinheubacher Tagung*, Miltenberg, Germany.

Paulus, A., J. Knapp, and T. F. Eibert (2017a), "Phaseless near-field far-field transformation utilizing combinations of probe signals", *IEEE Transactions on Antennas and Propagation*, vol. 65, no. 10, pp. 5492–5502.

– (2017b), "Phaseless near-field measurements and transformation for electrically large antennas", *5. Nationale Konferenz Satellitenkommunikation in Deutschland*, Bonn, Germany.

– (2017c), "Utilizing partial knowledge of phase differences in convex optimization for amplitude-only near-field far-field transformation", *11th European Conference on Antennas and Propagation (EuCAP)*, Paris, France, pp. 3766–3770.

– (2018b), "Phasenlose Nahfeld-Fernfeld Transformation mit Neuronalen Netzen", *Kleinheubacher Tagung*, Miltenberg, Germany.

Paulus, A., J. Knapp, J. Kornprobst, and T. F. Eibert (2020), "Improved-reliability phase-retrieval with broadband antenna measurements", *14th European Conference on Antennas and Propagation (EuCAP)*, Copenhagen, Denmark.

– (2022, early access), "Reliable linearized phase retrieval for near-field antenna measurements with truncated measurement surfaces", *IEEE Transactions on Antennas and Propagation*.

Paulus, A., J. Kornprobst, J. Knapp, and T. F. Eibert (2021a), "Linear phase retrieval for near-field measurements with locally known phase relations", *15th European Conference on Antennas and Propagation (EuCAP)*.

– (2021b), "Linear phase retrieval for near-field measurements with locally known phase relations", *15th European Conference on Antennas and Propagation (EuCAP)*, Düsseldorf, Germany.

Paulus, A., J. Kornprobst, R. A. M. Mauermayer, and T. F. Eibert (2019), "Comparison of source localization and scatterer modeling in near-field antenna measurements", *13th European Conference on Antennas and Propagation (EuCAP)*, Krakow, Poland.

Wang, K., A. Paulus, T. J. Wachter, U. Siart, and T. F. Eibert (2014), "Compact CW radar transceiver antennas with novel decoupling technique based on neutralization", *8th European Conference on Antennas and Propagation (EuCAP)*, The Hague, Netherlands, pp. 1309–1312.